SHAPING LIGHT EMISSION FOR SOLID STATE LIGHTING WITH PLASMON NANOANTENNAS

Cover image: Lighting is about technology, civilization, and art. Photograph was taken by Lars Freisem in *Tang Furong Garden*, Xi'an, China, during the Lantern Festival (Yuanxiao Jie), February 11th, 2017.

Ph.D. thesis University of Amsterdam, January 2018
Shaping light emission for solid state lighting with plasmon nanoantennas
Ke Guo

ISBN 978-94-92323-16-3

A digital version of this thesis can be downloaded from http://www.amolf.nl.

SHAPING LIGHT EMISSION FOR SOLID STATE LIGHTING WITH PLASMON NANOANTENNAS

ACADEMISCH PROEFSCHRIFT

ter verkrijging van de graad van doctor
aan de Universiteit van Amsterdam
op gezag van de Rector Magnificus
prof. dr. ir. K. I. J. Maex
ten overstaan van een door het College voor Promoties ingestelde
commissie, in het openbaar te verdedigen in de Agnietenkapel
op woensdag 10 januari 2018, te 14:00 uur

door

Ke Guo

geboren te Jiangxi, China

Promotor:	prof. dr. A. F. Koenderink	Universiteit van Amsterdam
Copromotor:	prof. dr. J. Gómez Rivas	Technische Universiteit Eindhoven
Overige leden:	prof. dr. M. P. van Exter	Universiteit Leiden
	dr. E. C. Garnett	AMOLF
	prof. dr. T. Gregorkiewicz	Universiteit van Amsterdam
	prof. dr. P. C. M. Planken	Universiteit van Amsterdam
	dr. R. Sapienza	Imperial College London
	prof. dr. F. E. Schreck	Universiteit van Amsterdam

Faculteit der Natuurwetenschappen, Wiskunde en Informatica

This work was carried out at the
Center for Nanophotonics, AMOLF,
Science Park 104, 1098 XG Amsterdam, The Netherlands,
where a limited number of copies of this dissertation is available.

This work is part of the research programme of
the Netherlands Organisation for Scientific Research (NWO)
and was performed at the research institute AMOLF.
This work is part of the research programme LEDMAP with project number 12754
which is (partly) financed by
the Netherlands Organisation for Scientific Research (NWO).

Contents

1

Introduction

1.1 Light matter interaction and solid state lighting

Light matter interaction is essential for life. Plants use photosynthesis to convert light into chemical energy that ultimately fuels almost all activities of life, and produces oxygen [1]. Light scattered by matters hits retinas in eyes and initiates a cascade of chemical and electrical events that ultimately result in vision, presenting one of the most important sensory inputs for the vast majority of animal lifeforms [2]. For human beings, light matter interaction is not only of biological significance, but is also utilized in a substantial number of technologies that have become indispensable in society. Artificial lighting devices have been used since millennia to bring light into the dark. Solar cells that convert sunlight into electricity are developing into a major renewable energy source, and are one of the most promising solutions to the growing energy problem [3, 4]. The displays of many everyday devices such as televisions, computers and smart phones, are essentially collections of micro light emitting components. Present-day internet relies on fiber-optic communication technology for long distance, large bandwidth data transmission [5]. The study of light-matter interaction is a vibrant branch of research in physics, material science and engineering that covers a wide range of research topics, such as photovoltaics, lighting, lasing, quantum communication, sensing, nano-medicine, etc. For most of the research and technologies involving light matter interaction, one important premise is efficient generation of light that provide the requisite properties regarding spectrum, directionality, and coherence properties. In this thesis, we focus on light generation for applications in lighting and projection.

Significant progress has been made in lighting technologies over the past 200 years, from the invention of first incandescent lamps and gas-discharge lamps in the 19th century, to the development of the currently popular lighting devices: halogen

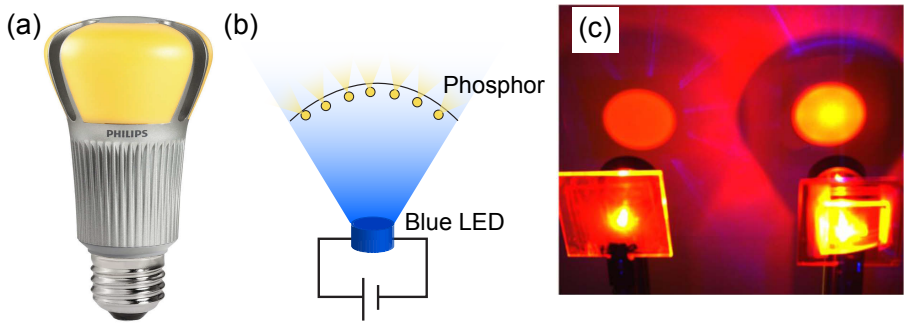

Figure 1.1: (a) A picture of a commercial white LED light bulb [6]. (b) An illustration of white LED composed of a blue LED and yellow phosphor. (c) Photograph of the emission from a phosphor layer (left) compared with the emission from phosphor layer enhanced by a hexagonal array of Al antennas (right) from Ref. [7].

incandescent lamps, compact fluorescent lamps and light emitting diodes (LEDs) [8]. Fig. 1.1(a) shows a typical commercial LED lamp. The major task of lighting technologies is to produce highly efficient, bright and robust lighting devices. The efficiency of a light source is measured by luminous efficacy, i.e., the ratio of luminous flux to consumed power [9]. Luminous flux is the perceived power flux of visible light, accounting not just for the photon flux emitted by a source but also for the sensitivity of human eyes at different wavelengths. Table 1.1 shows commonly used lighting devices and comparison of their luminous efficacy and lifetime summarized by Ref. [10]. Among them, LED-based lamps stand out for a high efficacy, similar to high-intensity discharge lamps, higher than fluorescent lamps, and seven times higher than traditional incandescent lamps. Meanwhile, LEDs have also shown advantages in ultra-long lifetime, strong vibration and shock resistance, ultra-short switching time (ms scale), and better light output quality (minimum ultraviolet and infrared radiation), making them ideal energy-saving lighting solutions. Thus, LED lighting contributes to solving the global energy crisis by saving energy [11]. Moreover, LEDs in tandem with solar cells are a transformative technology for third-world countries, as they allow lighting of homes without access to the electricity grid [12]. The development in LEDs have led to a new field of lighting technology, i.e., solid-state lighting (SSL), which is highlighted by the Nobel prize in physics in 2014 for the invention of the highly efficient blue LED [13].

High-brightness LEDs typically have spectral bands with FWHM of 10-100 nm [14], much narrower than the visible spectrum. Therefore, single LEDs do not produce white light individually and cannot correctly reveal the color of illuminated objects. The ability of faithfully rendering different colors compared with natural white light is measured with a so-called color rendering index (CRI) [15]. To generate white light with a good CRI, two approaches are often used. One is to mix the emission from multiple LEDs of different colors, typically three primary colors: red, blue and green [16]. This solution is handicapped in terms of luminous efficacy by the

Type	Efficacy (lm/W)	Lifetime (hour)
Fluorescent		
Linear fluorescent lamps	65-110	24,000-80,000
Compact fluorescent lamps	60-80	10,000
High-intensity discharge		
Metal Halide	70-115	5,000-30,000
High-pressure sodium	50-140	16,000-40,000
Incandescent		
Standard "A-19"	10-17	750-2,500
Halogen incandescent	12-22	1,000-4,000
Reflector	12-19	2,000-3,000
LEDs		
Ominidirectional lamps	70-130	25,000-50,000
Directional lamps	61-140	25,000-50,000

Table 1.1: Comparison of efficacy and lifetime of common lighting devices [10].

relatively lower efficiency of green-yellow LEDs, which can be attributed to the large defect density in the relevant InGaN semiconductors [17, 18]. A second drawback of combining RGB LEDS is that the human eye is sensitive to minute (1 to 2 nm) variations in wavelength, making it extremely hard to make white LEDS of a reproducible color white. The other approach is to use a phosphor to convert quasi-monochromatic light from a blue or UV LED to broad-spectrum white light [19]. The currently most popular white LED solution uses a blue LED and a yellow phosphor. Fig. 1.1(b) illustrates how white light is generated in such a system.

Challenges in high-efficiency phosphor converted LEDs mainly lie in two aspects. On the one hand, the conversion efficiency is limited by the absorbance and efficiency of phosphors. The absorbance determines the amount of phosphor material needed for the required amount of color conversion and enhancing the absorbance can reduce the material consumption. The efficiency of a phosphor determines the amount of green, yellow and red light that a phosphor emits after absorbing a given amount of blue light, in competition with non-radiative processes, and emission of infrared or deep red light that is invisible to human eyes.

A second challenge for high-efficiency phosphors lies in the distribution of their emission over angle. Phosphors usually have a Lambertian emission pattern, i.e., an emission intensity proportional to the cosine of the angle between the emission direction and the surface normal [20, 21]. How light spreads out in angle and area is described by etendue [22]. A simple phosphor-converted LED has a high etendue and is desirable for ambient lighting applications. However, for applications such as outdoor (street) lighting, automotive front lighting and projection, a low etendue, i.e., a highly directional light source with light emitting from a small area, is preferred [23]. Bulky secondary optics are usually used to collimate the light from Lambertian emitters [23],

but they limit the compactness of the device.

Researchers have found that plasmonic nanostructures, sometimes also referred to as "optical antennas", can be a potential solution that addresses both issues. It was demonstrated that the plasmon resonances supported by periodic arrays of metallic nanoantennas, can modify electric field distribution in the phosphor and enhance the absorption of the blue LED light [24, 25], leading to strongly enhanced directional emission [24, 26–28]. Fig. 1.1(b) (taken from Ref. [7]) shows a comparison of the emission from a simple unpatterned phosphor layer and the emission from the same phosphor layer with a hexagonal array of Al antennas, which is significantly brighter in the forward direction. Meanwhile, it was also shown that a phosphor layer embedded with arrays of metallic nanoantennas can work as a distributed feedback (DFB) laser [29–34], with the concomitant low etendue and narrow spectral bandwidth expected from lasers.

The current understanding of plasmon-based phosphor-converted LEDs and plasmon DFB lasers leave open several important questions. First, most reports so far have studied average enhancements in terms of fluorescence brightness as a function of pump geometry and lattice geometry [24–28], where averaging is over an entire ensemble of emitters. This leaves open the question how emission enhancements and penalties of plasmonic mechanisms depend on where fluorophores are in the unit cell. Second, it is an open question whether and how the plasmonic structures would influence emission rates, as opposed to just brightness. Further, one may ask how the array pattern could be optimized for lighting applications. In framework of driving plasmonic DFB lasers, it is unclear what the significant differences from traditional DFB lasers are, and what these differences could imply for applications. This thesis tries to answer some of these questions. We look into the emission control by plasmonic nanostructures in Chapter 2-4 and plasmon DFB lasers in Chapter 5-6.

Before introducing the work of the thesis, we review a few underlying physics concepts. In Section 1.2, we introduce how a phosphor converts blue light into green and red, i.e., the phenomenon of spontaneous emission. In Section 1.3, we discuss relevant mechanisms that plasmonic structures use to manipulate spontaneous emission, and current research progress in optical antennas. In Section 1.5, we introduce stimulated emission and lasers.

1.2 Spontaneous emission

Remote-phosphor based LEDs rely on spontaneous emission to generate longer wavelength light from incident blue pump light emitted by a blue LED. Spontaneous emission is a process in which a quantum mechanical system spontaneously decays from an excited energy state to a lower energy state by releasing the energy in the form of a photon [35]. It is widely involved in many common phenomena in nature and life, such as the chemiluminescent reaction responsible for the glow of fireflies [36]. Depending on whether the excited state is populated electrically, chemically, thermally, or by absorption of light, spontaneous emission can be further classified. The type of

spontaneous emission phenomenon in a remote phosphor is called fluorescence.

Fluorescence is the emission of light from a substance (fluorophore) excited by absorbing light. It is distinguished from a similar phenomenon called phosphorescence depending on the nature of the underlying quantum mechanical transition [37]. The relevant energy states and processes are usually illustrated by a Jablonski diagram [38], as shown in Fig. 1.2, which is typical for organic fluorescent molecules. Electrons in fluorophores are paired with opposite spins, forming a singlet state (S_0), with vibrational fine structure [39]. At room temperature, thermal energy ($k_B T \approx 26$ meV for 25 °C) is much lower than the energy required to populate the excited vibrational states (typically 150 to 200 meV apart) [39]. Therefore, absorption occurs mostly from fluorophores with the lowest vibrational energy. By absorbing a photon, a fluorophore can be excited to a higher vibrational level of the first (S_1) or second (S_2) excited electronic states. Most commonly, the excited molecule would rapidly relax to the lowest vibrational level of S_1 during a process called internal conversion. Internal conversion generally occurs within 10^{-12} s or less [39], which is much faster than other processes and is generally completed prior to the photon radiation.

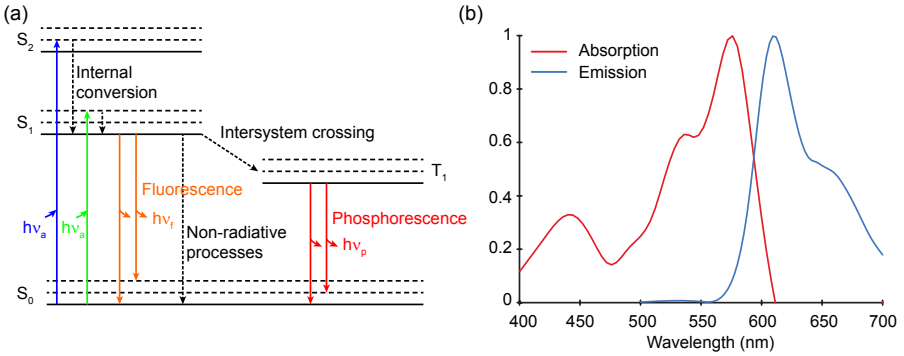

Figure 1.2: (a) An example of a Jablonski diagram showing energy states and transition processes involved in fluorescence. (b) Normalized absorption and emission spectra of LUMOGEN red F 305 in solvent CH_2Cl_2.

After internal conversion, the excited fluorophore can return to a vibrational level of S_0 by emitting a photon, typically in a time scale of 10^{-8} s, and then quickly reach thermal equilibrium (within 10^{-12} s) [39]. This photon emission is fluorescence. As the fluorophore can return to a higher vibrational ground state when emitting the photon, the emission spectrum usually shows the vibrational structure of S_0. As the excitation doesn't alter the nuclear geometry, the vibrational levels have similar spacings for S_0 and S_1. As a result, the emission spectrum is typically a mirror image of the absorption spectrum (for $S_0 \rightarrow S_1$ transition) at lower frequency. This rule of thumb is called the Franck-Condon principle [40, 41]. The associated frequency shift between absorption and emission maximum is called Stokes shift [42]. The Stokes shift allows phosphors to convert high frequency blue or UV light into lower frequency green, yellow or red light that is needed for white light. Apart from the spontaneous emission of the photon, non-

radiative processes are also commonly present. A fluorophore in state S_1 can convert to the first triplet state T_1 when one of the electron spins is flipped. This process is called intersystem crossing. Emission also happens during the transition from T_1 to S_0 and is called phosphorescence. This transition is generally spin forbidden and therefore is several orders of magnitude slower than fluorescence. In this thesis, we are only interested in fast photon emission processes and do not consider the phosphorescence photons. Intersystem crossing, as well as other non-radiative decays such as quenching and energy transfer, can happen within a similar time scale as fluorescence emission. They compete with fluorescence and reduce the photon output.

The performance of fluorophores is usually characterized by the fluorescence lifetime (τ) and quantum yield (QY). The fluorescence lifetime is the average time a molecule spends in the excited state before returning to the ground state [39]. From the Jablonski diagram, it can be easily seen that the fluorescence lifetime is determined by the rates of radiative and non-radiative decay (γ_r and γ_non) as

$$\tau = \frac{1}{\gamma_\mathrm{r} + \gamma_\mathrm{non}}. \tag{1.1}$$

For an ensemble of excited fluorophores with uniform decay rates, the decay process can be described with a single exponential function as

$$P(t) = P(0)e^{-(\gamma_\mathrm{r}+\gamma_\mathrm{non})t} = P(0)e^{-t/\tau}, \tag{1.2}$$

with $P(t)$ the time dependent population of the fluorophores at the excited state, which is proportional to the probability of emitting a photon.

The fluorescence QY is the ratio of the number of photons emitted to the number absorbed, and can be calculated by

$$\mathrm{QY} = \frac{\gamma_\mathrm{r}}{\gamma_\mathrm{r} + \gamma_\mathrm{non}}. \tag{1.3}$$

For luminous efficacy, a near-unity QY is desirable, which requires $\gamma_\mathrm{r} \gg \gamma_\mathrm{non}$. It should be noted that in a remote phosphor scenario one requires the conversion of blue to higher-wavelength photons, i.e., one requires a sizable Stokes shift. Therefore, remote phosphors fundamentally have a power efficiency below 100% even at near-unity QY, due to the energy difference between absorbed and emitted photon that is converted to heat.

To understand the emission process and quantum yield, it is important to understand the origin of the radiative and nonradiative decay rates of a fluorophore. The radiative rate γ_r is dependent both on electronic wavefunction properties of the emitter, and on the available photon modes supported by the optical system, i.e., the local density of optical states (LDOS) [43]. This can be understood from Fermi's golden rule, which states that the transition rate of a quantum system from state $|i\rangle$ to a continuum or discrete set of final states $|f\rangle$ is [44]

$$\gamma = \frac{2\pi}{\hbar^2} \sum_f |\langle f|\hat{H}'|i\rangle|^2 \delta(E_f - E_i). \tag{1.4}$$

Here H' is the interaction Hamiltonian and the δ function ensures energy conservation. The spontaneous emission of a fluorescent molecule can be described using the dipole operator dipole $\hat{\boldsymbol{\mu}}$ and the electric field operator at the emitter position $\boldsymbol{r}_0$ as $\hat{H}' = -\hat{\boldsymbol{\mu}} \cdot \hat{\boldsymbol{E}}(\boldsymbol{r}_0)$. This form indicates that a strong electric field resonant with the transition dipole can potentially enhance the spontaneous emission rate. Following quantum electrodynamics [43, 45], the above emission rate can be derived to have the form

$$\gamma = \frac{2\pi\omega_0}{3\hbar\varepsilon_0}|\boldsymbol{\mu}|^2\rho(\boldsymbol{r}_0,\omega_0), \tag{1.5}$$

where $\boldsymbol{\mu} = \langle f|\hat{\boldsymbol{\mu}}|i\rangle|$ is the transition dipole moment determined by the fluorophore. This transition dipole moment is strictly an electronic property of the molecule, depending on the wavefunction overlap between the ground and excited state. Instead, the LDOS $\rho(\boldsymbol{r}_0,\omega_0)$ at the position of the transition dipole $\boldsymbol{r}_0$, for emitted photon frequency ω_0 is strictly a property of the optical structure around the emitter only. For an optical system without a preferential dipole orientation or probed by a random ensemble of dipole orientations, the total LDOS is often defined as

$$\rho(\boldsymbol{r}_0,\omega_0) = \frac{2\omega_0}{\pi c^2}\mathrm{Im}\{\mathrm{Tr}[\boldsymbol{G}(\boldsymbol{r}_0,\boldsymbol{r}_0;\omega_0)]\}, \tag{1.6}$$

with $\boldsymbol{G}(\boldsymbol{r}_0,\boldsymbol{r}_0;\omega_0)$ the Green's function given by the optical environment [46].

Purcell in 1946 [47] first realized the important implication of the LDOS in Fermi's Golden rule: one can accelerate spontaneous emission by engineering resonances in LDOS. Modifications of spontaneous emission rates by a variety of optical systems have been demonstrated, including planar interfaces [48], cavities [49, 50], photonic crystals [51, 52] and metallic nanostructures [53–55]. While LDOS control is mainly pursued in context of quantum optics with single emitters, it can also contribute to solid-state lighting. Accelerating radiative rates can improve phosphor efficiency, thereby outcompeting nonradiative rates [56–58]. Also, if one can engineer the modes appearing in the LDOS to correspond to a narrow distribution of far-field wave vectors, one can preferentially coupled all emission into a narrow cone of angles [24, 26, 27, 59, 60]. In this thesis, we are interested in the modification of spontaneous emission by optical antennas that are introduced in the following section.

1.3 Optical antennas

Optical nanoantennas are analogues to radio antennas, which have been invented to convert the energy of free propagating radiation to localized energy, or vice versa [61]. They are usually metallic nanostructures. The free electron gas in metals like silver, gold and aluminium can sustain surface charge density oscillations that resonate with incident light at distinct frequencies and are known as surface plasmon resonances (SPRs) [62]. SPRs at a metal-dielectric interface can give rise to strongly enhanced optical near-fields which are spatially confined near the metal surface [63]. When the electron gas is confined in three dimensions, in a sub-wavelength metallic nanostructure,

the Coulomb interaction between the overall displaced electrons and the metal lattice can give rise to localized surface plasmon resonance (LSPR) with a charge density and electric field distributions that is strongly dependent on the geometry of the nanostructure [62]. A suitable geometry can enable extreme local charge accumulations, resulting in strongly enhanced optical fields on nanometer scale.

The most simple and well studied geometry for nanoantennas is a nanosphere. The optical response of spheres can be analytically calculated using Mie theory [64]. Nanospheres much smaller than the wavelength are usually approximated as point dipoles, with a dipole moment induced by the incident electric field $\boldsymbol{E}_0$ according to

$$\boldsymbol{\mu} = \varepsilon_m \alpha \boldsymbol{E}_0, \tag{1.7}$$

where the polarizability α is essentially the first coefficient in a Mie expansion. When estimated in the electrostatic approximation (setting the speed of light to infinity), the polarizability reads [65]

$$\alpha = 4\pi\varepsilon_0 r^3 \frac{\varepsilon_\mu - \varepsilon_m}{\varepsilon_\mu + 2\varepsilon_m}, \tag{1.8}$$

with ε_m and ε_μ the relative permitivity of the surrounding medium and of the sphere, and r the radius of the sphere. For metals, ε_μ is usually described by treating the electrons as free-electron gas in the Drude-Sommerfeld model as [43]

$$\varepsilon_\mu = 1 - \frac{\omega_p^2}{\omega^2 + \mathrm{i}\Gamma\omega}. \tag{1.9}$$

Here $\omega_p \sqrt{ne/(m_e\varepsilon_0)}$ is the volume plasma frequency with n the electron density, e and m_e the charge and effective mass of the electrons. $\Gamma = v_F/l$ is a damping term with v_F the Fermi velocity and l the electron mean free path. Typically, for metals like silver and gold ω_p is a frequency in the UV, while Ohmic loss can be quite small since $\Gamma < 0.01\omega_p$. For example, gold has $\omega_p = 13.8\times10^{15}\mathrm{s}^{-1}$ and $\Gamma = 1.075\times10^{14}\mathrm{s}^{-1}$ [66, 67]. Therefore, the real part of ε_μ is usually negative for metals in the visible spectrum. When $\mathrm{Re}\varepsilon_\mu = -2\varepsilon_m$, i.e., $\omega \approx \omega_p/\sqrt{3}$, an LSPR occurs. For aluminium, silver and gold, these resonances occur across the visible spectrum.

From the polarizability, the scattering and absorption cross-sections can be calculated as

$$\sigma_{\mathrm{scatt}} = \frac{k^4}{6\pi\varepsilon_0^2}|\alpha|^2, \tag{1.10}$$

$$\sigma_{\mathrm{abs}} = \frac{k}{\varepsilon_0}\mathrm{Im}\alpha, \tag{1.11}$$

with k the wave vector in the medium. Apart from nanospheres, point dipole approximations are also widely used on other nanoantenna geometries, with polarizabilities depending on the geometry [65], and sometimes consideration of magnetic dipole [68–71] and multi-polar effects [72].

SPRs enable optical antennas to manipulate the photoluminescence of nearby emitters through different mechanisms. These include enhancing the absorption of

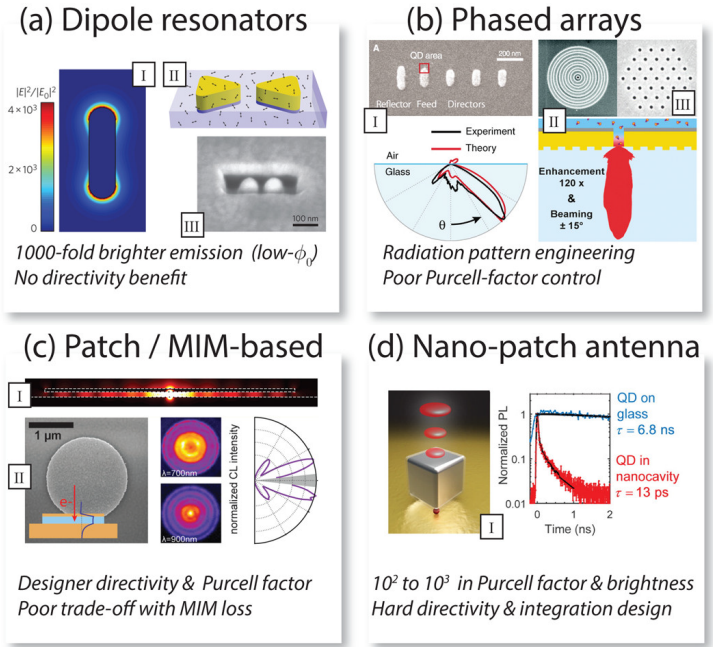

Figure 1.3: Single-photon nanoantenna classes of which metrics are reported in Table 1.2. Figure is adapted from Ref. [73], which is copyright of the American Chemical Society. (a) Dipole antennas like nanorods and dimer/gap antennas. (b) Phased array nanoparticle or nanohole antennas (c) Patch antennas. (d) nanopatch natennas based on a metal nanoparticle-dielectric-spacer-metal.

pump light, modifying radiation directivity, and accelerating emission (γ_r), at the risk of additional quenching due to absorption by the metal. The QY of the system can be modified by both the enhancement of γ_r and by the quenching associated by Ohmic loss in the metal. The net effect depends on the intrinsic QY of the emitter. For high QY emitters, enhancing γ_r does not help increasing the system QY, while the quenching can reduce the system QY. For low QY emitters, enhancing γ_r can significantly improve the system QY [73]. The physics of these effects has been studied in detail on the level of single emitters coupled to single antennas in the community of single-molecule microscopy. To achieve different functions, a variety of antenna designs have been reported, such as dipole antennas akin to the nanosphere [54, 55], patch antennas [74–76], nanopatch antennas [77, 78], and phased-array antennas [59, 60, 79–82]. These geometries are illustrated in Fig. 1.3 (from Ref. [73]). Based on the summary in Ref. [73], we list a few relevant performance metrics of different antennas that are reported by previous experimental works in Table 1.2. Dipole antennas have modest performances in emission enhancement, but are an ideal experimental system to test semi-analytical models. Patch and nanopatch antennas can provide record high Purcell enhancements up to 500 to 2000 times, at reported net quantum efficiencies of 20

to 50% [77, 78]. They are especially suitable for enhancing the efficiency of low QY emitters and manipulating the spectrum. Both dimer antennas and nanopatch antennas can achieve high pump enhancement up to 100-150 through the strong confinement of the pump field [77, 78, 83]. On the other hand, they provide little or only modest emission directivity control [77, 78]. This is because directional emission requires extended (wavelength-sized) field distributions due to the uncertainty principle for conjugate variables in Fourier transforms. Phased-array antennas are extended structures that have modest area-averaged Purcell enhancement and pump enhancement. They are usually designed for strong emission directivity control through particular array arrangements, such as Yagi-Uda [79, 80] , bull's eye [59, 60] and periodic antenna arrays [24, 26, 27, 82]. Their essential idea is that an emitter embedded in the antenna will polarize all the antenna elements in its near field. The radiation that finally ends up in the far field is the coherent sum of the field originally emitted by the emitter, plus the radiation from the induced secondary sources, in vein of Huygen's principle. By properly designing the geometry, one can achieve an extended, i.e., wavelength-sized distribution of sources with a relative phase that is conducive to directional emission.

1.4 Plasmonics for solid state lighting

A common phosphor material in SSL is cerium doped yttrium aluminum garnet (YAG:Ce), which is usually dispersed in an epoxy resin surrounding the LED [89]. When pumped with blue light, YAG:Ce emits with broad emission spectrum from 500 nm to 650 nm and a high QY of 97 % [90]. Therefore, the constraints in plasmonics for solid state lighting are quite different from the usual constraints in

	source QY (%)	system QY (%)	total brightness enh.	pump enh.	Rate enh.	LDOS
Nanosphere [54, 55]	100	50	13-20	25	22	~ 22
Nanorod [84, 85]	2	17	1000	130		~ 9
Bow tie [83]	2.5	20	1340	180	27	~ 800
Lithographic dimer [86]	8	57	1100	144	4	~315
DNA-bound dimer [87]	65	70	300		70	
DNA-bound dimer [88]	65	80	475			
DNA-bound dimer [88] (quencher added)	<10	75	5000			
Patch [74–76]	100	40			60-80	~60-80
Nanopatch [77, 78]	20	20-50	1900	170	>540	>2000
Yagi-Uda [79, 80]						
Bull's eye [59, 60]	30	60	80	5	2	

Table 1.2: Reported performance metrics from experiments on different antennas (remade based on Table 1 of Ref. [73]).

plasmon antenna studies. First, plasmon antennas are generally studied for obtain optimum performance for a single emitter that is judiciously placed with nanometric accuracy at a predetermined optimal location [59, 60, 78–80, 83, 91]. In contrast, bright emission from phosphors requires high performance when averaged over a spatial and orientational distribution of many fluorophores. A second difference is that the largest benefits of plasmon antennas have been reported in framework of improving intrinsically poor emitters by Purcell enhancement [78, 91]. However, Purcell enhancement can hardly enhance the QY of phosphors since it is already high. Nevertheless, the luminous efficacy can be optimized. Due to the different sensitivity of light of different colors to the human eye, a spectrum with 30-50 nm peaks in blue, green (, yellow) and red can potentially lead to higher luminous efficacy and similar CRI compared with a broad spectrum [92]. Therefore, the luminous efficacy can be improved if we can modify the emission spectrum of the remote phosphor using wavelength-dependent Purcell enhancements. Furthermore, remote phosphors can also benefit from pump enhancement [24, 25] and directivity control [24, 26–28] if it can be imparted by optical antennas without a detrimental absorption loss in the metal. Pump enhancement increases the conversion efficiency of the phosphor and can therefore reduce the material consumption. Directional enhancement may enable low etendue emission without using secondary optics.

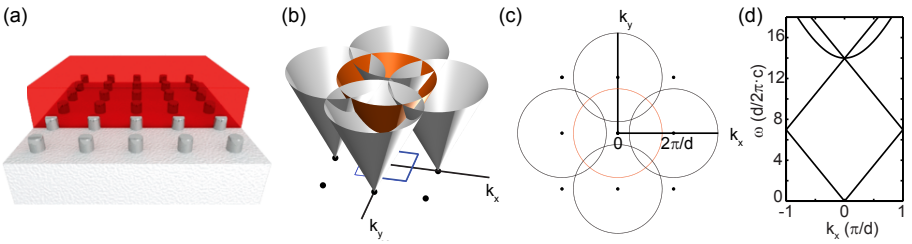

Figure 1.4: (a) An illustration of a periodic array of antennas embedded in a waveguide layer containing phosphors. Reprinted with permission from S. R. K. Rodriguez et al, Phy. Rev. B, 90, 235406, 2014 (Ref. [93], Figure 1(a)). Copyright (2014) by the American Physical Society. (a) An illustration of free folded photonic bands for a periodic antenna array. Orange cone represents a waveguide mode and silver cones are out-coupled waveguide modes by Bragg diffraction. (b) A cross-section of (a) at fixed frequency. (c) A cross-section of (a) at $k_y = 0$.

Due to reasons mentioned above, plasmonics for solid-stated lighting does not use the narrow-gap enhancements evident in bow tie [83], nanorod [84, 85], dimer [86] or nanopatch antennas [77, 78], but has instead converged on periodic lattices that act as extended phased arrays [24, 26–28]. Periodic antenna arrays are interesting for SSL in combination with phosphors embedded in a two dimensional waveguide layer. They can be cost-effectively integrated with the remote phosphors by means of soft-conformal imprint lithography, a technique that allows faithful replication of nanostructures without time-intensive tools like electron beam lithography [94]. Fig. 1.4 illustrates a typical optical system containing a periodic array of antennas and a phosphor waveguide layer. In a waveguide containing phosphors, the majority

of emission goes into the waveguide mode(s), carrying an in plane momentum of length $|\mathbf{k}_{\parallel,\mathrm{WG}}| = n_{\mathrm{WG}}\omega/c$, where n_{WG} is the mode index [95]. The periodic lattice causes diffraction according to the grating law $\mathbf{k}_{\parallel,\mathrm{out}} = \mathbf{k}_{\parallel,\mathrm{WG}} + \mathbf{G}$, with $\mathbf{G}$ a grating reciprocal lattice vector [96]. By judicious choice of grating pitch d, which sets the reciprocal lattice vector length $|\mathbf{G}| = 2\pi/d$, the emission into the waveguide mode can be diffracted to be normal to the phosphor layer, leading to efficient out-coupling. Reciprocally, pump light which matches the same relation $\mathbf{k}_{\parallel,\mathrm{in}} = \mathbf{k}_{\parallel,\mathrm{WG}} + \mathbf{G}$ can be efficiently coupled into the waveguide mode and be absorbed by the emitters, resulting in a pump enhancement.

The in-coupling and out-coupling of the waveguide mode can be described using the photonic band diagram illustrated in Fig. 1.4(b). The orange cone represents the waveguide mode. For simplicity, here we take n_{WG} as a constant, though actual waveguides have dispersion (frequency-dependent n_{WG} and cut-off). The silver cones represent the modes out-coupled by a square array, which appear as copies of the original cone displaced by a reciprocal lattice vector $\mathbf{G}$. Fig. 1.4(c-d) are cross-sections of Fig. 1.4(b) in two orthogonal planes. The bands cross at $k_x = k_y = 0$ when the waveguide propagating vector matches the Bragg condition, resulting in a strongly enhanced outcoupling of emission for the corresponding wavelength in the forward direction. It should be noted that the diagram in Fig. 1.4 represents an approximate result in the limit of very weak scattering. As the scattering strength of plasmon particles is large, crossings in the diagram turn into avoided crossings [96].

The photonic band structure of phased-array antennas is strongly dependent on the Fourier transform of the array. Both pump enhancement [24, 25] and directionality control [24, 26, 27] of emission from remote-phosphors have been demonstrated with square arrays [24–26] and hexagonal arrays [27] of plasmon antennas. For instance, Ref. [24] reports a 60-fold total enhancement on the forward emission of a highly efficient remote phosphor from a square array of Al antennas, of which 6-fold is attributed to the pump enhancement and 10-fold to the extraction efficiency enhancement from the directional control. The enhancement from such periodic structures usually has a narrow spectral bandwidth (a few nm) and anisotropic angular distribution due to their pure point Fourier transforms. Figure 1.5(a)(d) show a periodic array and its corresponding Fourier transform. For SSL, the narrow bandwidth and anisotropy are drawbacks. Deterministic quasi-periodic and aperiodic arrays (Fig. 1.5(b-c)) have singular continuous or absolute continuous Fourier transforms as shown in Fig. 1.5 (d-e). They can be promising alternative designs to overcome the limitations of periodic arrays [97–100].

1.5 Stimulated emission and lasers

Lasers feature high brightness and ultra-low etendue. In the context of SSL, lasers can be considered for two roles. First, instead of pumping a remote phosphor by LED light, one could pump with an electrically driven blue laser [101–103]. This can offer an advantage in efficiency since lasers can deliver their output as a high brightness

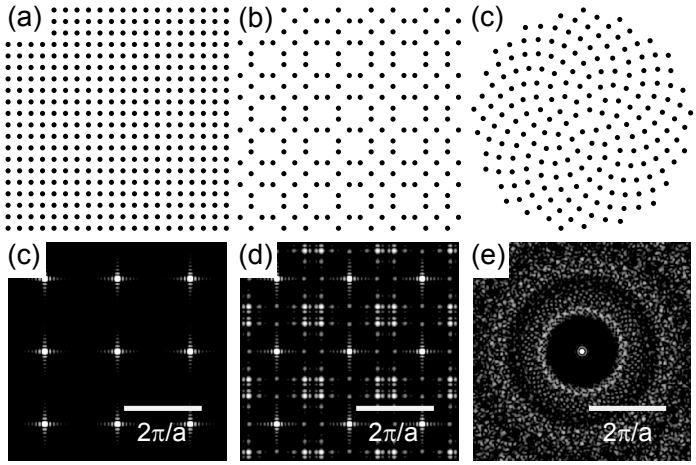

Figure 1.5: (a-c) Schematics and (d-f) Fourier transforms of (a)(d) a periodic array, (b)(e) a quasi-periodic (Fibonacci) array and (c)(f) an aperiodic (Vogel's spiral) array.

well-defined beam that may more efficiently couple into a phosphor than the emission of an equivalent LED. Second, applications like high-definition projection can be realized by using digital mirrors and lasers (covering the R, G and B color channel) with advantages in brightness and contrast due to the low etendue of lasers [104].

The word laser stands for "light amplification by stimulated emission of radiation". Stimulated emission is a process in which an incoming photon interacts with an excited state, causing it to return to a lower energy level by emitting another photon [35]. The emitted photon is identical with the incident photon in terms of polarization, phase, frequency and wave vector. The frequency of the incoming photon needs to match the energy difference between the excited and the lower energy state. Unlike the spontaneous emission rate which is independent of the photon population in the ambient electromagnetic field, the stimulated emission rate is proportional to incident light intensity [105]. The rate of a transition from a lower level to a higher level by absorbing a photon is also proportional to the light intensity. For a two-level system the rates of absorption and stimulated emission are identical [105]. In order to have a net amplification of light from an ensemble of fluorophores, the population of the excited state needs to be larger than that in the ground state. This situation is termed population inversion, as the population is opposite to that encountered in thermal equilibrium. Population inversion cannot be achieved in the optical regime for pure two-level systems and three- or four-level systems are commonly used for lasers [106]. The three different systems are illustrated in Fig. 1.6(a). In a three-level system, the emitter can be excited by higher frequency incident light to a high vibrational level of the excited state and immediately relax to the lowest vibrational level during internal conversion. The pump light does not match the frequency of the transition back to the ground state and the emitters can accumulate in the lowest vibrational level of

the excited state. With a four-level system, the emission happens between the lowest vibrational level of the excited state and a high vibrational level of the ground state. The lowest vibrational level of the excited states can be populated through optical pumping and the high vibrational level of the ground state is depleted by internal conversion. Population inversion can be obtained with weak pumping as long as the internal conversion rates are higher than the emission rate [106].

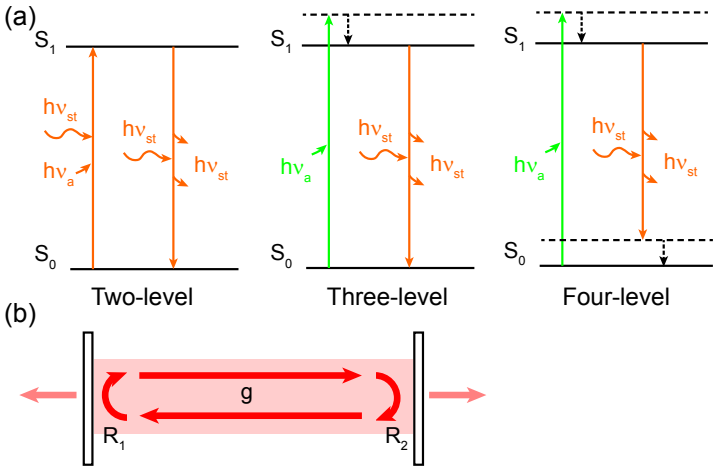

Figure 1.6: (a) An illustration of transitions in two-level, three-level and four-level systems. (b) An illustration of a laser based on a Fabry Pérot cavity, i.e., a gain medium between two parallel mirrors with reflectance of R_1 and R_2.

Stimulated emission provides the amplification of light, or in other words, gain. For a system to lase, two more elements are required, i.e., seed light and feedback. The seed light can be provided by spontaneous emission of the same emitters [106]. The feedback makes sure that the light is trapped in the gain medium for long enough before it escapes, so that enough amplification has been gained to compensate the losses incurred by radiation out of the lasing mode, and by other processes such as absorption in any component of the laser. Feedback is typically achieved using cavities, such as the canonical Fabry Pérot cavity [107] that can be treated in an analytical model as shown in Fig. 1.6(b). Lasing occurs when the electric field (E_0) at any point of the cavity returns to the original value after a round trip in the cavity, i.e. [108]

$$E_0\sqrt{R_1R_2}e^{(g-\alpha)L}e^{\mathrm{i}4\pi nL/\lambda} = E_0, \tag{1.12}$$

where R_1, R_2 are the reflection at the two mirrors, g is the gain coefficient, α is the propagation loss, n is the refractive index of the medium, and L is the length of the cavity (a half integer number of wavelengths). The minimum g satisfying the above relation is the threshold gain.

Besides Fabry-Perot cavities, lasing has been reported in a plethora of resonators including photonic-crystal cavities [109], microcavities [110, 111], microrings [112],

microdisks [113], nanowires [114–116] and metallic-dielectric nanoresonators [117–123]. Apart from cavities, lasing is also commonly realized with other feedback mechanisms such as random scattering [124, 125] and Bragg diffraction (DFB) in periodically corrugated waveguides [126].

In this thesis, we investigate plasmon particle DFB lasers. Plasmon lasers, sometimes also called spasers, were first proposed by Bergman and Stockman [127]. They rely on the amplification of SPRs by coupling to to a gain medium. Plasmon lasers feature an ultrasmall mode volume and are usually realized in metallic-dielectric nanoresonators [115–123, 128]. However, due to the intrinsic large momentum mismatch between the surface plasmon field and free space light, the outcoupling of laser light from such plasmon lasers is not very efficient. This drawback is overcome by plasmon DFB lasers. Plasmon DFB lasers use the in-plane Bragg diffraction of plasmon lattices for feedback. They are capable of highly directional light emission to free space using diffractive outcoupling, and feature a high degree of spectral selection. Two types of plasmon lattices are commonly used in plasmon DFB lasers, i.e., metal hole arrays [129, 130] and plasmon particle arrays [29–33].

Plasmon particle array DFB lasers consist of a periodic array of nanoantennas surrounded by a polymer or a solvent doped with fluorophores, which is very similar to a plasmon enhanced remote phosphor. They were first reported by Stehr et al. [29] and later intensively studied by Schokker et al. [32, 131–133] and the group of Odom [30, 31, 134–136]. They have the advantage of low etendue and have a structure that can be pumped by a blue LED, making them potentially useful for SSL. However, despite these advantages, it is still unclear whether the current plasmon particle DFB lasers are suitable for SSL applications. First, the gain medium used in plasmonic lasers has not been optimized in terms of gain coefficient, and resilience to intense pumping. Experiments with solid-state gain media so far have employed single-shot nanosecond pulsed excitation [32, 131–133]. Second, the luminous efficacy of plasmon DFB lasers is not optimized, which relies on systematic study of the many properties of the lasers, such as the efficiency depending on pump light properties, the threshold gain, metallic losses, slope efficiency, etc. Third, lasers have ultra-narrow emission bands and therefore intrinsically low CRI. Last but not least, plasmon DFB lasers have high spatial and temporal coherence, which can result in speckles in illumination applications, reducing imaging or illumination quality. This drawback calls for a study of how to multiplex many lasers on a small sample footprint to control coherence and obtain multi-spectral content.

1.6 Outline of the thesis

In the first half of this thesis, we focus on the manipulation of spontaneous emission of a remote phosphor by optical nanoantennas from two aspects: LDOS and directivity control. In Chapter 2, We study the LDOS introduced by periodic antenna arrays of nanoantennas. Mapping the LDOS in nanostructures is challenging, as it requires sub-wavelength resolution that is not available with conventional microscopic techniques.

We introduce a new method inspired by stochastic localization microscopy techniques, e.g., STORM and PALM [137–139]. This method allows us to map the LDOS with superresolution in periodic systems and study the influence of LSPRs and lattice resonances on the LDOS distribution.

In chapter 3, we look into a new type of optical antennas called "dendritic optical antennas". So far, state-of-the-art optical antennas are mostly designed for the optical functionalities and do not generally form a continuous electrical network. This largely differs them from radio antennas and hampers electrical addressing of active emitters that load the antenna. Kern et al. [140] for the first time created an electrically driven optical antenna in form of an optically connected bow-tie structure, which opens the perspective of designing antennas with both optical enhancement and electric driving capability. The dendritic optical antennas we propose here can be viewed as connected oligomers of nanorods that feature both electrical connection and optical activity. We study their optical response and potential emission enhancement from Purcell effect.

In Chapter 4, we study the directivity control from aperiodic nanoantenna arrays as an alternative to periodic arrays. Aperiodic arrays can offer a more distributed Fourier transform than periodic systems, as illustrated in Fig. 1.5 (c) for so-called Vogel's spirals [100]. One thus expects a more broadband operation characteristics for directionally enhanced emission than has been reported for periodic lattices. In this chapter, we report the optical response and directional emission enhancement measured on Vogel's spirals.

The second half of this thesis is focused on plasmon particle array DFB lasers. Over the past 5 years, a significant amount of research has been done on plasmon DFB lasers, proposing interesting performance metrics as compared to all-dielectric DFB lasers due to Purcell enhancements [30, 31, 134, 135] and due to wide stop gaps in dispersion [133], both associated with the plasmonic nature of the particles that provide feedback. However, none of these works addressed directly in real space the question how different a particle array plasmon laser is from a conventional complex coupled DFB laser based on metal gratings. In Chapter 5, we try to answer this question by studying the real space intensity distribution of plasmon DFB lasers based on coupled wave theory [141], which is widely used in describing conventional DFB lasers.

In Chapter 6, we study so-called "patchwork" plasmon DFB lasers. We introduce two designs for plasmon lasers based on patchworks of small periodic nanoantennas arrays. Each patch can work individually as lasers with slightly different lasing wavelengths. We measure the lasing threshold and spectra of the patchwork lasers, and discuss their potential application as multi-wavelength, low speckle contrast, high etendue light sources.

References

[1] J. Whitmarsh and Govindjee, *The Photosynthetic Process*, pages 11–51, Springer Netherlands, Dordrecht, 1999.

[2] S. Hecht, *Rods, cones, and the chemical basis of vision*, Physiol. Rev. **17**, 239 (1937).

[3] D. M. Chapin, C. S. Fuller, and G. L. Pearson, *A new silicon p-n junction photocell for converting solar radiation into electrical power*, J. Appl. Phys. **25**, 676 (1954).

[4] A. Polman, M. Knight, E. C. Garnett, B. Ehrler, and W. C. Sinke, *Photovoltaic materials: Present efficiencies and future challenges*, Science **352**, aad4424 (2016).

[5] G. Agrawal, *Fiber-Optic Communication Systems*, Wiley, 2012.

[6] Philips Lighting, *Ambientled*, 2017, https://www.usa.philips.com/c-p/046677409906/ambientled-energy-saving-household-light.

[7] A. Nikitin, M. Remezani, and J. Gómez Rivas, *Luminescent metamaterials for solid state lighting*, ECS J. Solid State Sci. Technol. **5**, R3164 (2016).

[8] D. DiLaura, *A brief history of lighting*, Opt. Photonics News **19**, 22 (2008).

[9] CIE, *International lighting vocabulary 17-729 luminous efficacy*.

[10] U.S. Department of Energy's Office, *Lighting basics*, 2013.

[11] U.S. Department of Energy, *Energy savings potential of solid-state lighting in general illumination applications 2010 to 2030*, 2010.

[12] E. Mills, *Job creation and energy savings through a transition to modern off-grid lighting*, Energy Sustain. Dev. **33**, 155 (2016).

[13] Class for Physics of the Royal Swedish Academy of Sciences, *Efficient blue light-emitting diodes leading to bright and energy-saving white light sources*, 2014.

[14] Lumileds, *Luxeon rebel color line product datasheet*, 2017, https://www.lumileds.com/uploads/265/DS68-pdf.

[15] CIE, *International lighting vocabulary 17-222 colour rendering index*.

[16] J. Kido, M. Kimura, and K. Nagai, *Multilayer white light-emitting organic electroluminescent device*, Science **267**, 1332 (1995).

[17] S. Yamamoto, Y. Zhao, C.-C. Pan, R. B. Chung, K. Fujito, J. Sonoda, S. P. DenBaars, and S. Nakamura, *High-efficiency single-quantum-well green and yellow-green light-emitting diodes on semipolar (2021) gan substrates*, Appl. Phys Express **3**, 122102 (2010).

[18] M. Auf der Maur, A. Pecchia, G. Penazzi, W. Rodrigues, and A. Di Carlo, *Efficiency drop in green* InGaN/GaN *light emitting diodes: The role of random alloy fluctuations*, Phys. Rev. Lett. **116**, 027401 (2016).

[19] P. Schlotter, R. Schmidt, and J. Schneider, *Luminescence conversion of blue light emitting diodes*, Appl. Phys. A **64**, 417 (1997).

[20] G. R. Elion, *Electro-optics handbook*, volume 2, CRC Press, 1979.
[21] Lumileds, *Luxeon rebel general purpose product datasheet*, 2017, https://www.lumileds.com/uploads/28/DS64-pdf.
[22] J. Chaves, *Introduction to Nonimaging Optics*, CRC Press, 2008.
[23] J. Bhardwaj, J. M. Cesaratto, I. H. Wildeson, H. Choy, A. Tandon, W. A. Soer, P. J. Schmidt, B. Spinger, P. Deb, O. B. Shchekin, and W. Götz, *Progress in high-luminance led technology for solid-state lighting*, Phys. Status Solidi (a) , 1600826 (2017).
[24] G. Lozano, D. J. Louwers, S. R. Rodriguez, S. Murai, O. T. Jansen, M. A. Verschuuren, and J. Gómez Rivas, *Plasmonics for solid-state lighting: enhanced excitation and directional emission of highly efficient light sources*, Light Sci. Appl. **2**, e66 (2013).
[25] K. Guo, G. Lozano, M. A. Verschuuren, and J. Gómez Rivas, *Control of the external photoluminescent quantum yield of emitters coupled to nanoantenna phased arrays*, J. Appl. Phys. **118**, 073103 (2015).
[26] K. H. Cho, J. Y. Kim, D.-G. Choi, K.-J. Lee, J.-H. Choi, and K. C. Choi, *Surface plasmon-waveguide hybrid polymer light-emitting devices using hexagonal Ag dots*, Opt. Lett. **37**, 761 (2012).
[27] G. Lozano, G. Grzela, M. A. Verschuuren, M. Ramezani, and J. Gómez Rivas, *Tailor-made directional emission in nanoimprinted plasmonic-based light-emitting devices*, Nanoscale **6**, 9223 (2014).
[28] J. DiMaria, E. Dimakis, T. D. Moustakas, and R. Paiella, *Plasmonic off-axis unidirectional beaming of quantum-well luminescence*, Appl. Phys. Lett. **103**, 251108 (2013).
[29] J. Stehr, J. Crewett, F. Schindler, R. Sperling, G. von Plessen, U. Lemmer, J. Lupton, T. Klar, J. Feldmann, A. Holleitner, M. Forster, and U. Scherf, *A low threshold polymer laser based on metallic nanoparticle gratings*, Adv. Mater. **15**, 1726 (2003).
[30] J. Y. Suh, C. H. Kim, W. Zhou, M. D. Huntington, D. T. Co, M. R. Wasielewski, and T. W. Odom, *Plasmonic bowtie nanolaser arrays*, Nano Lett. **12**, 5769 (2012).
[31] W. Zhou, M. Dridi, J. Y. Suh, C. H. Kim, D. T. Co, M. R. Wasielewski, G. C. Schatz, and T. W. Odom, *Lasing action in strongly coupled plasmonic nanocavity arrays*, Nat. Nanotechnol. **8**, 506 (2013).
[32] A. H. Schokker and A. F. Koenderink, *Lasing at the band edges of plasmonic lattices*, Phys. Rev. B **90**, 155452 (2014).
[33] M. Ramezani, A. Halpin, A. I. Fernández-Domínguez, J. Feist, S. R.-K. Rodriguez, F. J. Garcia-Vidal, and J. Gómez Rivas, *Plasmon-exciton-polariton lasing*, Optica **4**, 31 (2017).
[34] T. K. Hakala, H. T. Rekola, A. I. Väkeväinen, J.-P. Martikainen, M. Nečada, A. J. Moilanen, and P. Törmä, *Lasing in dark and bright modes of a finite-sized plasmonic lattice*, Nat. Commun. **8**, 13687 (2017).
[35] R. Paschotta, *Field Guide to Lasers*, volume 12, SPIE press, 2008.
[36] T. A. Hopkins, H. H. Seliger, E. H. White, and M. W. Cass, *Chemiluminescence of firefly luciferin. model for the bioluminescent reaction and identification of the product excited state*, J. Am. Chem. Soc. **89**, 7148 (1967).
[37] D. W. Ball, *Field guide to spectroscopy*, volume 8, Spie Press Bellingham, Washington, 2006.
[38] A. Jabłoński, *Über den Mechanismus der Photolumineszenz von Farbstoffphosphoren*, Zeitschrift fur Physik **94**, 38 (1935).
[39] J. Lakowicz, *Principles of Fluorescence Spectroscopy*, Springer US, 2007.
[40] J. Franck and E. G. Dymond, *Elementary processes of photochemical reactions*, Trans. Faraday Soc. **21**, 536 (1926).
[41] E. Condon, *A theory of intensity distribution in band systems*, Phys. Rev. **28**, 1182 (1926).

[42] G. G. Stokes, *On the change of refrangibility of light*, Philos. Trans. Roy. Soc. London **142**, 463 (1852).
[43] L. Novotny and B. Hecht, *Principles of nano-optics*, Cambridge University Press, 2012.
[44] P. A. M. Dirac, *The quantum theory of the emission and absorption of radiation*, Proc. R. Soc. A **114**, 243 (1927).
[45] R. Sprik, B. A. van Tiggelen, and A. Lagendijk, *Optical emission in periodic dielectrics*, EPL **35**, 265 (1996).
[46] W. L. Vos, A. F. Koenderink, and I. S. Nikolaev, *Orientation-dependent spontaneous emission rates of a two-level quantum emitter in any nanophotonic environment*, Phys. Rev. A **80**, 053802 (2009).
[47] E. M. Purcell, *Spontaneous emission probabilities at radio frequencies*, in *Confined Electrons and Photons*, pages 839–839, Springer, 1995.
[48] K. H. Drexhage, H. Kuhn, and F. P. Schäfer, *Variation of the fluorescence decay time of a molecule in front of a mirror*, Ber. Bunsenges. Phys. Chem. **72**, 329 (1968).
[49] D. Kleppner, *Inhibited spontaneous emission*, Phys. Rev. Lett. **47**, 233 (1981).
[50] P. Goy, J. M. Raimond, M. Gross, and S. Haroche, *Observation of cavity-enhanced single-atom spontaneous emission*, Phys. Rev. Lett. **50**, 1903 (1983).
[51] E. Yablonovitch, *Inhibited spontaneous emission in solid-state physics and electronics*, Phys. Rev. Lett. **58**, 2059 (1987).
[52] S. John, *Strong localization of photons in certain disordered dielectric superlattices*, Phys. Rev. Lett. **58**, 2486 (1987).
[53] W. P. Ambrose, P. M. Goodwin, R. A. Keller, and J. C. Martin, *Alterations of single molecule fluorescence lifetimes in near-field optical microscopy*, Science **265**, 364 (1994).
[54] P. Anger, P. Bharadwaj, and L. Novotny, *Enhancement and quenching of single-molecule fluorescence*, Phys. Rev. Lett. **96**, 113002 (2006).
[55] S. Kühn, U. Håkanson, L. Rogobete, and V. Sandoghdar, *Enhancement of single-molecule fluorescence using a gold nanoparticle as an optical nanoantenna*, Phys. Rev. Lett. **97**, 017402 (2006).
[56] N. Hecker, R. Höpfel, and N. Sawaki, *Enhanced light emission from a single quantum well located near a metal coated surface*, Physica E **2**, 98 (1998).
[57] J. Vučković, M. Lončar, and A. Scherer, *Surface plasmon enhanced light-emitting diode*, IEEE J. Quantum. Electron. **36**, 1131 (2000).
[58] A. Neogi, C.-W. Lee, H. O. Everitt, T. Kuroda, A. Tackeuchi, and E. Yablonovitch, *Enhancement of spontaneous recombination rate in a quantum well by resonant surface plasmon coupling*, Phys. Rev. B **66**, 153305 (2002).
[59] H. Aouani, O. Mahboub, E. Devaux, H. Rigneault, T. W. Ebbesen, and J. Wenger, *Plasmonic antennas for directional sorting of fluorescence emission*, Nano Lett. **11**, 2400 (2011).
[60] H. Aouani, O. Mahboub, N. Bonod, E. Devaux, E. Popov, H. Rigneault, T. W. Ebbesen, and J. Wenger, *Bright unidirectional fluorescence emission of molecules in a nanoaperture with plasmonic corrugations*, Nano Lett. **11**, 637 (2011).
[61] P. Bharadwaj, B. Deutsch, and L. Novotny, *Optical antennas*, Adv. Opt. Photonics **1**, 438 (2009).
[62] K. L. Kelly, E. Coronado, L. L. Zhao, and G. C. Schatz, *The optical properties of metal nanoparticles: The influence of size, shape, and dielectric environment*, J. Phys. Chem. B **107**, 668 (2003).
[63] S. A. Maier, *Plasmonics: fundamentals and applications*, Springer, 2007.
[64] G. Mie, *Beiträge zur Optik trüber Medien, speziell kolloidaler Metallösungen*, Ann. Phys.

330, 377 (1908).

[65] C. F. Bohren and D. R. Huffman, *Absorption and Scattering of Light by Small Particles*, John Wiley & Sons, 1983.

[66] S. Kawata, *Near-field microscope probes utilizing surface plasmon polaritons*, in *Near-Field Optics and Surface Plasmon Polaritons*, pages 15–27, Springer, 2001.

[67] P. B. Johnson and R. W. Christy, *Optical constants of the noble metals*, Phys. Rev. B **6**, 4370 (1972).

[68] G. Dolling, C. Enkrich, M. Wegener, J. F. Zhou, C. M. Soukoulis, and S. Linden, *Cut-wire pairs and plate pairs as magnetic atoms for optical metamaterials*, Opt. Lett. **30**, 3198 (2005).

[69] I. Sersic, M. Frimmer, E. Verhagen, and A. F. Koenderink, *Electric and magnetic dipole coupling in near-infrared split-ring metamaterial arrays*, Phys. Rev. Lett. **103**, 213902 (2009).

[70] I. Sersic, C. Tuambilangana, T. Kampfrath, and A. F. Koenderink, *Magnetoelectric point scattering theory for metamaterial scatterers*, Phys. Rev. B **83**, 245102 (2011).

[71] I. Sersic, M. A. van de Haar, F. B. Arango, and A. F. Koenderink, *Ubiquity of optical activity in planar metamaterial scatterers*, Phys. Rev. Lett. **108**, 223903 (2012).

[72] F. B. Arango and A. F. Koenderink, *Polarizability tensor retrieval for magnetic and plasmonic antenna design*, New J. Phys. **15**, 073023 (2013).

[73] A. F. Koenderink, *Single-photon nanoantennas*, ACS Photonics **4**, 710 (2017).

[74] R. Esteban, T. V. Teperik, and J. J. Greffet, *Optical patch antennas for single photon emission using surface plasmon resonances*, Phys. Rev. Lett. **104**, 026802 (2010).

[75] C. Belacel, B. Habert, F. Bigourdan, F. Marquier, J.-P. Hugonin, S. Michaelis de Vasconcellos, X. Lafosse, L. Coolen, C. Schwob, C. Javaux, B. Dubertret, J.-J. Greffet, P. Senellart, and A. Maitre, *Controlling spontaneous emission with plasmonic optical patch antennas*, Nano Lett. **13**, 1516 (2013).

[76] A. Mohtashami, T. Coenen, A. Antoncecchi, A. Polman, and A. F. Koenderink, *Nanoscale excitation mapping of plasmonic patch antennas*, ACS Photonics **1**, 1134 (2014).

[77] G. M. Akselrod, C. Argyropoulos, T. B. Hoang, C. Cirací, C. Fang, J. Huang, D. R. Smith, and M. H. Mikkelsen, *Probing the mechanisms of large Purcell enhancement in plasmonic nanoantennas*, Nat. Photonics **8**, 835 (2014).

[78] T. B. Hoang, G. M. Akselrod, and M. H. Mikkelsen, *Ultrafast room-temperature single photon emission from quantum dots coupled to plasmonic nanocavities*, Nano Lett. **16**, 270 (2016).

[79] A. G. Curto, G. Volpe, T. H. Taminiau, M. P. Kreuzer, R. Quidant, and N. F. van Hulst, *Unidirectional emission of a quantum dot coupled to a nanoantenna*, Science **329**, 930 (2010).

[80] D. Dregely, K. Lindfors, M. Lippitz, N. Engheta, M. Totzeck, and H. Giessen, *Imaging and steering an optical wireless nanoantenna link*, Nat. Commun. **5**, 4354 (2014).

[81] N. Yu, P. Genevet, M. A. Kats, F. Aieta, J.-P. Tetienne, F. Capasso, and Z. Gaburro, *Light propagation with phase discontinuities: Generalized laws of reflection and refraction*, Science **334**, 333 (2011).

[82] L. Langguth, D. Punj, J. Wenger, and A. F. Koenderink, *Plasmonic band structure controls single-molecule fluorescence*, ACS Nano **7**, 8840 (2013).

[83] A. Kinkhabwala, Z. Yu, S. Fan, Y. Avlasevich, K. Muellen, and W. E. Moerner, *Large single-molecule fluorescence enhancements produced by a bowtie nanoantenna*, Nat. Photonics **3**, 654 (2009).

[84] H. Yuan, S. Khatua, P. Zijlstra, M. Yorulmaz, and M. Orrit, *Thousand-fold enhancement*

of single-molecule fluorescence near a single gold nanorod, Angew. Chem, Int. Ed. **52**, 1217 (2013).

[85] S. Khatua, P. M. R. Paulo, H. Yuan, A. Gupta, P. Zijlstra, and M. Orrit, *Resonant plasmonic enhancement of single-molecule fluorescence by individual gold nanorods*, ACS Nano **8**, 4440 (2014).

[86] D. Punj, M. Mivelle, S. B. Moparthi, T. S. van Zanten, H. Rigneault, N. F. van Hulst, M. F. Garcia-Parajo, and J. Wenger, *A plasmonic 'antenna-in-box' platform for enhanced single-molecule analysis at micromolar concentrations*, Nat. Nanotechnol. **8**, 512 (2013).

[87] S. Bidault, A. Devilez, V. Maillard, L. Lermusiaux, J.-M. Guigner, N. Bonod, and J. Wenger, *Picosecond lifetimes with high quantum yields from single-photon-emitting colloidal nanostructures at room temperature*, ACS Nano **10**, 4806 (2016).

[88] A. Puchkova, C. Vietz, E. Pibiri, B. Wünsch, M. Sanz Paz, G. P. Acuna, and P. Tinnefeld, *Dna origami nanoantennas with over 5000-fold fluorescence enhancement and single-molecule detection at 25 μm*, Nano Lett. **15**, 8354 (2015).

[89] C. Lowery, *Multiple encapsulation of phosphor-led devices*, 1999, US Patent 5,959,316.

[90] P. Gorrotxategi, M. Consonni, and A. Gasse, *Optical efficiency characterization of led phosphors using a double integrating sphere system*, J. Solid State Light. **2**, 1 (2015).

[91] A. Rose, T. B. Hoang, F. McGuire, J. J. Mock, C. Cirací, D. R. Smith, and M. H. Mikkelsen, *Control of radiative processes using tunable plasmonic nanopatch antennas*, Nano Lett. **14**, 4797 (2014).

[92] J. Y. Tsao, M. H. Crawford, M. E. Coltrin, A. J. Fischer, D. D. Koleske, G. S. Subramania, G. T. Wang, J. J. Wierer, and R. F. Karlicek, *Toward smart and ultra-efficient solid-state lighting*, Adv. Opt. Mater. **2**, 809 (2014).

[93] S. R. K. Rodriguez, Y. T. Chen, T. P. Steinbusch, M. A. Verschuuren, A. F. Koenderink, and J. Gómez Rivas, *From weak to strong coupling of localized surface plasmons to guided modes in a luminescent slab*, Phys. Rev. B **90**, 235406 (2014).

[94] M. A. Verschuuren, *Substrate conformal imprint lithography for nanophotonics*, PhD thesis, Utrecht University, 2010.

[95] H. P. Urbach and G. L. J. A. Rikken, *Spontaneous emission from a dielectric slab*, Phys. Rev. A **57**, 3913 (1998).

[96] L. C. Andreani and M. Agio, *Photonic bands and gap maps in a photonic crystal slab*, IEEE J. Quantum. Electron. **38**, 891 (2002).

[97] L. Dal Negro and S. Boriskina, *Deterministic aperiodic nanostructures for photonics and plasmonics applications*, Laser Photonics Rev. **6**, 178 (2012).

[98] R. Dallapiccola, A. Gopinath, F. Stellacci, and L. D. Negro, *Quasi-periodic distribution of plasmon modes in two-dimensional fibonacci arrays of metal nanoparticles*, Opt. Express **16**, 5544 (2008).

[99] C. Forestiere, G. Miano, G. Rubinacci, and L. Dal Negro, *Role of aperiodic order in the spectral, localization, and scaling properties of plasmon modes for the design of nanoparticle arrays*, Phys. Rev. B **79**, 085404 (2009).

[100] J. Trevino, H. Cao, and L. D. Negro, *Circularly symmetric light scattering from nanoplasmonic spirals*, Nano Lett. **11**, 2008 (2011).

[101] K. A. Denault, M. Cantore, S. Nakamura, S. P. DenBaars, and R. Seshadri, *Efficient and stable laser-driven white lighting*, AIP Adv. **3**, 072107 (2013).

[102] Y. H. Song, E. K. Ji, B. W. Jeong, M. K. Jung, E. Y. Kim, and D. H. Yoon, *High power laser-driven ceramic phosphor plate for outstanding efficient white light conversion in application of automotive lighting*, Sci. Rep. **6**, 31206 (2016).

[103] A. F. George, S. Al-waisawy, J. T. Wright, W. M. Jadwisienczak, and F. Rahman, *Laser-*

driven phosphor-converted white light source for solid-state illumination, Appl. Opt. **55**, 1899 (2016).

[104] R. Knize, *Full color solid state laser projector system*, 1994, US Patent 5,317,348.

[105] A. Einstein, *Strahlungs-Emission und -Absorption nach der Quantentheorie*, Deutsche Physikalische Gesellschaft **18** (1916).

[106] K. Shimoda, *Introduction to laser physics*, volume 44, Springer, 1986.

[107] V. Kozlov, V. Bulovic, P. Burrows, and S. Forrest, *Laser action in organic semiconductor waveguide and double-heterostructure devices*, Nature **389**, 362 (1997).

[108] M. T. Hill and M. C. Gather, *Advances in small lasers*, Nat. Photonics **8**, 908 (2014).

[109] O. Painter, R. K. Lee, A. Scherer, A. Yariv, J. D. O'Brien, P. D. Dapkus, and I. Kim, *Two-dimensional photonic band-gap defect mode laser*, Science **284**, 1819 (1999).

[110] J. L. Jewell, J. P. Harbison, A. Scherer, Y. H. Lee, and L. T. Florez, *Vertical-cavity surface-emitting lasers: Design, growth, fabrication, characterization*, IEEE J. Quantum. Electron. **27**, 1332 (1991).

[111] N. Tessler, G. Denton, and R. Friend, *Lasing from conjugated-polymer microcavities*, Nature **382**, 695 (1996).

[112] S. V. Frolov, M. Shkunov, Z. V. Vardeny, and K. Yoshino, *Ring microlasers from conducting polymers*, Phys. Rev. B **56**, R4363 (1997).

[113] A. F. J. Levi, R. E. Slusher, S. L. McCall, T. Tanbun-Ek, D. L. Coblentz, and S. J. Pearton, *Room temperature operation of microdisc lasers with submilliamp threshold current*, Electron. Lett. **28**, 1010 (1992).

[114] M. H. Huang, S. Mao, H. Feick, H. Yan, Y. Wu, H. Kind, E. Weber, R. Russo, and P. Yang, *Room-temperature ultraviolet nanowire nanolasers*, Science **292**, 1897 (2001).

[115] R. F. Oulton, V. J. Sorger, T. Zentgraf, R.-M. Ma, C. Gladden, L. Dai, G. Bartal, and X. Zhang, *Plasmon lasers at deep subwavelength scale*, Nature **461**, 629 (2009).

[116] Y.-J. Lu, J. Kim, H.-Y. Chen, C. Wu, N. Dabidian, C. E. Sanders, C.-Y. Wang, M.-Y. Lu, B.-H. Li, X. Qiu, W.-H. Chang, L.-J. Chen, G. Shvets, C.-K. Shih, and S. Gwo, *Plasmonic nanolaser using epitaxially grown silver film*, Science **337**, 450 (2012).

[117] R.-M. Ma, R. F. Oulton, V. J. Sorger, G. Bartal, and X. Zhang, *Room-temperature sub-diffraction-limited plasmon laser by total internal reflection*, Nat. Mater. **10**, 110 (2011).

[118] M. T. Hill, Y.-S. Oei, B. Smalbrugge, Y. Zhu, T. de Vries, P. J. van Veldhoven, F. W. M. van Otten, T. J. Eijkemans, J. P. Turkiewicz, H. de Waardt, E. J. Geluk, S.-H. Kwon, Y.-H. Lee, R. N otzel, and M. K. Smit, *Lasing in metallic-coated nanocavities*, Nat. Photonics **1**, 589 (2007).

[119] M. T. Hill, M. Marell, E. S. P. Leong, B. Smalbrugge, Y. Zhu, M. Sun, P. J. van Veldhoven, E. J. Geluk, F. Karouta, Y.-S. Oei, R. Nötzel, C.-Z. Ning, and M. K. Smit, *Lasing in metal-insulator-metal sub-wavelength plasmonic waveguides*, Opt. Express **17**, 11107 (2009).

[120] K. Yu, A. Lakhani, and M. C. Wu, *Subwavelength metal-optic semiconductor nanopatch lasers*, Opt. Express **18**, 8790 (2010).

[121] M. P. Nezhad, A. Simic, O. Bondarenko, B. Slutsky, A. Mizrahi, L. Feng, V. Lomakin, and Y. Fainman, *Room-temperature subwavelength metallo-dielectric lasers*, Nat. Photonics **4**, 395 (2010).

[122] J. H. Lee, M. Khajavikhan, A. Simic, Q. Gu, O. Bondarenko, B. Slutsky, M. P. Nezhad, and Y. Fainman, *Electrically pumped sub-wavelength metallo-dielectric pedestal pillar lasers*, Opt. Express **19**, 21524 (2011).

[123] M. Khajavikhan, A. Simic, M. Katz, J. H. Lee, B. Slutsky, A. Mizrahi, V. Lomakin, and Y. Fainman, *Thresholdless nanoscale coaxial lasers*, Nature **482**, 204 (2012).

[124] V. M. Markushev, V. F. Zolin, and C. M. Briskina, *Luminescence and stimulated emission of neodymium in sodium lanthanum molybdate powders*, Sov. J. Quantum Electron. **16**, 281 (1986).

[125] W. L. Sha, C.-H. Liu, and R. R. Alfano, *Spectral and temporal measurements of laser action of rhodamine 640 dye in strongly scattering media*, Opt. Lett. **19**, 1922 (1994).

[126] H. Kogelnik and C. V. Shank, *Stimulated emission in a periodic structure*, Appl. Phys. Lett. **18**, 152 (1971).

[127] D. J. Bergman and M. I. Stockman, *Surface plasmon amplification by stimulated emission of radiation: Quantum generation of coherent surface plasmons in nanosystems*, Phys. Rev. Lett. **90**, 027402 (2003).

[128] S. J. Kress, J. Cui, P. Rohner, D. K. Kim, F. V. Antolinez, K.-A. Zaininger, S. V. Jayanti, P. Richner, K. M. McPeak, D. Poulikakos, and D. J. Norris, *Colloidal-quantum-dot spasers and plasmonic amplifiers*, arXiv:1611.09792 (2016).

[129] F. van Beijnum, P. J. van Veldhoven, E. J. Geluk, M. J. A. de Dood, G. W. 't Hooft, and M. P. van Exter, *Surface plasmon lasing observed in metal hole arrays*, Phys. Rev. Lett. **110**, 206802 (2013).

[130] X. Meng, J. Liu, A. V. Kildishev, and V. M. Shalaev, *Highly directional spaser array for the red wavelength region*, Laser Photon. Rev. **8**, 896 (2014).

[131] A. H. Schokker and A. F. Koenderink, *Statistics of randomized plasmonic lattice lasers*, ACS Photonics **2**, 1289 (2015).

[132] A. H. Schokker and A. F. Koenderink, *Lasing in quasi-periodic and aperiodic plasmon lattices*, Optica **3**, 686 (2016).

[133] A. H. Schokker, F. van Riggelen, Y. Hadad, A. Alù, and A. F. Koenderink, *Systematic study of the hybrid plasmonic-photonic band structure underlying lasing action of diffractive plasmon particle lattices*, Phys. Rev. B **95**, 085409 (2017).

[134] A. Yang, T. B. Hoang, M. Dridi, C. Deeb, M. H. Mikkelsen, G. C. Schatz, and T. W. Odom, *Real-time tunable lasing from plasmonic nanocavity arrays*, Nat. Commun. **6**, 6939 (2015).

[135] A. Yang, Z. Li, M. P. Knudson, A. J. Hryn, W. Wang, K. Aydin, and T. W. Odom, *Unidirectional lasing from template-stripped two-dimensional plasmonic crystals*, ACS Nano **9**, 11582 (2015).

[136] D. Wang, A. Yang, W. Wang, Y. Hua, R. D. Schaller, G. C. Schatz, and T. W. Odom, *Band-edge engineering for controlled multi-modal nanolasing in plasmonic superlattices*, Nat. Nanotechnol. **12**, 889 (2017).

[137] E. Betzig, G. H. Patterson, R. Sougrat, O. W. Lindwasser, S. Olenych, J. S. Bonifacino, M. W. Davidson, J. Lippincott-Schwartz, and H. F. Hess, *Imaging intracellular fluorescent proteins at nanometer resolution*, Science **313**, 1642 (2006).

[138] S. T. Hess, T. P. Girirajan, and M. D. Mason, *Ultra-high resolution imaging by fluorescence photoactivation localization microscopy*, Biophys. J. **91**, 4258 (2006).

[139] M. J. Rust, M. Bates, and X. Zhuang, *Sub-diffraction-limit imaging by stochastic optical reconstruction microscopy (STORM)*, Nat. Methods **3**, 793 (2006).

[140] J. Kern, R. Kullock, J. Prangsma, M. Emmerling, M. Kamp, and B. Hecht, *Electrically driven optical antennas*, Nat. Photonics **9**, 582 (2015).

[141] H. Kogelnik and C. V. Shank, *Coupled-wave theory of distributed feedback lasers*, J. Appl. Phys. **43**, 2327 (1972).

2

Superresolution imaging of the local density of states in plasmon lattices

This chapter introduces a method of mapping the local enhancement of spontaneous emission rates of emitters coupled to periodic nanostructures based on stochastic super-resolution imaging. Periodic plasmonic nanostructures have been found promising in controlling photoluminescence directivity and efficiency for a wide variety of applications. Due to the inhomogeneous spatial distribution of the photonic resonances of periodic plasmonic nanostructures, their influence on emission is strongly dependent on the position of emitters relative to the nanostructures. Therefore, mapping the local dependence of directivity, efficiency and emission rate enhancements is key to understanding and optimizing the devices. As an example, we show super-resolved measurements of the local density of states (LDOS) at 605 nm induced by a hexagonal lattice of aluminum nanoantennas with a spatial resolution of 40 nm, defined by the size of the colloidal nanosources we use as randomly dispersed probes. We demonstrate that our method is superior to near-field mapping of emission rates. Comparison with electrodynamic simulations indicates that the variation of the decay rate of the emitters in the investigated sample is hardly influenced by the lattice modes and mainly governed by single-particle LDOS variations and nearest-neighbor interactions.

2.1 Introduction

Collective electron excitations in plasmonic nanostructures, known as localized surface plasmon resonances (LSPRs), enable the manipulation of photoluminescence at the nanoscale [1–5]. The underlying physics is that plasmonic nanostructures support optical resonances that are associated with very strong scattering cross sections, large optical polarizabilities, and strong electromagnetic near fields, because many electrons contribute [6, 7]. Coupling these optical resonances to emitters enhances the absorption of pump light by emitters, allows their radiation to be redirected in preferred directions, and gives rise to emission rate enhancements, due to enhanced local density of states (LDOS) effects [1, 2]. Moreover, periodic plasmonic nanostructures, particularly arrays of plasmonic nanoantennas [8], can support lattice modes which are delocalized. These modes can couple to emitters in a much broader range of distances than just the nanometer vicinity of the metal particles. Consequently they are well suited to enhance emission of ensembles of fluorophores, and have been found promising in applications such as solid state lighting [9–11], lasing [12–15], photovoltaics [16–19], surface-enhanced Raman spectroscopy [20–23] and sensing [24, 25].

Due to the inhomogeneous spatial distribution of the photonic-plasmonic resonances of periodic plasmonic nanostructures, their influence on emission enhancement can depend strongly on the position of emitters relative to the nanostructures [1, 2, 26–28]. Therefore, mapping the local dependence of emission rates, efficiency and directivity is key to optimizing the relevant plasmon-enhanced light-emitting devices. Indeed, enhanced LDOS effects are frequently measured by fluorescence lifetime measurements to characterize the influence of nanostructures on emission efficiency enhancements [2, 26–29]. In addition, Fourier images [30] are frequently measured to characterize the influence of nanostructures on emitter directivity. However, to date, these methods are applied mainly on the level of ensembles of emitters, without spatial resolution in the unit cell. Since unit cells are typically wavelength sized, and plasmon near fields have spatial features on the scale of 10-50 nm, mapping as a function of fluorophore position is highly challenging. Conventional diffraction-limited optical microscopes enable optical measurements at the scale of the wavelength, but are insufficient for studying local optical properties of nanostructures with sub-wavelength resolution.

Super-resolution techniques such as near-field scanning optical microscopy (NSOM) [31] using scanning probes have been employed to the study of nanostructures to overcome the diffraction limit. Several groups have pursued scanning emitter microscopy, where the scanning probe is a single fluorophore attached to a sharp tip, such as an atomic force microscopy probe, or a glass fiber tapered to nanometric size [1, 2, 4, 5, 26, 27, 32–39]. These techniques use fragile scanning tips which require accurate feedback systems, and carry a high risk of failure due to tip breakage. Moreover, since tips are scanned over the surfaces of the samples, measurements are limited to those surfaces and can be affected by topological artifacts. An alternative approach to *scanning* the source to obtain an image, is to use selective positioning of single nanoprobes on many identical nanostructures for measurement

with sub-wavelength resolution. This could be arranged by lithographically attaching nano-emitters [40, 41] in the nanostructure during sample fabrication, or alternatively by pushing nanoprobes using nanopositioning techniques such as atomic force microscopy [3, 42–44]. These methods typically require advanced nanofabrication or nanopositioning techniques. Measurements on nanoprobes randomly casted on nanostructures have also been conducted [28, 29]. However, since the nanoprobes are immobile and isolated in space, it is impossible to measure on two positions closer than the diffraction limit and therefore the measurements do not result in complete maps. Another state-of-art super-resolution technique is photo-activation localization microscopy (PALM), or stochastic optical reconstruction microscopy (STORM), which has revolutionized fluorescence microscopy, as recognized by the 2015 Nobel prize [45–47]. While localization microscopy is usually used to map spatial distributions of molecules in biophysical systems, it can also be used to map other quantities. Indeed super-resolution localization microscopy has already been utilized to characterize the local field enhancement of plasmonic nanostructures. Super-resolution on single structures was achieved by isolating nanoprobes with temporal photoactivation [48, 49] or using (slow) diffusion in an immersion liquid [50–54] and retrieving the positions of the nanoprobes by fitting snapshot fluorescent images with the point spread function (PSF). Such a photo-activation approach requires very particular fluorophores, while using diffusion assumes particular solvents that in turn limit the dielectric environment of the system being imaged.

In this chapter, we demonstrate a simple stochastic super-resolution technique for mapping of the LDOS from periodic plasmonic nanostructures using randomly deposited nanoprobes that is not subject to the aforementioned limitations. For periodic nanostructures, since any one position in the unit cell is replicated in all other unit cells, measurement results from different unit cells are combined to construct a map of the primitive unit cell. The method is applied to determining a map of the LDOS of a hexagonal array of aluminum nanoantennas, which has previously been shown to be highly effective for enhancing the directional emission of remote phosphors for solid-state lighting [11]. We obtain a spatial resolution of 40 nm (at 605 nm wavelength), defined by the size of the nanoprobes used in the measurement. We compare the data to measurements on the same array with a scanning-excitation technique based on NSOM. This comparison reveals that super-resolution imaging is advantageous in simplicity of operation, required infrastructure, and fidelity, since it does not suffer from the topography artifacts of NSOM. Finally, we use FDTD simulations to understand the observed LDOS variations. We show that the variation of the decay rate of the emitters in the investigated sample is hardly influenced by the lattice modes and governed mainly by single-particle LDOS variations and nearest neighbor couplings.

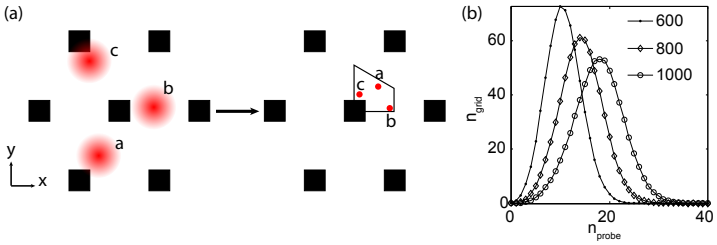

Figure 2.1: (a) A schematic of the super-resolution method applied on a hexagonal array of nanoantennas. Nanoprobes randomly deposited on the sample are measured with their positions determined as the centroid of their fluorescence image. The measurement results are translated into one primitive cell of the sample to construct a map. (b) Histograms showing distribution of probes obtained from Monte Carlo experiments. n_{grid} is the average number of grid points which have n_{probe} nanoprobes falling into each of the averaging area (Δ_A) with the total number of probes (N_{probe}) indicated in the legend.

2.2 Design considerations for the experimental method

Our approach to stochastic super-resolution imaging of LDOS in periodic systems is to randomly distribute single nanoprobes over a large sample area containing many unit cells. The proposed experimental method then requires two major steps: (i) *localization*, i.e., determination of the position of the nanoprobes and the nanostructure with sub-diffraction limited accuracy and (ii) optical measurements on individual nanoprobes quantifying LDOS, i.e., fluorescence lifetime. Relevant questions regarding the first step are, firstly, how accurately one can localize a nanoprobe and the plasmonic lattice, and secondly, how many nanoprobes one needs to measure for an accurate probing of the unit cell.

Regarding localization, the position of a nanoprobe relative to the nanostructure can be determined from a combination of the fluorescence image of the nanoprobes - which does not show the plasmon lattice - and a white light reflection image of the nanostructure - which does not show the nanoprobe, provided the two images can be acquired without relative shift. The absolute position of a nanoprobe in a fluorescent image can be accurately obtained as the centroid of its fluorescence image, i.e., a diffraction limited spot. The accuracy of this localization is then determined by the diffraction limit and the signal-to-noise ratio (SNR), which could reach a few nanometers given high SNR [55]. The unit cell of the nanostructure near the nanoprobe is identified from a reflection image measured with the very same optical path (including using the same microscope filter set) as the fluorescence measurement.

Optical measurements are done in a confocal measurement scheme to allow fluorescence lifetime measurements of individual nanoprobes. An important question is how the nanoprobes must be distributed, and how many need to be sampled. Clearly the separation of the nanoprobes must exceed the diffraction limit so that they are resolvable in the fluorescence image and to avoid excitation of multiple nanoprobes simultaneously. We thus require a dilute sprinkling of fewer than one nanoprobe per square micron.

By repeating the position determination and optical measurements on a number of nanoprobes, we will obtain the dependence of the measured lifetime on the position in the primitive cell. In order to construct a complete map, the nanoprobes need to be ergodically distributed on the periodic nanostructure. The resolution and completeness of the map will depend on the number of measured nanoprobes. First, for a given target sampling density or "pixel size", one can ask how many probes are required so that the chance of all pixels having a nanoprobe is near-unity. Second, averaging the results from different nanoprobes at similar positions in the primitive cell helps to reduce the statistical error due to (i) the statistical error in the optical measurements (ii) differences between different nanoprobes (iii) and differences between unit cells of the nanostructure.

Here we estimate the number of nanoprobes to be measured for a statistically significant map. Assuming a primitive cell with an area of A_{map} divided into a square grid of sampling pixels, for each grid point we calculate the average of the measured LDOS of nanoprobes in an area of Δ_A around the grid point, where Δ_A can be chosen on the basis of the grid spacing, or on the basis of the accuracy of the localization. The probability that at least M out of N_{probe} measured nanoprobes fall into Δ_A around a given grid point is:

$$P(M; N_{\mathrm{probe}}) = 1 - \sum_{i=0}^{M-1} \binom{i}{N_{\mathrm{probe}}} \left(\frac{\Delta_A}{A_{\mathrm{map}}}\right)^i \left(1 - \frac{\Delta_A}{A_{\mathrm{map}}}\right)^{N_{\mathrm{probe}}-i}. \tag{2.1}$$

This probability is close to unity as long as $N_{\mathrm{probe}} \gg M, A_{\mathrm{map}}/\Delta_A$.

For a map, one would at least require $M = 1$ for all pixels (no empty pixel), setting a minimum required N_{probe}. Furthermore it is advantageous to require $M > 1$ so that averages of optical observables can be determined for a more accurate map. To have an idea about how to choose N_{probe} for given target M, we performed a numerical experiment. As an example we consider a hexagonal plasmonic lattice with a pitch of 550 nm (relevant for solid state lighting), which contains particles with a rounded square base, as we study in the experiment below. All information about this structure (for scalar quantities) is contained in 1/4th of the primitive unit cell, leading to an area $A_{\mathrm{map}} \approx 6.5 \times 10^4$ nm^2 that requires mapping. In our work we will use 40 nm sized beads as nanoprobes, which we assume are bound for the accuracy of the localization and thereby defining the area $\Delta_A \approx 1.3 \times 10^3$ nm^2 in our example. Typically, to obtain accurate spatial maps one would oversample compared to the resolution. In this example, we assume that we sample the map at 10 nm grid spacing, leading to ~650 grid cells. Fig. 2.1(b) shows an averaged histogram obtained from 1000 Monte Carlo experiments with different N_{probe}, where n_{grid} is the (average) number of grid points which receive n_{probe} nanoprobes in their vicinity of Δ_A, and particles are assumed to be deposited with uniform, uncorrelated probability.

Measuring 600 nanoprobes is enough for constructing a rough map, in the sense that all the pixels are expected to receive at least one nanoprobe ($n_{\mathrm{grid}}(n_{\mathrm{probe}} = 0) = 0$). With 1000 nanoprobes, almost all of the pixels have at least 4 nanoprobes ($n_{\mathrm{grid}}(n_{\mathrm{probe}} < 4) < 1$), meaning a reduction of statistical errors in the observable by a factor of 2, assuming normally distributed errors in the observable.

2.3 Realization of the method

We apply the method to a plasmonic nanostructure that is a hexagonal array of Al nanoantennas with a lattice constant of d = 550 nm. This type of plasmonic nanostructure has been demonstrated to exhibit lattice resonances that are able to couple light into defined directions and therefore are beneficial for improving LED-pumped remote phosphors in solid state lighting systems [11]. Apart from enhanced brightness due to out-coupling in particular desired angular ranges, also enhancement in the absorption of pump light and in the fluorescence quantum yield of emitters due to LDOS enhancement can contribute to the enhancement of light emission. Thus, it is unclear whether the reported [11] directional brightness enhancement is actually accompanied by an increased or decreased LDOS, and hence by an increased or decreased internal quantum efficiency. The distribution of the LDOS of such a nanostructure has not been mapped and the contribution of the lattice modes to the LDOS enhancement is unknown. Scanning electron microscope (SEM) images of the array and of an individual antenna are shown in Fig. 2.2(a). The array of Al nanoantennas is fabricated over an area of $\sim 5 \times 5$ mm^2 on a fused silica glass substrate by combining substrate conformal imprint lithography with reactive ion etching [11, 56]. Each nanoantenna is shaped like a nanocone with a height of 150 nm and a rounded square section with a lateral size of 80 nm at the top and 140 nm at the base, which introduces asymmetry in forward-backward emission and is suited for solid state lighting [57]. Spherical polystyrene particles with a diameter of 40 nm loaded with fluorescent dye molecules are used as nanoprobes. They absorb green light and emit around 605 nm [Invitrogen FluoSpheres, product number F-8793]. On top of the array a $\sim$ 30 nm polystyrene layer is spin-coated to provide a hydrophobic surface for protection of the Al nanoantennas from corrosive degradation and meanwhile making it easier to sparsely deposit the nanoprobes and avoid clustering. A drop of a 0.02 mM suspension of nanoprobes in water is dropped over the sample and slowly blown away with a pressurized air gun. Repeating the process multiple times, we are able to attach the nanoprobes randomly on the surface of the sample with a density of $\rho_{\mathrm{probe}} \sim 0.15\ \mu\mathrm{m}^{-2}$. Compared with classical spincoating, this method requires much lower probe concentration and therefore is much less wasteful.

The experimental setup is based on a confocal microscope (Nikon), the schematic of which is shown in Fig. 2.2(b). A pulsed laser (Time Bandwidth, Lynx) with a wavelength of 532 nm and a repetition rate of 10 MHz is used to excite the nanoprobes for the fluorescence measurements. For localization, the laser is focused on the back-focal plane of the objective (Nikon, Plan APO VC, oil) so that an area with a diameter of $\sim$ 30 µm on the sample is illuminated and the image of fluorescence is recorded with a CCD camera (Nikon, DS-Qi1MC). The reflection of the array is measured with the same detection path by illuminating the sample with a halogen lamp so that the position of the nanoprobes and the array can be accurately correlated. It is essential that fluorescence and reflection are measured using the same filter and beam-splitter set in the transmission path, to avoid the ~50 nm image shifts that are associated with unavoidable filter wedging. To this end, we use a microscope with two filter

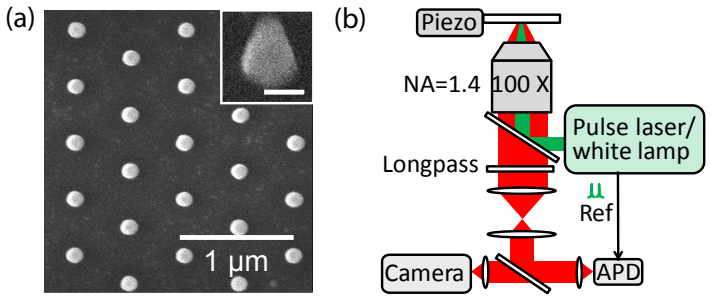

Figure 2.2: (a) A SEM image of the nanoantenna array. Inset shows the SEM image of a nanoantenna taken at an angle of 45°with scalebar = 100 nm. (b) A schematic of the setup.

turrets stacked above each other. The green laser light is reflected into the microscope off a dichroic filter in the upper cube. White light is inserted via a regular 50/50 beam splitter in the lower filter cube that also contains a longpass filter to suppress the laser light. Subsequent to localization we switch to confocal mode, focusing the laser to a diffraction limited spot. The fluorescence lifetime is measured on individual nanoprobes with an avalanche photodiode (APD, Id Quantique, SPAD) based on time-correlated single photon counting (with Becker & Hickl DPC-230 correlator card), where piezos are used for sample position scanning.

Fig. 2.3(a) shows examples of fluorescence and reflection images of the sample. The nanoprobes are identified as diffraction limited peaks in the fluorescence image. The nanoprobes appear to have different intensities mainly due to the inhomogeneity of the excitation spot, which is bright in the center and contains speckles. Meanwhile, the different dye doping in the probes as well as the influence of the array on the excitation, quantum yield and detection efficiency can also contribute to the variation. However, absolute intensity (as long as the required SNR is reached), does not affect the imaged variable, i.e., lifetime, which is uniform across probes to within 7%. The position of each nanoprobe ($\boldsymbol{r}_{\text{probe}}$) is determined by fitting its fluorescence image with a 2D Gaussian function ($I(\boldsymbol{r}) = I_0 e^{-(\boldsymbol{r}-\boldsymbol{r}_{\text{probe}})^2/2s^2}$) assuming Poisson noise. An area within 250 nm from the center of each peak is selected for the fit. The uncertainty of the position determination can be calculated according to Ref. [55] (Eq. 14) as $\sim$ 20 nm, given our photon budget, i.e., given the acquisition time that we choose. Since the radius of the nanoprobes is 20 nm, in this experiment there is no need to collect more counts. The resolution could be improved by using smaller probes. Since the same shot noise localization limits apply as for PALM and STORM, however, also the number of acquired photons per nanoprobe would need to be increased. We note that at targeted resolutions of a few nanometer, the plasmonic structures might cause systematic localization artefacts, as studied by [54, 58], for instance since scattered light may appear to be radiated by antennas, not probes. There is a small probability for nanoprobes to be separated by less than the diffraction limit, in which case localization would be inaccurate. Based on density, we estimate at most 3% of our

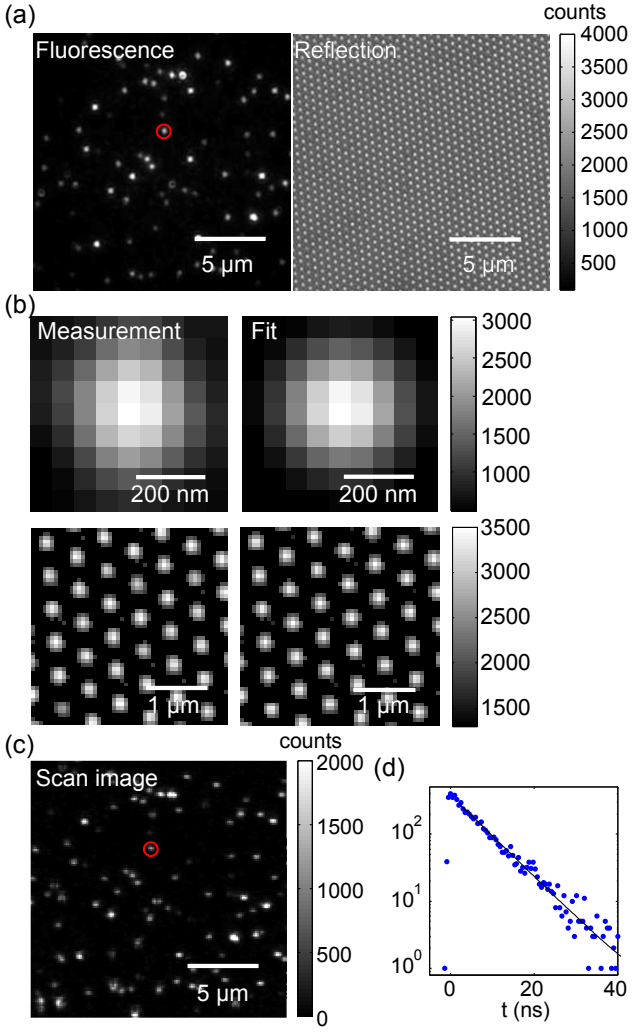

Figure 2.3: (a)Measured images of (left) fluorescence and (right) reflection from the same area of the sample. (b) Measured (top-left) fluorescence image from the nanoprobe marked with a red circle in (a) and (bottom-left) reflection image from vicinity nanoantennas compared to (right) their fits. (c) The scan image corresponding to (a). (d) Measured decay histogram of the nanoprobe marked by the red circles in (a)(c) and the single exponential fit to it.

measurement points to be affected, and likely less since we discard those nanoprobes whose fluorescence images are larger than the diffraction limit. This potential problem can be further reduced by diluting the probes.

The hexagonal array of nanoantennas is clearly resolved in the reflection image in Fig. 2.3(a). Prior to probe deposition, the nanoantennas look highly uniform in

brightness. Once probes are deposited, approximately 10% of antennas appear slightly dimmer, which we attribute to a slight modification of antenna scattering due to the dielectric perturbation formed by a probe. The positions of the Al nanoantennas near the nanoprobes are determined by fitting the reflection image with a sum of 2D Gaussian functions arranged in a hexagonal array. An area of about 3×3 µm around each nanoprobe is selected to determine the position of the nearest Al particle to the nanoprobe which we define as the origin of the unit cell. We note that white light imaging of periodic structures is not trivial due to the Talbot effect [59], that causes additional image features. We found that the robustness of the fit procedure can be improved by suppressing the Talbot effect in the data simply by ignoring all pixels that are below 50% of the image maximum. Fig. 2.3(b) shows an example of the fractions of fluorescence and reflection images used to determine the position of a nanoprobe and the corresponding images of the fit results. The precision of the localization of the nanoantennas has similar dependence on the SNR and total number of counts. Due to the larger fitting area, the error is only about 7 nm and is negligible compared with the size of the nanoprobes. Finally the position of the nanoprobes is translated into a quarter of the primitive cell of the hexagonal array defined by the boundaries of the primitive cell and the symmetry axes as illustrated in Fig. 2.1(a).

The LDOS of each nanoprobe is proportional to the total decay rate of electromagnetic channels including both the radiative decay and quenching in the metallic nanoparticles [60, 61]. Considering the existence of intrinsic non-radiative decay channels that are unaffected by the array, the enhancement of LDOS can be determined from the fluorescent lifetime according to the relation:

$$\begin{aligned} \mathrm{LDOS}(\boldsymbol{r}) &= \left(\frac{1}{\tau(\boldsymbol{r})} - \gamma_{\mathrm{non}}^{0}\right) \cdot \frac{1}{\gamma_{\mathrm{r}}^{0}} \\ &= \left(\frac{1}{\tau(\boldsymbol{r})} - (1-\mathrm{QY}^{0})\frac{1}{\tau^{0}}\right) \cdot \frac{\tau^{0}}{\mathrm{QY}^{0}}, \end{aligned} \tag{2.2}$$

where γ_{r}^{0} and $\gamma_{\mathrm{non}}^{0}$ are the intrinsic radiative and non-radiative decay rates of the nanoprobes, QY^{0} is the intrinsic quantum yield. The superscript 0 indicates the environment of the reference, i.e., dye molecules embedded in polystyrene spheres on a glass substrate without the influence from the nanoantenna array. Apart from lifetime, enhancement of the fluorescence intensity has also been used to characterize the LDOS. The disadvantage of using intensity as a measure for LDOS, however, is that intensity is the convoluted result of local pump field enhancement, LDOS enhancement, quenching, probe-to-probe variations, and quenching during the measurement procedure. Therefore, here we choose the fluorescence lifetime to determine the LDOS of plasmonic antenna systems.

To measure the fluorescent lifetime (τ) of individual nanoprobes, we focus the laser on the sample and scan the sample position so that only one nanoprobe is excited in each measurement. Fig. 2.3(c) shows an example of the fluorescence intensity detected by the APD as a function of sample position obtained from such a confocal scan, which corresponds well with the camera image in Fig. 2.3(a). The apparent

mismatch between probe intensity detected in the camera image and the scan image is due to the different excitation methods, i.e., inhomogeneous collimated illumination, versus focused illumination at constant power. The lifetime of each nanoprobe is obtained by fitting a single exponential function to the decay histogram obtained for the pixels corresponding to each probe in the confocal lifetime scan. Fig. 2.3(d) shows an example of the decay histogram and the fit for the nanoprobe marked with red circles in Fig. 2.3(a) and (c).

2.4 Results

Repeating the measurements on 1044 different nanoprobes, we obtain the fluorescence lifetime as a function of position as shown in Fig. 2.4. The fluorescence lifetime shows a clear dependence on probe position. The lifetime is low in the region close to the Al nanoantenna, which agrees with the fact that the electric field intensity is usually much higher in this regime due to the LSPRs. The lifetime increases with increasing distance from the nanoantenna and slightly decreases near the boundaries of the primitive cell. As regards the spatial distribution of sampling points, we note that almost no nanoprobe is detected at the position of the nanoantenna (consider a 20 nm uncertainty in the position accuracy and the nanoantenna size) while the density of the nanoprobes is large at the particle edge. This could be due to the fact that any nanoprobes that are deposited on top of the nanoantennas tend to aggregate at the nanoantenna base during the drying process.

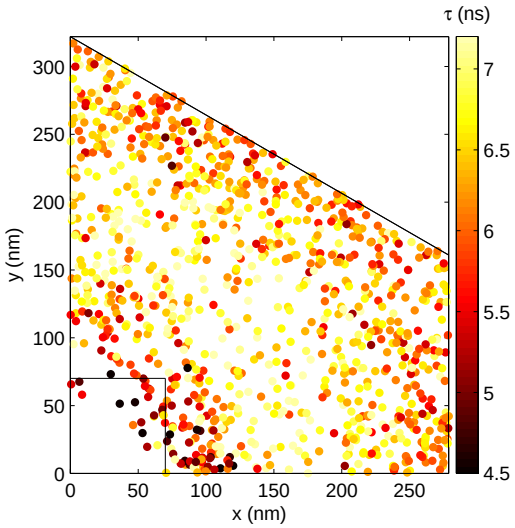

Figure 2.4: Measured fluorescence lifetime from 1044 nanoprobes as a function of probe position. Black lines indicate the boundary of the primitive cell and estimated edges of the nanoantenna.

To convert the random cloud of sampling points into a map of lifetime, we divide the quarter of the primitive cell into a square grid with a pixel size of 10 nm, corresponding to $N_{\text{grid}} \sim 650$ grid points. The lifetime at the each grid point is determined as the averaged lifetime of nanoprobes within 20 nm from the grid point.

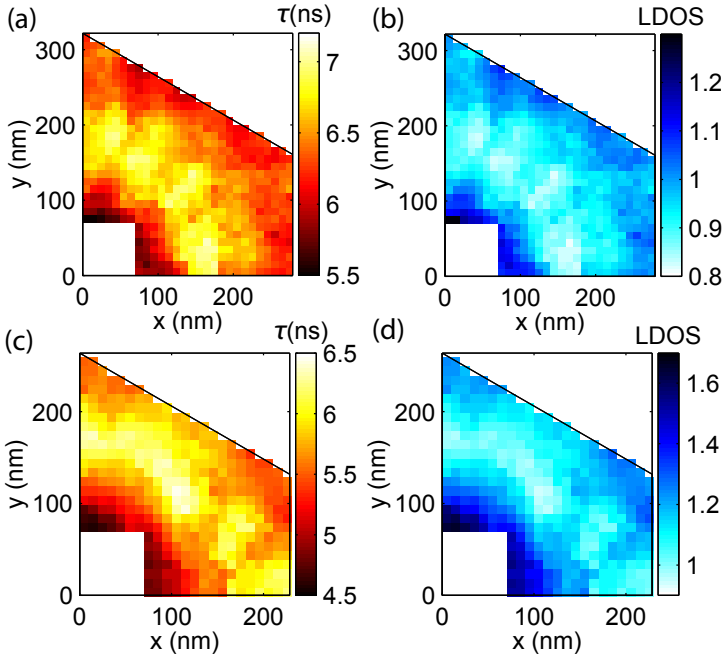

Figure 2.5: Constructed map of (a) and (c) fluorescence lifetime and (b) and (d) LDOS. (a-b) Pitch = 550 nm; (c-d) pitch = 450 nm.

Fig. 2.5(a) shows the map of measured lifetime constructed from the data in Fig. 2.4, as obtained by averaging the lifetime of all probes in an area ΔA (40 nm across) centered at each pixel (pixel spacing 10 nm), as per the example discussed in Section 2.2. This representation brings out more clearly than the scatter plot that the lifetime is suppressed to below 5.5 ns within 20 nm from the particles, while it is above 6.6 ns further away from the particles. To convert measured lifetime data in an LDOS map, one requires a reference lifetime measurement, as well as a quantum yield estimate for the emitters. To obtain a reference, the lifetime of 28 nanoprobes deposited on a substrate without plasmon particles was measured. As intrinsic lifetime (τ_0) of the nanoprobes we find 6.21±0.09 ns. The standard deviation (0.46 ns) yields a 7% lifetime variation between different nanoprobes, showing the necessity of averaging multiple probes per pixel. The average lifetime agrees with the results measured by Kwadrin et al.[62], in which the intrinsic radiative and non-radiative decay rates of similar nanoprobes (Invitrogen Fluospheres F8801, same dye but 100 nm size) are determined to be $\gamma_{\text{r}}^0 = 0.10 \pm 0.01$ ns^{-1} and $\gamma_{\text{non}}^0 = 0.07 \pm 0.01$ ns^{-1} based on Drexhage's

method. Taking the quantum yield from Ref. [62] in combination with our lifetime measurement, we obtain a map of LDOS in Fig. 2.5(b).

For the range of positions probed, and given the spatial averaging over the probe size, we obtain an LDOS variation in the band from 0.85 (slight inhibition when away from the Al nanoparticles) to 1.35 (moderate enhancement near the Al nanoparticles), meaning a total variation by a factor 1.6. The increase of LDOS near the Al nanoparticles is only moderate compared to other reported LDOS enhancement, that are typically up to ~20 for single molecule measurements near simple metal particles [2], and on the order of 3 to 5 for nanosized emitters [3]. This can be attributed to the fact that both the thin polymer layer covering the structures, and the radius of the nanoprobes we used keep the emitters from entering the ~ 10 nm shell around the metal surface where the LSPR are strongest. Also averaging over the nanoprobe size reduces the apparent LDOS variation, since each nanoprobe contains an ensemble of molecules, thereby biasing our signal towards measuring molecules that are least quenched, hence least close to the metal where LDOS is highest. We note that this limitation can be lifted by performing localization microscopy with single emitters rather than nanoprobes (at the price of photon count rate). The fact that emission is inhibited in a ring between the particle and the edge of the primitive cell may appear surprising, but is further confirmed by theory outlined in Section 2.5.

Similar measurements are done on a nanoantenna array with the same antenna design and a different lattice constant of 450 nm. Fig. 2.5(c-d) show the maps of measured lifetime and LDOS obtained from 717 nanoprobes. The LDOS has a similar distribution and in general a slightly larger value compared with that of the array with 550 nm pitch, namely a large enhancement (~1.6) near the nanoparticle, slight inhibition or no change away from the nanoparticle and slight enhancement (~1.2) near the boundary of the primitive cell. This result indicates that the lattice constant of the investigated nanoantenna arrays does not significantly influence the LDOS distribution. The LDOS enhancement can be slightly increased by reducing the separation of the nanoantennas.

Finally, we check if the nanoprobes are distributed as we predict from the Monte Carlo experiments, by making a histogram of the number of probes per pixel. Fig. 2.6 shows the comparison between the actual distributions of the nanoprobes and the results from Monte Carlo experiments. Here we consider that the nanoprobes have avoided the position of the nanoantennas, i.e., we assume no nanoprobe distributed in the area of $x, y < 60$ nm. The distribution of the nanoprobes for 550 nm pitch agree well with our prediction, which confirms our estimate for the required number of nanoprobes. For 450 nm pitch, the distribution deviates more from the prediction. This can be attributed to the aggregation of nanoprobes near the edge of the nanoparticles, which becomes more pronounced with a decreasing pitch.

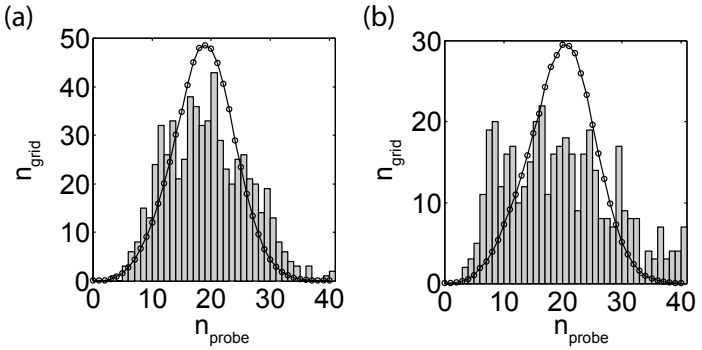

Figure 2.6: Histograms plotting the number of grid cells n_{grid} (vertical axis) in the measured spatial map with exactly n_{probe} (horizontal axis) nanoprobes in their averaging area. Overplotted over the histograms from experiment (gray bars) are the results from Monte Carlo experiments (connected dots). (a) Pitch = 550 nm; (b) pitch = 450 nm.

2.5 Comparison to near-field LDOS measurement

Up to this point, we have introduced a method to map the LDOS of plasmonic nanostructures with stochastic super-resolution and realized it on a hexagonal array of Al nanoparticles. The remainder of the chapter consists of two parts, namely interpreting the veracity and quality of the measured LDOS map first on the basis of complementary measurements, and second on the basis of calculations. As a complementary measurement technique with sub-diffraction limited resolution, we have also performed lifetime measurements using an NSOM head mounted on top of the same microscope as shown in Fig. 2.7(a). We use the near-field tip as a fluorescence excitation source. The tip is a tapered glass fiber coated with a ~ 150 nm Al layer. The end of the tip is polished with focused ion beam milling to form a ~ 100 nm aperture [63]. For fluorescence excitation the green excitation laser is coupled into the cleaved untapered end of the fiber, resulting in a strong electric field confined at the tip aperture. As a source of fluorescence, a 15 nm layer of polystyrene doped with 3 wt % dye molecules (BASF Lumogen F305) is spin-coated on the nanoantenna array, which has similar absorption and emission spectra as the nanoprobes. With a standard tuning-fork shear-force feedback loop, the tip is approached to ~ 10 nm of the surface of the sample so as to excite the dye molecules with the near field under the aperture (estimated diameter of $\lesssim$ 150 nm). To obtain lifetime data, the lateral (XY) position of the tip is held stationary in the microscope focus, while the same sample scanning piezos are used to scan the sample as in our confocal measurements. In this manner the fluorescence is collected by the microscope with the intensity and lifetime measured by the APD as function of excitation position on the sample. Meanwhile the topography of the sample surface is measured according to the shear-force feedback. The scan is operated under a speed of 0.72 μm/s, with x-axis the fast axis and a detection time of

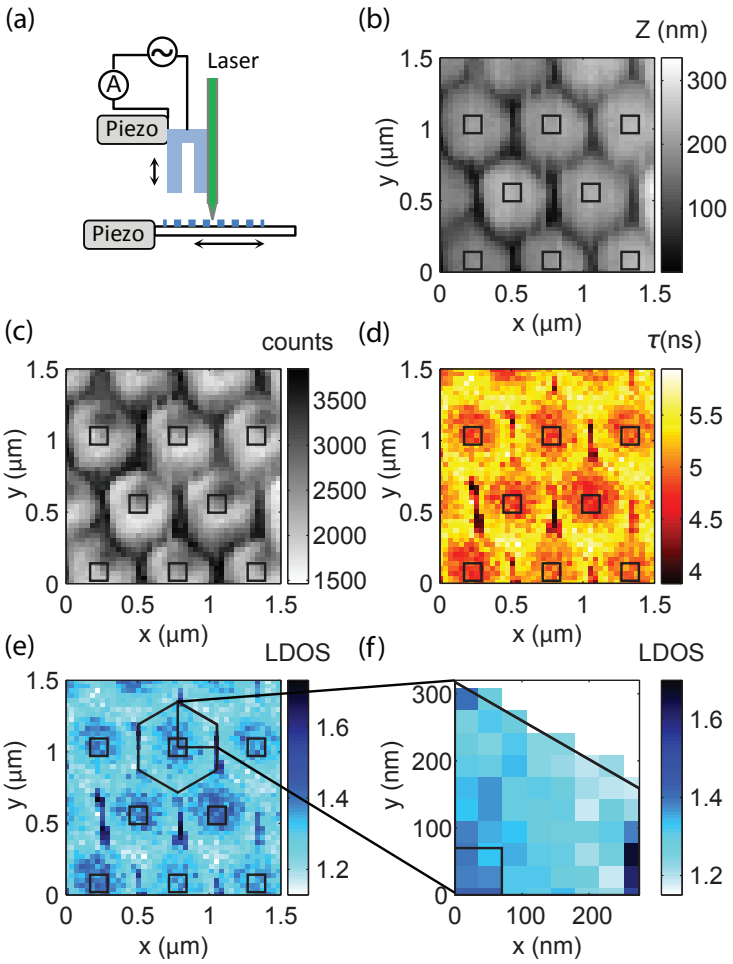

Figure 2.7: (a) A schematic of the NSOM head. Measured maps of (b) topography, (c) fluorescence intensity, (d) lifetime and (e) LDOS calculated from the measured lifetime. (f) A fraction of (e) representing the LDOS in a a quarter of a primitive cell of the array.

2.5 ms per pixel. We plot only the backward scan direction.

Fig. 2.7(b-d) show maps of topography, fluorescence intensity, and lifetime of the dye molecules with x and y axes parallel with the edges of the nanoantennas. The periodicity of the topography map agrees with the SEM image of the array. The fluorescence intensity varies with the variation in topography, which indicates a good correspondence between the position determined from the topography map and the fluorescence excitation spot. From the topography map we estimate the position of the nanoantennas as illustrated by the black squares. From the lifetime map, we calculate the LDOS a function of the excitation position ($\boldsymbol{r}$) according to Eq. (2.2) with $\tau^0 = 5.2$

ns the intrinsic lifetime of the dye molecules measured on a similar dye layer on flat substrate and $QY^0 = 76$ % the intrinsic quantum yield of the dye molecules in the dye layer measured with an integrating sphere. Fig. 2.7(e) shows the LDOS obtained from the lifetime map and for direct comparison with Fig. 2.5(b), we show in Fig. 2.7(f) a fraction of Fig. 2.7(e) which represents the LDOS in a quarter of a primitive cell. The LDOS is high close to the nanoantennas and decreases with increasing distance from the nanoantennas. Along the boundary which is parallel with the vertical edges of the nanoantennas, there is a sharp increase of LDOS within 2 pixels (~ 60 nm).

Compared with the stochastic super-resolution method introduced in previous sections, the NSOM method also reports an increase of the LDOS near the nanoparticles. However, despite the fact that this measurement uses a state-of-the-art NSOM head and tip, the spatial confinement of the LSPRs that is evident from the super-resolution map is lost due to the lower resolution of NSOM, and the small increase of LDOS near the boundary of the primitive cell is not detected. Moreover, we interpret the sharp LDOS increase along vertical stripes as a topographic artifact. These stripes occur farthest away from the metal particles, and the topography signal shows that they coincide with the tip most closely approaching the dye, as it fits in its entirety in between the metal particles. Crucially, it should be noted that since the tip has a metal coating, it can itself cause LDOS variations that strongly depend on the tip-sample distance [26]. On the other hand, the NSOM method can not be salvaged by using uncoated tips, as this in itself spoils resolution. All measurements in Fig. 2.4 require only 20 independent confocal lifetime imaging scans. While in our system each scan took about 30 minutes, acquisition times could be reduced by for instance, using a higher rep-rate laser, or performing line-by-line imaging with a streak camera. The NSOM method only requires a single scanning measurement of about the same duration, yet has a large overhead in tip fabrication time.

To sum up, the stochastic super-resolution method is (1) easier to operate, (2) superior in resolution, (3) free from topography artifacts and the influence of the metalized tip which can introduce significant errors, and therefore in all aspects superior to the scanning-excitation technique based on NSOM.

2.6 Analysis based on FDTD simulation

To validate the comparison of the two experimental methods presented in the previous sections, we have simulated the LDOS near the center of a finite hexagonal array of 300 Al nanopyramids (an area of 11×11 μm^2) with a pitch of 550 nm on a glass substrate with the finite difference time-domain (FDTD) method [64]. An electric dipole of unit dipole moment $\boldsymbol{p}$ is placed at the probe position, 50 nm above the air-glass interface, as a source. The LDOS is obtained from monitoring the radiated flux out of, and the absorbed power inside a box enclosing the dipole source and the center nano-antenna of the array, using frequency domain monitors. The sum of the transmitted and absorbed power gives the total power required to drive the fixed strength source dipole ($P(\boldsymbol{p}, \boldsymbol{r})$),

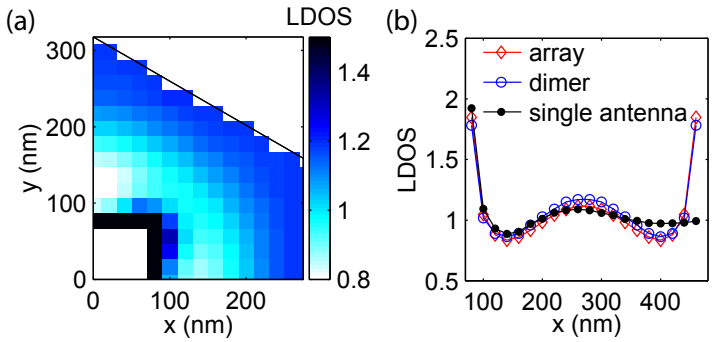

Figure 2.8: (a) Simulated map of LDOS enhancement of a hexagonal array with a pitch of 550 nm. Corresponding measurement result is shown in Fig. 2.5(b). (b) Comparison of simulated LDOS enhancements of an array and a dimer.

and thereby the LDOS enhancement ($\mathrm{LDOS}_{\boldsymbol{p}}(\boldsymbol{p},\boldsymbol{r})$) can be calculated as:

$$\mathrm{LDOS}_{\boldsymbol{p}}(\boldsymbol{p},\boldsymbol{r}) = \frac{P(\boldsymbol{p},\boldsymbol{r})}{P_0(\boldsymbol{p})}, \tag{2.3}$$

with $P_0(\boldsymbol{p})$ the radiative power of dipole $\boldsymbol{p}$ at the same height above a glass substrate. Assuming that the dye molecules are randomly oriented in the nanoprobes, we calculate the average LDOS of dye molecules in a nanoprobe ($\mathrm{LDOS}_{\mathrm{probe}}(\boldsymbol{r})$) by averaging over three orthogonal dipole orientations [65].

Fig. 2.8(a) shows the simulated average LDOS in a quarter of a primitive cell in the center of the array. The result agrees well with the result measured from the stochastic super-resolution method (Fig. 2.5), i.e., the LDOS is large (more than 1.5) near the Al nanoparticle, decreases immediately to about 0.8 as the dipole moves away from the Al nanoparticle and slightly increases to about 1.3 near the boundary of the primitive cell. There is a large gradient of the LDOS near the Al nanoparticles as expected, which is not accessible in the experiment due to the finite radius of the probes. At positions away from the Al nanoparticles, the measurement results agree well both qualitatively and quantitatively with the simulation (5 to 10% error, with all major features reproduced). We note that the absence of dielectric encapsulation of the source in FDTD is expected to hardly influence the result. Previous studies on photonic crystals and layered systems have shown that dielectric encapsulation of LDOS probes only introduces a multiplicative local field factor and has almost no effect on the LDOS distribution [66–68]. While the correspondence between super-resolution measurement and FDTD results is good, the result measured with NSOM markedly differs. This furthermore validates that the stochastic super-resolution method has overwhelming advantages over the scanning-excitation technique based on NSOM, in particular because it avoids topographic artifacts and the large influence of the tip itself on the LDOS.

Finally, aside from the pure methodological point of view of super-resolution LDOS

mapping, one can also wonder what physically determines the LDOS distribution. While the LDOS distribution near single metal nanoparticles is well understood, for instance from Mie calculations [69], in periodic plasmon particle systems it is not. We investigated the origin of the LDOS distribution based on further FDTD simulations. The LDOS can be hypothesized to be modified by the antenna array through three distinct mechanisms: LSPRs generated by individual nanoantennas, coupling between neighboring nanoantennas, and/or collective lattice modes of the array. To distinguish the contribution of these three possible mechanisms, we compare the LDOS in the lattice with the LDOS introduced by a single nanoantenna, and the LDOS along the axis between a pair of nanoantennas for a dimer with separation equal to the lattice constant of the array. As shown in Fig. 2.8(b), the LDOS introduced by the single nanoantenna (black) is high near the edge of the nanoantenna due to the LSPR. As the dipole moves away, the influence of the nanoantenna decreases and the LDOS starts to oscillate around 1 with a decreasing amplitude. The oscillation can be attributed to the interference of the dipole field and its reflection from the nanoantenna. Almost the same results are obtained for the array (measurement as well as FDTD result) and the dimer for $x < 200$ nm. As the dipole moves further, instead of decreasing, the LDOS continues increasing resulting in a peak in the middle of two nanoantennas. This is commensurate with the notion that the field reflected off both particles can form a standing wave, given that the particle separation is of the order of a wavelength. Since the blue and red curves for the dimer and a full array respectively show the same position dependence, we conclude that the LDOS modification is well captured by a dimer-model, without requiring recourse to the lattice modes.

2.7 Conclusion

We have introduced an experimental method to map the local density of states in periodic nanostructures based on stochastic super-resolution. This method has been realized on a hexagonal array of Al nanoantennas to map the LDOS at a wavelength of 605 nm with a resolution of ~ 40 nm, the result of which agrees with FDTD simulation.

In our implementation we were limited to structures with periodicities exceeding the wavelength, to surface probing, and to moderate (40 nm) resolutions. Already in this limit, the stochastic super-resolution method is superior to scanning-excitation NSOM in terms of both simplicity and accuracy. However, also the limitations of our method can be easily overcome. This method applies to any nanostructure with repeated units, provided that the nanostructure can be located in a white light image. If fiducial, isolated markers can be added around a structure at fabrication time, they can be used to pinpoint the structure with nanometer accuracy even if the structure itself can not be resolved due to a sub-diffraction pitch. Although the measurements introduced in this chapter are conducted on the surface of nanoantenna arrays, we note that the method is not limited to surface measurements. For example, three-dimensional mapping can be performed by embedding the nanoprobes in a dielectric layer on the nanostructure at different height slices, or by using axial localization techniques [70].

As regards resolution, at the price of photon count rate and hence acquisition time, this method could be used with single molecules as probes, thereby allowing an order of magnitude resolution improvement.

Using our method for LDOS mapping, we were able to resolve a simple, yet important question regarding the physics of fluorescence in plasmonic lattices, as we could confirm that LDOS variations are well explained by single-particle properties and nearest-neighbor coupling, without invoking lattice mode physics. We argue that our method extends to many other aspects of photophysics in plasmonic lattices. For example, our method equally applies to other optical measurements such as polarimetry and Fourier imaging [71], thereby allowing to pinpoint where in the unit cell a source must be placed to obtain optimal brightness, emission polarization, and Purcell factor.

References

[1] P. Anger, P. Bharadwaj, and L. Novotny, *Enhancement and quenching of single-molecule fluorescence*, Phys. Rev. Lett. **96**, 113002 (2006).

[2] S. Kühn, U. Håkanson, L. Rogobete, and V. Sandoghdar, *Enhancement of single-molecule fluorescence using a gold nanoparticle as an optical nanoantenna*, Phys. Rev. Lett. **97**, 017402 (2006).

[3] S. Schietinger, M. Barth, T. Aichele, and O. Benson, *Plasmon-enhanced single photon emission from a nanoassembled metal-diamond hybrid structure at room temperature*, Nano Lett. **9**, 1694 (2009).

[4] T. Taminiau, F. Stefani, F. Segerink, and N. Van Hulst, *Optical antennas direct single-molecule emission*, Nat. Photonics **2**, 234 (2008).

[5] R. J. Moerland, T. H. Taminiau, L. Novotny, N. F. van Hulst, and L. Kuipers, *Reversible polarization control of single photon emission*, Nano Lett. **8**, 606 (2008).

[6] R. H. Ritchie, *Plasma losses by fast electrons in thin films*, Phys. Rev. **106**, 874 (1957).

[7] L. Novotny and B. Hecht, *Principles of nano-optics*, Cambridge university press, 2012.

[8] P. Mühlschlegel, H.-J. Eisler, O. J. F. Martin, B. Hecht, and D. W. Pohl, *Resonant optical antennas*, Science **308**, 1607 (2005).

[9] K. H. Cho, J. Y. Kim, D.-G. Choi, K.-J. Lee, J.-H. Choi, and K. C. Choi, *Surface plasmon-waveguide hybrid polymer light-emitting devices using hexagonal Ag dots*, Opt. Lett. **37**, 761 (2012).

[10] G. Lozano, D. J. Louwers, S. R. Rodríguez, S. Murai, O. T. Jansen, M. A. Verschuuren, and J. Gómez Rivas, *Plasmonics for solid-state lighting: enhanced excitation and directional emission of highly efficient light sources*, Light Sci. Appl. **2**, e66 (2013).

[11] G. Lozano, G. Grzela, M. A. Verschuuren, M. Ramezani, and J. Gómez Rivas, *Tailor-made directional emission in nanoimprinted plasmonic-based light-emitting devices*, Nanoscale **6**, 9223 (2014).

[12] J. Stehr, J. Crewett, F. Schindler, R. Sperling, G. von Plessen, U. Lemmer, J. Lupton, T. Klar, J. Feldmann, A. Holleitner, M. Forster, and U. Scherf, *A low threshold polymer laser based on metallic nanoparticle gratings*, Adv. Mater. **15**, 1726 (2003).

[13] W. Zhou, M. Dridi, J. Y. Suh, C. H. Kim, D. T. Co, M. R. Wasielewski, G. C. Schatz, and T. W. Odom, *Lasing action in strongly coupled plasmonic nanocavity arrays*, Nat. Nanotechnol. **8**, 506 (2013).

[14] A. H. Schokker and A. F. Koenderink, *Lasing at the band edges of plasmonic lattices*, Phys. Rev. B **90**, 155452 (2014).

[15] X. Meng, J. Liu, A. V. Kildishev, and V. M. Shalaev, *Highly directional spaser array for the red wavelength region*, Laser Photon. Rev. **8**, 896 (2014).

[16] S. Mokkapati, F. J. Beck, A. Polman, and K. R. Catchpole, *Designing periodic arrays of metal nanoparticles for light-trapping applications in solar cells*, Appl. Phys. Lett. **95**, (2009).

[17] R. Chriki, A. Yanai, J. Shappir, and U. Levy, *Enhanced efficiency of thin film solar cells using a shifted dual grating plasmonic structure*, Opt. Express **21**, A382 (2013).

[18] R. A. Pala, J. White, E. Barnard, J. Liu, and M. L. Brongersma, *Design of plasmonic thin-film solar cells with broadband absorption enhancements*, Adv. Mater. **21**, 3504 (2009).

[19] V. E. Ferry, L. A. Sweatlock, D. Pacifici, and H. A. Atwater, *Plasmonic nanostructure design for efficient light coupling into solar cells*, Nano Letters **8**, 4391 (2008).

[20] F. Le, D. W. Brandl, Y. A. Urzhumov, H. Wang, J. Kundu, N. J. Halas, J. Aizpurua, and P. Nordlander, *Metallic nanoparticle arrays: A common substrate for both surface-enhanced raman scattering and surface-enhanced infrared absorption*, ACS Nano **2**, 707 (2008).

[21] P. Kühler, M. Weber, and T. Lohmüller, *Plasmonic nanoantenna arrays for surface-enhanced raman spectroscopy of lipid molecules embedded in a bilayer membrane*, ACS Appl. Mater. Inter. **6**, 8947 (2014).

[22] L. Billot, M. L. de la Chapelle, A.-S. Grimault, A. Vial, D. Barchiesi, J.-L. Bijeon, P.-M. Adam, and P. Royer, *Surface enhanced raman scattering on gold nanowire arrays: Evidence of strong multipolar surface plasmon resonance enhancement*, Chem. Phys. Lett. **422**, 303 (2006).

[23] N. Félidj, J. Aubard, G. Lévi, J. R. Krenn, M. Salerno, G. Schider, B. Lamprecht, A. Leitner, and F. R. Aussenegg, *Controlling the optical response of regular arrays of gold particles for surface-enhanced raman scattering*, Phys. Rev. B **65**, 075419 (2002).

[24] V. G. Kravets, F. Schedin, A. V. Kabashin, and A. N. Grigorenko, *Sensitivity of collective plasmon modes of gold nanoresonators to local environment*, Opt. Lett. **35**, 956 (2010).

[25] P. Offermans, M. C. Schaafsma, S. R. K. Rodriguez, Y. Zhang, M. Crego-Calama, S. H. Brongersma, and J. Gómez Rivas, *Universal scaling of the figure of merit of plasmonic sensors*, ACS Nano **5**, 5151 (2011).

[26] W. P. Ambrose, P. M. Goodwin, R. A. Keller, and J. C. Martin, *Alterations of single molecule fluorescence lifetimes in near-field optical microscopy*, Science **265**, 364 (1994).

[27] M. Frimmer, Y. Chen, and A. F. Koenderink, *Scanning emitter lifetime imaging microscopy for spontaneous emission control*, Phys. Rev. Lett. **107**, 123602 (2011).

[28] J. P. Hoogenboom, G. Sanchez-Mosteiro, G. Colas des Francs, D. Heinis, G. Legay, A. Dereux, and N. F. van Hulst, *The single molecule probe: Nanoscale vectorial mapping of photonic mode density in a metal nanocavity*, Nano Lett. **9**, 1189 (2009).

[29] V. Krachmalnicoff, E. Castanié, Y. De Wilde, and R. Carminati, *Fluctuations of the local density of states probe localized surface plasmons on disordered metal films*, Phys. Rev. Lett. **105**, 183901 (2010).

[30] M. A. Lieb, J. M. Zavislan, and L. Novotny, *Single-molecule orientations determined by direct emission pattern imaging*, J. Opt. Soc. Am. B **21**, 1210 (2004).

[31] D. W. Pohl, W. Denk, and M. Lanz, *Optical stethoscopy: Image recording with resolution λ/20*, Appl. Phys. Lett. **44**, 651 (1984).

[32] J. Michaelis, C. Hettich, J. Mlynek, and V. Sandoghdar, *Optical microscopy using a single-molecule light source*, Nature **405**, 325 (2000).

[33] L. Aigouy, Y. D. Wilde, and M. Mortier, *Local optical imaging of nanoholes using a single*

fluorescent rare-earth-doped glass particle as a probe, Appl. Phys. Lett. **83**, 147 (2003).

[34] S. Kühn, C. Hettich, C. Schmitt, J.-P. Poizat, and V. Sandoghdar, *Diamond colour centres as a nanoscopic light source for scanning near-field optical microscopy*, J. Microsc. **202**, 2 (2001).

[35] Y. Sonnefraud, N. Chevalier, J.-F. Motte, S. Huant, P. Reiss, J. Bleuse, F. Chandezon, M. T. Burnett, W. Ding, and S. A. Maier, *Near-field optical imaging with a CdSe single nanocrystal-based active tip*, Opt. Express **14**, 10596 (2006).

[36] H. Gersen, M. F. García-Parajó, L. Novotny, J. A. Veerman, L. Kuipers, and N. F. van Hulst, *Influencing the angular emission of a single molecule*, Phys. Rev. Lett. **85**, 5312 (2000).

[37] A. Cuche, O. Mollet, A. Drezet, and S. Huant, *"Deterministic" quantum plasmonics*, Nano Lett. **10**, 4566 (2010).

[38] V. Krachmalnicoff, D. Cao, A. Cazé, E. Castanié, R. Pierrat, N. Bardou, S. Collin, R. Carminati, and Y. D. Wilde, *Towards a full characterization of a plasmonic nanostructure with a fluorescent near-field probe*, Opt. Express **21**, 11536 (2013).

[39] R. Beams, D. Smith, T. W. Johnson, S.-H. Oh, L. Novotny, and A. N. Vamivakas, *Nanoscale fluorescence lifetime imaging of an optical antenna with a single diamond NV center*, Nano Lett. **13**, 3807 (2013).

[40] A. G. Curto, G. Volpe, T. H. Taminiau, M. P. Kreuzer, R. Quidant, and N. F. van Hulst, *Unidirectional emission of a quantum dot coupled to a nanoantenna*, Science **329**, 930 (2010).

[41] D. M. Koller, U. Hohenester, A. Hohenau, H. Ditlbacher, F. Reil, N. Galler, F. R. Aussenegg, A. Leitner, A. Trügler, and J. R. Krenn, *Superresolution Moiré mapping of particle plasmon modes*, Phys. Rev. Lett. **104**, 143901 (2010).

[42] A. Huck, S. Kumar, A. Shakoor, and U. L. Andersen, *Controlled coupling of a single nitrogen-vacancy center to a silver nanowire*, Phys. Rev. Lett. **106**, 096801 (2011).

[43] T. van der Sar, E. C. Heeres, G. M. Dmochowski, G. de Lange, L. Robledo, T. H. Oosterkamp, and R. Hanson, *Nanopositioning of a diamond nanocrystal containing a single nitrogen-vacancy defect center*, Appl. Phys. Lett. **94** (2009).

[44] S. Kumar, A. Huck, and U. L. Andersen, *Efficient coupling of a single diamond color center to propagating plasmonic gap modes*, Nano Lett. **13**, 1221 (2013).

[45] E. Betzig, G. H. Patterson, R. Sougrat, O. W. Lindwasser, S. Olenych, J. S. Bonifacino, M. W. Davidson, J. Lippincott-Schwartz, and H. F. Hess, *Imaging intracellular fluorescent proteins at nanometer resolution*, Science **313**, 1642 (2006).

[46] S. T. Hess, T. P. Girirajan, and M. D. Mason, *Ultra-high resolution imaging by fluorescence photoactivation localization microscopy*, Biophys. J. **91**, 4258 (2006).

[47] M. J. Rust, M. Bates, and X. Zhuang, *Sub-diffraction-limit imaging by stochastic optical reconstruction microscopy (storm)*, Nat. Methods **3**, 793 (2006).

[48] H. Lin, S. P. Centeno, L. Su, B. Kenens, S. Rocha, M. Sliwa, J. Hofkens, and H. Uji-i, *Mapping of surface-enhanced fluorescence on metal nanoparticles using super-resolution photoactivation localization microscopy*, ChemPhysChem **13**, 973 (2012).

[49] E. Johlin, J. Solari, S. A. Mann, J. Wang, T. S. Shimizu, and E. C. Garnett, *Super-resolution imaging of light-matter interactions near single semiconductor nanowires*, Nat. Commun. **7**, 13950 (2016).

[50] H. Cang, A. Labno, C. Lu, X. Yin, M. Liu, C. Gladden, Y. Liu, and X. Zhang, *Probing the electromagnetic field of a 15-nanometre hotspot by single molecule imaging*, Nature **469**, 385 (2011).

[51] L. Wei, C. Liu, B. Chen, P. Zhou, H. Li, L. Xiao, and E. S. Yeung, *Probing single-molecule fluorescence spectral modulation within individual hotspots with subdiffraction-limit image*

resolution, Anal. Chem. **85**, 3789 (2013).

[52] C. Ropp, Z. Cummins, S. Nah, J. T. Fourkas, B. Shapiro, and E. Waks, *Nanoscale probing of image-dipole interactions in a metallic nanostructure*, Nat. Commun. **6** (2015).

[53] Y. V. Miklyaev, S. A. Asselborn, K. A. Zaytsev, and M. Y. Darscht, *Superresolution microscopy in far-field by near-field optical random mapping nanoscopy*, Appl. Phys. Lett. **105** (2014).

[54] E. Wertz, B. P. Isaacoff, J. D. Flynn, and J. S. Biteen, *Single-molecule super-resolution microscopy reveals how light couples to a plasmonic nanoantenna on the nanometer scale*, Nano Lett. **15**, 2662 (2015).

[55] R. E. Thompson, D. R. Larson, and W. W. Webb, *Precise nanometer localization analysis for individual fluorescent probes*, Biophys. J. **82**, 2775 (2002).

[56] M. A. Verschuuren, *Substrate Conformal Imprint Lithography for Nanophotonics*, PhD thesis, Utrecht University, 2010.

[57] S. R. K. Rodriguez, F. B. Arango, T. P. Steinbusch, M. A. Verschuuren, A. F. Koenderink, and J. Gómez Rivas, *Breaking the symmetry of forward-backward light emission with localized and collective magnetoelectric resonances in arrays of pyramid-shaped aluminum nanoparticles*, Phys. Rev. Lett. **113**, 247401 (2014).

[58] K. L. Blythe, E. J. Titus, and K. A. Willets, *Comparing the accuracy of reconstructed image size in super-resolution imaging of fluorophore-labeled gold nanorods using different fit models*, J. Phys. Chem. C **119**, 19333 (2015).

[59] H.F. Talbot Esq. F.R.S., *LXXVI. Facts relating to optical science. No. IV*, Philos. Mag. Series 3 **9**, 401 (1836).

[60] K. Joulain, R. Carminati, J.-P. Mulet, and J.-J. Greffet, *Definition and measurement of the local density of electromagnetic states close to an interface*, Phys. Rev. B **68**, 245405 (2003).

[61] P. Bharadwaj, B. Deutsch, and L. Novotny, *Optical antennas*, Adv. Opt. Photon. **1**, 438 (2009).

[62] A. Kwadrin and A. F. Koenderink, *Gray-tone lithography implementation of Drexhage's method for calibrating radiative and nonradiative decay constants of fluorophores*, J. Phys. Chem. C **116**, 16666 (2012).

[63] J. A. Veerman, A. M. Otter, L. Kuipers, and N. F. van Hulst, *High definition aperture probes for near-field optical microscopy fabricated by focused ion beam milling*, Appl. Phys. Lett. **72**, 3115 (1998).

[64] *LUMERICAL, FDTD solutions*.

[65] W. L. Vos, A. F. Koenderink, and I. S. Nikolaev, *Orientation-dependent spontaneous emission rates of a two-level quantum emitter in any nanophotonic environment*, Phys. Rev. A **80**, 053802 (2009).

[66] I. S. Nikolaev, W. L. Vos, and A. F. Koenderink, *Accurate calculation of the local density of optical states in inverse-opal photonic crystals*, J. Opt. Soc. Am. B **26**, 987 (2009).

[67] F. A. Inam, T. Gaebel, C. Bradac, L. Stewart, M. J. Withford, J. R. Rabeau, and M. J. Steel, *Modification of spontaneous emission from nanodiamond colour centres on a structured surface*, New J. Phys. **13**, 073012 (2011).

[68] A. Mohtashami and A. F. Koenderink, *Suitability of nanodiamond nitrogen-vacancy centers for spontaneous emission control experiments*, New J. Phys. **15**, 043017 (2013).

[69] H. Mertens, A. F. Koenderink, and A. Polman, *Plasmon-enhanced luminescence near noble-metal nanospheres: Comparison of exact theory and an improved gersten and nitzan model*, Phys. Rev. B **76**, 115123 (2007).

[70] B. Huang, W. Wang, M. Bates, and X. Zhuang, *Three-dimensional super-resolution imaging*

by stochastic optical reconstruction microscopy, Science **319**, 810 (2008).

[71] C. I. Osorio, A. Mohtashami, and A. F. Koenderink, *K-space polarimetry of bullseye plasmon antennas*, Sci. Rep. **5**, 9966 (2015).

3

Dendritic Optical Antennas

With the development of nanotechnology, researchers have brought the concept of antenna to the optical regime to manipulate light matter interaction on the nano-scale. Most optical nanoantennas optimize optical functions, but are not electrically connected. In order to realize functions that require electrical addressing, optical nanoantennas that are electrically continuous are desirable. In this chapter, we study the optical response of a type of electrically connected nanoantennas, which we propose to call "dendritic" antennas. While they are connected, they follow antenna hybridization trends similar to unconnected plasmon phased array antennas. The optical resonances supported by this type of nanoantennas are mapped both experimentally and theoretically to unravel their optical response. Photoluminescence measurements indicate a potential Purcell enhancement by a factor of more than 58.

3.1 Introduction

Resonant optical nanoantennas [1] enable efficient light matter interaction at nanometer scales, with large promise for a wide range of fields including light emission [2–7], lasing [8–11], sensing and nano-medicine [12–16], photovoltaics [17–20], and optical information processing [21–24]. Well-developed radio antenna theory has inspired the design of a variety of optical antennas such as dipole [25, 26], bow-tie [11, 27] and Yagi-Uda antennas [28] in order to achieve different functionalities. In particular, narrow gaps between sharp structures are pursued for high local fields, while oligomers

of plasmonic particles [29] are designed to reach strong directivity and control over extinction and scattering spectra, on the basis of plasmon hybridization and phased-array effects.

Contrary to many radio antennas, state-of-the-art optical antennas do not generally form a continuous electrical network, hampering electrical addressing of active matter that loads the antenna. Recently, Kern et al. [30] for the first time created an electrically driven optical antenna in form of an optically connected bow-tie structure. Electrically connected antennas open the perspective of designing antennas that both provide optical enhancement and allow electric driving of active or nonlinear matter that loads the antenna. Similar perspectives could apply to linear and nonlinear metasurfaces to control the amplitude, phase, and spin/orbital angular momentum content of light [31, 32], if they could be made in connected metallic form. Here we study the optical properties of antennas that are electrically connected and at the same time benefit from the plasmon hybridization effects known from hybridization of discrete particle plasmon resonances. In particular, we study so-called "dendritic" antennas, that can be viewed as oligomers of nanorods that are electrically connected together to form a connected structure in a brickwork pattern. This design brings a dendritic RF antenna design that originally targeted RF communication and transduction, to the optics domain.

In this chapter, we study disconnected oligomers and the corresponding connected, dendritic antennas. Through mid-IR, IR and visible extinction spectroscopy, we map the optical resonances as a function of the connectors, and as function of antenna "generation", which quantifies how far the brickwork extends. We interpret the mode structure through two independent theoretical methods. The finite element method (FEM) allows to study driven antennas, while we use the volumetric method of moments (V-MoM) with group theoretical analysis to identify a classification scheme for the intrinsic eigenmodes. FEM simulation furthermore predicts large Purcell enhancements for emitters placed in a narrow gap that one could fabricate in the central antenna element. Finally, we present a preliminary, i.e., ensemble-averaged, photoluminescence (PL) brightness and decay rate enhancement study using overcoated high-efficiency and low-efficiency organic dyes.

3.2 Dendritic antenna design

The basic design for dendritic optical antennas is illustrated in Fig. 3.1. Through an iterative growth rule one can build a hierarchy of antenna generations, where each generation spans a larger size. Starting with a single nanorod of length L_1 (165 nm in our work) and width W_1 (90 nm), we compose a pentamer of five identical, yet disconnected rods. For identification, we mark the central element a and the four added rods as b as shown in Fig. 3.1(a,b). The first generation of the dendritic optical antenna family is obtained by connecting the central element a to the side arms b with vertical connectors (geometrical parameters $L_2 = 140$ nm $W_2 = 60$ nm) as shown in Fig. 3.1(b,c). This design can be extended to generation $n+1$ from generation n by adding a column

of $2n+1$ arms (again of size L_1, W_1) to both the left and right, and again connecting those with vertical connectors. In principle an electrically connected network can be made in this way. This design is somewhat similar to fractal antennas [33, 34]. However, while fractals are generated by subdividing or filling a given area with ever smaller features, in our design the typical element size remains the same, but the full antenna size grows linearly with generation. One could envision that for sufficiently large generation number, one obtains a macroscopically sized connected electric network, with the original element a as a unique single-point constriction. In this work we study the first and second generation dendritic antenna in comparison with their unconnected counterparts, to elucidate the mode structure.

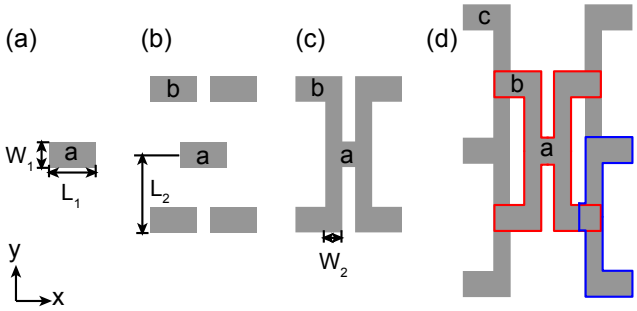

Figure 3.1: Schematics of (a) the single antenna element, (b) the disconnected pentamer, (c) the first and (d) second generation of dendritic antennas. The red and blue outlines in (d) indicate the first generation in (b) and an appended half of it respectively.

3.3 Sample fabrication and measurement setups

Samples are fabricated on silica substrates using electron beam lithography (20 kV, ZEP-resist), evaporation of 30 nm of Ag or Au, and subsequent liftoff. To obtain reasonable signal strength in ensemble transmission measurements, the antennas are arranged in dilute square arrays with a pitch of 1.75 µm.

We measure the transmittance of the samples using the setup illustrated in Fig. 3.2(a). We couple the white light from a halogen lamp to a 50 µm fiber, which is polarized in the direction of the antenna arms with a linear polarizer and imaged on the sample with two lenses with a magnification of 1. The transmission is collected by two lenses and imaged on the detectors. We measure transmittances over a huge spectral range of f = 50 - 500 THz (6 µm to 0.6 µm in wavelength). This large range is required due to the inverse scaling of antenna fundamental frequency, and the length over which charge separation occurs [35, 36]. Therefore, three different detectors are used for different spectral ranges. An Ocean Optics fiber-coupled grating spectrometer is used for the visible to near-infrared spectrum (f = 320 - 500 THz). For lower frequency, we use Fourier transform infrared (FTIR) spectroscopy. FTIR spectroscopy

is based on a interferometer illustrated in Fig. 3.2(b). The intensity that arrives at the detector is dependent on the input spectrum ($E(\omega)$) and the optical path difference of the two arms (δ):

$$I(\delta) = \int \left| \frac{E(\omega)}{2} e^{\mathrm{i}(kr-\omega t)} + \frac{E(\omega)}{2} e^{\mathrm{i}(kr-\omega t+k\delta)} \right|^2 \mathrm{d}\omega = \int \frac{|E(\omega)|^2}{2} (1+\cos\frac{\omega}{c}\delta)\mathrm{d}\omega \quad (3.1)$$

As we scan δ by moving the scanning mirror, we obtain an interferogram ($I(\delta)$), the Fourier transform of which gives the input spectrum. We use a commercial HYPERION Series FT-IR Microcope for the mid-infrared frequency range (50 to 150 THz), and home built FTIR setup with a commercial interferometer (Interspec FTNIR 402-X) and an InGaAs diode for the near-infrared frequency range (150 to 330 THz). We convert the transmission T into effective extinction cross sections per antenna through $\sigma_{\mathrm{ext}}(f) = (1-T)\cdot A_{\mathrm{cell}}$, with $A_{\mathrm{cell}} = 3.1\ \mu\mathrm{m}^2$ the unit cell area of our arrays.

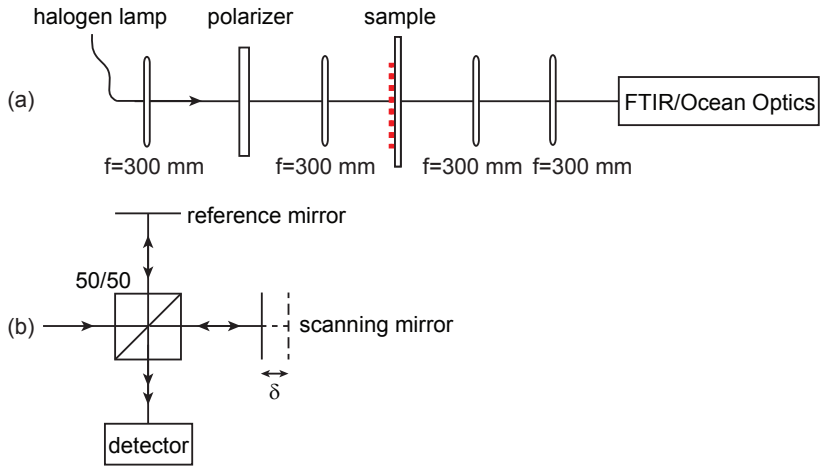

Figure 3.2: Schematics of (a) the setup for transmittance measurements in the visible and near infrared and (b) the basic geometry of a FTIR component.

We measure the PL intensity and lifetime with a confocal microscope that is the same as the one used in Chapter 2 (Fig. 2.1(b)). A pulsed diode laser with a wavelength of 650 nm and a repetition rate of 10 MHz (Picoquant, ps pulses) is used to excite the dye molecules. The emission to the substrate side is collected by an objective with NA = 1.4 and detected by an avalanche photodiode (APD) after passing a longpass filter at 680 nm. The APD (IdQuantique id100-20ULN) measures the PL intensity and lifetime based on time-correlated single photon counting (Becker& Hickl, DPC230).

3.4 Extinction

Fig. 3.3(a-c) show scanning electron microscope (SEM) images of a Au pentamer, a first and a second generation of dendritic antenna, all made by electron beam lithography.

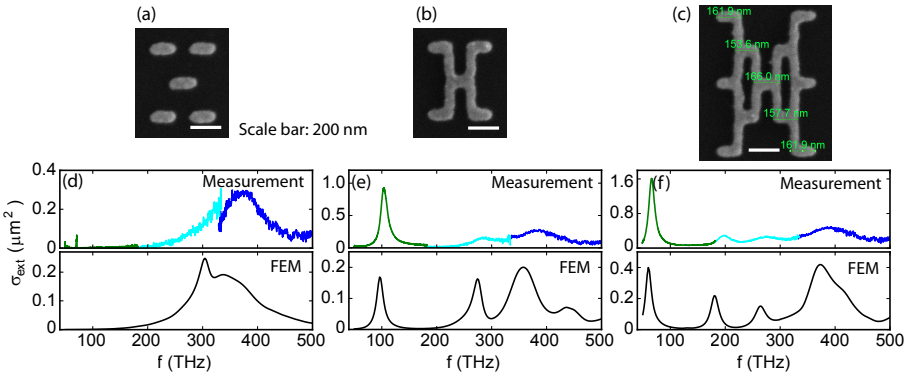

Figure 3.3: SEM images and comparison of measured (colored lines) and simulated (black lines) extinction cross sections of (a)(d) the pentamer, (b)(e) the first and (c)(f) the second generation of dendritic antennas. The extinction cross section is measured with three detectors for different frequency ranges. Green: Bruker HYPERION Series FTIR; cyan: Interspec FTNIR 402-X; blue: Ocean optics fiber-coupled grating spectrometer.

Alongside, Fig. 3.3(d-f) show the extinction cross sections per antenna for x-polarized driving (polarized along the rods) measured from three setups spanning a frequency range from 50 to 500 THz. The measurement results from different setups agree well at their overlapping frequencies except for the pentamer case near 320 THz, where the FTIR operates at the limit of its sensitivity range. The pronounced peaks in extinction cross sections indicate the different x-polarized optical modes supported by the antennas. As expected, the pentameter composed of unconnected rods only shows a response near 350 THz, i.e., near the single-rod dipole resonance. At similar frequencies two modes are found for the first and the second generations of the dendritic antennas. The first generation, however, also presents one new mode at a dramatically lower frequency around 100 THz, while the second generation offers two new modes around 180 THz and 60 THz respectively. In addition to the antennas studied here, we have studied the extinction of many similar antennas, i.e., antennas made by the same geometrical rule, but different geometrical parameters (arm length, connector length), and also made of Ag instead of Au. We generally find the same spectral progression, however with an overall redshift of features at larger geometrical parameters, as expected from size-scaling arguments.

To confirm the presence of distinct resonances in extinction, we conducted FEM simulations (COMSOL Multiphysics) on single antennas, assuming normally incident plane wave illumination with x-polarization. We calculate extinction as the sum of scattering and absorption in a total-field scattered-field calculation, including the glass substrate, and using optical constants for Au from Etchegoin (Ref. [37]). The simulated extinction cross sections are shown in Fig. 3.3(d-f), each plotted below the corresponding measurement. Calculations in general accurately predict the resonances observed in the extinction measurements. Small shifts and disagreement in amplitude can be attributed to the difference between the simulated geometry and the actual

sample geometry.

3.5 Finite element mode analysis

Examining the calculated extinction in itself does not explain the underlying mode structure. Rather, one must inspect simulated near-fields and current densities. In this section, we discuss the mode assignments for the pentamer and the dendritic antennas one by one. We label the resonant modes obtained in the simulation as $n-m$, with n indicating the antenna generation (0 for pentamer), and m the mode number. For each mode we plot the electric field and current distributions in a 2D cross section at select frequencies, and the volume-averaged induced current in the x-direction.

Fig. 3.4(a-c) and (f) show results for the pentamer which displays physics very similar to the well known plasmon heptamer [29, 38–41]. The pentamer has all its hybridized modes close to the single-rod resonance, i.e., near 300 THz, with a distinct Fano feature in extinction cross section that can be attributed to a superradiant mode (all dipole moments aligned), and a subradiant mode (central arm has dipole moment against the outer arms), as shown in Fig. 3.4(a-c). The field and current plots (Fig. 3.4(f)) evidence that the response is dominated by the outer arms for f=302 THz (peak labelled as 0-1 in Fig. 3.4(a-c)), with the central arm out of phase with the outer arms. At f = 340 THz (extinction peak labelled 0-2 in Fig. 3.4(a-c)), all arms respond in phase. At the intermediate frequency f = 320 THz, the central arm is a quarter cycle out of phase. While the Fano-feature in exctinction calculations is not as clear as for the famous heptamer in literature [41] due to imperfect tuning of the modes, these are the characteristic features of a plasmonic Fano resonance. The Fano feature, which does not constitute a main claim of this work, is not easily verified in our experiment due to the transition between two detector windows.

We can now understand the physics of the connected first generation antenna based on the pentamer modes. Fig. 3.4(d) shows the simulated extinction cross section and net current in the x direction of the first generation of dendritic antenna. The lowest energy mode, Mode 1-1 has large current flowing from left to right through the entire antenna, without any node as shown in Fig. 3.4(g). Essentially, this mode can be seen as the fundamental $\lambda/2$ mode of a long rod, which one can envision by unfolding the three arms plus the two vertical connectors. This viewpoint is similar to the viewpoint on modes of folded metal structures first put forward by Rockstuhl et al. for split rings [36]. Mode 1-2 and Mode 1-3 directly derive from the subradiant and superradiant modes of the pentamer, both without current flowing in the connecting arms. The subradiant mode (central rod polarized against the outer ones) is redshifted while the superradiant mode is blue shifted. At even higher frequency a fourth mode appears in which the vertical connecting rods do participate (Mode 1-4).

Fig. 3.4 (e) and (h) shows how these results generalize to the second generation. The lowest order mode, Mode 2-1 is even further redshifted to 60 THz, and again shows currents flowing across the entire structure with no node. The longer wavelength is consistent with its larger size [36]. Modes 2-2 and Mode 2-3 (at 180 THz and 264

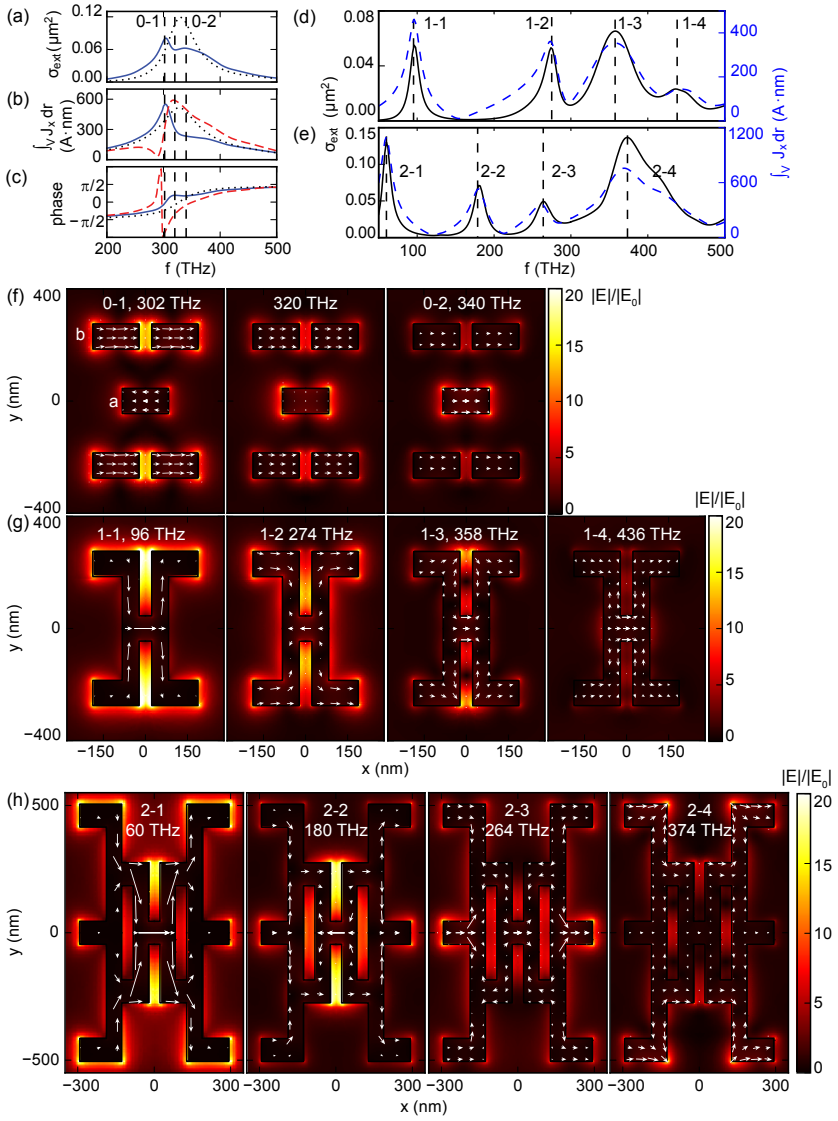

Figure 3.4: (a) Simulated extinction cross section of the pentamer (blue line) compared with that of a single rod multiplied by 5 (black dots). (b) Simulated amplitude and (c) phase of net current in the *x*-direction in a (blue line) and b (red dashed line) compared with the current in a single rod (black dots). (d-e) Simulated extinction coefficient (black line) and amplitude of net current in the *x*-direction (blue dashed line) of (d) the first and (e) the second generations of dendritic antennas. (f-h) Simulated maps of electrical field and current distribution in a cross section of (f) the pentamer, (g) the first and (h) the second generations of the dendritic antennas at resonant frequencies specified by the black dashed lines in (a-e).

THz) can be considered as arising from Mode 1-2 (current in central arm opposed to its 4 neighbors), hybridized in turn either in phase or out of phase with the bright mode of the six outer arms. Finally, Mode 2-4 at 374 THz has currents in the same direction in all the arms with nodes in the connectors, and is therefore similar to the superradiant Mode 0-2 of the pentamer, and the superradiant Mode 1-3 of the first generation. The shoulder in the extinction spectrum above 400 THz indicates further higher order modes similar to mode 1-4, in which also the connecting rods carry current.

To summarize, we hypothesize that the following mode structure is responsible for the optical properties. First, the dendritic antennas have a fundamental $\lambda/2$ resonance that extends across the entire structure and hence redshifts with increasing generation number. Second, near 370 THz, the dendritic antennas have a mode in which all arms are in phase and the connecting rods are largely irrelevant, that coincides in character and in frequency with the superradiant mode of the pentamer. At frequencies in between the superradiant mode and the fundamental mode, various modes occur as hybrids of the pentamer subradiant mode with the outer arms.

3.6 V-MoM with group theory analysis for classification of eigenmodes

The FEM simulation revealed resonant responses of dendritic antennas upon external driving by a plane wave. In any driven problem, one relies on a non-zero projection of the drive on the modes of the system to identify modes. In this section, we extend the mode assignment discussion in the previous section by combining an excitation independent eigenmode analysis with a group theory approach that were developed by our collaborators Xuezhi Zheng and Guy. A. E. Vandenbosch.

As this would be difficult to implement in COMSOL, the light interaction with a nano-scatterer is formulated in the framework of electric field - volume integral equations (EF-VIEs) [42–46] For the sake of conciseness, the electric field volume integral equation is summarized in an operator form,

$$\boldsymbol{Z}(\boldsymbol{r},\boldsymbol{r'};\omega)\cdot\boldsymbol{J}(\boldsymbol{r'},\omega)=\boldsymbol{E}_{\text{inc}}(\boldsymbol{r},\omega). \tag{3.2}$$

In Eq.(3.2) $\boldsymbol{J}(\boldsymbol{r'},\omega)$ represents the full solution, i.e. the induced current (and charge) flowing in a nanostructure due to an incident field $\boldsymbol{E}_{\text{inc}}$, while the impedance operator $\boldsymbol{Z}(\boldsymbol{r},\boldsymbol{r'};\omega)$ incorporates the Green's function that describes how any part of the nanostructure (source point $\boldsymbol{r'}$) electromagnetically interacts with another part (at point $\boldsymbol{r}$). At any frequency, Eq. (3.2) can be analyzed as an eigenvalue problem [47]

$$\boldsymbol{Z}(\boldsymbol{r},\boldsymbol{r'};\omega)\cdot\boldsymbol{J}_n(\boldsymbol{r'},\omega)=\lambda_n(\omega)\boldsymbol{J}_n(\boldsymbol{r'},\omega). \tag{3.3}$$

In Eq. (3.3), $\boldsymbol{J}(\boldsymbol{r'},\omega)$ is a complex spatial distribution which is independent of the incident field distribution. The corresponding eigenvalue $\lambda_n(\omega)$ can be viewed as a generalized (inverse) polarizability. For any given incident field, the coupling

coefficients c_n for coupling to each eigenvector are given by

$$c_n(\omega) = \frac{\int_V \boldsymbol{J}_n(\boldsymbol{r'},\omega)\cdot\boldsymbol{E}_{\mathrm{inc}}(\boldsymbol{r'},\omega)\mathrm{d}\boldsymbol{r'}}{\lambda_n(\omega)}, \tag{3.4}$$

where the integration runs over the antenna volume. By combining the contributions from all the eigenvectors, we are able to recover the full solution,

$$\boldsymbol{J}(\boldsymbol{r'},\omega) = \sum c_n(\omega)\boldsymbol{J}_n(\boldsymbol{r'},\omega). \tag{3.5}$$

Conveniently, in this implementation eigenvectors and their coupling coefficients can be traced continuously as function of frequency. When the magnitude of an eigenvalue becomes minimal, this implies a resonance in the induced current.

A distinct advantage of this formulation as an eigen-problem is that the finite-dimensional approximation to the impedance operator Z that appears in numerical analysis is amenable to symmetry analysis using group theory [48]. Our experimental system, i.e., a single structure on an air-glass interface, under normal incidence in x-polarization, implies C_{2v} symmetry, an Abelian group of order 4 with four irreducible representations. Combining the group's irreducible representations and its transformation operators for vector fields, a set of projection operators [47, 49, 50] $\mathscr{P}_j$ can be constructed which allow to block-diagonalize the impedance matrix as

$$Z = \bigoplus_{j=1}^{4} Z_j, \quad \text{with } Z_j = \mathscr{P}_j Z. \tag{3.6}$$

Instead of decomposing the eigenvalues of the original impedance operator as in Eq. (3.3), the eigenvalue decomposition is applied to the projected matrices Z_j, homing in on the eigenvectors and eigenvalues that belong within a certain irreducible representation. The excitation used in this work projects only on the irreducible representation Γ_4, and accordingly only excites resonances in this representation. Note that oblique incidence, or incidence with different polarization would allow to excite also modes in several other irreducible representations. The strength of our experiment and the use of group theory is that by selecting the excitation condition according to symmetry, just a selected set of modes is relevant. For the pentamer, out of a total of five modes, two fall within Γ_4, corresponding to the subradiant and superradiant modes underlying Fano resonance as shown in Fig. 3.5 (a-b) and (e). The modes within an irreducible representation are not necessarily orthogonal in an inner product sense [41, 47] and can thus interfere to generate a Fano-line in extinction.

For the first and second generation of dendritic antennas, eigenmodes with similar frequencies and current distributions to the modes found by FEM simulation are obtained by the combination of group theory and V-MoM. For the first generation, 14 modes are found between 50 and 500 THz, of which five fall within Γ_4. Fig. 3.5 (c) and (f) show the coupling coefficients and charge distributions for the first four resonances (with the lowest frequency, f = 103, 294, 382, and 459 THz). These results confirm that the fundamental mode is essentially a $\lambda/2$ resonance spanning the entire structure,

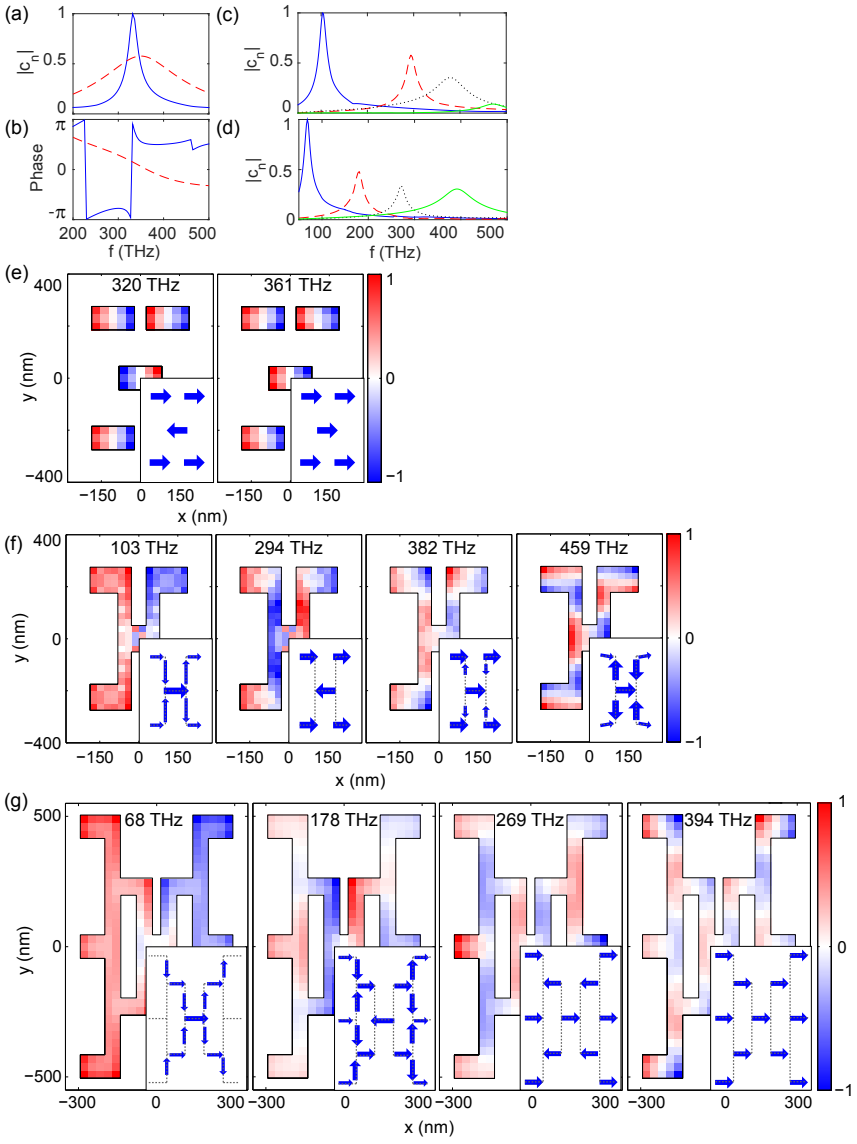

Figure 3.5: (a) Amplitude (normalized to the maximum) and (b) phase of the coupling coefficients of the the superradiant (blue solid lines) and subradiant (red dashed lines) modes supported by the pentamer. (c-d) Amplitude (normalized to the maximum) of the coupling coefficients of eigenmodes of (c) the first and (d) the second generations of the dendritic antennas. Normalized instantaneous charge distribution of eigenmodes obtained from V-MoM within the Γ_4 representation for (e) the pentamer, (f) the first and (g) the second generations of the dendritic antennas. Insets illustrate the directions of instantaneous net current.

that the mode at 294 THz is a (redshifted) subradiant mode, and that the resonance at 382 THz is essentially the original superradiant mode of the pentamer. The mode at 459 THz has significant $y-$oriented currents.

For the second generation, in total 36 modes between 50 and 500 THz are identified, of which most are not coupled to normal-incidence plane waves. Figure 3.5(d) and (g) show the first four resonances in Γ_4 with a resonant coupling coefficient between 50 and 500 THz, again showing that the qualitative identification that we derived from the FEM simulations is correct and complete.

3.7 Analysis of Purcell enhancement

Having identified the mode structure of dendritic antennas, we ask whether they are interesting for spontaneous emission control. As a starting point, the rationale is that if one would couple a single emitter to the central nanorod, the pentamer superradiant mode would aid in obtaining bright emission. Further, if one would replace the central nanorod of the pentamer by a nanorod with a narrow gap in the center, one could at the same time benefit from the high LDOS in the narrow gap [1], and the superradiant dipole physics of the pentamer. Since the dendritic antennas support essentially the same superradiant modes, it is interesting to ask if dendritic antennas retain or improve the dipole array antenna physics. If so, an advantage of dendritic antennas would be electrical addressability of the gap where the emitter sits.

Optical antennas can modify various photoluminescence observables through different mechanisms that trade off depending on emitter efficiency. They can (1) enhance the absorption of pump light, (2) modify radiation patterns, (3) accelerate emission, and (4) introduce additional quenching due to absorption by the metal. The joint effect of (3) and (4) depends on intrinsic quantum yield (QY_0) of the fluorophores chosen. Intrinsically high QY_0 allows to accelerate decay by the Purcell effect, with a drawback in efficiency due to the quenching. In contrast, an inefficient emitter ($\mathrm{QY}_0 \ll 1$) will gain in efficiency when Purcell enhanced rates out-compete intrinsic nonradiative rates, even if the total decay rate is only modestly affected. Expressed mathematically, we have the following expectations for the rate enhancement [51]

$$\frac{\gamma}{\gamma_0} \approx \begin{cases} \rho_{\mathrm{tot}}, & \text{when } \mathrm{QY}_0 \approx 1 \\ 1, & \text{when } \mathrm{QY}_0 \approx 0, \end{cases} \tag{3.7}$$

resp. the change in emission efficiency

$$\frac{\mathrm{QY}}{\mathrm{QY}_0} \approx \begin{cases} \rho_{\mathrm{r}}/\rho_{\mathrm{tot}}, & \text{when } \mathrm{QY}_0 \approx 1 \\ \rho_{\mathrm{r}}, & \text{when } \mathrm{QY}_0 \approx 0, \end{cases} \tag{3.8}$$

where ρ_{tot} indicates the enhancement of total emission rate, i.e., the local density of states of which the radiative part is ρ_{r}.

We perform FEM simulations assuming a single dipole source oriented in the x direction in the center of the antennas, in a 30 nm gap. For fluorescence measurements

as reported below, one typically requires covering the antennas by a thin polymer layer that is doped with fluorophores. To compensate the red-shifts of antenna resonances due to polymer coverage, we use Ag instead of Au antennas, to maintain the resonances at the visible and near-infrared range to be comparable with most fluorophores. Extinction calculations verify that swapping the material from Au to Ag, overcoating with polymer, and creating a narrow gap, leaves the character of the modes unchanged modulo a frequency shift. Fig. 3.6 shows the calculated ρ_{tot} and $\rho_{\mathrm{r}}/\rho_{\mathrm{tot}}$ on Ag antennas. Referring to Eq. (3.7) and (3.8), the results demonstrate that while the pentamer gives a modest enhancement (below 100) in emission rate over the simulated frequency range, the dendritic antennas provide much larger enhancements (more than 200) accompanied by a drop of efficiency by 20 % to 80 %.

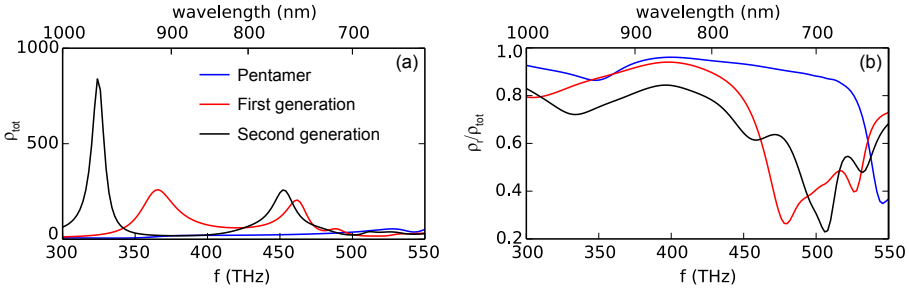

Figure 3.6: (a) Total decay rate enhancement ρ_{tot} from the Ag pentamer, first and second generation of dendritic antennas and (b) $\rho_{\mathrm{r}}/\rho_{\mathrm{tot}}$, i.e., maximum achievable antenna quantum efficiency, as simulated by FEM.

3.8 Fluorescence experiment

Instead of an ideal experiment using single fluorophores, we have performed a preliminary, ensemble-level experiment on Ag pentamers, first- and second- generation dendritic antennas with a 30 nm gap in the center. Conversely, the brightness of emission for intrinsically low-efficiency dye reports on a radiative local density of states. In practice, in such a measurement one would measure PL enhancement (PLE) from the antennas which consists of three contributions:

$$\mathrm{PLE} = \frac{\mathrm{PL}}{\mathrm{PL}_0} = \frac{\mathrm{A}}{\mathrm{A}_0} \cdot \frac{\mathrm{D}}{\mathrm{D}_0} \cdot \frac{\mathrm{QY}}{\mathrm{QY}_0}, \tag{3.9}$$

where A and A_0 denote the absorption of pump light with and without antennas, D and D_0 denote collection efficiencies per radiated photon and QY is the QY modified due to Purcell effect and quenching. Measurement of PLE on a single sample cannot be easily separated into its constituent effects, but measurements in two regimes of QY aids unraveling the physics determining PLE. To do this, we make use of a dye system that can operate with both low and reasonably high efficiencies, depending on the thermal treatment on the sample.

The dye molecules we use are Rh 800 molecules (emitting at 710 nm) doped in polymer (polystyrene) with a weight concentration of 10 %, and spincoated to form a 45 nm layer. After spin-coating, the sample is either only exposed to ambient conditions, or baked at 150 °C for 30 min prior to optical measurements. Baking promotes solvent evaporation and polymer crosslinking, causing a physical and chemical change in the environment of the dye molecules. Fig. 3.7(a) shows the measured fluorescence decay with and without baking. The unbaked dye layer exhibits a single exponential decay, which can be fitted with the convolution of the instrument response function (IRF) and a 1.7 ns decay. As reported in Ref. [52], Rh 800 molecules have a QY of 0.25 and a lifetime of 1.93 ns in absolute ethanol, meaning a radiative decay rate of 0.13 ns^{-1}. Accounting for the refractive index of polystyrene, one would expect a radiative decay rate of 0.15 ns^{-1} in the unbaked dye layer. Hence the 1.7 ns decay time is consistent with an essentially unchanged quantum efficiency. The baked dye layer exhibits a double exponential decay. The fast decay channel almost overlaps with the IRF, indicating a much shorter lifetime than the IRF lifetime which therefore cannot be accurately fitted. The slow decay channel follows the decay curve of the unbaked dye layer. Therefore, we understand the baked dye layer as containing two molecular species: a fraction unaffected by the thermal treatment, and a fraction that has a significantly lower QY. From a double exponential fit we derive the ratio of the numbers of photons from the low QY dye molecules and the high QY dye molecules to be $\alpha_l : \alpha_h \approx 0.54 : 1$.

We perform confocal imaging of PL intensity and lifetime at the antenna array as shown in Fig. 3.7. For the unbaked dye layer (Fig. 3.7(b-g)), the PL intensity hardly changes in the center of the pentamer and is reduced in the center of the first generation and second generation by 30% and 60% respectively. This reduction is the product of pump field enhancement/reduction, directivity and quenching induced by the antennas. The lifetime is reduced by about 20 % (pentamer and first generation) to 50 % (second generation) as shown in Fig. 3.7(e-g), which respectively correspond to $\rho_{\mathrm{tot}} \approx 2$ and 3 compared to the total density of states without antennas, if one accounts for QY=0.25.

In contrast with the unbaked dye layer, the emission of the baked dye layer is strongly enhanced near the center of the antennas as shown in Fig. 3.7(h-j). This behavior is consistent with the notion that for poor efficiency emitters only, Purcell enhancement can express itself as a brightness enhancement. Mathematically, suppose that we start with an emitter with nonradiative decay rate γ_{non} and radiative decay rate γ_{r} so that $\mathrm{QY}_0 = \gamma_{\mathrm{r}}/(\gamma_{\mathrm{non}} + \gamma_{\mathrm{r}})$. If we place this emitter in an environment which provides a local density of states change ρ_{tot} of which the radiative part is ρ_{r}, the change of emission rate can be written as

$$\begin{aligned}\frac{\gamma}{\gamma_0} &= \frac{\gamma_{\mathrm{r}}\rho_{\mathrm{tot}} + \gamma_{\mathrm{non}}}{\gamma_{\mathrm{r}} + \gamma_{\mathrm{non}}} \\ &= 1 + (\rho_{\mathrm{tot}} - 1)\mathrm{QY}_0 \\ &\approx \begin{cases} \rho_{\mathrm{tot}}, & \text{when } \mathrm{QY}_0 \approx 1 \\ 1, & \text{when } \mathrm{QY}_0 \approx 0, \end{cases}\end{aligned} \tag{3.10}$$

while the change of QY due to the antennas can be expressed as

$$\begin{aligned}\frac{\mathrm{QY}}{\mathrm{QY}_0} &= \frac{\rho_\mathrm{r}\gamma_\mathrm{r}}{\rho_\mathrm{tot}\gamma_\mathrm{r}+\gamma_\mathrm{non}}\cdot\frac{\gamma_\mathrm{r}+\gamma_\mathrm{non}}{\gamma_\mathrm{r}} \\ &= \frac{\rho_\mathrm{r}}{1+(\rho_\mathrm{tot}-1)\mathrm{QY}_0} \\ &\approx \begin{cases}\rho_\mathrm{r}/\rho_\mathrm{tot}, & \text{when } \mathrm{QY}_0\approx 1\\ \rho_\mathrm{r}, & \text{when } \mathrm{QY}_0\approx 0.\end{cases}\end{aligned} \tag{3.11}$$

Considering the different contribution of the low and high QY dye molecules, the PLE of the baked dye layer can be expressed as:

$$\mathrm{PLE}^\mathrm{baked} = \frac{\mathrm{A}}{\mathrm{A}_0}\cdot\frac{\mathrm{D}}{\mathrm{D}_0}\cdot\frac{1}{\alpha_l+\alpha_h}\cdot\left(\alpha_l\rho_\mathrm{r}+\frac{\alpha_h\rho_\mathrm{r}}{1+(\rho_\mathrm{tot}-1)\mathrm{QY}_0^h}\right),$$

where $\mathrm{QY}_0^h \approx 0.25$ is the QY of the high QY dye molecules.

Comparing the PLE of the baked and unbaked dye layers enables separation of the total decay rate enhancement from the influence of the pump enhancement and the modification of radiation pattern with:

$$\begin{aligned}\frac{\mathrm{PLE}^\mathrm{baked}}{\mathrm{PLE}^\mathrm{unbaked}} &= \frac{1}{\alpha_l+\alpha_h}\cdot\left(\alpha_l\rho_\mathrm{r}+\frac{\alpha_h\rho_\mathrm{r}}{1+(\rho_\mathrm{tot}-1)\mathrm{QY}_0^h}\right)\cdot\frac{1+(\rho_\mathrm{tot}-1)\mathrm{QY}_0^h}{\rho_\mathrm{r}} \\ &\approx \frac{\alpha_l(1+(\rho_\mathrm{tot}-1)\mathrm{QY}_0^h)+\alpha_h}{\alpha_l+\alpha_h}.\end{aligned} \tag{3.12}$$

where the effect of directivity and pump field enhancement drop out. From Fig. 3.7, we estimate $\mathrm{PLE}^\mathrm{baked}/\mathrm{PLE}^\mathrm{unbaked}$ to be 3.5, 2.8 and 6.0 respectively for the pentamer, and the first and second generation dendritic antenna. Accordingly, the measured change in local density of states ρ_tot amounts to 30, 22 and 58 for the three antennas.

We note that the measurements have been conducted on a 45 nm layer with a confocal resolution of about 300 nm. Due to averaging, the data provides a lower bound to the local density of states at the antenna center. In the low- and high-QY measurement scenario, the weighting is quite different. For the measurement on the unbaked sample (efficient emitters), a dominant effect is that emitters with the most strongly enhanced rate are underrepresented, as their efficiency drops due to quenching. Consequently, the ρ_tot obtained from the lifetime is much lower than the actual ρ_tot in the center of the antennas. Conversely,for the low-QY molecules in the baked sample, the emission efficiency for emitters at the antenna center is enhanced. Therefore, the ρ_tot obtained from the PLE gives a much higher estimate for the LDOS change. The results from both the lifetime and PLE measurement show that all the investigated antennas are able to enhance the emission rate of a low efficiency dye near 710 nm. The second generation of the dendritic antenna has a much higher enhancement than the pentamer and the first generation, as in the simulation in Fig. 3.6.

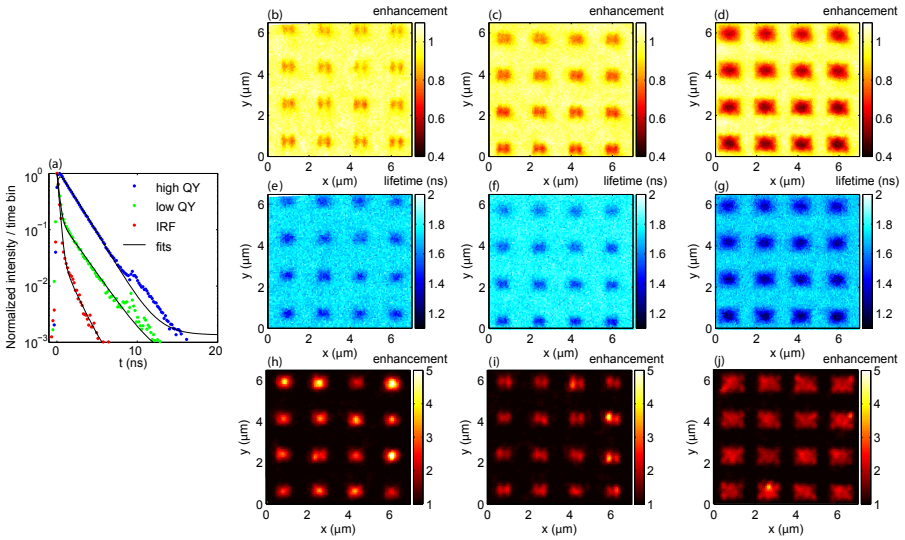

Figure 3.7: (a) Measured decay curves of the baked and unbaked dye layers, IRF of the laser and the fits to them.(b-d) PL enhancement and (e-g) lifetime measured from unbaked dye layers on (b,e) the pentamer, (c,f) first and (d,g) second generation of dendritic antennas. (h-j)PL enhancement measured from baked dye layers on (h) the pentamer, (i) first and (j) second generation of dendritic antennas.

3.9 Conclusion

We have fabricated a new type of electrically connected antennas devised according to a generic growth rule that can provide space-filling dendritic networks. These antennas are potentially suitable for optically and electrically functional devices. Using extinction spectroscopy, we have measured the optical response of the pentamer, the first and second generation of the dendritic antennas in mid-IR, IR and visible. The measured optical resonances are identified using two independent theoretical methods (FEM and V-MoM). With FEM simulation, we have furthermore found the potential of using these modes to enhance the emission efficiency of emitters placed in a narrow gap in the center of the antennas. This enhancement is confirmed by preliminary measurements on the PL intensity and lifetime of thin dye-doped polymer layers on the antennas.

References

[1] P. Mühlschlegel, H.-J. Eisler, O. J. F. Martin, B. Hecht, and D. W. Pohl, *Resonant optical antennas*, Science **308**, 1607 (2005).

[2] S. Kühn, U. Håkanson, L. Rogobete, and V. Sandoghdar, *Enhancement of single-molecule fluorescence using a gold nanoparticle as an optical nanoantenna*, Phys. Rev. Lett. **97**, 017402 (2006).

[3] P. Anger, P. Bharadwaj, and L. Novotny, *Enhancement and quenching of single-molecule fluorescence*, Phys. Rev. Lett. **96**, 113002 (2006).

[4] R. J. Moerland, T. H. Taminiau, L. Novotny, N. F. van Hulst, and L. Kuipers, *Reversible polarization control of single photon emission*, Nano Lett. **8**, 606 (2008).

[5] H. Gersen, M. F. García-Parajó, L. Novotny, J. A. Veerman, L. Kuipers, and N. F. van Hulst, *Influencing the angular emission of a single molecule*, Phys. Rev. Lett. **85**, 5312 (2000).

[6] T. Taminiau, F. Stefani, F. Segerink, and N. Van Hulst, *Optical antennas direct single-molecule emission*, Nat. Photonics **2**, 234 (2008).

[7] G. Lozano, D. J. Louwers, S. R. Rodríguez, S. Murai, O. T. Jansen, M. A. Verschuuren, and J. G. Rivas, *Plasmonics for solid-state lighting: enhanced excitation and directional emission of highly efficient light sources*, Light Sci. Appl. **2**, e66 (2013).

[8] R. F. Oulton, V. J. Sorger, T. Zentgraf, R.-M. Ma, C. Gladden, L. Dai, G. Bartal, and X. Zhang, *Plasmon lasers at deep subwavelength scale*, Nature **461**, 629 (2009).

[9] A. H. Schokker and A. F. Koenderink, *Lasing at the band edges of plasmonic lattices*, Phys. Rev. B **90**, 155452 (2014).

[10] J. Stehr, J. Crewett, F. Schindler, R. Sperling, G. von Plessen, U. Lemmer, J. Lupton, T. Klar, J. Feldmann, A. Holleitner, M. Forster, and U. Scherf, *A low threshold polymer laser based on metallic nanoparticle gratings*, Adv. Mater. **15**, 1726 (2003).

[11] N. Yu, E. Cubukcu, L. Diehl, D. Bour, S. Corzine, J. Zhu, G. Höfler, K. B. Crozier, and F. Capasso, *Bowtie plasmonic quantum cascade laser antenna*, Opt. Express **15**, 13272 (2007).

[12] P. Offermans, M. C. Schaafsma, S. R. K. Rodriguez, Y. Zhang, M. Crego-Calama, S. H. Brongersma, and J. Gómez Rivas, *Universal scaling of the figure of merit of plasmonic sensors*, ACS Nano **5**, 5151 (2011).

[13] P. Kühler, M. Weber, and T. Lohmüller, *Plasmonic nanoantenna arrays for surface-enhanced raman spectroscopy of lipid molecules embedded in a bilayer membrane*, ACS Appl. Mater. Inter. **6**, 8947 (2014).

[14] X. Huang, I. H. El-Sayed, W. Qian, and M. El-Sayed, *Cancer cell imaging and photothermal therapy in the near-infrared region by using gold nanorods*, J. Am. Chem. Soc. **128**, 2115 (2006).

[15] W. Zhang, L. Huang, C. Santschi, and O. J. F. Martin, *Trapping and sensing 10 nm metal nanoparticles using plasmonic dipole antennas*, Nano Lett. **10**, 1006 (2010).
[16] A. K. Salem, P. C. Searson, and K. W. Leong, *Multifunctional nanorods for gene delivery*, Nat. Mater. **2**, 668 (2003).
[17] S. Pillai, K. R. Catchpole, T. Trupke, and M. A. Green, *Surface plasmon enhanced silicon solar cells*, J. Appl. Phys. **101**, 093105 (2007).
[18] K. R. Catchpole and A. Polman, *Plasmonic solar cells*, Opt. Express **16**, 21793 (2008).
[19] V. E. Ferry, L. A. Sweatlock, D. Pacifici, and H. A. Atwater, *Plasmonic nanostructure design for efficient light coupling into solar cells*, Nano Lett. **8**, 4391 (2008).
[20] C. Rockstuhl, S. Fahr, and F. Lederer, *Absorption enhancement in solar cells by localized plasmon polaritons*, J. Appl. Phys. **104**, 123102 (2008).
[21] W. L. Barnes, A. Dereux, and T. W. Ebbesen, *Surface plasmon subwavelength optics*, Nature **424**, 824 (2003).
[22] S. A. Maier, P. G. Kik, H. A. Atwater, S. Meltzer, E. Harel, B. E. Koel, and A. A. Requicha, *Local detection of electromagnetic energy transport below the diffraction limit in metal nanoparticle plasmon waveguides*, Nat. Mater. **2**, 229 (2003).
[23] S. I. Bozhevolnyi, J. Erland, K. Leosson, P. M. W. Skovgaard, and J. M. Hvam, *Waveguiding in surface plasmon polariton band gap structures*, Phys. Rev. Lett. **86**, 3008 (2001).
[24] J. R. Krenn, A. Dereux, J. C. Weeber, E. Bourillot, Y. Lacroute, J. P. Goudonnet, G. Schider, W. Gotschy, A. Leitner, F. R. Aussenegg, and C. Girard, *Squeezing the optical near-field zone by plasmon coupling of metallic nanoparticles*, Phys. Rev. Lett. **82**, 2590 (1999).
[25] T. H. Taminiau, F. D. Stefani, and N. F. van Hulst, *Optical nanorod antennas modeled as cavities for dipolar emitters: Evolution of sub- and super-radiant modes*, Nano Lett. **11**, 1020 (2011).
[26] P. Zijlstra, P. M. Paulo, and M. Orrit, *Optical detection of single non-absorbing molecules using the surface plasmon resonance of a gold nanorod*, Nat. Nanotechnol. **7**, 379 (2012).
[27] A. Kinkhabwala, Z. Yu, S. Fan, Y. Avlasevich, K. Müllen, and W. Moerner, *Large single-molecule fluorescence enhancements produced by a bowtie nanoantenna*, Nat. Photonics **3**, 654 (2009).
[28] A. G. Curto, G. Volpe, T. H. Taminiau, M. P. Kreuzer, R. Quidant, and N. F. van Hulst, *Unidirectional emission of a quantum dot coupled to a nanoantenna*, Science **329**, 930 (2010).
[29] M. Hentschel, M. Saliba, R. Vogelgesang, H. Giessen, A. P. Alivisatos, and N. Liu, *Transition from isolated to collective modes in plasmonic oligomers*, Nano Lett. **10**, 2721 (2010).
[30] J. Kern, R. Kullock, J. Prangsma, M. Emmerling, M. Kamp, and B. Hecht, *Electrically driven optical antennas*, Nat. Photonics **9**, 582 (2015).
[31] E. Maguid, I. Yulevich, D. Veksler, V. Kleiner, M. L. Brongersma, and E. Hasman, *Photonic spin-controlled multifunctional shared-aperture antenna array*, Science **352**, 1202 (2016).
[32] F. Yue, D. Wen, J. Xin, B. D. Gerardot, J. Li, and X. Chen, *Vector vortex beam generation with a single plasmonic metasurface*, ACS Photonics **3**, 1558 (2016).
[33] G. Volpe, G. Volpe, and R. Quidant, *Fractal plasmonics: subdiffraction focusing and broadband spectral response by a Sierpinski nanocarpet*, Opt. Express **19**, 3612 (2011).
[34] S. Gottheim, H. Zhang, A. O. Govorov, and N. J. Halas, *Fractal nanoparticle plasmonics: The Cayley tree*, ACS Nano **9**, 3284 (2015).
[35] L. Novotny, *Effective wavelength scaling for optical antennas*, Phys. Rev. Lett. **98**, 266802 (2007).
[36] C. Rockstuhl, F. Lederer, C. Etrich, T. Zentgraf, J. Kuhl, and H. Giessen, *On the*

reinterpretation of resonances in split-ring-resonators at normal incidence, Opt. Express **14**, 8827 (2006).

[37] P. G. Etchegoin, E. C. Le Ru, and M. Meyer, *An analytic model for the optical properties of gold*, J. Chem. Phys. **125**, 164705 (2006).

[38] E. Prodan, C. Radloff, N. J. Halas, and P. Nordlander, *A hybridization model for the plasmon response of complex nanostructures*, Science **302**, 419 (2003).

[39] N. A. Mirin, K. Bao, and P. Nordlander, *Fano resonances in plasmonic nanoparticle aggregates*, J. Phys. Chem. A **113**, 4028 (2009).

[40] V. A. Tamma, Y. Cui, J. Zhou, and W. Park, *Nanorod orientation dependence of tunable fano resonance in plasmonic nanorod heptamers*, Nanoscale **5**, 1592 (2013).

[41] M. Frimmer, T. Coenen, and A. F. Koenderink, *Signature of a Fano resonance in a plasmonic metamolecule's local density of optical states*, Phys. Rev. Lett. **108**, 077404 (2012).

[42] G. A. E. Vandenbosch and A. R. Van de Capelle, *Mixed-potential integral expression formulation of the electric field in a stratified dielectric medium-application to the case of a probe current source*, IEEE Trans. Antennas Propag. **40**, 806 (1992).

[43] F. J. Demuynck, G. A. E. Vandenbosch, and A. R. Van de Capelle, *The expansion wave concept. i. efficient calculation of spatial green's functions in a stratified dielectric medium*, IEEE Trans. Antennas Propag. **46** (1998).

[44] M. Vrancken and G. A. E. Vandenbosch, *Hybrid dyadic-mixed-potential and combined spectral-space domain integral-equation analysis of quasi-3-d structures in stratified media*, IEEE Trans. Microwave Theory Tech. **51**, 216 (2003).

[45] Y. Schols and G. A. E. Vandenbosch, *Separation of horizontal and vertical dependencies in a surface/volume integral equation approach to model quasi 3-d structures in multilayered media*, IEEE Trans. Antennas Propag. **55**, 1086 (2007).

[46] G. A. E. Vandenbosch, V. Volski, N. Verellen, and V. V. Moshchalkov, *On the use of the method of moments in plasmonic applications*, Radio Sci. **46** (2011).

[47] X. Zheng, N. Verellen, D. Vercruysse, V. Volskiy, P. Van Dorpe, G. A. E. Vandenbosch, and V. Moshchalkov, *On the use of group theory in understanding the optical response of a nanoantenna*, IEEE Trans. Antennas Propag. **63**, 1589 (2015).

[48] D. W. Brandl, N. A. Mirin, and P. Nordlander, *Plasmon modes of nanosphere trimers and quadrumers*, J. Phys. Chem. B **110**, 12302 (2006).

[49] M. Tinkham, *Group theory and quantum mechanics*, 2003.

[50] E. Wigner and J. Griffin, *Group Theory and Its Application to the Quantum Mechanics of Atomic Spectra*, Pure and applied Physics, 1959.

[51] A. F. Koenderink, L. Bechger, H. P. Schriemer, A. Lagendijk, and W. L. Vos, *Broadband fivefold reduction of vacuum fluctuations probed by dyes in photonic crystals*, Phys. Rev. Lett. **88**, 143903 (2002).

[52] A. Alessi, M. Salvalaggio, and G. Ruzzon, *Rhodamine 800 as reference substance for fluorescence quantum yield measurements in deep red emission range*, J. Lumin. **134**, 385 (2013).

4

Broadband light scattering and photoluminescence enhancement from plasmonic Vogel's golden spirals

Periodic arrays of plasmonic nanoantennas can enhance the directionality of light emission of nearby fluorophores and therefore have a great potential for a broad range of applications. Unfortunately, their narrow spectral bandwidth and the anisotropy of their optical resonances limit the use of these structures in applications such as solid state lighting. In this chapter, we study an alternative for periodic structures: Vogel's golden spirals. These spirals are deterministic structures with an approximate circular symmetry and a Fourier transform that is much more broadband than that of periodic lattices. Combining k-space Stokes polarimetry and theoretical calculations, we first investigate the light scattering from Vogel's arrays and the coupling between individual nanoantennas. Next, photoluminescence measurements show that the spirals can enhance the forward emission of incoherent fluorescent sources embedded in a waveguide that also encloses the spiral. The enhancement occurs over a broad spectral band, proving the potential of Vogel's golden spirals for broadband light-emitting devices.

4.1 Introduction

The manipulation of light emission using optical antennas including accelerating spontaneous emission, redirecting usually omnidirectional fluorescence into narrow beams, and controlling polarization is an important topic of research for microscopy, spectroscopy and solid-state lighting [1–12]. The plasmon resonances in optical antennas guarantees strong effects, albeit at the cost of Ohmic loss. In addition to single resonant antennas [1–8], one can use arrays of them [9–12], where the position of each antenna is an additional degree of freedom that can be tailored to achieve a desired functionality. In particular, periodic lattices of plasmonic nanoantennas are able to significantly enhance directional emission of nearby fluorophores [10–12]. However, periodic structures have two major drawbacks. First, the anisotropy of lattices hinders their use in applications that require cylindrically symmetric sources such as general lighting. Second, the use of diffractive resonances implies narrow bandwidth of enhancement (a few nm [11, 12]), limiting the efficiency of the enhancement for most emitters such as quantum dots and organic dyes, which usually have larger bandwidths at room temperature. These two drawbacks are results of the anisotropic and pure-point Fourier transform of periodic arrays. Therefore, for cylindrically symmetric and broadband manipulation of light emission, it is useful to arrange antenna array so that the Fourier transform is isotropic and broadband.

Deterministic quasi-periodic and aperiodic nanoantenna arrays with singular continuous or absolute continuous Fourier transforms [13] are considered a promising alternative design to overcome the limitations of periodic lattices [14–16]. Among these structures, plasmonic Vogel's golden spirals [17], like the one shown in Fig. 4.1(a), have been proposed as particularly interesting because they exhibit circularly symmetric and broadband light scattering features [16], as derived from the Fourier transform of the spiral array, shown in Fig. 4.1(b). In this chapter, we study fluorescence enhancement from plasmonic Vogel's golden spirals. To this end, we first unravel the optical response of spirals using darkfield microscopy and k-space Stokes polarimetry [18–21]. We take into account the polarization response that is not available in Ref. [16], and investigate how far theoretical modeling should include antenna-antenna interactions. Next, we discuss studies on fluorescent samples where the spiral is embedded in an organic fluorescent waveguide layer. Directivity and spectra of fluorescence enhancement from the spirals are mapped using both Fourier imaging and Fourier spectral imaging techniques. We demonstrate that the investigated spirals can enhance the forward emission of incoherent sources in a waveguide over a very broad spectral band, which can be beneficial for cylindrically symmetric and broadband light-emitting devices.

4.2 Vogel's spiral

The Vogel's golden spiral shown in Fig. 4.1(a) consists of $N = 1000$ particles placed according to the generation rule

$$r = a\sqrt{n}, \qquad \theta = \theta_g \cdot n, \quad n = 1 \dots N \tag{4.1}$$

where (r, θ) denotes the polar coordinates of the nth particle, and $\theta_g = 137.508°$ is the golden angle approximated by ratios of Fibonacci numbers, while a is a constant scaling parameter [17]. This array has a quasi-isotropic particle distribution with inter-particle separation varying from $1.67a$ to $1.75a$. As a consequence, the Fourier transform of the array shown in Fig. 4.1(b) exhibits concentric double-ring structures near multiples of $0.59 \cdot 2\pi/a$ from the origin, with fine speckles. Meanwhile, the asymmetries in the array result in a dense phase fluctuation in the phase of the Fourier transform. The finite thicknesses of the rings in the Fourier transform suggests broad spectral and angular bandwidths of the geometric scattering of spirals, much broader than would appear for periodic lattices that have a pure-point Fourier transform. It should be noted that for θ slightly away from θ_g one obtains handed spirals. In this chapter we limit ourselves to golden spirals, while we have studied various pitches a, and particles numbers N.

In the limit that multiple scattering can be ignored, the Fourier transform of a structure is a first order approximation to its diffraction pattern upon illumination with a normal plane wave. Moreover, if the structure is a plasmon lattice embedded in a 2D fluorescent waveguide layer, a first approximation to the radiation pattern can be simply obtained from antenna theory [22]. The rationale is that emitters will dominantly emit into the waveguide mode, meaning that all emission will be characterized by having an in plane wave vector $\mathbf{k}_{||}$ of length $k_{\mathrm{WG}} = n_{\mathrm{WG}}\omega/c$ where ω is emission frequency, c the speed of light and n_{WG} the mode index. The expected outcoupled light distribution can be constructed by considering how each in-plane wave vector $\mathbf{k}_{||}$ diffracts, followed by summation over all excited wave vectors. Mathematically, in the limit of single scattering, this means that one obtains the radiation pattern by convoluting the spiral Fourier transform with the wave vector distribution of emission, which is a circle in k-space of radius k_{WG} [23, 24]. As illustrated in Fig. 4.1(c), when the propagation constant of the waveguide mode (k_{WG}) exactly matches the radius $k_{\mathscr{F}}$ of the first ring in the Fourier transform of the structure, the scattering of the array shifts the waveguide modes by $k_{\mathscr{F}}$ in all directions, resulting in an overlap of the outcoupled waveguide modes at the origin. This intuitive picture suggests that emission enhancement from the spiral array will appear in the forward direction for appropriately chosen size parameter. Compared with the case of square arrays illustrated in Fig. 4.1(d-f), this enhancement has the advantage of being isotropic and having a broadband spectral band.

However, the above qualitative analysis does not take into account three factors that may have an significant influence on the emission enhancement. First, coupling between individual antennas can affect the scattering pattern of the array making the Fourier transform an inaccurate prediction. Second, the sketch in Fig. 4.1(c) does not contain the phase variations in Fig. 4.1(b), indicating that interference effects could

require further analysis. Finally, an actual device contains an ensemble of incoherent emitters randomly distributed in the waveguide layer, at different positions relative to the array. The incoherent average of emission from all emitter positions could result in an emission pattern significantly different from emission patterns that individual sources give. In the following sections, we study plasmonic Vogel's golden spirals to take into account these three factors.

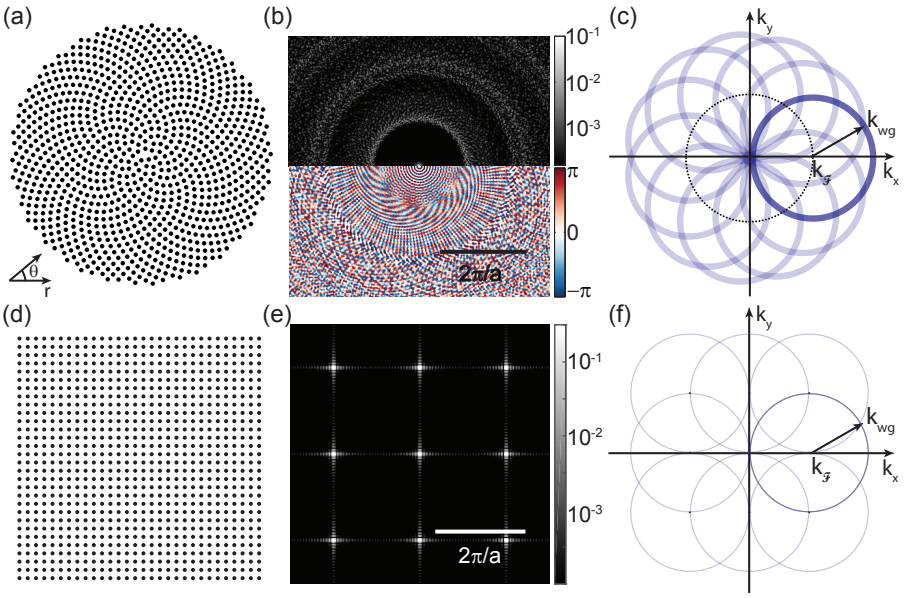

Figure 4.1: (a) A Vogel's golden spiral composed by 1000 elements. (b) The absolute value (top, normalized) and phase (bottom) of the Fourier transform of (a). (c) An illustration of the distribution of waveguide modes outcoupled by a Vogel's golden spiral. (d) A square array composed of 900 elements. (e) The absolute value of the Fourier transform of (a). (e) An illustration of the distribution of waveguide modes outcoupled by a square array.

4.3 Sample fabrication and setups

The investigated spirals are fabricated on silica substrates ($n = 1.51$) using electron beam lithography (20 kV, ZEP-resist), thermal evaporation of Au, and subsequent liftoff. The resulting Au nanoantennas have a cylindrical shape and a height of 30 nm. The sample geometries that we explore include various antenna size, effective pitch parameter a, and particle number N.

We perform measurements on the spirals using dark-field microscopy, Fourier microscopy, k-space Stokes polarimetry and spectrally resolved Fourier microscopy. The dark-field microscopy is performed using a reflection-configuration. A halogen lamp is focused by either a 50× dark field objective with NA = 0.8 or a 20× dark

field objective with NA = 0.45, illuminating the samples through the substrate. The same objective collects the back-scattered light and sends it to a 70/30 beam splitter. A fraction of 70% of the scattered light is transmitted and imaged on a camera (The Imaging Source DFK 21AU04). The remaining 30% is reflected to a multi-mode fiber with a core of 400µm and NA = 0.39, which is connected to a spectrometer (Avaspec 2048TEC-2-USB2) with a detection wavelength range of 500 to 1000 nm.

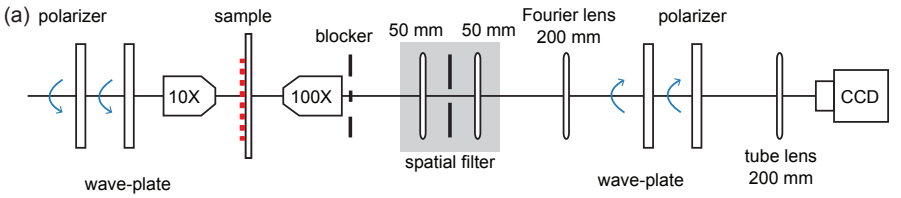

Figure 4.2: A schematic of the setup for Fourier microscopy and k-space Stokes polarimetry.

The Fourier microscopy and k-space Stokes polarimetry are performed used a setup illustrated in Fig. 4.2, which is similar to that used in Ref. [21, 25]. A super-continuum laser (NKT SuperK Extreme) that is weakly focused by a 10× objective illuminates the sample from the air side in the normal direction, with the output wavelength selected by an acousto-optic tunable filter (AOTF). A 100× oil immersion objective with a NA = 1.4 collects the scattered light from the side of the substrate and sends it through a telescope. In the center of the telescope, where the sample is imaged with a magnification of 25×, a 200 µm pin-hole is used to select light from the central part of the spiral and block the light transmitted from the surrounding substrate. Behind the telescope, a Fourier lens and a tube lens are used to image the back-focal plane of the objective onto a CCD camera (Roper, CoolSnap EZ) with 1× magnification. The Fourier images of the scattering by the spirals are dominated by the zero-order transmittance which appears as a bright spot in the center of the Fourier image. In addition a ring appears of diffracted light. To suppress the zero-order transmittance, we place a disk-shaped beam block with a diameter of ~ 500 µm in the center of the back focal plane, leaving a detection range of $0.18k_0 < |k| < 1.4k_0$. For k-space Stokes polarimetry, two polarimeters are placed respectively before and after the sample to select the polarization of the illumination and detection. We obtain the Stokes parameters (S_0, S_1, S_2, S_3) of the Fourier images of the scattering by fixing the illumination polarization and doing six measurements with different polarimeter settings in the detection path. The Stokes parameters are defined as:

$$\boldsymbol{S} = \begin{pmatrix} S_0 \\ S_1 \\ S_2 \\ {}_S3 \end{pmatrix} = \begin{pmatrix} I_H + I_V \\ I_H - I_V \\ I_{45} - I_{-45} \\ I_R - I_L \end{pmatrix}. \tag{4.2}$$

The corresponding polarization analysis choices are selected by a polarimeter consisting of a quarter wave plate and a linear polarizer according to the settings listed in Table 4.1.

	H	V	45	-45	R	L
LP	0	90	45	-45	0	0
QWP	0	90	45	-45	45	-45

Table 4.1: Settings of the linear polarizer (LP) and quarter-wave plate (QWP) for different polarization required polarization analysis choices according to Stokes polarimetry.

To obtain spectrally resolved Fourier images, we use the setup of Ref. [26]. The spirals are excited from the substrate side through a 100×/ 1.45NA objective using a 532 nm microchip laser (Teem Photonics, type STG-03E-1S0). The laser is focused near the backfocal plane of the objective and an iris is used to ensure that the whole spiral, but no region around it, is illuminated. The emission is collected by the same objective. After removing laser light by a longpass filter (cut-off at 550 nm), the backfocal plane of the objective is imaged on the entrance plane of a Andor Shamrock 303i spectrometer with an iDus CCD camera. The slit of the spectrometer is placed at the center of the Fourier image to select the emission near $k_x = 0$. Using the spectrometer CCD in imaging mode, we are thus able to obtain a spectrally resolved Fourier image, with emission intensity as a function of k_y and λ. Dividing the Fourier spectra images from the dye layer on spirals by the images from the reference, we obtain the PLE.

4.4 Scattering

4.4.1 Results from dark-field microscopy

We investigate the spectral response of the spirals using dark-field microscopy. Fig. 4.3 shows dark-field images of spirals composed by 55 nm radius antennas with $a = 300$, 250 and 200 nm, taken with a 50× objective (a-c) and a 20× objective (e-g) with identical, fixed white balance camera settings for all images. The qualitative color variations observable in the images are confirmed by the scattering spectra in Fig. 4.3(d) and (h). For $a = 300$ nm, individual antennas can be resolved by the 50× objective, which appear as orange diffraction-limited spots, reflecting a localized resonance of individual antennas at $\lambda \approx 600$ nm. For smaller scales a, the spiral structure becomes unresolvable and the color appearance of the spirals becomes distinctly different. In particular, we observe three phenomena. First, we note that the color appearance of the spirals depends on the location within the spiral. Second, as the pitch a is reduced, the color impression strongly varies giving rise, for instance, to deep blue for $a = 250$ nm in panel (f) and purple (a combination of blue and red) in panel (g). Third, the color impression strongly depends on the numerical aperture of the microscope objectives.

Two possible explanations for these phenomena are that dipole-dipole coupling between antennas causes resonances to shift, i.e., of plasmon hybridization [27, 28], or alternatively that the diffraction by clusters of the antennas that make up the spiral is angle dependent, resulting in a difference in the collection efficiency of scattered light depending on color and pitch. Since in these systems the particle spacing is

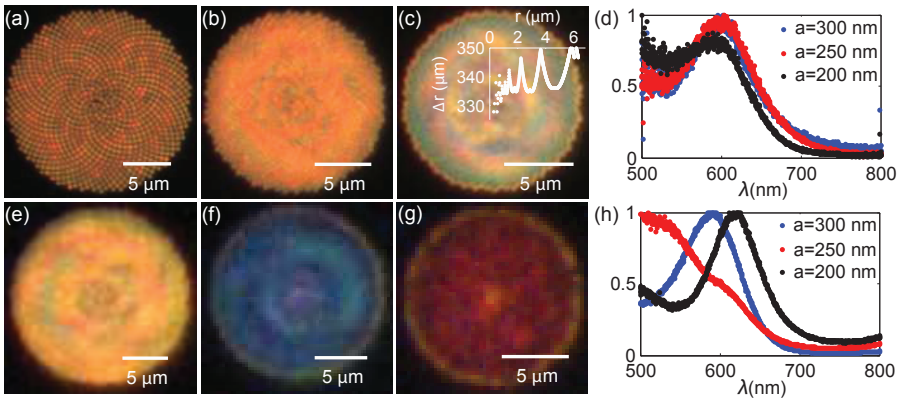

Figure 4.3: Dark field images of spirals with (a)(e) $a = 300$ nm, (b)(f) 250 nm and (c)(g) 200 nm and dark field scattering spectra measured with (a-d) a 50× objective and (e-h) a 20× objective. (c) is over-plotted with the nearest-neighbor distance for each nanoantenna as a function of its distance to the center.

comparatively large (mean nearest neighbor distance is $\sim 1.7a$) the dominant effect is diffraction, not shifting of resonances due to hybridization. The strong dependence of color appearance on the numerical aperture of the objective corroborates this interpretation. The illumination through a narrow cone of angles is defined by the objective mantle. Color appearance depends on whether this narrow cone is diffracted into or away from the objective collection lens. For instance, the apparent absence of the plasmon feature in the NA=0.45 spectrum at $a = 250$ nm and concomitant blue camera appearance is commensurate with the fact that the strong scattering at the plasmon resonances is diffracted into large angles outside the detection cone. To support this reasoning, we take dark field images from golden spirals with different antenna sizes and identical pitch ($a = 200$ nm), as shown in Fig. 4.4. The images show similar coloration, albeit that the dark field intensity increases with increasing antenna size. This furthermore rules out the influence of plasmon hybridization that is strongly dependent on the antenna size. Additional evidence for the conclusion that diffraction

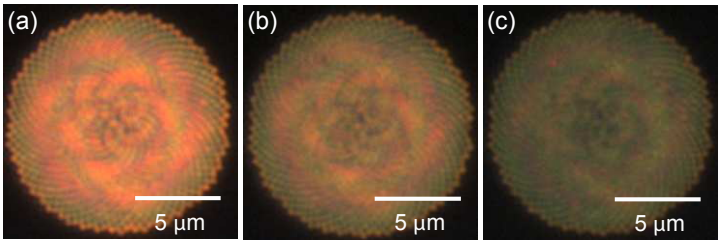

Figure 4.4: Dark field images of golden spirals with antenna radius of (a) 95 nm, (b) 80 nm, (c)55 nm, taken with a 100× objective with NA = 0.9. $a = 200$ nm, $N = 1000$.

is determining for appearance is provided by the strong correlation of color appearance with nearest neighbor distance. The inset in panel 4.3(c) shows the nearest-neighbor distance as a function of the distance to the spiral center. Small variations of around 15 nm around the mean (< 5% variations around 340 nm for the $a = 200$ nm spiral) correlate directly with color appearance. Similar results are found with non-golden spirals, as shown in Fig. 4.5.

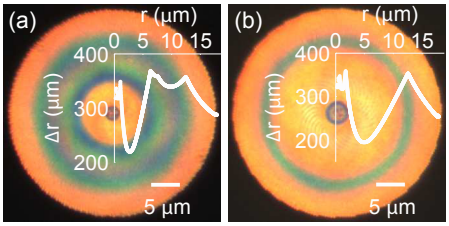

Figure 4.5: Dark field images measured with a 50× objective from α spirals from $r = a\sqrt{n}, \theta = \alpha \cdot n, n = 1...N$. (a) $\alpha = 137.3°$, (b) $\alpha = 137.6$. $a = 200$ nm, $N = 8000$. Over-plotted are nearest-neighbor distances as a function of distance to the center.

4.4.2 Results from Fourier microscopy and k-space Stokes polarimetry

Having established that golden spirals show strong diffraction colors, we perform Fourier microscopy to measure angle-dependent diffraction patterns at normal incidence. For this study we choose antennas with 95 nm radius for strong scattering intensity, and vary the particle number N, the pitch parameter a and the wavelength λ. Figure 4.6(a) shows a back focal plane image (with zero order transmission blocked) of a spiral with $a = 300$ nm, illuminated with a vacuum wavelength of $\lambda = 600$ nm. The image presents low intensity for low k ($0.18k_0 < |k| < k_0$), surrounded by a distinct bright ring at $|k| \approx 1.1k_0$, corresponding to diffraction at angles around 46° off the sample normal into the glass substrate. The position of the ring corresponds well to the Fourier transform in Fig. 4.1. We verify that the radius in k-space of the ring scales as expected with pitch a and wavelength λ, meaning that it remains at the same $|k|/k_0 = 0.59\lambda/a$ independent of the dimensionless ratio a/λ, while scaling with both independently, shown in Fig. 4.6(a-c). As is the case in the calculated structure factor (Fig. 4.1(b)), the scattering ring has a speckled appearance. For a fixed set of a and λ, the speckle size is coarsest for least number of particles, reducing with increasing N from 200 to 1000, as shown in Fig. 4.6(d-f). This agrees with the fact that, in general, the size of speckles or diffraction features generated from a radiating object in the Fourier plane is inversely proportional to its size. Nonetheless, already very small spirals with $N = 200$ represent the main physics, i.e., a distinct isotropic diffraction ring in k-space.

So far both dark field and Fourier microscopy have shown diffractive features of the spirals, but no evidence on the interaction between individual antennas. To confirm

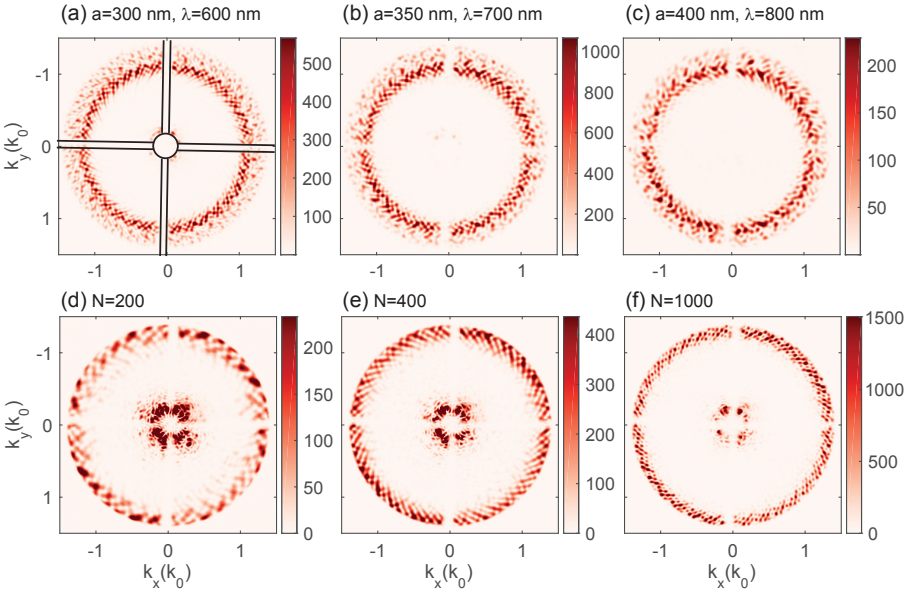

Figure 4.6: (a-c) Back focal plane images of light scattering from spirals with a fix ratio $a/\lambda = 0.5$ and $N = 1000$. (a)$a = 300$ nm, (b) 350 nm and (c) 400 nm. (d-f) Back focal plane images of light scattering from spirals with $a = 200$ nm, $\lambda = 490$ nm and different N. (d) $N = 200$, (e) 400 and (f) 1000. Black lines in (a) illustrate the shape and position of the beam block.

that the investigated spirals are indeed diffractive structures consisting of essentially uncoupled scatterers, we perform k-space Stokes polarimetry [18–21]. Figure 4.7(a-b) show the Stokes parameters for linearly and circularly polarized excitation. As shown in Fig. 4.7(a), for horizontally polarized input, the total scattering intensity from the spiral (S_0) resembles its Fourier transform, presenting a distinct, speckled, circular band. In addition, as a factor apparently multiplying the Fourier transform, the intensity is high at small k_x and low at large k_x. This asymmetric intensity distribution rotates with the incident polarization, and indicates that the scattering is essentially the product of the structure factor of the array, and the emission pattern of a linearly polarized dipole oriented along the incident polarization [24, 25]. At positions where the total intensity S_0 is low, S_1/S_0, S_2/S_0 and S_3/S_0 have random values. For most of the positions in the Fourier space where $|k| < k_0$ and S_0 is above the noise, S_1/S_0 is close to 1 and both $|S_2/S_0|$ and $|S_3/S_0|$ are low, meaning that the polarization of the scattered light has been mostly preserved. However, near $|k_x| = |k_y|$, $|k| = k_0$ where the image diagonals intersect the $NA = 1$ circle, $|S_1/S_0| \approx 0$ and $|S_2/S_0| \approx 1$ indicating a rotation of the polarization by $\sim 45°$. Just outside the NA = 1 circle and at $|k_x| = |k_y|$ both $|S_1/S_0|$ and $|S_2/S_0|$ are low and $|S_3/S_0| \approx 1$, indicating that circularly polarized light has been generated despite the linear driving polarization. For circular input polarization (Fig. 4.7(b)), the scattered light shows a scattering pattern that is rotationally symmetric

(S_0), with essentially circular polarization identical to the input field for $|k| < k_0$, and conversion to linear polarization at $|k| > k_0$. Thanks to the circular symmetry of the spiral, the Stokes parameters associated to linear polarization, S_2 and S_1, are equal to each other but rotated by 45°. We have verified that these features remain unchanged when varying a, barring the expected scaling of the diffraction ring with a.

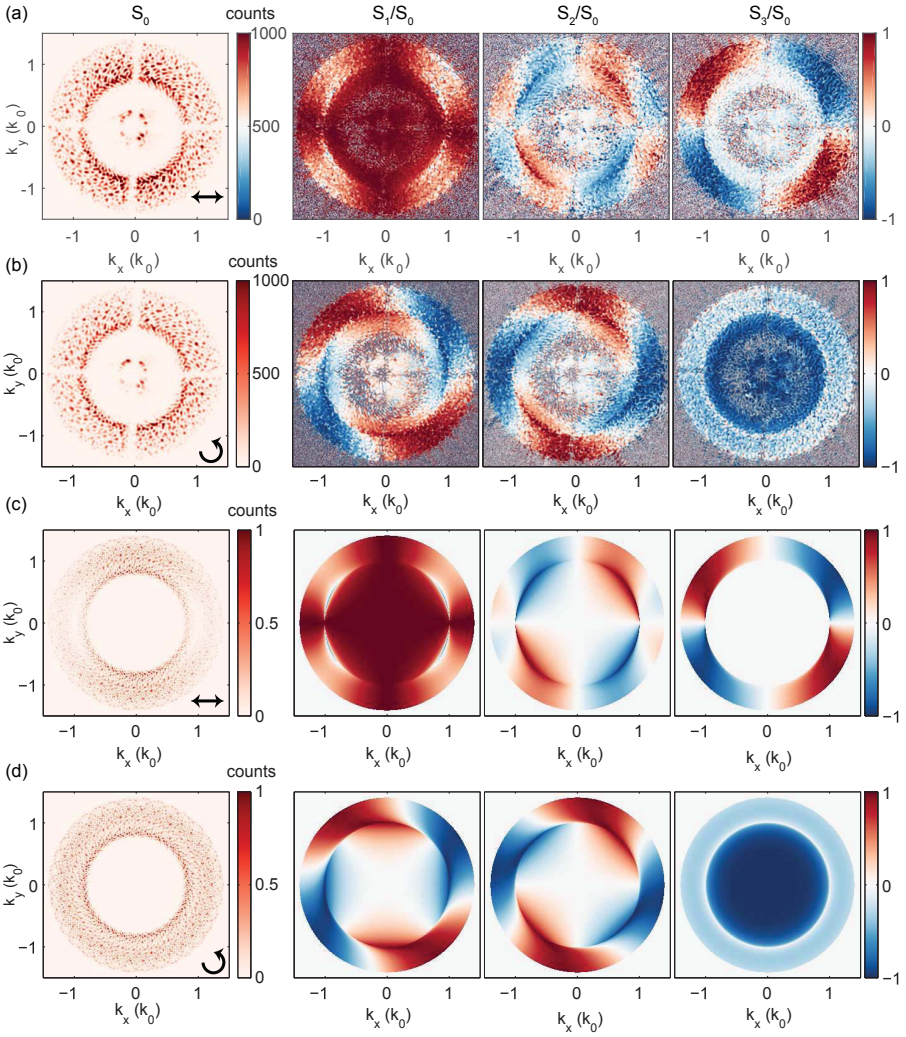

Figure 4.7: Measured (a-b) and calculated (c-d) Stokes parameters of the scattered light from the spiral with (a) and (b) horizontally and (c) and (d) left-handed circularly polarized input. $a = 400$ nm, $N = 1000$.

To answer the question whether the antenna-antenna interactions have a significant influence on the scattering pattern of the spiral, we model the sample as an array of

point dipoles 15 nm (half the particle thickness) above a substrate. When multiple scattering is weak and the coupling between the antennas is negligible, the radiation pattern is essentially the coherent superposition of the radiation from many identically aligned induced dipoles, which have a dipole polarization inherited from the incident field polarization. Under this assumption, we calculate the scattering intensity S_0 as the product of the array structure factor, i.e., the Fourier transform, and the single dipole radiation pattern (acting as form factor). S_1/S_0, S_2/S_0, S_3/S_0 are calculated from a single point dipole in the x direction on a substrate [29, 30]. Fig. 4.7(c) shows the calculated Stokes parameters of the radiation from a spiral array of uncoupled point dipoles with equal dipole moment in the horizontal direction, which have the same distribution for the intensity and polarization of scattering that we measured, shown in Fig. 4.7(a). This implies that the response of the investigated spiral to the incident field can indeed be predicted from the Fourier transform of a group of uncoupled dipoles without invoking plasmon hybridization. This conclusion can be generalized to similar deterministic aperiodic structures, making the prediction of their scattering pattern much easier. Notice that for $k \geq 1$, the change of polarization results from the air-substrate interface instead of the spiral arrangement. The radiation pattern of a dipole above a substrate incorporates the Fresnel-coefficient of the interface. The difference in amplitude of the transmission coefficients for TM and TE polarizations rotates the polarization and the difference in phase generates circular polarization. Similar agreement between measurement and a model of uncoupled dipoles that inherit their dipole moment from the drive polarization has been found with left-hand circularly polarized input as shown in Fig. 4.7(d). The conversion of circular polarization to linear polarization at $|k| > k_0$ is also a result of the difference in transmission coefficients. The spiral arrangement only determines the scattering intensity (S_0) distribution and has no influence on the polarization of scattered light (S_1/S_0, S_2/S_0, S_3/S_0).

4.5 Photoluminescence enhancement

In this section, we investigate the photoluminescence (PL) enhancement of the Vogel's spirals. A 600 nm polystyrene layer ($n = 1.6$ at $\lambda = 600$ nm) doped with 3 wt. % dye molecules (Lumogen Red F305 (BASF)) was spin-coated on the sample, resulting in a waveguide with fundamental TE- and TM-modes with effective refractive index of $n_{WG} \sim 1.58$ in the visible (numbers from mode calculation [31]). The dye molecules have an absorption spectrum in the green (maximum absorption near 560 nm) and an emission spectrum in the red (620 nm). The geometry of a waveguide layer with this dye was chosen because it has been shown to be very effective for directional photoluminescence enhancements when used in conjunction with periodic plasmon particle arrays [11]. In order to outcouple the waveguide modes into the forward direction, we choose a to be around 225 nm, as for this pitch the first ring in the Fourier transform occurs at $1.58k_0$ for the emission wavelength, which overlaps with the waveguide modes in k-space, commensurate with the directional out-coupling criterion constructed in Fig.4.1(c).

4.5.1 Directivity of the photoluminescence enhancement

We performed Fourier-plane microscopy on the PL using the same setup as in the scattering measurements but without polarimeters. The sample was excited with wavelength of 550 nm and the emission wavelengths were selected with a 10 nm bandpass filter at 620 nm. Figure 4.8(a) shows the Fourier image of PL from a dye layer on a bare substrate used as reference. The Fourier image appears as a disk with a size determined by the NA of the objective and high intensity at $1 < |k| < \mathrm{NA}$, which agrees with the emission pattern expected from an ensemble of randomly oriented dipoles in a waveguide [30]. Figure 4.8(b) shows the Fourier image of PL from the dye layer on the spiral with $a = 225$ nm and Fig. 4.8(c) shows a comparison between the PL from the spiral sample and the reference in an image slice taken at $k_y = 0$. The emission in the forward direction is significantly enhanced due to out-coupling of the waveguide modes through diffraction by the spiral. We calculate the PL enhancement (PLE) by dividing the spiral-enhanced PL by the reference PL. Figure 4.9 shows the measured PLE of spirals with $a = 200$, 225, 250 and 275 nm. All the spirals show circularly symmetric PLE at small $|\boldsymbol{k}|$, with PLE enhancement values from 1.5 to 2. With increasing a, the enhancement shifts from being a ring $|\boldsymbol{k}| \approx 0.2k_0$ (8° in the glass) to a central maximum at $|\boldsymbol{k}| = 0$ and increases until it is maximized in the forward direction with $a = 225$ nm. For $a = 250$ nm, the enhancement decreases and furthermore reverts to being a ring at $|\boldsymbol{k}| \approx 0.3k_0$ (11° in the glass). Stokes parameter polarimetry measurements of the output show that the enhanced fluorescence intensity is entirely unpolarized, as shown in Fig. 4.10, as might be naively expected from a random ensemble of emitters and a plasmonic structure with no preferential orientation. This is a remarkable difference of the investigated spiral arrays from periodic arrays, from which the diffractive surface lattice resonances can carry a strong polarization signature [32].

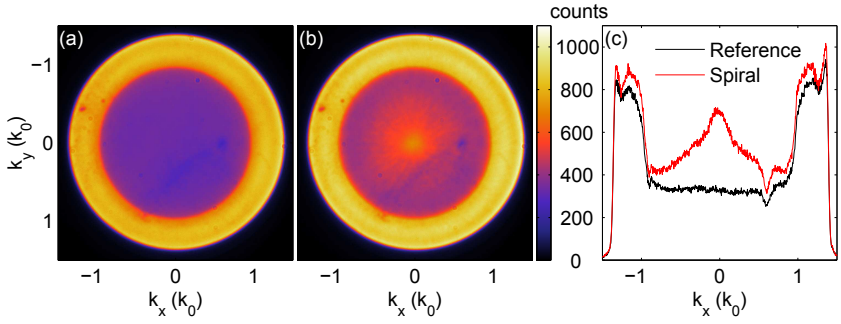

Figure 4.8: Measured Fourier images of fluorescence at λ=620 nm from (a) the reference, which is a 600 nm dye layer (b) and the same dye layer on the spiral. $a = 225$ nm, $N = 1000$. (c) Cuts from (a) and (b) at $k_y = 0$, plotted with the same scale of the colorbar.

We model the dispersion of the enhancement by assuming the nanoantenna array as a group of identical uncoupled point dipoles that coherently radiate into the far field, after having been driven by a point source that isotropically excites the waveguide

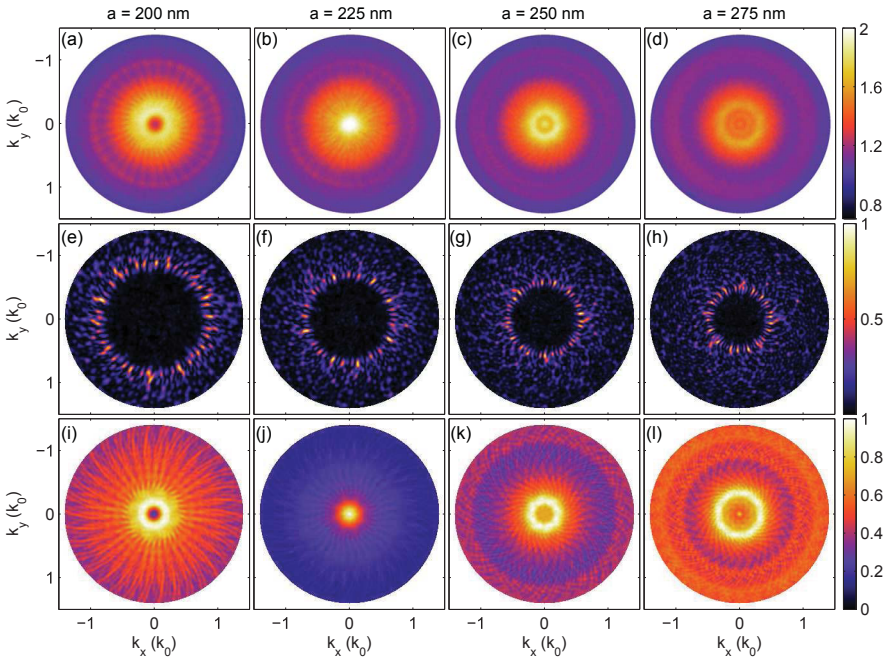

Figure 4.9: Fourier images of PLE on a 600 nm dye layer from spirals. (a-d) are measurement results. (e-h) are calculated from Eq. (4.4) and (i-l) are calculated from Eq. (4.7). (a)(e)(i) $a = 200$ nm, (b)(f)(j) 225 nm, (c)(g)(k) 250 nm, (d)(h)(l) 275 nm. (e-h) are normalized to the maximum of (f). (i-l) are normalized to the maximum of (j). $N = 1000$.

mode supported by the dye layer, which mimics a fluorophore. According to radio wave antenna theory, if the induced dipole moment of an antenna at location $\boldsymbol{r}$ is $p = \alpha E_D(\boldsymbol{r})$, with local driving field $E_D(\boldsymbol{r})$ and scalar polarizability of each nanoantenna α, the radiation pattern follows by summation over all antennas

$$\begin{aligned} E(\mathbf{k}_{||}) &\propto \sum_{n\in\text{spiral}} E_D(\boldsymbol{r}_n)\alpha e^{-\mathrm{i}\boldsymbol{k}_{||}\cdot\boldsymbol{r}_n} \\ &\propto \alpha \int_{\text{plane}} E_D(\mathbf{r}) \cdot \sum_{n\in\text{spiral}} \delta(\mathbf{r}-\mathbf{r}_n) e^{-\mathrm{i}\boldsymbol{k}_{||}\cdot\boldsymbol{r}}, \end{aligned} \tag{4.3}$$

with $\boldsymbol{r}_n$ the position of each nanoantenna. In this expression a common prefactor that is a spherical wave has been suppressed. Using the convolution theorem, the far field distribution is the convolution of the driving field E_D transformed to k-space, and the Fourier transform ($\mathscr{F}$) of the spiral structure, i.e.

$$E(\boldsymbol{k}_{||}) \propto \mathscr{F}[E_D] \star \mathscr{F}[\sum_{n\in\text{spiral}} \delta(\boldsymbol{r}_n)]. \tag{4.4}$$

In our sample, the driving field is dominated by the waveguide modes generated by the fluorescence of randomly distributed incoherent dye molecules. For an emitter

located at the origin that predominantly emitted into the waveguide mode, the driving field in k-space simply is a circle with radius given by the waveguide mode index. More formally stated, it is approximated as the Fourier space representation of the 2D Green function of the Helmholtz equation, i.e., $|\boldsymbol{k}^2 - n_{WG}^2 k_0^2|^{-1}$, with n_{WG} the mode index. The emitted power ($P_{\boldsymbol{k}} = |E_{\boldsymbol{k}}|^2$) as calculated from the convolution is expected to be a speckled ring at large wave vector and low intensity at the origin as shown in Fig. 4.9(e-h). In earlier work on periodic plasmon array systems it has been reported that the radiation pattern of a single emitter in the unit cell already predicts very well the radiation pattern of an incoherent ensemble [23]. Instead, here we see a striking difference between the measured ensemble-averaged pattern, and the distribution of emission that one would expect for just a single source at the origin. This contradiction indicates that (i) the dense fluctuation in the phase of the Fourier transform has a significant influence and (ii) likely, emitters in different positions result in a very different emission pattern in terms of amplitude and phase. Indeed, the predictions in Fig. 4.9(e-h) show angularly narrow speckle, and destructive interference that suppresses the forward emission, while for other source positions we predict quite different patterns. Therefore, to make a more accurate prediction, we need to consider an incoherent sum of contributions from random source positions.

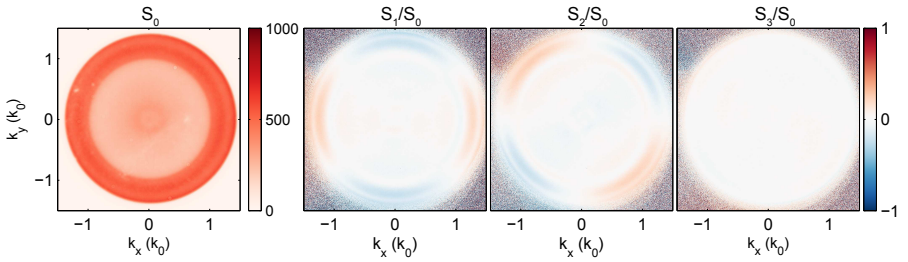

Figure 4.10: Measured Stokes parameters of photoluminescence from a 600 nm dye layer enhanced by a golden spiral. $a = 250$ nm, $N = 1000$.

The Fourier shift theorem states that a shift in position by $\boldsymbol{r}_D$ of the driving source only results in a phase shift of the Fourier transform of the driving field [23] as:

$$\mathscr{F}[E_D(\boldsymbol{r}_D)] = e^{\mathrm{i}\boldsymbol{k}_{||}\cdot\boldsymbol{r}_D}\mathscr{F}[E_D(0)]. \tag{4.5}$$

Thus, the total emission power from an ensemble of randomly distributed incoherent sources can be calculated as:

$$P_{\boldsymbol{k}_{||}} \propto \int \mathrm{d}\boldsymbol{r}_D \left| e^{\mathrm{i}\boldsymbol{k}_{||}\cdot\boldsymbol{r}_D}\mathscr{F}[E_D(0)] \star \mathscr{F}[\sum_{n\in\text{spiral}} \delta(\boldsymbol{r}_n)] \right|^2. \tag{4.6}$$

By expanding $|.|^2$ as a product, writing out the convolution integrals and then switching the order of integration, we can simplify the above formula to

$$P_{\boldsymbol{k}} \propto |\mathscr{F}[E_D(0)]|^2 \star |\mathscr{F}[\sum_{n\in\text{spiral}} \delta(\boldsymbol{r}_n)]|^2. \tag{4.7}$$

This is a generally useful and remarkable result for periodic and non-periodic plasmonic array structures aimed at controlling the directivity of random uniformly distributed ensembles of incoherent emitters. It states that, while the radiation pattern of a single emitter is given by the k-space convolution of the single emitter field and the complex structure factor, the radiation pattern of the incoherent ensemble is the k-space convolution of the single emitter intensity and the absolute value squared of the structure factor. Practically, this means that the rapid phase fluctuations in Fig. 1(b) simply average out. Fig. 4.9 (i-l) show the calculated emission patterns for the four measured spirals assuming such incoherent averaging. We find excellent agreement with the measurements in terms of enhancement position and relative strength. We conclude that, while spirals are not very suited for beam shaping of single emitters because of their tendency to imprint a rapidly fluctuating amplitude and phase pattern, in fact on the ensemble level the investigated spirals are able to out-couple ensemble emission in a phosphor layer in a directional manner.

4.5.2 Bandwidth of the photoluminescence enhancement

Finally we study the bandwidth of the enhancement measuring the spectrally resolved Fourier image of the four spirals. Figures 4.11(a-f) show PLE for samples with 6 different pitches, plotted as function of dimensionless parameter $k_y \cdot a$ and dimensionless frequency $\omega a/2\pi c = a/\lambda$. Under the condition of negligible dispersion in the waveguide index, one would expect this scaling to align the diffractive features in all samples. Indeed, according to Eq. (4.6), the PLE has approximately the same dependence on $\boldsymbol{k}$ and a/λ for all the four spirals. The maximum value of enhancement is slightly below that in Fig. 4.9, which we attribute to a difference in pump wavelength and angle. Nevertheless, the dispersion of the enhancement agrees well. The enhancement is maximized at $k_y \cdot a = 0$ and $a/\lambda \approx 0.36$ ($a = 225$ nm for $\lambda = 620$ nm) and then shifts to larger $k_y \cdot a$ as a/λ continues increasing. At $a/\lambda \approx 0.36$ the photoluminescence at small angle is suppressed.

With the same model used for Fig. 4.9(i-l), we obtain the theoretical dispersion of PLE in Fig. 4.11(g), which again agrees with the measurement result in terms of both the position of the enhancement and the relative strength of the enhancement. Both the experiment and theory show a broadband enhancement near the forward direction over $a/\lambda = 0.34$ to 0.38, corresponding to a bandwidth of around 60 nm for $a \approx 200$ nm, much larger than the bandwidth reported for periodic structures. This bandwidth makes spirals suitable for enhanced directional emission of many promising light-emitting devices that use quantum dots [33–36] and organic dyes for conversion to white light. These fluorophores have a typical bandwidth of $30 - 100$ nm at room temperature.

4.6 Conclusion

We have fabricated Au nano-antenna arrays arranged as Vogel's golden spirals and characterized their scattering properties using dark field microscopy and k-space

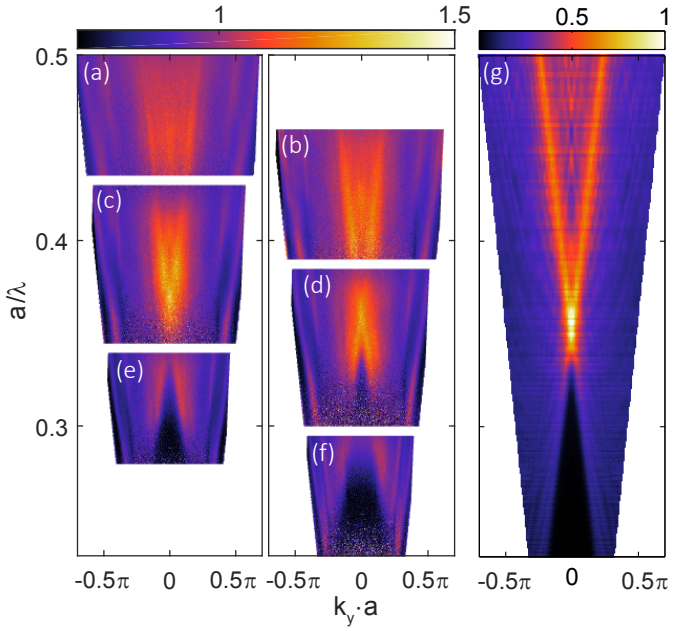

Figure 4.11: Measured Fourier spectra of Fluorescence enhancement on the 600 nm dye layer from spirals with (a) $a = 300$ nm (b) 275 nm, (c) 250 nm, (d) 225 nm, (e) 200 nm and (f) 175 nm, $N = 1000$. (e) Emission enhancement predicted from Eq. (4.7) normalized to the maximum.

polarimetry microscopy. The dark field images reveal a localized surface plasmon resonance near 600 nm for individual nanoantennas in the spirals, yet strong diffractive coloring for spirals with $a < 300$ nm. Comparing Fourier-space polarimetry results with a theoretical model, we have furthermore concluded that the investigated spirals ($a = 400$ nm) react to the incident field as uncoupled dipole arrays, meaning that one obtains scattering pattern determined by the spiral Fourier transform, and polarization characteristics inherited from that of single dipole scatterers at the air-substrate interface. Finally we have measured and modeled the directional fluorescence enhancement from the spirals. We demonstrate that the spirals can enhance the forward emission from incoherent sources in a waveguide by out-coupling the waveguide modes. The peak directional emission enhancement is only modest, at approximately a factor 2 compared to an unpatterned reference. This value appears small compared to the directional enhancement of up to a factor 60 achieved in periodic systems, which benefit from a stronger, but discretely distributed, Fourier spectrum [11]. However, in the case of periodic systems, the enhancement at the optimal wavelength spans only a cone of 3° around the normal, (solid angle < 0.01 sr). In contrast, the enhancement provided by the spiral encompasses up to $k/k_0 = 0.3$ (values taken at half-maximum), corresponding to a 30 times larger solid angle. We conclude that spirals are (at least) as effective as periodic systems in terms of the total amount of emission that is outcoupled from

the waveguide, with a complementary application window in terms of angular range (tens of degrees, not a few degrees). Moreover, the large spectral bandwidth offered by spirals is very well suited to remote phosphor applications. Emission of a typical YAG:Cerium phosphor typically has 100 nm bandwidth. Reported periodic plasmon system [11] only enhance over 5% of that spectrum, whereas the Vogel's spiral covers over 50% (60 nm bandwidth). For future work, we note that the strength of the enhancement may be further boosted through the design of each of the nanoantennas. For example, optimizing the shape, size and material of the nanoantennas can increase the scattering strength and therefore further enhance the out-coupling. We further note that the enhancement is only dependent on the amplitude of the Fourier transform and not the phase. Therefore, similar ideas could be pursued in other structures with similar strongly banded rotationally symmetric structure factors, such as hyperuniform lattices [37–39].

References

[1] A. Kinkhabwala, Z. Yu, S. Fan, Y. Avlasevich, K. Mullen, and E. W. Moerner, *Large single-molecule fluorescence enhancements produced by a bowtie nanoantenna*, Nat. Photonics **3**, 654 (2009).

[2] S. Kühn, U. Håkanson, L. Rogobete, and V. Sandoghdar, *Enhancement of single-molecule fluorescence using a gold nanoparticle as an optical nanoantenna*, Phys. Rev. Lett. **97**, 017402 (2006).

[3] H. Mertens, A. F. Koenderink, and A. Polman, *Plasmon-enhanced luminescence near noble-metal nanospheres: Comparison of exact theory and an improved Gersten and Nitzan model*, Phys. Rev. B **76**, 115123 (2007).

[4] P. Anger, P. Bharadwaj, and L. Novotny, *Enhancement and quenching of single-molecule fluorescence*, Phys. Rev. Lett. **96**, 113002 (2006).

[5] R. J. Moerland, T. H. Taminiau, L. Novotny, N. F. van Hulst, and L. Kuipers, *Reversible polarization control of single photon emission*, Nano Lett. **8**, 606 (2008).

[6] H. Gersen, M. F. García-Parajó, L. Novotny, J. A. Veerman, L. Kuipers, and N. F. van Hulst, *Influencing the angular emission of a single molecule*, Phys. Rev. Lett. **85**, 5312 (2000).

[7] P. Mühlschlegel, H.-J. Eisler, O. J. F. Martin, B. Hecht, and D. W. Pohl, *Resonant optical antennas*, Science **308**, 1607 (2005).

[8] T. H. Taminiau., F. D. Stefani, F. B. Segerink, and N. F. van Hulst, *Optical antennas direct single-molecule emission*, Nat. Photonics **2**, 234 (2008).

[9] A. G. Curto, G. Volpe, T. H. Taminiau, M. P. Kreuzer, R. Quidant, and N. F. van Hulst, *Unidirectional emission of a quantum dot coupled to a nanoantenna*, Science **329**, 930 (2010).

[10] K. H. Cho, J. Y. Kim, D.-G. Choi, K.-J. Lee, J.-H. Choi, and K. C. Choi, *Surface plasmon-waveguide hybrid polymer light-emitting devices using hexagonal Ag dots*, Opt. Lett. **37**, 761 (2012).

[11] G. Lozano, D. J. Louwers, S. R. Rodriguez, S. Murai, O. T. Jansen, M. A. Verschuuren, and J. Gómez Rivas, *Plasmonics for solid-state lighting: enhanced excitation and directional emission of highly efficient light sources*, Light Sci. Appl. **2**, e66 (2013).

[12] G. Lozano, G. Grzela, M. A. Verschuuren, M. Ramezani, and J. Gómez Rivas, *Tailor-made directional emission in nanoimprinted plasmonic-based light-emitting devices*, Nanoscale **6**, 9223 (2014).

[13] L. Dal Negro and S. Boriskina, *Deterministic aperiodic nanostructures for photonics and plasmonics applications*, Laser Photonics Rev. **6**, 178 (2012).

[14] R. Dallapiccola, A. Gopinath, F. Stellacci, and L. D. Negro, *Quasi-periodic distribution of plasmon modes in two-dimensional fibonacci arrays of metal nanoparticles*, Opt. Express **16**, 5544 (2008).

[15] C. Forestiere, G. Miano, G. Rubinacci, and L. Dal Negro, *Role of aperiodic order in the spectral, localization, and scaling properties of plasmon modes for the design of nanoparticle arrays*, Phys. Rev. B **79**, 085404 (2009).

[16] J. Trevino, H. Cao, and L. D. Negro, *Circularly symmetric light scattering from nanoplasmonic spirals*, Nano Lett. **11**, 2008 (2011).

[17] H. Vogel, *A better way to construct the sunflower head*, Math. Biosci. **44**, 179 (1979).

[18] C. Fallet, T. Novikova, M. Foldyna, S. Manhas, B. H. Ibrahim, A. De Martino, C. Vannuffel, and C. Constancias, *Overlay measurements by mueller polarimetry in back focal plane*, J. Micro/Nanolith. **10**, 033017 (2011).

[19] O. Arteaga, B. M. Maoz, S. Nichols, G. Markovich, and B. Kahr, *Complete polarimetry on the asymmetric transmission through subwavelength hole arrays*, Opt. Express **22**, 13719 (2014).

[20] S. S. Kruk, M. Decker, I. Staude, S. Schlecht, M. Greppmair, D. N. Neshev, and Y. S. Kivshar, *Spin-polarized photon emission by resonant multipolar nanoantennas*, ACS Photonics **1**, 1218 (2014).

[21] C. I. Osorio, A. Mohtashami, and A. F. Koenderink, *K-space polarimetry of bullseye plasmon antennas*, Sci. Rep. **5** (2015).

[22] C. A. Balanis, *Antenna Theory: Analysis and Design*, Wiley, 3rd edition, 2012.

[23] L. Langguth, A. H. Schokker, K. Guo, and A. F. Koenderink, *Plasmonic phase-gradient metasurface for spontaneous emission control*, Phys. Rev. B **92**, 205401 (2015).

[24] L. Langguth, D. Punj, J. Wenger, and A. F. Koenderink, *Plasmonic band structure controls single-molecule fluorescence*, ACS Nano **7**, 8840 (2013).

[25] I. Sersic, C. Tuambilangana, and A. F. Koenderink, *Fourier microscopy of single plasmonic scatterers*, New J. Phys **13**, 083019 (2011).

[26] A. H. Schokker and A. F. Koenderink, *Lasing at the band edges of plasmonic lattices*, Phys. Rev. B **90**, 155452 (2014).

[27] P. Nordlander, , C. Oubre, E. Prodan, K. Li, , and M. I. Stockman, *Plasmon hybridization in nanoparticle dimers*, Nano Lett. **4**, 899 (2004).

[28] E. Prodan and P. Nordlander, *Plasmon hybridization in spherical nanoparticles*, J. Chem. Phys. **120**, 5444 (2004).

[29] W. Lukosz and R. E. Kunz, *Light emission by magnetic and electric dipoles close to a plane dielectric interface. ii. radiation patterns of perpendicular oriented dipoles*, J. Opt. Soc. Am. **67**, 1615 (1977).

[30] L. Novotny and B. Hecht, *Principles of nano-optics*, Cambridge university press, 2012.

[31] H. P. Urbach and G. L. J. A. Rikken, *Spontaneous emission from a dielectric slab*, Phys. Rev. A **57**, 3913 (1998).

[32] M. Cotrufo, C. I. Osorio, and A. F. Koenderink, *Spin-dependent emission from arrays of planar chiral nanoantennas due to lattice and localized plasmon resonances*, ACS Nano **10**, 3389 (2016).

[33] Q. Sun, Y. A. Wang, L. S. Li, D. Wang, T. Zhu, J. Xu, C. Yang, and Y. Li, *Bright, multicoloured light-emitting diodes based on quantum dots*, Nat. Photonics **1**, 717 (2007).

[34] P. O. Anikeeva, J. E. Halpert, M. G. Bawendi, and V. Bulović, *Quantum dot light-emitting devices with electroluminescence tunable over the entire visible spectrum*, Nano Lett. **9**, 2532 (2009).

[35] J. M. Caruge, J. E. Halpert, V. Wood, V. Bulovic, and M. G. Bawendi, *Colloidal quantum-*

dot light-emitting diodes with metal-oxide charge transport layers, Nat. Photonics **2**, 247 (2008).

[36] S. Coe, W.-K. Woo, M. Bawendi, and V. Bulovic, *Electroluminescence from single monolayers of nanocrystals in molecular organic devices*, Nature **420**, 800 (2002).

[37] M. Florescu, P. J. Steinhardt, and S. Torquato, *Optical cavities and waveguides in hyperuniform disordered photonic solids*, Phys. Rev. B **87**, 165116 (2013).

[38] A. Utgenannt, R. Maspero, A. Fortini, R. Turner, M. Florescu, C. Jeynes, A. G. Kanaras, O. L. Muskens, R. P. Sear, and J. L. Keddie, *Fast assembly of gold nanoparticles in large-area 2d nanogrids using a one-step, near-infrared radiation-assisted evaporation process*, ACS Nano **10**, 2232 (2016).

[39] M. Castro-Lopez, M. Gaio, S. Sellers, G. Gkantzounis, M. Florescu, and R. Sapienza, *Reciprocal space engineering with hyperuniform gold disordered surfaces*, APL Photonics **2**, 061302 (2017).

5

Spatial intensity distribution of light in plasmonic particle array distributed feedback lasers

Plasmon DFB lasers based on periodic particle arrays feature fast response and strong feedback from the strong resonances of the plasmon particles. So far, most of the works reporting on particle array plasmon DFB lasers have focused on the role of Purcell enhancement and the band structure of the lasers. In this chapter, we study the real space intensity distribution of plasmon DFB lasers based on rectangular arrays of Ag nanoparticles. In the context of coupled wave theory developed for conventional DFB lasers such real space distributions should give direct access to socalled "coupling strengths", parameters that quantify how effectively the plasmonic particles provide feedback and outcoupling loss by Bragg diffraction. We demonstrate that on the one hand, coupled wave theory can indeed parametrize the real space intensity distribution of the investigated lasers. On the other hand, the derived coupling strength parameters turn out to be inconsistent with measured shifts of stop band edges in the lattice dispersion diagrams, two quantities which for dielectric DFB lasers are directly linked. We attribute this to the strong resonant localized scattering potential that Ag particles constitute for light, which cannot be accurately described by low order plane wave expansions such as coupled mode theory.

5.1 Introduction

Plasmon lasers or spasers were first proposed by Bergman and Stockman [1], and rely on the amplification of surface plasmon resonances by coupling to a gain medium. Surface plasmons have the ability to tightly localize electromagnetic field at the nanoscale, thereby differentiating plasmon lasers from conventional lasers by presenting an ultrasmall mode volume [2, 3]. Meanwhile, it has been predicted that the short plasmon lifetime and the high Purcell factor in plasmonic systems allow plasmon lasers to operate with a potentially femtosecond switching time [4, 5]. Therefore, plasmon lasers have been proposed as an ideal solution to ultrafast, deep sub-wavelength, coherent light sources, which would present an essential building block for, e.g., active photonic circuits [6] and integrated bio-sensing devices [7]. Reported realizations of plasmon lasers include a plasmon nanosphere laser [8], hybrid nanowire-gap lasers [2, 9] and commonly lasers based on different types of metallic-dielectric nanoresonators [10–16].

Due to the intrinsic large momentum mismatch between the surface plasmon field and free space light, the outcoupling of laser light from plasmon lasers is not intrinsically very efficient. One way to overcome this drawback is to use diffractive plasmonic structures. Periodic structures have already been utilized in laser science in the context of distributed feedback (DFB) lasers, typically realized as optically or electrically driven polymer systems, and III-V semiconductor photonic crystal lasers [17–22]. These structures use in-plane Bragg diffraction for feedback, are capable of highly directional light emission to free space using diffractive outcoupling, and they feature a high degree of spectral selection. Plasmon lattices such as metal hole arrays and metal nanoparticle arrays can provide both surface plasmon resonances and distributed feedback, and therefore have been used as platforms for realizing highly directional plasmon lasers [23–32]. On one hand, metal hole array plasmon lasers [23–26] use the Bragg reflection of surface plasmon polaritons guided at the interface of a metal and a gain medium on holes made into the metal film. Conversely, particle array plasmon lasers [27–32] use dielectric layers to provide both gain and a waveguide mode, while feedback relies on the hybridization of the waveguide with the particle plasmons. Metal hole array and particle plasmon arrays have in common that they use diffractive resonances for feedback. However, while holes in metal films are weak and nonresonant scatterers, plasmon particles provide localized plasmon resonances and large scattering cross sections.

Over the past five years, a significant body of literature has appeared on the physics of particle array plasmon lasers. Multiple features of the plasmon resonances have been invoked to explain the various observations. Notably, the group of Odom focused on Purcell enhancement due to strong field confinement [28, 29, 33, 34] to explain the occurrence and time scales underlying lasing. In contrast, in a different realization using efficient instead of inefficient dyes as gain medium, Schokker et al. [35, 36] have claimed that plasmon particle array lasers stand out not due to strong Purcell enhancements, but rather due to strong feedback as compared to dielectric DFB lasers. For instance, their study showed a remarkable robustness to disorder due to random

removal of plasmon particles from the lattices, indicating that very few scattering events are required to reach sufficient feedback for lasing [35, 36]. While in those measurements the underlying plasmon band structure was studied, none of these works addressed directly in real space the question how different a particle array plasmon laser is from a conventional DFB laser based on a corrugation in refractive index (real coupling) and/or a corrugation in loss and gain (complex coupling). Almost as early as the invention of the DFB lasers, Kogelnik and Shank developed a coupled wave theory in 1972 to describe DFB lasers [37] and afterwards, numerous studies have been done to extend the theory to different 1D and 2D DFB laser geometries [38–41]. In coupled wave theory a laser is described as a waveguide with a very weak periodic perturbation in the optical constant which lead to the coupling between in-plane forward and backward propagating waves. These waves furthermore experience gain from the gain medium, and are subject to outcoupling loss alongside coupling due to Bragg diffraction. Given the coupling strength parameters as input to the model, coupled mode theory predicts the photonic bandstructure, the lasing frequency and threshold gain. Furthermore, in a perturbative framework valid for dielectric gratings, the coupling parameters can be estimated from the Fourier coefficients of the dielectric constant. Particular for coupled mode theory is that it predicts a nontrivial spatial distribution of the laser field that characterizes the coupling strength and the lateral size of the laser. A good agreement between coupled mode theory and experiments has recently been demonstrated for metal hole array plasmon lasers [24, 25], both for band structures and real space intensity distributions. In contrast, for particle array plasmon lasers, theory mainly focused on coupled dipole approximations [32, 42] rather than the coupled wave theory. A difference between hole and particle systems is that individual holes in metal are not resonant, while plasmonic nanoparticles are strong scatterers with a frequency-dispersive resonance. Therefore, it is unclear whether the coupled wave theory would apply at all to particle array plasmon lasers. If it does, it is unclear how the coupling strength would relate to the plasmonic nature of the particles. Answering these questions can be key to differentiate plasmon particle array lasers from conventional DFB lasers.

In this chapter, we study the coupling strength of plasmonic DFB lasers based on rectangular lattices of Ag nanoparticles, by measuring their spatial intensity distributions and bandstructure using real and Fourier space imaging. In our work, we have the advantage of being able to tune the particle resonance near the lasing frequency through tuning the size of the particles. By comparing experiment and calculation, we try to answer two questions: (i) whether the coupled mode theory meant for weakly scattering systems applies to the strongly scattering plasmonic lattices in terms of parametrizing spatial intensity distributions, and if so, (ii) how the plasmon resonance near the lasing condition influences the apparent coupling strength, and the bandstructure. Finally, we present measurements of spatial coherence through a double-slit experiment.

5.2 Recapitulation of coupled mode theory and expected spatial intensity distributions

In this chapter we primarily discuss lasing in rectangular plasmon particle lattices, as opposed to the square lattices studied by Schokker et al. [30, 42]. The advantage of rectangular lattices is that the feedback is due to diffraction along only one axis, as only one of two pitches ($a_y = 370$ nm in our work) is chosen to obtain a diffraction resonance in the gain window (around 570 nm in our work). The second pitch ($a_x = 320$ nm) is chosen to provide feedback only at a wavelength shorter than the laser pump wavelength. Fig. 5.1 shows a schematic of the typical samples that we use, consisting of silver particles of about 30 nm high and between 30 and 90 in diameter. The particles are embedded in a 2D polymer waveguide (SU8 in our case) on a glass substrate that supports TE and TM waveguide modes with effective refractive indices around 1.55. The (0,2) Bragg diffraction (second order in the y direction) couples the waveguide modes in $+y$ and $-y$ directions as feedback for the lasing action, while the (0,1) Bragg diffraction couples the lasing waveguide modes out to the direction normal to the lattice plane. We neglect the influence of other diffraction orders as they do not match the waveguide mode dispersion. As the TE and TM waveguide modes have (slightly) different propagation vectors and orthogonal polarizations, the coupling between TE and TM modes are relatively weaker than the coupling within the TE or TM modes. We therefore also neglect the hybridization between the TE and TM modes. With these assumptions, the lasing process can be viewed as one dimensional DFB lasing action. These lasers implement the coupled mode theory scenario of Kogelnik and Shank [37, 38], barring the fact that the perturbing scatterers are plasmonic. Furthermore we simplify the electric fields of the waveguide modes by only considering their amplitude and treat the lasing fields as scalars in the following theoretical discussions.

5.2.1 Coupling of forward and backward waves

In coupled wave theory [37, 38], the light field is reduced to the sum of two counter propagating scalar waves (here corresponding to either the TE or TM waveguide mode) $S(y)\mathrm{e}^{\mathrm{i}G_y y}$ and $R(y)\mathrm{e}^{-\mathrm{i}G_y y}$ travelling in the $-y$ and y directions that are coupled through the first and second order Bragg diffractions of the periodic array. The phase factors express that we expect lasing operation near the second order Bragg diffraction, i.e., at wave vector near $G_y = 2\pi/a_y$ (with a_y the lattice constant in the y direction). The essence of coupled mode theory is to find equations governing the spatial dependence of the slowly varying envelopes of the forward and backward wave R and S, which take the following form [38]

$$-R'(y) + \left[\frac{g}{2} - \frac{\mathrm{i}}{2G_y}\left(n_{\mathrm{wg}}^2\left(\frac{\omega}{c}\right)^2 - G_y^2\right) - \kappa_{\mathrm{out}}\right] R(y) - (\mathrm{i}\kappa_{\mathrm{back}} + \kappa_{\mathrm{out}}) S(y) = 0, \quad (5.1)$$

$$S'(y) + \left[\frac{g}{2} - \frac{\mathrm{i}}{2G_y}\left(n_{\mathrm{wg}}^2\left(\frac{\omega}{c}\right)^2 - G_y^2\right) - \kappa_{\mathrm{out}}\right] S(y) - (\mathrm{i}\kappa_{\mathrm{back}} + \kappa_{\mathrm{out}}) R(y) = 0, \quad (5.2)$$

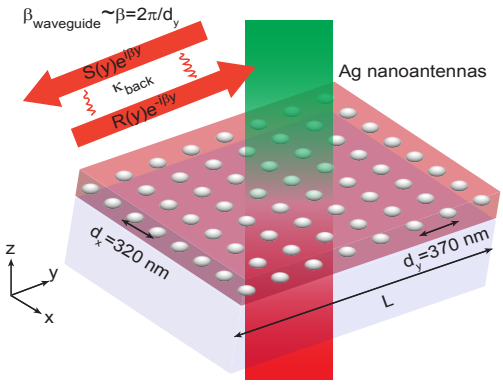

Figure 5.1: A schematic of our typical sample geometry. Our samples consist of rectangular lattices of cylindrical plasmonic particles on a glass substrate (n=1.52), covered by about 350 nm of SU8 (n=1.60) doped with Rh6G. The layer provides a single TE and TM waveguide mode. The Rh6G molecules in SU8 provide gain when pumped by green light.

where n_{wg} is the effective refractive index of the waveguide mode, and g represents the (net) gain coefficient, controlled by the pump strength and the nature of the gain medium. Furthermore, κ_{back} is the coupling strength of the two waves through the second order Bragg diffraction that is responsible for feedback, while κ_{out} is related to the coupling between the guided waves and the out of plane radiation through the first order Bragg diffraction, i.e., the radiation loss.

5.2.2 Coupling constants

According to Kazarinov et al. [38], κ_{back} and κ_{out} can be explicitly calculated in the case of weak index contrast periodic gratings, applicable to both index-coupling (scattering) and gain-coupling (spatial modulation of loss or gain, instead of refractive index) as

$$\kappa_{\mathrm{back}} = \left(\frac{1}{2G_y}\right)\left(\frac{\omega}{c}\right)^2 \int \varepsilon_{02}(z)\phi_z(z)^2 \mathrm{d}z \Big/ \int \phi_z(z)^2 \mathrm{d}z, \tag{5.3}$$

$$\kappa_{\mathrm{out}} = -\left(\frac{1}{2G_y}\right)\left(\frac{\omega}{c}\right)^4 \int\int \varepsilon_{01}(z)\varepsilon_{01}(z')\phi_z(z)\phi_z(z')G(z,z')\mathrm{d}z\mathrm{d}z' \Big/ \int \phi_z(z)^2 \mathrm{d}z. \tag{5.4}$$

Here ε_{01} and ε_{02} are the 2D Fourier coefficients of the relative permittivity of the scattering particles embedded in the waveguide background at $(0, G_y)$ and $(0, 2G_y)$ respectively. The origin of this result is a Fourier modal expansion, or plane wave expansion as commonly used in grating theory and photonic crystal band structure theory to describe the eigenmodes of photonic structures [43]. For weak index contrast cases such an expansion can be limited to just a few plane waves, i.e., those with wave vector $k_y = G_y, -G_y$ and 0, corresponding to the forward wave, backward wave and outcoupled wave in coupled mode theory. The vertically stratified structure causes a

weighting of the Fourier coefficients by the waveguide mode profile $\phi(z)$, namely, the electrical field distribution of the relevant waveguide mode in the z direction. $G(z_1, z_2)$ is a Green's function associated with the wave out-coupled by the first order Bragg diffraction. This result is similar to that of Andreani and Agio [44] for approximating the band structure of high-index 2D dielectric photonic crystals in layered, waveguiding systems, but limited to just a few waves, i.e., accounting for only two diffraction orders, instead of the 10^2 that are commonly used in the plane wave method for photonic crystals. Considering that our samples are based on particles of only 30 nm high, 10% of the waveguide layer thickness, we neglect the electric field variation within the particle and simplify the above expressions to

$$\kappa_{\text{back}} \approx \left(\frac{1}{2G_y}\right)\left(\frac{\omega}{c}\right)^2 \varepsilon_{02}(z_0)\phi_z(z_0)^2 h / \int \phi_z(z)^2 \mathrm{d}z, \tag{5.5}$$

$$\kappa_{\text{out}} \approx -\left(\frac{1}{4G_y^2}\right)\left(\frac{\omega}{c}\right)^4 \left(\varepsilon_{01}(z_0)\phi_z(z_0)\right)^2 h^2 / \int \phi_z(z)^2 \mathrm{d}z, \tag{5.6}$$

where $h = 30$ nm is the thickness of the particles and $z_0 = 15$ nm is the height of the particle center. When particles are much smaller than a unit cell, as in our case $V_{\text{Ag}}/V_{\text{SU8}} < 0.01$, the results of Eq. (5.5) and Eq. (5.6) have the following ordering relation: $\kappa_{\text{out}} \ll \kappa_{\text{back}} \ll k_0$.

5.2.3 Solutions

Returning to the coupled mode description of the slowly varying envelopes R ans S themselves, we note that their form is independent of the precise evaluation of the coupling constants κ_{back} and κ_{out}. The general solutions have the form:

$$\begin{aligned} R &= r_1 \mathrm{e}^{\gamma y} + r_2 \mathrm{e}^{-\gamma y}, \\ S &= s_1 \mathrm{e}^{\gamma y} + s_2 \mathrm{e}^{-\gamma y}, \end{aligned} \tag{5.7}$$

with

$$\gamma^2 = (\kappa_{\text{back}} - \mathrm{i}\kappa_{\text{out}})^2 + \left[\frac{g}{2} - \frac{\mathrm{i}}{2G_y}\left(n_{\text{wg}}^2\left(\frac{\omega}{c}\right)^2 - G_y^2\right) - \kappa_{\text{out}}\right]^2. \tag{5.8}$$

It is easy to see from Eq. (5.7) that $\mathrm{Im}\gamma$ plays the role of wave vector. Indeed, Eq. (5.8) reproduces the photonic band structure of the samples with $k_y = \pm\mathrm{Im}\gamma$ that one expects under the approximation of weak scattering, as we discussed in Chapter 1, Fig. 1.4. When the net gain is set to 0, the equation for γ reduces to

$$\gamma^2 \approx \kappa^2 - \left(G_y \frac{\delta\omega}{\omega_0} - \mathrm{i}\kappa_{\text{out}}\right)^2 \tag{5.9}$$

with $\delta\omega = \omega - \omega_0 \ll \omega_0$, $\omega_0 = cG_y/n_{\text{wg}}$ and $\kappa = \kappa_{\text{back}} - \mathrm{i}\kappa_{\text{out}}$. When $\mathrm{Re}\kappa \gg \mathrm{Im}\kappa$, the photonic bands split at $k_y = G_y$ and $k_y = 0$ with a gap in frequency, with $\delta\omega \approx \frac{\omega_0}{G_y}(-\mathrm{i}\kappa_{\text{out}} \pm \kappa)$. The radiation loss ($\kappa_{\text{out}}$) can result in an asymmetry in the stop gap. If

$\kappa_{back} \gg \kappa_{out}$, the splitting in frequency is symmetric around the crossing point at $\kappa = 0$, as illustrated in Fig. 5.2(a). Furthermore we note that if $\mathrm{Re}\kappa \ll \mathrm{Im}\kappa$, the photonic bands do not show a splitting in frequency, but instead show a splitting in wave vector, with a wave vector stop gap of width set by $\mathrm{Im}\kappa$ around $k_y = 0$. This type of wave vector gap, instead of frequency gap, corresponds to periodic corrugations dominated by spatial variations in loss/gain, instead of in the real part of the dielectric constant.

Having assessed that equation (5.8) for γ provides the photonic dispersion relation with stop gaps at conditions of near-zero net gain (far below threshold), we turn to solutions at threshold condition, with non-zero gain. To obtain solutions for the lasing condition and concomitant spatial intensity profiles, we consider a laser length L, and apply boundary conditions $S(-L/2) = R(L/2),\ S(L/2) = R(-L/2) = 0$ to the above equations [37]. This gives us the amplitude dependence of the two waves on y:

$$R(y) = \sinh\gamma(y + \frac{1}{2}L), \tag{5.10}$$

$$S(y) = \pm\sinh\gamma(y - \frac{1}{2}L), \tag{5.11}$$

$$\tag{5.12}$$

where now γ is determined by

$$\pm\, \mathrm{i}\gamma/\sinh\gamma L = \kappa. \tag{5.13}$$

As Eq. (5.8) has to simultaneously apply, we also obtain a relation that sets the threshold gain g_{thr}:

$$g_{thr} = 2\mathrm{Re}(\gamma\coth\gamma L + \kappa_{out}). \tag{5.14}$$

To understand the solution-space we refer to Figure 5.2(b,c) and (d). For a given complex coupling constant κ and laser size L one can find an infinite set of solutions that specify a combination of threshold gain g_{thr} and complex-valued γ. These solutions correspond to a discrete spectrum of longitudinal modes. For illustration, Figure 5.2(b) traces out the two solutions with lowest net threshold gain ($g_{thr} - 2\mathrm{Re}\kappa_{out}$) in (part of) the parameter space spanned by the real and imaginary part of κ. Evidently, one requires a non-zero value of κ to obtain a finite threshold (i.e., feedback is required for lasing), and both real and imaginary κ can provide feedback for lasing. In this work we focus on the mode with the lowest threshold gain. Since the parameter γ determines the spatial profile of the mode, it is useful to map its value as a function of the coupling constant κ. Figure 5.2(c) maps the real and imaginary part of γ versus κ. From the maps, we note that the $\mathrm{Re}\gamma$ has a strong dependence on $|\kappa|$, while $\mathrm{Im}\gamma$ is more dependent on $\mathrm{Arg}\kappa$. At low values of the coupling constant κ, the lasing mode will be characterized by predominantly real γ, corresponding to backward and forward amplitudes with a largely exponential form, peaking at the sample edge (sinh shape in Eqs. (5.10,5.11)). At large coupling the lasing mode will be characterized by predominantly imaginary γ, turning the corresponding backward and forward amplitudes into oscillatory instead of exponential spatial dependencies.

5.2.4 Observable intensity distributions

The theory outlined above reports on the amplitude and phase of the coupled forward and backward wave inside the laser resonator for the lowest threshold mode. In an experiment, however, one does not have access to the forward and backward wave local field in the laser. Instead one relies on imaging the intensity of the lasing field that is out-coupled by the first order Bragg diffraction. The resulting images arise from the interference of contributions of the two modes, where two further factors must be taken into account: mode symmetry and polarization.

Regarding mode symmetry, we note that the righthand side of Eq. (5.11) carries a sign choice, corresponding to symmetric resp. antisymmetric modes. These modes are standing waves that are distinguished by having either their antinodes (symmetric) or nodes (antisymmetric mode) at the nanoparticles. For TE modes with wave vector along the y direction, we take the polarization basis vector in the positive x direction for both R and S waves. The out-coupled field is also x-polarized, and under this convention, the symmetric mode with positive sign in Eq. (5.11) will result in an intensity distribution of $|R+S|^2 = |\sinh\gamma(y+L/2) + \sinh\gamma(y-L/2)|^2$. Fig. 5.2(d) shows examples of such spatial intensity distributions for the lowest threshold mode as the red curves for three regimes of the coupling coefficient κ: overcoupled, critically coupled and overcoupled. When $|\kappa L| \ll 1$ (undercoupled), the emission profile essentially reports on the sinh tails in Eq. (5.10,5.11). As $|\kappa|$ increases, the laser transits from critically coupled to overcoupled ($|\kappa L| \gg 1$), and γ goes from small and real to large and complex. In this case, the emission peaks in the center. The antisymmetric mode will have an intensity distribution of $|R+S|^2 = |\sinh\gamma(y+L/2) - \sinh\gamma(y-L/2)|^2$, always with zero intensity in the center as illustrated by the black curves in Fig. 5.2(d).

In an ideal case, these TE modes would not be observable at all in y-polarization as TE waves propagating along y carry no y polarization. However, in lasers of finite extent in the x direction, the envelopes S and R do carry a small k_x wave vector component, and hence a small signal will be apparent in the y-polarized detection channel. Since the two modes counterpropagate, these y polarizations have opposite symmetry to the x-polarized fields. Therefore, for the symmetric TE mode that appears as $|\sinh\gamma(y+L/2) + \sinh\gamma(y-L/2)|^2$ in x-polarization, one should record an antisymmetric $|\sinh\gamma(y+L/2) - \sinh\gamma(y-L/2)|^2$ profile in the y-polarization, and vice versa a symmetric profile for the antisymmetic modes. Generally, emission polarized at right angles to the wave vectors shows the mode symmetry, while co-polarized detection has opposite parity. Similar arguments can be set up for TM-polarized modes. In this case detection in the polarization channel along the wave vectors shows the mode symmetry. It is important to keep these polarization rules in mind, in order not to misinterpret any asymmetric spatial profiles as corresponding to an undercoupled lasing regime.

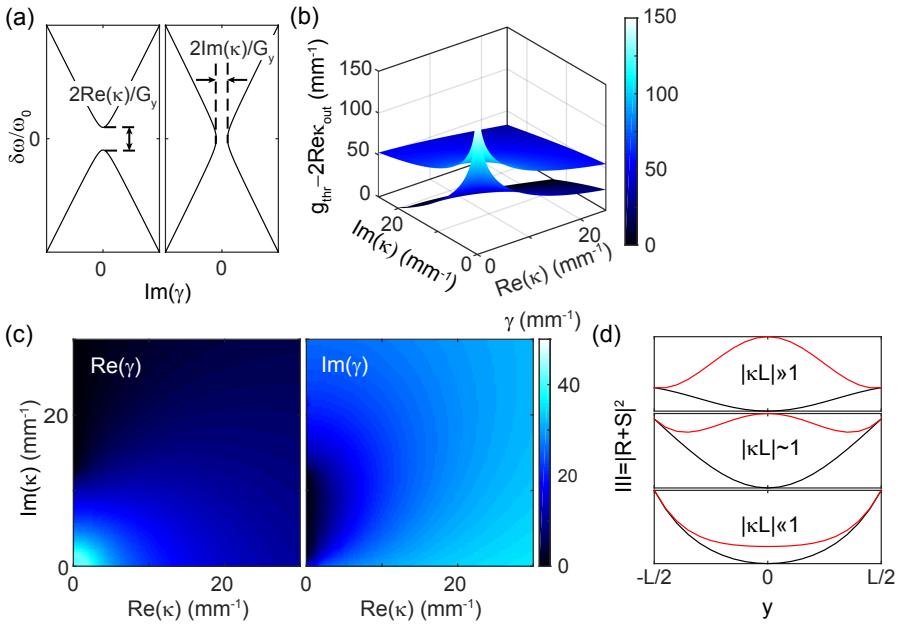

Figure 5.2: (a) Illustrations of the photonic band diagram of a rectangular array of Ag antennas, with $\kappa_{back} \gg \kappa_{out}$. The real part of the coupling coefficient results in a band gap in frequency while the imaginary part of the coupling coefficient results in a band gap in wave vector. (b) Threshold gain ($g_{thr} - \mathrm{Re}\kappa_{out}$) as a function of κ for two lowest threshold modes. (c) Reγ and Imγ as a function of κ for the lowest threshold mode in (b). (d) Illustrations of intensity profiles of out-coupled lasing modes (lowest threshold) in three regimes of κ. Red: $|\sinh\gamma(y+L/2)+\sinh\gamma(y-L/2)|^2$, black: $|\sinh\gamma(y+L/2)-\sinh\gamma(y-L/2)|^2$.

5.3 Sample fabrication and experimental setup

We perform experiments on a plasmon particle array lasers building on the work of Schokker et al. [30], focusing on a very similar sample geometry. This section serves to introduce the sample and set up.

5.3.1 Sample fabrication

The investigated plasmonic DFB lasers consist of rectangular lattices of Ag nanoparticles covered by a dye-doped SU8 waveguide on a glass coverslip. The Ag nanoparticles were fabricated using electron beam lithography, and successive thermal evaporation and liftoff (details in Ref. [30]). Each Ag nanoparticle has a height of 30 nm and a diameter that we systematically vary from 40 nm to 90 nm in different arrays. We fabricated both square arrays of 370 nm as studied by Schokker et al., and rectangular arrays with lattice constants of 320 nm in the x direction and 370 nm in the y direction with sizes varying from $40 \times 40\ \mu m^2$ to $80 \times 80\ \mu m^2$. Fig. 5.3 (b) shows an example SEM image of a rectangular array with particle diameter of 80 nm. A 350 nm SU8

layer doped with about 2.5 wt% Rh6G molecules is spincoated on the arrays as a gain medium. Because SU8 has a refractive index of about 1.60 (measured by ellipsometry) exceeding the index of the glass substrate (n=1.52), this layer supports fundamental TE and TM waveguide modes with a mode index of about 1.55. The in-plane wave vectors of these modes match the second order Bragg diffraction condition for a wavelength of about 570 nm, in the gain window, in the y direction for pitch 370 nm. We hence expect feedback and lasing to occur along y.

5.3.2 Experimental setup

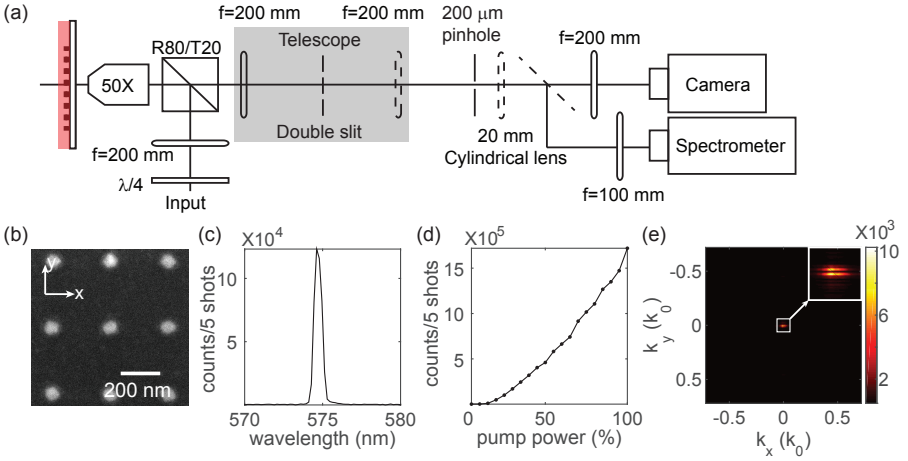

Figure 5.3: (a) A schematic of the optical setup. The sample (far left) is pumped through a 50x Nikon L Plan objective via a 80/20 beam splitter. Light is collected by the same objective and either a real or Fourier space image is formed on a CCD or spectrometer entrance slit. The first (left) lens of the telescope also works as a Fourier lens. When the second (right) lens is moved away, the back focal plane of the objective is imaged on the camera with a magnification of 1 or on the spectrometer with a magnification of 0.5. The pinhole right after the telescope filters out the high wave vector components of the emission. It is used in some measurements to suppress speckles. For double slit experiments, a double slit is placed in the center of the telescope and a cylindrical lens is added after the telescope. Double slit experiments are conducted without the pinhole. (b) Scanning electron microscope (SEM) image of an Ag particle (80 nm diameter) array before deposition of the gain medium. (c) A typical above threshold emission spectrum at 50 % pump power (80×80 μm^2 plasmon DFB laser with particle diameter of 80 nm). (d) Corresponding threshold curve (counts in lasing spectral band versus pump power set by AOM) and (e) Fourier image of the x-polarized emission showing a narrow beam as output. The inset of (e) shows a zoomed-in detail of the Fourier image near $k_x = k_y = 0$.

The setup used for the measurements in this chapter is a modified version of the setup of Ref. [30]. A schematic is shown in Fig. 5.3 (a). It is essentially an inverted fluorescence microscope equipped with real-space and backfocal plane (Fourier-space) imaging, as well as spectral (Fourier) imaging. Samples are placed on the platform of the inverted microscope with the substrate facing the objective (Nikon L PLAN, 50×, NA=0.7). The samples are pumped through the objective and substrate side with

collimated laser pulses of 532 nm wavelength (Teem Photonics, type STG-03E-1S0), with a beam diameter at the sample of ~120 μm. Each pulse has a width of 500 ps and maximum power of ~ 1μJ per pulse. The laser power is controlled by a computer-controlled acousto-optic modulator. Traditionally, inverted microscopes use dichroic beam-splitters that pass through fluorescence and reflect pump light. However, we noted that the dichroic mirror (SemRock, Di01-R532-25x36) in our setup can cause small polarization changes of transmitted light. While for some measurement, we use the dichroic beam-splitter at 532 nm for higher throughput, we use a R80/T20 beam splitter for all our polarized measurements. A quarter waveplate is used to convert the laser polarization from linear to circular, to avoid anisotropy induced by the pump polarization. The emission is passed through a set of long pass filters (Chroma, HHQ545lp) to remove pump laser light, and is imaged on either a thermo-electrically controlled Si CCD camera (Andor CLARA) or a Shamrock303i spectrometer with an (Andor Ivac) Si CCD detector, through the same objective and beam-splitter, and a 1× telescope and a tube lens. These detectors have quantum efficiencies in excess of 60%, and low read noise, allowing to take images and spectra of single laser shots. The first lens (counted from the sample side) of the telescope is placed at its focal distance from the back focal plane of the objective, and therefore also works as a Fourier or "Bertrand" lens when the second lens of the telescope is removed. When the back focal plane of the objective is imaged on the spectrometer, the entrance slit (20 μm) selects a vertical slice in the center of the Fourier image ($k_x = 0$) so that the emission intensity as a function of k_y and ω is imaged on the spectrometer camera. As demonstrated by Schokker [30], the resulting spectral images show distinct features that trace out the band structure of the sample, when operated below threshold. Similarly, in real space imaging the spectrometer slit spatially selects a 8 μm strip (when slit width is 20 μm) of the sample. Above threshold, these techniques allow to determine the lasing spectrum, and the spatial distribution of lasing modes.

5.3.3 Double slit experiment for spatial coherence measurements

To measure the transverse spatial coherence of the output from the lasing samples, we conduct double slit experiments. Based on the original setup described above, a pair of parallel slits oriented in the horizontal direction is placed in the center of the telescope where the sample is imaged with a magnification of 50. The slits are fabricated in a chrome layer on a glass substrate (ordered from Delta Mask b.v.), with a width of 0.3 mm and a center-center distance of 3 mm. A cylindrical lens ($f = 20$ mm in the vertical direction) is placed after the telescope, imaging the focal plane of the second lens of the telescope on the camera or spectrometer in the vertical direction with a magnification of 10 or 5. The resulting image is a (magnified) Fourier transform in the vertical direction of the product of the (magnified) laser emission and the slits.

When the laser is fully coherent in space, the image will have a fringe pattern in

the y (k_y) direction that follows:

$$I(k_y) \propto \frac{\sin^2(k_y k_0 W/2)}{k_y^2} \cdot [1 + \cos(k_y k_0 D)], \tag{5.15}$$

with W the slit width and D the slit distance. When the laser is partially coherent while we still assume it is fully coherent within the single slits, the intensity becomes

$$I(k_y) \propto \frac{\sin^2(k_y k_0 W/2)}{k_y^2} \cdot [1 + \cos(k_y k_0 D)] \cdot v + \frac{\sin^2(k_y k_0 W/2)}{k_y^2} \cdot (1 - v), \tag{5.16}$$

where v is the proportion of coherent light and can be calculated from the visibility of the fringes:

$$v = \frac{I_{\max} - I_{\min}}{I_{\max} + I_{\min}}. \tag{5.17}$$

These expressions assume identical transmitted intensity through the slits, which would require symmetric placement of the slits around the center of the arrays according to the coupled mode theory amplitude profiles.

5.3.4 Initial characterization

Schokker et al. [30] already reported evidence of lasing in this type of sample with square arrays, consisting of threshold behavior and spectral narrowing, spectral tunability of the lasing spectrum by lattice pitch, and a transition to highly directional output above threshold. For the rectangular array samples we find very similar behavior. Fig. 5.3(c-e) show measurement results a laser with a 80×80 μm^2 rectangular lattice (a_x = 320 nm, a_y = 370 nm) of Ag disks with diameter of 80 nm. When pumped with sufficiently high laser power, typically at 10% of the AOM range, the observed emission spectrum changes from the broad fluorescence spectrum of R6G in SU8 to a narrow peak at around 575 nm. The observed bandwidth of about 1.5 nm as shown in Fig. 5.3 (c) is wider than the bandwidth of typical plasmonic DFB lasers with a square lattice studied by Schokker et al. [30]. They reported lines limited by the spectrometer resolution, i.e. 0.6 nm with the same spectrometer and grating (300 lines / 500 mm). We attribute the broadening of the spectrum to the presence of multiple lasing modes with different wave vectors, which will be discussed in the following sections. The emission intensity in a narrow band (±1.5 nm) around the lasing wavelength as a function of pump power measured from the same sample is shown in Fig. 5.3 (d). The significantly different slopes before and after 10 % pump power indicate typical threshold behavior with a transition from spontaneous emission to lasing. When crossing the threshold, the laser output furthermore shows a strong change in directivity, from a Lambertian profile to a highly directional beam, as shown in Fig. 5.3(e). In the remainder of this chapter we do not discuss further the input-output curves, on the understanding that all the samples that we report on are probed above lasing threshold, unless otherwise noted.

Figure 5.4 shows typical real space intensity profiles for lasing samples operated above threshold, as obtained for a rectangular array laser and two square array lasers (equal pitches of 370 nm) with different field sizes and particle sizes. First, we observe a grainy fine structure on the scale of the diffraction limit, i.e., speckles in Fig. 5.4(a-b). Speckles are indications of spatial coherence and thus a sign of lasing, as analyzed for plasmon lattice lasers in Ref. [35]. These speckles can be suppressed using a Fourier-space aperture in the imaging path, at the cost of spatial resolution (Fig 5.4(c-d)). The second feature apparent in the images is an overall gradual intensity dependence, which appears as an envelope function multiplying the speckle pattern. We attribute this to the spatial dependence of forward and backward propagating waves as embodied in coupled mode theory, i.e., Eq. (5.10) and (5.11). For the rectangular lattices, the patterns are mirror symmetric through $y = 0$, indicating that feedback is only along the k_y direction. From spectral measurements, we know that the sample of Fig. 5.4(a-b) has one lasing mode (a single peak in the spectral output). The two polarizations of the mode have significantly different spatial profiles. The x polarization component (Fig. 5.4(a)) has maximum intensity at the array edge and near-zero intensity in the center, while the y polarization (Fig. 5.4(b)) shows high intensity in the center. From the discussion in Section 5.2, we conclude that the measured mode is antisymmetric (defined by the x polarization component), with a large coupling coefficient in the overcoupled regime. Fig. 5.4(c-d) show real space images of square arrays. In order to suppress the speckles so that the long range spatial profiles stand out, we have placed a 200 μm pinhole on the focal plane after the second lens of the telescope, where the Fourier space of the emission is imaged. The pinhole filters out high wavevector components of the emission which cause the speckles. In square arrays, feedback can simultaneously occur from four reciprocal lattice vectors. In Fig. 5.4(c), we again obtain signatures of edge-emission. Fig. 5.4(d) shows emission from both the center and the edge with a diagonal symmetry. We attribute this to the fact that four modes couple on a square area, leading to two instead of just one quantum number (similar to the $\sin(m\pi x/L)\sin(n\pi y/L)$ wavefunctions for a square box in quantum mechanics). Combinations of quantum numbers will give distributions that are not mirror symmetric in x or y axis, as evaluated for the case of photonic crystal lasers [39, 45]. These data demonstrate why in the remainder of this chapter we study rectangular arrays: their mode structure is far simpler.

5.4 Characterization of the laser modes

We characterize the laser modes in more detail by measuring the polarized Fourier and real space spectra of a representative lasing array (L = 80 μm, d = 90 nm) in Fig. 5.5. Fig. 5.5(a-b) and (e-f) show the below threshold band diagrams of the sample for two different slices in k-space, i.e., at $k_y = 0$ and at $k_x = 0$ respectively. The lasing modes originate from the waveguide modes along the feedback direction, namely, the y-direction. When coupled out by the first order Bragg diffraction, the waveguide modes in the y-direction appear as two crossing lines in the $k_x = 0$ plane and a parabolic

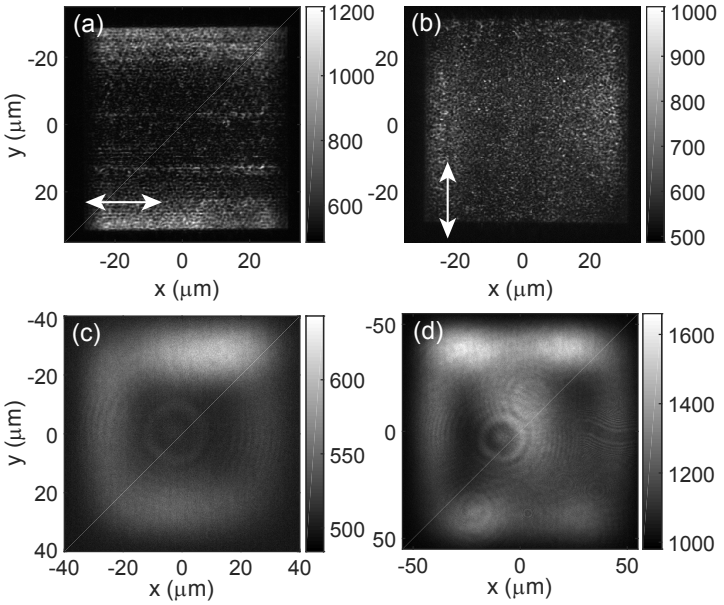

Figure 5.4: Above threshold real space images of (a-b) 60×60 μm^2, (c) a 60 × 60 μm^2 square array and (d) a 80 × 80 μm^2 square array. (a) and (b) are measured at x and y polarizations respectively. (c-d) include both polarizations. Ag antenna diameters are 90 nm in (a-b), 190 nm in (c) and 165 nm in (d).

band in the $k_y = 0$ plane, as shown in Fig. 5.5(a-b,e-f). By measuring the polarization of the banddiagram at $k_x = 0$ (Fig. 5.5(e-f)), we are able to separate the contributions of TE and TM waveguide modes as explained in section 5.2.4. Our data shows that both fundamental TM (marked with green arrows) and TE (marked with white arrows) modes are supported by the sample, consistent with simple slab-waveguide dispersion calculations [46]. The TE feature appears strongest, while the TM mode leaves only a weak signature in the k-space fluorescence spectra. This is consistent with the fact that the TM mode has weak in-plane electric field and therefore is not strongly scattered by the plasmon particles, which predominantly have an in-plane polarizability tensor due to their flat shape.

The above-threshold images in Fig. 5.5(c-d) and (g-h) show that the sample lases at band edges of both TE and TM modes with two distinct frequencies. While the TM mode lases in y polarization, the TE mode yields laser output in both x and y polarization channels. This can be explained from the band diagrams in Fig. 5.5(a-b). The TM mode has hardly any x polarization components and therefore mostly laser emission is obtained with y polarization. The TE mode instead has x polarization components for all (small) k_x and additionally y polarization components for $k_x \neq 0$. Accordingly, the TE lasing mode is polarized in the x direction at $k_x = 0$ and has both x and y polarization components at $k_x \neq 0$. There is a slight mismatch of the lasing

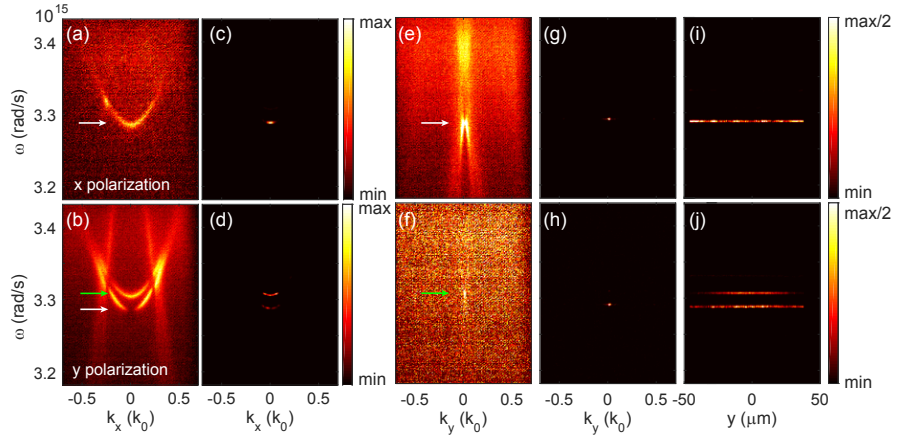

Figure 5.5: (a-h) Measured polarized Fourier spectra near (a-d) $k_y = 0$ and (e-h) $k_x = 0$ (a-b,e-f) below and (c-d,g-h) above threshold. (i-h) Measured above threshold spectra. (a,c,e,g,i): x polarization; (b,d,f,h,j): y polarization. Green arrows: TM mode; white arrows: TE modes. $L = 80$ μm, $d = 90$ nm. (a-b, e-f) represent the band diagram of the TE and TM waveguide modes. (c-d,g-h) show lasing at the bandedges of both TE and TM modes. The real space spectra in (i-j) show distinctive spatial profiles of the TE and TM modes depending on polarization.

intensity in different figures due to a small misalignment of the spectrometer entrance slit and the Fourier image center. The small angular range of the laser emission makes the detection efficiency of the spectrometer very sensitive to the alignment.

The different lasing wavelengths of the TE and TM modes provide a spectroscopic means to extract the spatial intensity distribution of each of the two modes separately as shown in Fig. 5.5(i-j), by spatially imaging the lasing array onto the spectrometer slit such that the entrance slit matches the center ($x \approx 0$) of the array. The TE mode has high intensity on the edge of the sample and low intensity in the center for x polarization and high intensity in the center for y polarization, similar to the results shown in Fig. 5.4(a-b). According to Section 5.2, it is an over-coupled antisymmetric mode. This agrees with the conclusion in Ref. [42] that the lasing of the TE mode occurs at the band edge where the nodes of the standing wave formed by the counter propagating TE modes are at the nanoparticles. The TM mode has high intensity in the center for y polarization and the x polarization component is not measurable. Similarly, the TM mode is also antisymmetric according to Section 5.2. These conclusions are in line with the notion that the lowest loss modes must be those that have low amplitude at the nanoparticles, thereby minimizing absorption and radiation losses.

5.5 Coupling strength of plasmon lattices

Having established the symmetries of the different lasing modes and their appearance in the different polarization channels, we compare measured spatial intensity distributions

with the coupled wave theory, and extract the apparent coupling strength κ. We systematically vary the diameter of the nanoparticles (40 nm to 90 nm) to obtain different coupling strengths, while for each particle size, we also vary the array size ($L = 80$ μm, 60 μm and 40 μm), in order to verify the predicted influence on the spatial intensity distribution patterns as predicted by Eq. (5.10)-(5.13). We note that all the investigated arrays lase at the TE mode with both x and y polarization components, while only arrays with big particles (larger than 70 nm) show lasing at the TM mode within the range of pump intensities we use. Moreover, since only the y polarization component of the TM mode can be measured, it is difficult to obtain the coupling strength accurately. Therefore, in the remainder we focus on analyzing the TE modes only.

We obtain the spatial intensity distribution in the y direction for the two polarizations of the TE mode by summing the intensity in a bandwidth within 1 nm around the lasing wavelength from spectral images shown in Fig. 5.5(i-j). This small wavelength range allows us to single out just one lasing mode, and at the same time rule out the contribution of spontaneous emission as the spontaneous emission spectrum of Rh6G spans from 60 to 100 nm. The lasers are pumped with 60-100 % laser power for a good count rate, which is about 6 times the threshold. We found that within the investigated above-threshold pump power range, pump power does not significantly influence the (normalized) spatial intensity distribution.

Fig. 5.6(a-b) shows examples of measured spatial intensity distribution from samples with different particle sizes and field sizes for both polarization channels. In all cases, the x-polarized laser emissions have near zero intensity in the center of the sample and highest intensity on the edges as shown in Fig. 5.6 (a). On the other hand, the y-polarized emission (Fig. 5.6 (b)) shows a clear transition from an under-coupled profile with low intensity in the center from arrays with small width (bottom row) or small particles (right column), to critically coupled profiles (center row and center column), and eventually to an over-coupled profile with intensity higher in the center than at the edges as the array width and particle diameter increase to 80 μm and 90 nm (top left). Apart from the high-spatial frequency features of data due to speckle (this dataset was taken with no Fourier-plane filter), the spatial intensity distributions of the investigated family of lasers qualitatively follow the predictions of one dimensional coupled mode theory.

Moving on from a qualitative comparison, we proceed to a quantitative comparison by fitting coupled mode theory predictions to data. In principle fitting measurement results to Eq. (5.10) and (5.11) should show in how far the coupled mode theory applies (quality of fit), and give access to the coupling strength (fit parameter) versus particle size. Unfortunately, random speckle in the emission pattern introduce large high-frequency and high-amplitude oscillations on top of the envelopes. Effectively this can be viewed as noise that does not follow a Gaussian distribution. Hence it is not easy to obtain robust fits using least squares fitting to each individual data set. Since the coupling strength must be only dependent on the size of the nanoparticles, we argue that the data should be fitted simultaneously from all samples with the same particle diameter but different field sizes and polarizations. This strongly constrains

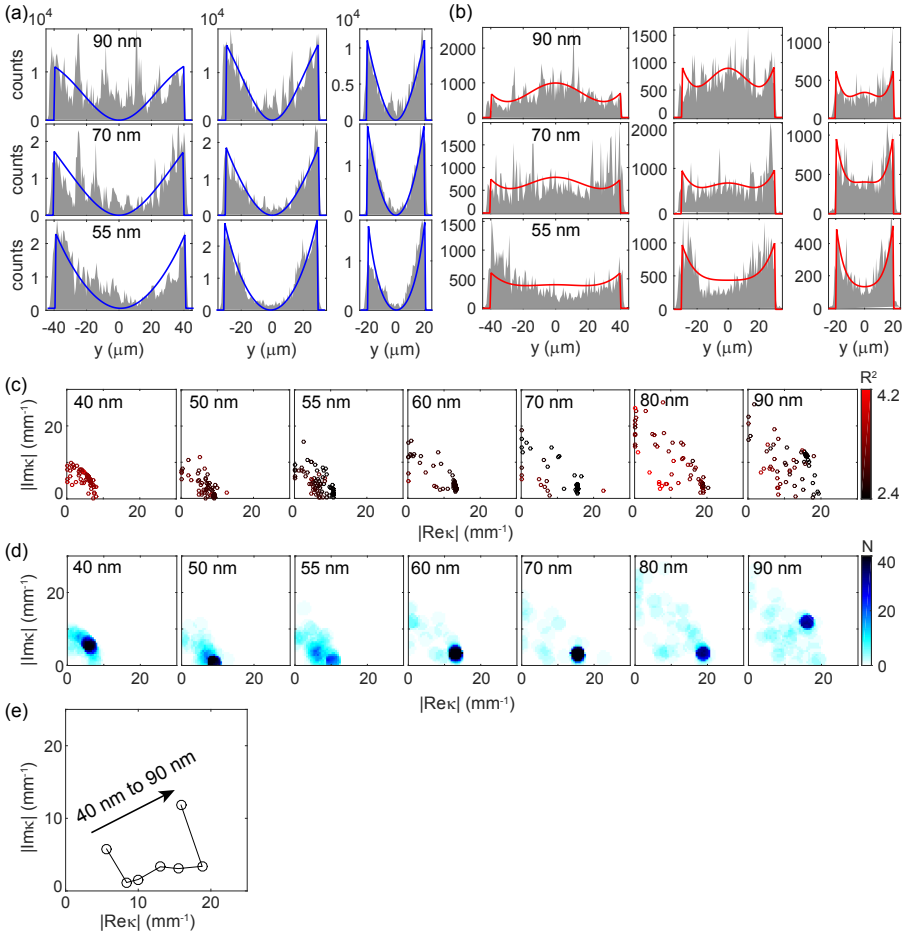

Figure 5.6: Measured lasing intensity as a f unction of y from samples with different particle sizes, over plotted with the fits. (a): x polarization; (b): y polarization. From bottom to top: particle diameter = 55, 70, 90 nm. While the x polarization results always show anti-symmetric intensity profiles, the y polarization results show a transition from under-coupled to over-coupled regime. (c) Values of κ obtained by fitting to the measured spatial intensity profiles of arrays with different particles sizes, using different starting points for κ. Color indicates the associated residual of the fit. (d) Histograms of κ values in (c). (e) Average value of κ over the densest bin (averaging radius of 2 mm^{-1}) in (c). Arrow indicates increase of particle diameter from 40 nm to 90 nm.

the fit, and should improve the robustness of the fit result, i.e., the fitted values of γ. Note that we use the conversion from γ to κ specified in Figure 5.2(c) derived for the lowest-threshold mode to extract the coupling parameter κ. This extraction determines κ in the first quadrant of the complex plane* To check the robustness of

*Note that γ and $-\gamma$ are equivalent in the definition Eq. (5.10)(5.11), while the intensity observables $|R \pm S|^2$ are agnostic to $\gamma \to \gamma^*$. This means we determine |Reκ| and |Imκ|.

the fit procedure, we conducted the fit using different starting values for κ that are evenly distributed in the first quadrant of the complex space within $|\kappa| < 0.03\ \mu m^{-1}$. This covers the under-coupled regime and the transition to the over-coupled regime. To avoid bias due to different signal strengths in the various data sets, the residual is weighted as

$$R^2 = \sum_{i=1,2,3} \sum_{y} \frac{(I_i(y) - I_i^0(y))^2}{N_i \overline{I_i(y)}}, \tag{5.18}$$

where i denotes the three different field sizes considered, N_i is the number of data points in each field, and I_i and I_i^0 are the fitted and measured data. By minimizing the residual, we obtain the results of the fit. The blue and red solid lines in Fig. 5.6(a-b) show examples of fits to the corresponding measured intensity distributions. While there are some clear differences between the measurement and fit results related to speckles and asymmetries in the measurement data, overall the fitted curves represent well the measured intensity profiles on large length scales.

Having established that the measured spatial distributions can indeed be fit by the coupled mode theory of Kogelnik and Shank [37, 38], we proceed to discuss the obtained κ values. Fig. 5.6 (c) shows the distribution of fitted κ values from different starting κ values for arrays with different particle sizes, in which the associated residual of the fit is indicated by the color scale. We note that although the fit routine reports convergence at different values depending on the starting parameter estimate, the results with lowest residuals cluster in small regions in the complex plane. Moreover, it appears that the amplitude $|\kappa|$ tends to be more accurately estimated then the phase. This is because the intensity distribution is determined by hyperbolic sine functions of γ and therefore is more dependent on Reγ than on Imγ. From Section 5.2, we notice that Reγ is mostly dependent on $|\kappa|$ and hardly dependent on Argκ. Consequently, we are able to determine $|\kappa|$ more accurately than Argκ from the intensity profile.

In order to determine the best global parameter estimate, we bin the fitted values in discrete boxes in κ-space of 2 mm^{-1} width. Fig. 5.6(d) shows the resulting 2D histogram in the complex plane. The fitted κ clearly cluster at distinct complex values with $|\kappa|$ increasing with increasing particle size, as expected from the fact that larger Ag particles scatter more strongly. By taking the average over the densest bin (averaging radius of 2 mm^{-1}), we obtain the average values of κ for different particle diameters in Fig. 5.6(e). They ranges from 5 to 20 mm^{-1}. In other words, $|\kappa/k_0| \approx 0.0003 - 0.0012$. Surprisingly, it is similar to the backcoupling coefficient of conventional index coupled DFB lasers ($0 - 20\ mm^{-1}$ [38]), but much lower than expected from complex-coupled DFB lasers (normalized: $50 - 200\ mm^{-1}$ [47] with metal gratings and surface plasmon lasers ($\kappa/k_0 = 0.012 - 0.017$ [24, 25]) based on metal hole arrays. This is surprising because plasmonic lattice lasers have been reported to benefit from the strong coupling between light and metal nanoparticles [29, 35]. Indeed, while holes in metal hole arrays are not resonant scatterers, the metal nanoparticles in plasmon lasers have large resonant scattering cross sections. Earlier evidence for the role of this strong scattering on plasmon lattice lasers comes from the fact that plasmon lattices show wide stop gaps in their band structures with relative stop gap widths of over 3% in

frequency reported. According to standard coupled mode theory this would directly imply $\kappa / k_0 = 0.03$. Instead, the spatial intensity distributions do not point at remarkable values of κ compared with other types DFB lasers.

5.6 Interpretation of fitted coupling strengths

In the previous section, we have established that coupled mode theory describes the spatial intensity distribution observed from finite-sized plasmon lattice lasers, but without attaching any interpretation to the observed values of the coupling coefficient κ. Coupled mode theory in itself provides no handles to interpret coupling coefficients, as it is a theory that takes these coefficients as a priori assumption. For dielectric DFB lasers one would commonly use approximations for κ that derive from plane wave expansions, or guided-mode Bloch wave expansions, such as Eq. (5.5) and (5.6). This approach invariably leads to the result that (1) κ should be calculable from the Fourier coefficients of the dielectric perturbation, and (2) κ directly relates to the relative bandwidth of the stop gap measured in band diagrams, or the shift of each band away from the geometrical diffraction condition (with any asymmetry in the shift helping to distinguish κ_{back} and κ_{out}). For plasmonic particle lattices, the main problem is that the resonant behavior of plasmon particles is much more accurately described in real space by a strongly localized point scatterer with resonant polarizability (α) than in Fourier space. Indeed, plane-wave expansion methods for calculating diffraction by plasmon lattices converge very poorly as the large discontinuity in dielectric contrast and gradients in field are difficult to resolve by a Fourier series [48]. How to improve the description of plasmon lattice band structures is only partially understood. Notably, Schokker et al. [42] found a qualitative correlation between relative stop gap with and scatterer extinction cross section. In this work, we take the following approach. First, we investigate the shift of the band edges of the plasmon lasers based on both experiment results and FEM simulation. Next, we examine the band edge shifts and the coupling strengths κ fitted to real-space intensity distributions, in order to establish if the correspondence between band edge shift and coupling strength in coupled mode theory carries over from weak index-contrast dielectric systems to plasmonics. Finally, we compare the coupling strength and band edge shifts to two theoretical models: the perturbative expression Eq. (5.5) and (5.6) and a polarizability-based empirical model.

We determine the positions of the TE band edges from the below threshold emission spectra of the lasers at $k_x = k_y = 0$ and compare them with the results obtained from the FEM simulation. The emission spectra are obtained by summing the intensity at $|k_y| < 0.02 k_0$ from measured x-polarized Fourier spectral images at $k_x = 0$ (e.g., Fig. 5.5(e)), as shown in Fig. 5.7(a). From the peaks of the spectra, we find two band edges. The upper band edge is always near $\omega \approx 3.28 \times 10^{15}$ rad/s within less than 0.5 % variation, and the corresponding spectral feature has a narrow bandwidth. It corresponds to the asymmetric lasing mode (nodes at the metal nanoparticles). On the other hand, the lower band edge presents a spectral feature with a much broader bandwidth. It moves towards smaller frequencies as the particle diameter increases

from 40 nm to 50 nm and disappears as the particle size further increases.

To confirm the connection between the measurement results and the designed sample geometry, we also simulate the band structure using FEM method (COMSOL). To do so, we simulate the zero-order transmittance of an x polarized plane wave incident at $k_x = 0,\ k_y = 0.006k_0$ on infinite rectangular arrays of Ag nanocylinders (height = 30 nm) in an 350 nm thick air-SU8-glass waveguide. We take the optical constants of Ag from Ref. [49], and n=1.60 and 1.50 for SU8 and glass respectively. We choose a slightly off-normal incidence, as the coupling to the narrow bandedge is forbidden by symmetry at exactly normal incidence. This results in a corresponding inaccuracy (approx. 0.6 %) in the frequency of the band edges. Similar to the measurement results, we find a narrow upper band that hardly shifts, and a lower band that redshifts and broadens with increasing particle size. The broadening of the lower band indicates an increasing Ohmic and radiative loss, which can be the reason of the vanishing of lower band edges in the measurement. Apart from the similarity, there is an approx. 0.3×10^{15} rad/s shift in the frequencies of the band edges between measurement and simulations. This indicates that the sample waveguide has a mode index approx. 1 % smaller than the simulated waveguide, which leads to $n_{\mathrm{wg}} \approx 1.55$. The band at $\omega \sim 3.4 \times 10^{15}$ rad/s is a surface lattice resonance at the SU8-glass interface and is irrelevant to the lasing experiment.

Next our aim is to directly compare the shifts of band edges with measured coupling strengths. Figure 5.7(c) shows the estimated shifts of the band edges from the theoretical band crossing point $\omega_0 = c/n_{\mathrm{wg}}G_y$. In order to construct a "master diagram" in which we can plot different data sets alongside our measurements and that clearly accounts for the plasmonic resonance of the particles we convert the particle size into a detuning parameter that measures the detuning from the localized plasmon resonance of a single particle in SU8 to the lasing condition ω_0. This normalized detuning is defined as the difference between lasing frequency and the single-particle plasmon resonance frequency, divided by the single-particle plasmon resonance width. The single-particle properties were derived from scattering cross-section calculations using the FDTD method in Ref. [42]. In the same plot, we combine three independent data sets. The closed blue and red points in Figure 5.7(c) indicate band edges extracted from the samples studied in this work. The red and blue open diamonds were extracted from Ref. [30], which used square lattices with the same gain medium as studied in this work, but much larger particles. Finally the red and blue open circles are extracted from Ref. [42], which again used square lattices of particles in SU8, with a lasing condition tuned far to the red by using a larger pitch and different fluorophore for gain. The three datasets together cover the case of red detuning [42], near-zero detuning, and blue detuning [30]. The three different sets of measurements combined show the general features of plasmonic laser band structure across the plasmon resonance frequency. The stop gap that opens up at the second order Bragg diffraction, i.e., at $k_x = k_y = 0$ has one band edge that barely shifts from the geometric Bragg diffraction condition, and one band edge that shifts away from the Bragg condition. The band that strongly shifts corresponds to the symmetric mode (antinodes at the particles) and concomitantly shows a frequency shift that depends strongly in magnitude on

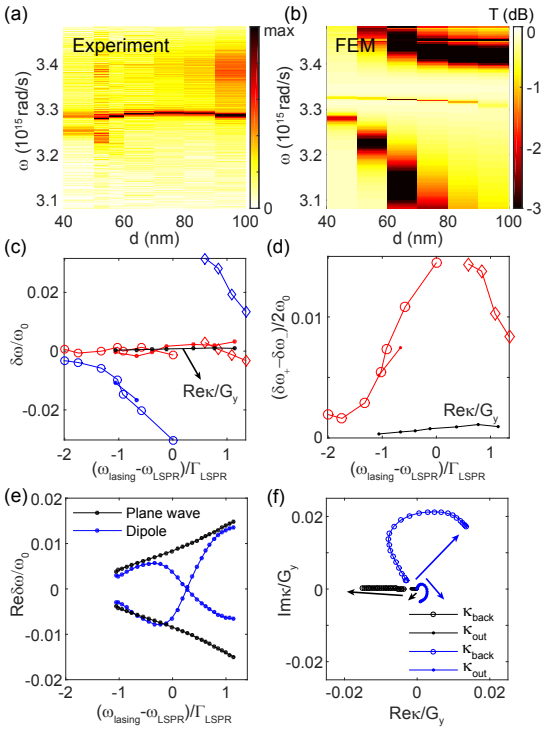

Figure 5.7: (a) Measured below-threshold emission spectra of the lasers depending on particle diameters. Each spectrum is normalized to its maximum. (b) Zero-order transmittance of the lasers depending on particle diameters obtained from FEM simulation. (c) Measured shift of the lasing band edges (red: lasing band edge, blue: non-lasing band edge) compared with $\mathrm{Re}\kappa/G_y$ (black) obtained from lasing experiments. (d) Measured half band gaps (red) compared $\mathrm{Re}\kappa/G_y$ (black) obtained from lasing experiments. Diamonds and circles in (c-d) correspond to data from Ref. [30] and Ref. [42] respectively. Dots correspond to the data from samples of this chapter. (e) Band shift and (f) coupling coefficients calculated using two models based on plane wave expansion (black) and dipole approximation (blue).

the detuning from the plasmon resonance. Notably, the shift is larger if it is closer to the plasmon resonance, and the sign of the shift is dependent on the sign of the detuning. This behavior qualitatively agrees with the notion that the particles show a dispersive polarizability (real part changes sign upon crossing zero detuning). The band that hardly shifts corresponds to the antisymmetric mode which has nodes at the particles, and is also the mode that lases in the experiments in this chapter. Earlier work on the stop gap in these systems [42] only examined the relative stop gap width (Figure 5.7(d)), which displays a clear maximum near zero detuning. However, it overlooked the large asymmetry in the two band shifts relative to ω_0. This asymmetry is very different from the symmetric shifts expected from coupled mode theory with $\kappa_{\mathrm{out}} \ll \kappa_{\mathrm{back}}$ as discussed in Section 5.2.

According to Eq. (5.9), the coupling parameter κ fitted to the real space intensity

profiles should be directly comparable to the band shifts (in case of symmetric bandshifts), or half the relative stop gap width. For this comparison we convert the fitted κ to a dimensionless quantity according to $\mathrm{Re}\kappa/G_y$ and take the required $\mathrm{Re}\kappa$ from Figure 5.6(e). Comparing the black dots in Figure 5.7(c) and (d) to the band edges extracted from spectra we conclude that the coupling strength $\mathrm{Re}\kappa/G_y$ that characterizes the spatial intensity profiles stays far below the values that one would expect from the splitting between the two bands (panel (d)). Instead, the small increase of $\mathrm{Re}\kappa/G_y$ with increasing particle diameter to at best 0.5 % is consistent with the very small shift in frequency of the upper band edge, i.e., the band edge responsible for lasing.

Within the conventional framework of coupled mode theory, these results are surprising. First, in standard coupled mode theory, the coupling strength obtained from real space profiles should be directly consistent with the stop gap width in spectra. Secondly, within coupled mode theory a large asymmetry in the band shifts would directly indicate $|\mathrm{Im}\kappa_{\mathrm{out}}| \gg |\mathrm{Re}\kappa_{\mathrm{back}}|$, inconsistent with what we expect for small particles according to Eq. (5.5) and Eq. (5.6). Thirdly, if indeed $\kappa_{\mathrm{out}} \gg \kappa_{\mathrm{back}}$, the coupling strength obtained from the lasing experiment would be much larger than the shift of the upper band, which is again different from our observation. Putting these discrepancies together, our hypothesis is that standard coupled wave theory fails. Indeed, the standard coupled wave theory is a perturbative plane wave expansion framework and is unable to account for the fact that metal particles are localized and resonant scattering centers. This problem is well known from the convergence-problems encounted by plane-wave based calculation methods for metal gratings [48]. To explain the measurement results, we propose that the results of coupled mode theory are qualitatively still applicable if one accepts that the two band edges should be described by different effective values of the coupling coefficients. This can motivated by noting that FEM simulations show a strong modification of the field distribution (in the z direction) of the waveguide modes by the plasmon resonances [42], which furthermore depends strongly on frequency. Since the coupling coefficients are dependent on the overlap of the waveguide mode with the Ag particles according to Eq. (5.5, 5.6), it stands to reason that the coupling coefficients may not be identical for the two band edges. This hypothesis can explain the large asymmetric in the band shift and the disagreement between the band gap and the coupling coefficient obtained from lasing measurement. Further test of this hypothesis would require above-threshold, and below-threshold full-wave simulations that include gain, that include noise to start the lasing process, and that do not use periodic boundary conditions. If those were available one could correlate band shifts below threshold, near-field overlap of modes with particles, and above-threshold real-space intensity distributions. Such simulations appear outside the scope of possibilities even of leading groups in theory of plasmon lasers.

5.6.1 Theoretical estimation of coupled coefficient

Here, we continue to make a theoretical estimate of the coupling coefficient and the band edge shifts expected from the geometry of our lasers in the context of coupled

wave theory. Eq. (5.5,5.6), originally derived by Kazarinov and Henry [38] already give an estimate for the coupling coefficients based on plane wave expansion. However, the plane wave expansion method cannot accurately describe the resonant behavior of the particles. Instead, they are much more accurately described as point dipoles with a resonant polarizability. Therefore, apart from the plane wave expansion method (Eq. (5.5)(5.6)), we introduce a second model, in which we attempt to make a link to the resonant point dipole theory for lattices. To do so, we turn to the formulation of the so called "photonic strength" for colloidal photonic crystals proposed by Spry and Kosan [50] and Vos et al. [51, 52]. Photonic strength measures the interaction strength of light and photonic crystals and according to Vos et al. [51, 52] equals the relative stop gap width ($\Delta\omega/\omega$). For a 3D photonic crystal of spheres, it is expressed as

$$\Psi = 4\pi \frac{\alpha}{V} f(GR) \qquad \text{with} \qquad f(x) = \frac{j_1(x)}{x}. \tag{5.19}$$

In this equation, $\alpha = 3V_{\text{sphere}}(\varepsilon_{\text{sphere}} - \varepsilon_{\text{host}})/4\pi(\varepsilon_{\text{sphere}} + 2\varepsilon_{\text{host}})$ is the (electrostatic) polarizability of the spheres and V is the volume of the unite cell. $f(GR)$ is proportional to the Fourier transform of the sphere geometry, with j_1 the spherical Bessel function of the first kind with order 1, G the length of the relevant reciprocal lattice vector and R the radius of the sphere. The parameter Ψ is well known in the dynamical diffraction theory for X-ray crystals (limit of very small polarizabilities) as the parameter that relates unit-cell structure to the amplitude and width of diffraction peaks [53]. To explain how this expression relates to results from the plane wave expansion method, we note that the plane wave method for a 3D photonic crystals of spheres predicts in first approximation [54]

$$\frac{\Delta\omega}{\omega} = \frac{\varepsilon_G}{\bar{\varepsilon}} = \frac{\varepsilon_{\text{sphere}} - \varepsilon_{\text{host}}}{\bar{\varepsilon}} \frac{4\pi R^3}{V} f(GR), \tag{5.20}$$

where ε_G is the Fourier transform of the relative permittivity and $\bar{\varepsilon}$ is the volume averaged relative permittivity. Note that Eq. (5.19) is actually different from Eq. (5.20), as $\alpha = 3V_{\text{sphere}}(\varepsilon_{\text{sphere}} - \varepsilon_{\text{host}})/4\pi(\varepsilon_{\text{sphere}} + 2\varepsilon_{\text{host}})$ does not actually equal $V_{\text{sphere}}(\varepsilon_{\text{sphere}} - \varepsilon_{\text{host}})/4\pi\bar{\varepsilon}$. Empirically Eq. (5.19) turns out to be a better description of band gaps of high index contrast photonic crystals than Eq.(5.20) [51, 52]. Although Eq. (5.19) was not designed for plasmonic crystals at all, it has the merit of capturing the intuitively expected plasmon resonance embodied in α.

Equations (5.5) and (5.6) for the corrugated waveguide geometry can be similarly treated. First we evaluate the Fourier coefficient ϵ_{01} and ϵ_{02}, and subsequently identify any occurrence of $(\epsilon_{\text{sphere}} - \epsilon_{\text{SU8}})/n_{\text{WG}}^2 V$ as $4\pi\alpha$, replicating the Ansatz postulated by Vos [51, 52]. This procedure leads to the following result

$$\frac{\kappa_{\text{back}}}{G_y} = \frac{4\pi\alpha}{V_{\text{eff}}} f(2G_y R), \tag{5.21}$$

$$\frac{\kappa_{\text{out}}}{k} = -kh_{\text{eff}} \left(\frac{4\pi\alpha}{V_{\text{eff}}} f(G_y R) \right)^2, \qquad \text{with} \qquad f(x) = \frac{J_1(x)}{x}. \tag{5.22}$$

In this case the standard (cylindrical) Bessel function appears, as opposed to the spherical Bessel function. Also the unit cell volume is now replaced by an effective unit cell volume that is the product of the unit cell area with the effective mode height associated with the antenna waveguide system, i.e

$$h_{\text{eff}} = \frac{\int |\phi(z)|^2 dz}{|\phi(z_0)|^2}. \tag{5.23}$$

We evaluate the above expressions using a fixed lasing wavelength (374 nm), and an estimate for the polarizability for differently sized particles obtained by matching calculated extinction cross sections from full-wave simulations for Ag particles in the glass-SU8-air system to polarizability via $\sigma_{\text{ext}} = 4\pi k \text{Im}\alpha$.

We calculate the coupling coefficients and band shift with the two theoretical models based on plane wave expansion and dipole approximation, as plotted in Fig. 5.7(e-f). Fig. 5.7(f) shows the values of κ_{back}/G_y and κ_{out}/G_y calculated using Eq. (5.5,5.6) based on plane wave expansion method, and Eq. (5.21,5.22) based on the dipole approximation. In both models, κ_{out} is much smaller than κ_{back}. $|\kappa_{\text{back}}/G_y|$ reaches about 0.02, which is in a similar order of magnitude as the 3% stop gap width in Fig. 5.7(c-d), but is one order of magnitude higher than the coupling coefficient obtained from the lasing experiments. The major difference of the two model lies in the phase of the coupling coefficients. While κ_{back}/G_y and κ_{out}/G_y are nearly real according to the plane wave expansion model, the dipole approximation predicts complex values of κ_{back}/G_y and κ_{out}/G_y. As a function of detuning (by increasing particle diameter), κ_{back} traces a circle from negative real with blue detuning, to imaginary on resonance, and finally to positive real with red detuning. This is reminiscent of the fact that the symmetric mode (localized at the particles) flips the sign of its band edge shift when going through zero detuning (Figure 5.7(c)). The band shift is calculated from the values of the coupling coefficients, using $\delta\omega \approx \frac{\omega_0}{G_y}\text{Re}(-i\kappa_{\text{out}} \pm \kappa)$, as plotted in Figure. 5.7(e). Both models predicts shifts from 0.5 % to 1.5 %. While the plane wave expansion predicts monotonically increasing band shifts from blue to red detuning, the dipole approximation predicts a decrease in band shift and a sign switch of the two band edges at resonance. Neither of the results from the two models agree with the measured asymmetric band shift. We further note that, according to the dipole approximation, κ_{back} has a large imaginary component near zero detuning. From Fig. 5.2(a), we know that this would result in a splitting of the bands in k_y instead of in ω. In this case, the band shift and band gap in ω are no longer accurate measure for the coupling strength.

To conclude, the coupling coefficients we obtained from the two theoretical models based on plane wave expansion and dipole approximation have a similar order of magnitude as the measured stop gap width, but are much larger than the value obtained from the lasing spatial profiles. Inserting these coupling coefficients into coupled mode theory, we obtained distinctively different band shifts compared to the measurement results. This disagreement further confirms the notion that plane wave approximations like coupled wave theory perform very poorly on strongly scattering plasmonic constituents.

5.7 Spatial coherence

Finally, we also conduct experiments to study the spatial coherence of lasing (TE mode only), using a double slit experiment. Here we report on the 80 μm × 80 μm lasers as representative example. With a pair of parallel slits with a width of 0.3 mm and a center-center distance of 3 mm, we measure the coherence between the emission from two 6 μm wide slices that are 60 microns apart on the sample, each positioned near one edge of the sample. We took care to place the slits symmetrically around the sample center to balance the emission intensities. Figure 5.8(a)(b) show the x polarized interference images measured with the CCD camera from the laser with particle diameter $d = 90$ nm, with the x- or y-direction of the laser aligned along the direction of the slits respectively. Figure 5.8(a) shows a quite homogeneous intensity distribution in the x direction and clear interference fringes in the y direction, indicating a strong spatial coherence of the laser in the y direction. On the contrary, Figure 5.8(b) does not show any interference fringes in the x direction, but shows an intensity distribution in the y direction that is similar to the intensity distribution of the whole laser. This result is consistent with coupled mode theory for a laser with feedback along y only.

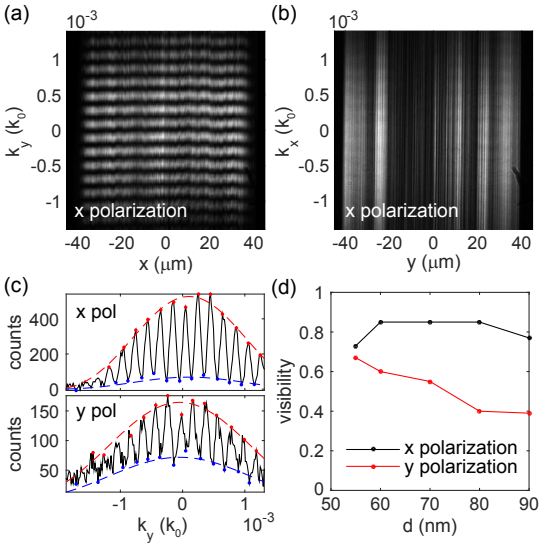

Figure 5.8: (a-b) Double slit interference patterns for x polarization with slits parallel to (a) x direction and (b) y direction. (c) Double slit interference patterns for (upper) x and (lower) y polarizations at wavelength of the TE lasing mode, with peaks and valleys fitted to two sinc functions. (d) Visibilities of the x and y polarization of the TE mode obtained from the fit for lasers with different particle sizes. Laser size: 80 μm × 80 μm. (a-c): $d = 90$ nm

To eliminate the influence of spontaneous emission background and the TM mode of the lasers, we use the spectrometer to select the emission at the wavelength of the TE mode of the lasers near $x = 0$. Figure 5.8(c) shows an example of a resulting spectrally

filtered interference pattern ($d = 90$ nm laser) in two different polarization channels. We select the peaks and valleys in the intensity curves and fit them simultaneously with two sinc functions that are centered in the same location (red and blue lines), with which we obtain the visibility according to Eq. (5.16) and (5.17). Figure 5.8(d) reports the visibility for the TE mode emission from lasers with different particles sizes for both polarization detection channels. The x polarization has a visibility around 0.8, i.e., high coherence for all measured lasers. The measured visibility is always smaller than 1. We attribute this to two possible causes. First, there can be a small difference between the emission intensity transmitted through each slit, either due to a small misalignment of the slits relative to the array center or due to speckles from scattering off defects. The intensity difference between the two slits can reduce the visibility. Second, as shown in Fig. 5.5 (c-d,g-h), lasing from rectangular arrays does not happen purely at $k_x = k_y = 0$, but at a small range of non-zero k_x. Particularly, in Fig. 5.5 (d) we note that the lasing emission at different k_x has slightly different frequencies, which indicates multiple lasing modes. Adding up the emission of multiple lasing modes can also result in a reduction of the visibility. The y polarization has a visibility that reduces from 0.7 to 0.4 as the particle size increases from 55 nm to 90 nm (from undercoupled to critically couple regime).

5.8 Conclusion

In this chapter, we have studied the real space intensity distribution of particle array plasmon DFB lasers in the context of understanding the lasers using the seminal coupled wave theory of Kogelnik and Shank [37]. We have systematically measured the real space intensity profile of a set of plasmon DFB lasers based on Ag particle arrays with different array sizes and particle diameters. Strong variations in the intensity distribution have been found, qualitatively agreeing with predictions by the coupled wave theory. With increasing Ag particle diameter and array size, a clear transition from the undercoupled regime to the overcoupled regime is observed, commensurate with the notion that larger plasmon particles yield stronger feedback to their larger polarizability at the lasing condition. From the intensity profiles, we have retrieved the coupling coefficients as a function of Ag particle diameter. The amplitude of the coupling coefficients increases from approximately 5 to 20 mm^{-1} as the particle diameter increases from 40 nm to 90 nm. These values are within the range of coupling coefficients commonly obtained from conventional DFB lasers. This is surprising because the coupling coefficient is usually directly related to the stop band width, which in these systems was measured to be larger, larger than in conventional DFB lasers. Instead of examining the stop band width, i.e., the splitting between band edge, we also examined the frequency shift of each band relative to the geometrical diffraction condition. Experiment and FEM simulation both show a strong asymmetry in the band shift near the band gap at $k_x = k_y = 0$. One of the photonic bands shows a clear shift that reaches a maximum at the plasmon resonance of the Ag particles, and reverses in sign when the detuning between lasing condition and plasmon resonance is reversed in

sign. This is consistent with the notion of a standing wave that overlaps strongly with the plasmon particles and is thereby shifted in frequency in proportion to the real part of particle polarizability. The other band hardly shifts, commensurate with the notion of a standing wave that has zeroes right at the plasmon particles. This is the band that appears to correspond to the lasing mode, which fits with the fact that this mode avoids both the scattering and Ohmic loss that the particles provide. The amplitude of the measured coupling coefficients derived from the spatial intensity profiles is consistent with the negligible shift of the lasing band, but is much smaller than would be expexted from the large stop gap.

In summary, the real space intensity distribution of the investigated plasmon DFB lasers can to some extent be described with the coupled wave theory designed for conventional DFB lasers. However, while coupled mode theory parametrizes the spatial intensity distributions, the derived coupling constants are not selfconsistently related to the dispersion relation implied by the same coupled mode theory. We attribute the discrepancy to the strong scattering of the Ag particles, which cannot be accurately described by only considering a few plane waves. We hypothesize that an effective description may be obtained by assigning different coupling constants to the two bands. Open questions include how to put such a hypothesis on a more solid yet still tractable footing by finding a way to directly relate the band structure and coupling constants to particle polarizability. Moreover, an open question is how to reconcile the low coupling constants reported here, which are on par with standard low-index contrast DFB lasers, with claims of a remarkable robustness to disorder and removing particles that appear unique to the plasmonic lattice lasers.

References

[1] D. J. Bergman and M. I. Stockman, *Surface plasmon amplification by stimulated emission of radiation: Quantum generation of coherent surface plasmons in nanosystems*, Phys. Rev. Lett. **90**, 027402 (2003).

[2] R. F. Oulton, V. J. Sorger, T. Zentgraf, R.-M. Ma, C. Gladden, L. Dai, G. Bartal, and X. Zhang, *Plasmon lasers at deep subwavelength scale*, Nature **461**, 629 (2009).

[3] X. Meng, A. V. Kildishev, K. Fujita, K. Tanaka, and V. M. Shalaev, *Wavelength-tunable spasing in the visible*, Nano Lett. **13**, 4106 (2013).

[4] M. I. Stockman, *The spaser as a nanoscale quantum generator and ultrafast amplifier*, J. Opt. **12**, 024004 (2010).

[5] D. A. Genov, R. F. Oulton, G. Bartal, and X. Zhang, *Anomalous spectral scaling of light emission rates in low-dimensional metallic nanostructures*, Phys. Rev. B **83**, 245312 (2011).

[6] S. I. Bozhevolnyi, V. S. Volkov, E. Devaux, J.-Y. Laluet, and T. W. Ebbesen, *Channel plasmon subwavelength waveguide components including interferometers and ring resonators*, Nature **440**, 508 (2006).

[7] J. N. Anker, W. P. Hall, O. Lyandres, N. C. Shah, J. Zhao, and R. P. Van Duyne, *Biosensing with plasmonic nanosensors*, Nat. Mater. **7**, 442 (2008).

[8] M. A. Noginov, G. Zhu, A. M. Belgrave, R. Bakker, V. M. Shalaev, E. E. Narimanov, S. Stout, E. Herz, T. Suteewong, and U. Wiesner, *Demonstration of a spaser-based nanolaser*, Nature **460**, 1110 (2009).

[9] Y.-J. Lu, J. Kim, H.-Y. Chen, C. Wu, N. Dabidian, C. E. Sanders, C.-Y. Wang, M.-Y. Lu, B.-H. Li, X. Qiu, W.-H. Chang, L.-J. Chen, G. Shvets, C.-K. Shih, and S. Gwo, *Plasmonic nanolaser using epitaxially grown silver film*, Science **337**, 450 (2012).

[10] R.-M. Ma, R. F. Oulton, V. J. Sorger, G. Bartal, and X. Zhang, *Room-temperature sub-diffraction-limited plasmon laser by total internal reflection*, Nat. Mater. **10**, 110 (2011).

[11] M. T. Hill, Y.-S. Oei, B. Smalbrugge, Y. Zhu, T. de Vries, P. J. van Veldhoven, F. W. M. van Otten, T. J. Eijkemans, J. P. Turkiewicz, H. de Waardt, E. J. Geluk, S.-H. Kwon, Y.-H. Lee, R. N otzel, and M. K. Smit, *Lasing in metallic-coated nanocavities*, Nat. Photonics **1**, 589 (2007).

[12] M. T. Hill, M. Marell, E. S. P. Leong, B. Smalbrugge, Y. Zhu, M. Sun, P. J. van Veldhoven, E. J. Geluk, F. Karouta, Y.-S. Oei, R. Nötzel, C.-Z. Ning, and M. K. Smit, *Lasing in metal-insulator-metal sub-wavelength plasmonic waveguides*, Opt. Express **17**, 11107 (2009).

[13] K. Yu, A. Lakhani, and M. C. Wu, *Subwavelength metal-optic semiconductor nanopatch lasers*, Opt. Express **18**, 8790 (2010).

[14] M. P. Nezhad, A. Simic, O. Bondarenko, B. Slutsky, A. Mizrahi, L. Feng, V. Lomakin, and Y. Fainman, *Room-temperature subwavelength metallo-dielectric lasers*, Nat. Photonics **4**, 395 (2010).

[15] J. H. Lee, M. Khajavikhan, A. Simic, Q. Gu, O. Bondarenko, B. Slutsky, M. P. Nezhad, and Y. Fainman, *Electrically pumped sub-wavelength metallo-dielectric pedestal pillar lasers*, Opt. Express **19**, 21524 (2011).

[16] M. Khajavikhan, A. Simic, M. Katz, J. H. Lee, B. Slutsky, A. Mizrahi, V. Lomakin, and Y. Fainman, *Thresholdless nanoscale coaxial lasers*, Nature **482**, 204 (2012).

[17] H. Kogelnik and C. V. Shank, *Stimulated emission in a periodic structure*, Appl. Phys. Lett. **18**, 152 (1971).

[18] B. E. Kruschwitz and T. G. Brown, *Complex-coupled distributed feedback laser with negative differential coupling*, Appl. Phys. Lett. **67**, 461 (1995).

[19] G. A. Turnbull, P. Andrew, M. Jory, W. Barnes, and I. Samuel, *Relationship between photonic band structure and emission characteristics of a polymer distributed feedback laser*, Phys. Rev. B **64**, 125122 (2001).

[20] G. Heliotis, R. D. Xia, G. A. Turnbull, P. Andrew, W. L. Barnes, I. D. W. Samuel, and D. D. C. Bradley, *Emission characteristics and performance comparison of polyfluorene lasers with one- and two-dimensional distributed feedback*, Adv. Funct. Mater. **14**, 91 (2004).

[21] I. D. W. Samuel and G. A. Turnbull, *Organic semiconductor lasers*, Chem. Rev. **107**, 1272 (2007).

[22] H. Matsubara, S. Yoshimoto, H. Saito, Y. Jianglin, Y. Tanaka, and S. Noda, *Gan photonic-crystal surface-emitting laser at blue-violet wavelengths*, Science **319**, 445 (2008).

[23] F. van Beijnum, P. J. van Veldhoven, E. J. Geluk, M. J. A. de Dood, G. W. 't Hooft, and M. P. van Exter, *Surface plasmon lasing observed in metal hole arrays*, Phys. Rev. Lett. **110**, 206802 (2013).

[24] M. P. van Exter, V. T. Tenner, F. van Beijnum, M. J. A. de Dood, P. J. van Veldhoven, E. J. Geluk, and G. W. 't Hooft, *Surface plasmon dispersion in metal hole array lasers*, Opt. Express **21**, 27422 (2013).

[25] V. T. Tenner, M. J. A. de Dood, and M. P. van Exter, *Measurement of the phase and intensity profile of surface plasmon laser emission*, ACS Photonics **3**, 942 (2016).

[26] X. Meng, J. Liu, A. V. Kildishev, and V. M. Shalaev, *Highly directional spaser array for the red wavelength region*, Laser Photon. Rev. **8**, 896 (2014).

[27] J. Stehr, J. Crewett, F. Schindler, R. Sperling, G. von Plessen, U. Lemmer, J. Lupton, T. Klar, J. Feldmann, A. Holleitner, M. Forster, and U. Scherf, *A low threshold polymer laser based on metallic nanoparticle gratings*, Adv. Mater. **15**, 1726 (2003).

[28] J. Y. Suh, C. H. Kim, W. Zhou, M. D. Huntington, D. T. Co, M. R. Wasielewski, and T. W. Odom, *Plasmonic bowtie nanolaser arrays*, Nano Lett. **12**, 5769 (2012).

[29] W. Zhou, M. Dridi, J. Y. Suh, C. H. Kim, D. T. Co, M. R. Wasielewski, G. C. Schatz, and T. W. Odom, *Lasing action in strongly coupled plasmonic nanocavity arrays*, Nat. Nanotechnol. **8**, 506 (2013).

[30] A. H. Schokker and A. F. Koenderink, *Lasing at the band edges of plasmonic lattices*, Phys. Rev. B **90**, 155452 (2014).

[31] M. Ramezani, A. Halpin, A. I. Fernández-Domínguez, J. Feist, S. R.-K. Rodriguez, F. J. Garcia-Vidal, and J. Gómez Rivas, *Plasmon-exciton-polariton lasing*, Optica **4**, 31 (2017).

[32] T. K. Hakala, H. T. Rekola, A. I. Väkeväinen, J.-P. Martikainen, M. Nečada, A. J. Moilanen,

and P. Törmä, *Lasing in dark and bright modes of a finite-sized plasmonic lattice*, Nat. Commun. **8**, 13687 (2017).

[33] A. Yang, T. B. Hoang, M. Dridi, C. Deeb, M. H. Mikkelsen, G. C. Schatz, and T. W. Odom, *Real-time tunable lasing from plasmonic nanocavity arrays*, Nat. Commun. **6**, 6939 (2015).

[34] A. Yang, Z. Li, M. P. Knudson, A. J. Hryn, W. Wang, K. Aydin, and T. W. Odom, *Unidirectional lasing from template-stripped two-dimensional plasmonic crystals*, ACS Nano **9**, 11582 (2015).

[35] A. H. Schokker and A. F. Koenderink, *Statistics of randomized plasmonic lattice lasers*, ACS Photonics **2**, 1289 (2015).

[36] A. H. Schokker and A. F. Koenderink, *Lasing in quasi-periodic and aperiodic plasmon lattices*, Optica **3**, 686 (2016).

[37] H. Kogelnik and C. V. Shank, *Coupled-wave theory of distributed feedback lasers*, J. Appl. Phys. **43**, 2327 (1972).

[38] R. Kazarinov and C. Henry, *Second-order distributed feedback lasers with mode selection provided by first-order radiation losses*, IEEE J. Quantum. Electron. **21**, 144 (1985).

[39] K. Sakai, E. Miyai, and S. Noda, *Two-dimensional coupled wave theory for square-lattice photonic-crystal lasers with tm-polarization*, Opt. Express **15**, 3981 (2007).

[40] M. Koba and P. Szczepanski, *The threshold mode structure analysis of the two-dimensional photonic crystal lasers*, Progress In Electromagnetics Research **125**, 365 (2012).

[41] Y. Liang, C. Peng, K. Sakai, S. Iwahashi, and S. Noda, *Three-dimensional coupled-wave analysis for square-lattice photonic crystal surface emitting lasers with transverse-electric polarization: finite-size effects*, Opt. Express **20**, 15945 (2012).

[42] A. H. Schokker, F. van Riggelen, Y. Hadad, A. Alù, and A. F. Koenderink, *Systematic study of the hybrid plasmonic-photonic band structure underlying lasing action of diffractive plasmon particle lattices*, Phys. Rev. B **95**, 085409 (2017).

[43] J. D. Joannopoulos, S. G. Johnson, J. N. Winn, and R. D. Meade, *Photonic crystals: molding the flow of light*, Princeton university press, 2011.

[44] L. C. Andreani and M. Agio, *Photonic bands and gap maps in a photonic crystal slab*, IEEE J. Quantum. Electron. **38**, 891 (2002).

[45] K. Sakai, E. Miyai, and S. Noda, *Coupled-wave theory for square-lattice photonic crystal lasers with te polarization*, IEEE J. Quantum. Electron. **46**, 788 (2010).

[46] H. P. Urbach and G. L. J. A. Rikken, *Spontaneous emission from a dielectric slab*, Phys. Rev. A **57**, 3913 (1998).

[47] M. Kamp, J. Hofmann, F. Schäfer, M. Reinhard, M. Fischer, T. Bleuel, J. Reithmaier, and A. Forchel, *Lateral coupling-a material independent way to complex coupled dfb lasers*, Opt. Mater. **17**, 19 (2001).

[48] L. Li and C. W. Haggans, *Convergence of the coupled-wave method for metallic lamellar diffraction gratings*, J. Opt. Soc. Am. A **10**, 1184 (1993).

[49] P. B. Johnson and R. W. Christy, *Optical constants of the noble metals*, Phys. Rev. B **6**, 4370 (1972).

[50] R. J. Spry and D. J. Kosan, *Theoretical analysis of the crystalline colloidal array filter*, Appl. Spectroscopy **40**, 782 (1986).

[51] W. L. Vos, R. Sprik, A. van Blaaderen, A. Imhof, A. Lagendijk, and G. H. Wegdam, *Strong effects of photonic band structures on the diffraction of colloidal crystals*, Phys. Rev. B **53**, 16231 (1996).

[52] W. L. Vos, M. Megens, C. M. van Kats, and P. Bösecke, *Transmission and diffraction by photonic colloidal crystals*, J. Phys. Condens. Matter **8**, 9503 (1996).

[53] W. H. Zachariasen, *Theory of X-ray diffraction in crystals*, Dover Publications, 1945.

[54] H. S. Sözüer, J. W. Haus, and R. Inguva, *Photonic bands: Convergence problems with the plane-wave method*, Phys. Rev. B **45**, 13962 (1992).

6

Plasmon "patchwork" lasers: towards low etendue, speckle free light sources

Despite the attractive properties of lasers, like high brightness and good directivity, applying lasers in solid state lighting (SSL) is difficult because of speckle formation from the interference of coherent laser light. To overcome this issue, we propose two types of lasers based on patchworks of small plasmon lattices with different lattice constants. The premise is that they could ultimately form a blue-led pumped broad-area directive emitter with reduced spatial coherence to suppress speckle. An important question is whether different patches couple when assembled together, and how this affects spatial and spectral profiles. In this chapter, we show measurement results on the patchwork lasers and discuss their potential application as low etendue and speckle free sources in SSL.

6.1 Introduction

Lasers have the advantages of high brightness and low etendue, and are widely used in many applications that crucially depend on properties such as high power, collimated output, coherence, or narrow bandwidth. In framework of solid-state lighting, lasers are relevant either as pump source in laser-driven white light sources like laser-driven remote phosphors [1–3], or as illumination source in projection [4]. For instance, high-end cinema projection can use digital mirror device (DMD) beam scanning

of red, green and blue laser channels to offer superior projection brightness and reduced maintenance compared to Xenon lamps [5]. However, high quality lighting or projection using lasers is challenging because of speckle formation. Speckles are high contrast random interference patterns which occur due to high temporal and spatial coherence of lasers and can cause degradation of images [6]. To reduce speckle contrast in, e.g., projection, a variety of methods have been developed based on superimposing statistically independent speckle configurations. This includes using (multiple) sources with different wavelengths, illumination angles and polarizations [7, 8], reducing spatial coherence of the sources [9], dynamically changing the illumination beam or target screen [10–13], etc. Most of these methods require multiple light sources or bulky optics and motors. A compact laser with instantaneous multi-wavelength and low spatial coherence emission could be desirable for creating small, speckle free projection systems.

In Chapter 5, we have introduced plasmon DFB lasers based on arrays of plasmon nanoantennas. Benefiting from the strong plasmon resonance of the arrays, they feature the possibility of lasing from a very small sample area, and flexible "flat-optics" control of frequency and emission pattern through array patterning [14–16]. One could thus envision making plasmonic laser substrates that multiplex many plasmon lasers, and thereby tailor function in the spatial, spectral, and wave vector domain. To use plasmon DFB lasers in lighting and projection applications, two major questions need to be answered. First, what is the efficiency and stability of the plasmon DFB lasers? Second, how can we achieve multi-wavelength, low etendue and speckle free output for high quality lighting or projection?

In this chapter, we consider the possibility of making multi-wavelength, low etendue, speckle free plasmon DFB lasers using so-called patchwork arrays. We introduce two types of arrays: "checkerboards" and "random patchworks". Both are based on patchworks of small plasmon lattices, each of which could operate individually as a DFB laser, similar to the ones studied in the last chapter. The patchwork patterns are similar to the plasmon particle superlattices in Ref. [16], which can also be viewed as collections of single plasmon lattices. Compared with the superlattices in Ref. [16], the patchwork arrays we investigate in this chapter feature different pitches in different patches, and smaller inter-patch distances (a few hundred nm compared with a few micron in Ref. [16]), which can result in quite different inter-patch interaction. From the outset it is unclear if these lasers will operate independently when assembled together in one array, or whether different patches will couple to each other, thereby giving rise to different lasing phenomena. We measure the lasing properties of these patchwork lasers, including the lasing threshold, spectra, angular distribution of lasing emission and spatial coherence. Through these measurements, we investigate the coupling of the patches and look into their potential for low entendue emission and speckle reduction.

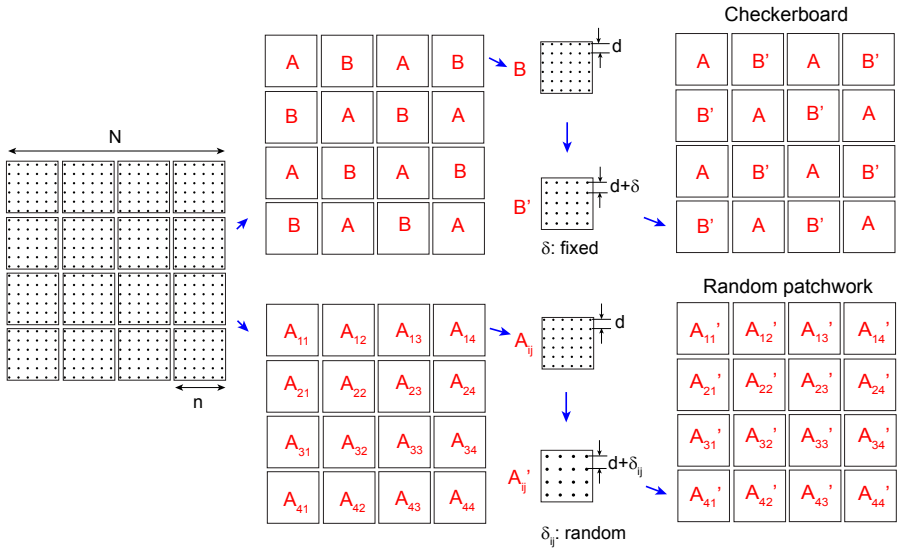

Figure 6.1: A schematic of the sample design. A $N \times N$ square array is divided into patches of $n \times n$. To make a checkerboard array, we change the pitch of the B patches from d to $d+\delta$. The particle numbers are reduced so that the resulting B' patches are not larger than the original B patches. For the Random patchwork arrays, we change the pitches in every patch to $d+\delta_{ij}$ and also change the particle numbers accordingly to fit in the original patch size.

6.2 Sample geometry

We design two types of lasers based on patchworks of Ag particle arrays as illustrated in Fig. 6.1. We start from a square array of $N \times N$ particles with pitch $d = 370$ nm. As introduced in Chapter 5, such arrays can work as lasers at $\lambda_0 \approx 574$ nm ($\omega_0 \approx 3.28 \times 10^{15}$ rad/s), when fabricated on glass and covered with a 350 nm SU8 layer doped with Rh6G. To create patchworks we divide the array into sub-arrays of size $n \times n$, with the divisor N/n an integer. The first design is like a "checkerboard", in which we alternatingly assign the sub-arrays into two groups A and B. The arrays of type A are kept unchanged. For B arrays, we fix the position of the array center, and increase the pitch to $d' = d + \delta$. We note that the size of the B arrays scales with the pitch. To avoid overlapping of particles, we reduce the number of particles in B' to $n' \times n'$, with $n' = [nd/d']$, so that the B' arrays are as large as or smaller than the original B arrays. This design results in a 45 degree rotated super-square-lattice of A and B' with a period of $\sqrt{2}n \cdot d$. In this chapter, we consider $n = 10$, 20, 40, 60, and $\delta = 1$, 2, 4 nm. For all combinations of n and δ, we have $n' = n - 1$. The difference in particle number results in an approximately $d/2$ shift of the B' arrays in x and y directions with respect to the original B arrays.

We call the second design "random patchwork". In this cases each sub-array is expanded or shrunk by adding random numbers δ_{ij} (uniformly distributed over $[-\delta, \delta]$)

to the pitches of each sub-array. Again, to avoid array overlap, we increase or decrease the particle number to $n' \times n'$, with $n' = [nd/d']$. This design results in a collection of sub-arrays of different pitches with their centers fixed in a square lattice with a period of $n \cdot d$.

The designs are implemented with electron beam lithography and lift-off procedures used in Chapter 5, resulting in Ag nanoparticles fabricated on glass substrates. We fix the original pitch and size of the array to be $d = 370$ nm and $N = 240$, and vary n, δ and the range of δ_{ij}. Since the lateral resolution of the electron beam is 0.2 nm, the δ_{ij} are set as random integer multiples of 0.2 nm. The resulting Ag nanoparticles have a cylindrical shape with a diameter of about 60 nm and a height of 30 nm. On top of the arrays, we spin coat a 350 nm thickness SU8 layer doped with about 2.5 wt% Rh6G molecules as a gain medium.

6.3 Analysis of the array geometry

Both the checkerboard and the random patchwork designs can be considered as collections of small square array lasers closely packed in a surface-covering tiling. Depending on whether these small arrays mutually couple, different outputs are expected. In one extreme scenario one would envision each array to lase independently. In this case, the output would be the incoherent sum of emission from individual arrays, at multiple wavelengths (two for the checkerboard, of order $(N/n)^2$ for the random patchworks) determined by the different periods of the patches. Due to the small size of the patches, the lasers would have effectively a small cavity length (L in Eq. (1.12)) and likely require a higher threshold gain compared with a full sized square array. Meanwhile, a small coherent area means a higher angular spread, i.e., a higher etendue according to the uncertainty principle for conjugate variables in Fourier transforms.

The alternative extreme scenario is that the patches couple leading to new extended modes which are coherent over the whole $N \times N$ area. In this case, we would expect the lasing condition and k-space output to be determined by the band structure of the whole array geometry. While a full calculation of such a band structure is a formidable challenge, an estimate can be obtained in the so-called nearly-free photon approximation. This approximation predicts the physics of band folding and band crossing in the limit of very weak scattering by the plasmon particles, but not the formation of stop bands. In this approximation, the band structure of the waveguide modes can be simply estimated by convolving the dispersion of waveguide modes with the Fourier transform of the array geometry (known as "structure factor" or "array factor" in X-ray respective antenna literatures), as we have introduced in Chapter 4. In the following, we examine the Fourier transforms of the checkerboard and random patchworks and estimate the resulting band structure.

By way of example, consider the Fourier transform of a checkerboard array with $n = 10$, $\delta = 1$ nm. The array can be viewed as a square superlattice with pitch $\sqrt{2}nd$ rotated by 45° and convolved with a dimer of neighboring A and B' arrays. According to the convolution theorem, the Fourier transform of the checkerboard is the product

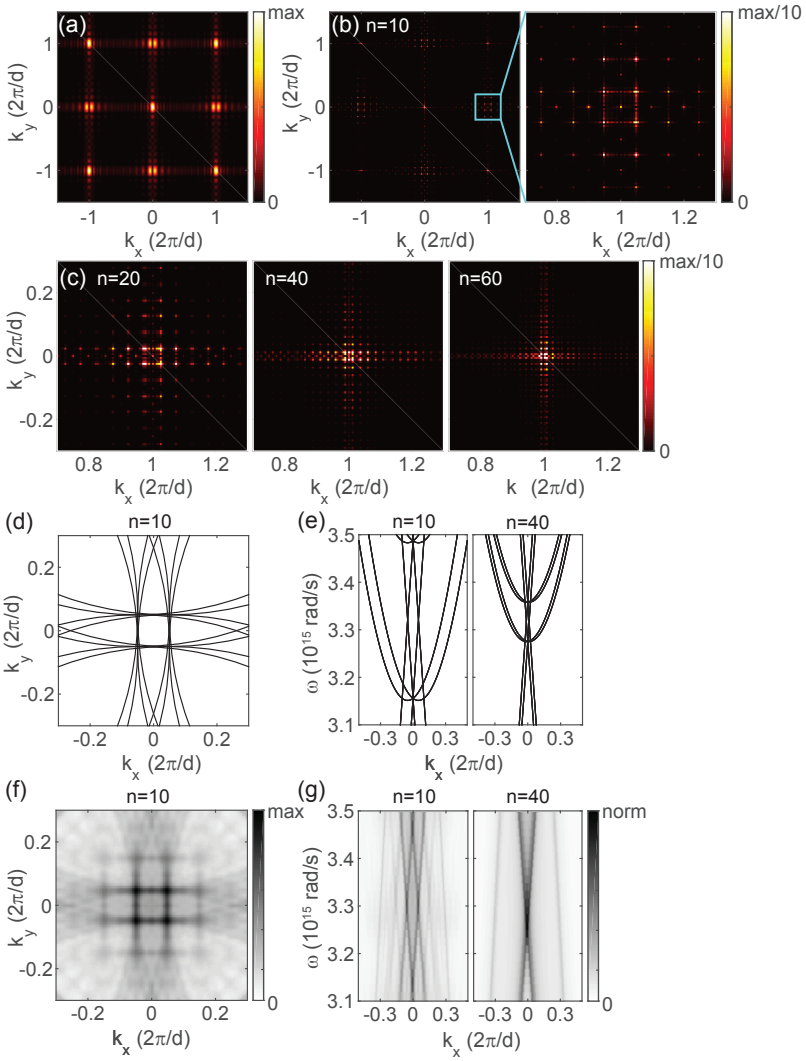

Figure 6.2: (a) Calculated absolute value of Fourier transform of a A-B' dimer with $n = 10$ and $\delta = 1$ nm. (b) Calculated absolute value of Fourier transform of a checkerboard laser with $n = 10$ and $\delta = 1$ nm (left). Groups of peaks occur near $(\pm 1, 0)G$ and $(0, \pm)G$ near (G,0) (right). (c) Calculated absolute value of Fourier transform of a checkerboard laser with $n = 20$, 40, 60 and $\delta = 1$ nm near (G,0). All Fourier transforms are normalized to 1/10 of the maximum at $k_x = k_y = 0$, which equals to the number of particles in the array. (d-e) Illustrations of simplified band structures of checkerboard lasers with $\delta = 1$ nm at (d) ω_0 and (e) $k_y = 0$. (f-g) Calculated band structures of checkerboard lasers with $\delta = 1$ nm at (d) ω_0 and (e) $k_y = 0$. (d)(f) n =10. (e)(g) $n = 10$, 40. (e) is normalized to the maximum. The band structures in (g) are normalized to a normalization factor equal to the maximum of the band structure for $n = 40$.

of the Fourier transform of the rotated lattice, i.e., a 45° rotated square lattice with pitch $G/(\sqrt{2}n)$, with $G = 2\pi/d$, and that of an A-B' dimer. The Fourier transform of an A-B' dimer is shown in Fig. 6.2(a). The half period shift of the B' array leads to destructive interference of Fourier transforms of A and B'. Consequently double peak structures centered around $(\pm1,0)G$ and $(0,\pm1)G$ arise with a dip right at $(\pm1,0)G$ and $(0,\pm1)G$. Multiplication of the two Fourier transforms results in groups of peaks near $(\pm1,0)G$ and $(0,\pm1)G$, at $(\pm1,0)G+(i,j)G/(2n)$ and $(0,\pm1)G+(i,j)G/(2n)$, with $i,j = 0,\pm1$, ... Particularly, four peaks are pronounced in each of the groups, i.e., $(\pm1,0)G+(\pm1,\pm1)G/(2n)$ or $(0,\pm1)G+(\pm1,\pm1)G/(2n)$. The original first order diffraction peaks at $(\pm1,0)G$ and $(0,\pm1)G$ appear to be much weaker due to destructive interference. We note from the above discussion that the *locations* of the peaks are set by the lattice constant of the superlattice, i.e., $\sqrt{2}nd$. On the other hand, δ only has an influence on the Fourier transform of an A-B' dimer and hence determines only the amplitude of the peaks. Figure. 6.2(c) shows a comparison of the Fourier transforms from lattices with varying n. Indeed, the spacing of the peaks scales inversely with n as shown in Figure. 6.2(c). We also find that increasing δ to 2 or 4 nm does not change the position of the peaks in the array factor.

To obtain the band structure, we convolute the calculated absolute value squared Fourier transform of the array with the dispersion of the TE waveguide mode (assuming constant mode index and no cut off) as introduced in Chapter 4. First, we simplify the Fourier transform to δ-peaks at the main maxima $(\pm1,0)G+(\pm1,\pm1)G/(2n)$ and $(0,\pm1)G+(\pm1,\pm1)G/(2n)$. The resulting simplified band structure consists of multiple cones in the $\omega - k_x - k_y$ space, similar as the band structure in Fig. 1.4(b). Fig. 6.2(d) illustrates a constant frequency cut of the band structure of a checkerboard laser with $n = 10$ and $\delta = 1$ nm at $\omega 0$. The waveguide modes at ω_0 with wave vector of $(\pm1,0)G$ and $(0,\pm1)G$ can couple with each other through the diffraction at $(\pm1,0)G+(\pm1,\pm1)G/(2n)$ and $(0,\pm1)G+(\pm1,\pm1)G/(2n)$, and can be coupled out with wave vector of $(\pm1,\pm1)G/2n$. Therefore, most of the bands cross at $(\pm1,\pm1)G/2n$ in Fig. 6.2(d). Fig. 6.2(e) illustrates the band structures of checkerboard lasers with $n = 10$, 40, $\delta = 1$ nm, at $k_y = 0$. When $n = 10$, instead of two straight lines and a parabola crossing at ω_0 and $k_x = 0$ which is expected from square lattices, the band structure of the checkerboard arrays shows four straight lines. These straight lines result from shifting the bands of a square lattice by $(\pm1,\pm1)G/(2n)$ and $(\pm1,\pm1)G/(2n)$ in Fourier space and intersect at two points at $\omega \approx \omega_0$. The parabolas are also shifted in both frequency and $\boldsymbol{k}$. A n increases to 40, the straight bands converge to the two straight bands of a square array with the their intersections converge to ω_0 and $k_x = k_y = 0$. The parabolas are shifted closer to ω_0. To confirm the above simplification, we also calculate the band structure directly from the Fourier transform, as shown in Fig. 1.4(f-g). Indeed, the simplified line structures in Fig. 1.4(d-e) give a good representation of the major photonic bands from the direction calculation.

We apply similar Fourier transform methodology to random patchwork lasers. Depending on the choices of δ_{ij}, the random patchwork arrays can have different realizations. Here in order to make a representative analysis, we consider the average of 20 realizations with -10 nm $< \delta_{\mathrm{ij}} < 10$ nm and calculate the root mean square

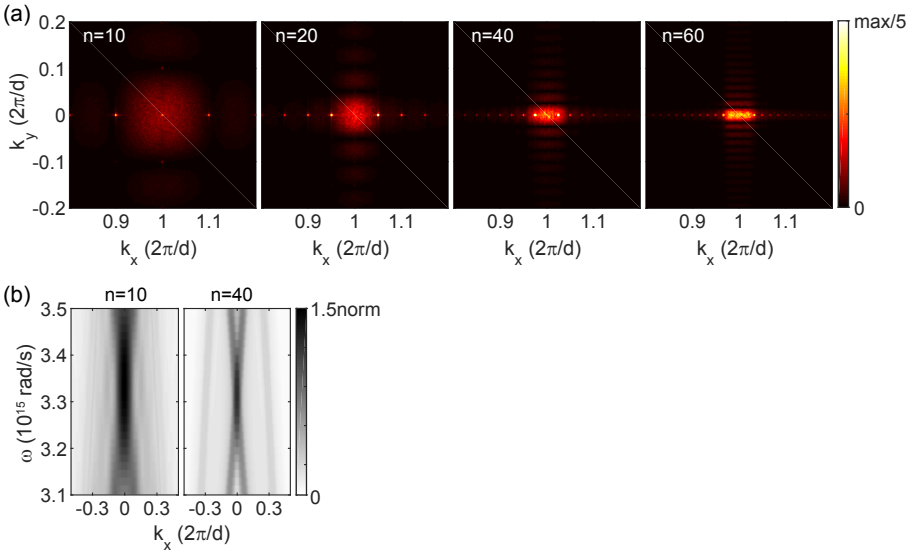

Figure 6.3: (a) Calculated root mean square of Fourier transforms of 20 realizations of random patchwork lasers with $n = 10, 20, 40, 60$ and $|\delta_{ij}| < 10$ nm near $(\pm 1, 0)G$ and $(0, \pm 1)G$. All images are normalized to 1/5 of the maximum at $k_x = k_y = 0$, which equals to the number of particles in the array. (b) Calculated band structures of random patchwork arrays with $n = 10$, 40 and $|\delta_{ij}| < 10$ nm. They are normalized to 1.5 times the normalization factor in Fig. 6.2(g).

of the absolute values of the Fourier transforms from different realizations, for $n = 10, 20, 40, 60$. The calculated patterns also feature high intensity near $(\pm 1, 0)G$ and $(0, \pm 1)G$. Therefore, we plot the results near $(1, 0)G$ in Fig. 6.3(a). Compared to the infinite square array reciprocal lattice, the diffraction orders are broadened (sinc-type broadening expected for small patches), and show speckled patterns. On top of that, the centers of the A_{ij} arrays form a square superlattice, which results in peaks at $(1, 0)G + (i, j)G/n$ with $i,\ j = 0, \pm 1, \pm 1, ...$ Fig. 6.3(b) shows the calculated band structures for the TE modes at $k_y = 0$ for $n = 10$ and 40. The broadening of the Fourier transform near $(\pm 1, 0)G$ and $(0, \pm 1)G$ results in a blurring in the band structure. When $n = 10$, the band structure appear as one major broad band near $k_x = k_y = 0$. When $n = 40$, the random patchwork has similar band structure as that of a square array, with two straight bands and a parabolic band that is blurred in the direction of the frequency. According to this structure factor the waveguide modes in a random patchwork laser are expected to have access to a range of Bragg conditions, suggesting that lasing will involve a distribution of spectral components and output wave vectors.

To recapitulate this section, we can envision two distinct scenarios of operation. In the first scenario, the laser patches will act as independent lasers which should result in multi-wavelength operation (two lines versus $(N/n)^2$ lines for checkerboards and random patchworks), low spatial coherence and a significant threshold penalty. In the alternative scenario, the superlattices offer distributed modes according to the structure

factor analysis. The Fourier transforms and band structures given by the nearly-free-photon approximation indicate that the checkerboard arrays should then tend to lase at $\omega = \omega_0$ and $\boldsymbol{k} = (\pm 1, \pm 1)G/(2n)$. With large n, new lasing modes can occur at the edges of the parabolic bands when they enter the emission spectrum window of the lasing dye (Rh6G). Spatially coherent random patchwork lasers are expected to lase over a spectral range near ω_0 with a blurred Fourier space pattern.

6.4 Measurements

In this section, we report measurements of basic optical properties of the checkerboard and the random patchwork lasers, to investigate their potential application as low-etendue light source for projections. We use the same experimental set up as in Chapter 5. First, we check the analysis in Section 6.3 by measuring the (below threshold) band structure of the arrays. Second, through pump power dependent output measurements, we study the advantages or disadvantages of the checkerboard and the random patchwork lasers in terms of lasing threshold. Third, we examine lasing spectra for potential speckle reduction with multi-wavelength emission. After that, we study the angular distribution, which we obtain by measuring the Fourier space images. Finally, we check the coherence between different patches using double slit experiments.

6.4.1 Band structure

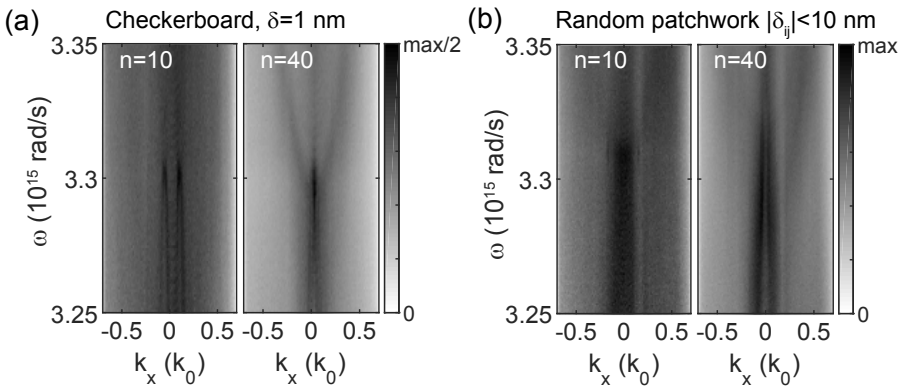

Figure 6.4: Measured band structures at $k_y = 0$ of (a) checkerboard and (b) random patchwork lasers with $n = 10, 40, 60$, $\delta = 1$ nm and $|\delta_{ij}| < 5$ nm. All images are spectrometer camera images first normalized by the corresponding spectra (sum over k_x) and then normalized to the maximum of each resulting image. (a) is obtained with 1000 pulses at 7 % pump power. (b) is obtained with 1000 pulses at 10 % pump power.

We measure the (below threshold) band structures of the checkerboard and random patchwork arrays through spectrally resolved Fourier imaging introduced in Chapter 5.

As shown in Fig. 6.4(a), the checkerboard array with $n = 10$ has four bands crossing at finite k_x near $\omega \approx 3.31 \times 10^{15}$ rad/s, which is similar to the prediction in Fig. 6.2(e). As n increases to 40, the band structure converges to a band structure similar to that of a square array. The random patchwork with $n = 10$ has a broad band near $k_x = 0$ (Fig. 6.4(b)), which is similar with the prediction in Fig. 6.3(b). When $n = 40$, the band structure converges to two straight bands. We are not able to recognize the parabolic band predicted by the calculation as it is too weak. To sum up, the measured band structures of both checkerboard and random patch work lasers show qualitative agreement with the predictions in Section 6.3.

6.4.2 Lasing threshold

We study the input-output behavior by measuring spectra as function of input pulse energy, where we control the input pulse energy using a computer controlled acousto-optical modulator (AOM). The maximum (AOM at 100%) pulse energy corresponds to about 1 μJ, which spreads over an approximately 120 μm wide spot, slightly overfilling the patchwork arrays. The spectrometer collects the emission near $k_y = 0$ with a 10 μm slit. Summing the emission over different k_x, we obtain emission spectra. Figure 6.5(a) shows measured emission spectra from single shot excitations as a function of pump power on different checkerboard lasers with n = 10, 20, 40, 60, and δ=1 nm. All checkerboard arrays show sharp emission peaks (width< 0.5 nm) starting from about 20 % of the maximum pump energy. Similar results are obtained with random patchwork lasers with n = 10, 20, 40, 60, and δ_{ij} <10 nm. To confirm that these peaks are indeed lasing modes, we check their threshold behavior. For each of the samples, we select the modes that emerge at lowest pump power (indicated by the white arrows in Fig. 6.5(a)) and plot the pump power dependence of the emission intensity (within 0.5 nm of the peak wavelength) of these modes, as shown in Fig. 6.5(c) for the checkerboard lasers. All plotted modes have near-zero emission with low pump power, and a drastic increase of the slope of the emission vs pump at about 20 % of the total pump power. The narrow spectral width and non-linear behavior confirm that the checkerboard samples indeed lase.

We fit the curves from 40 % to 80 % pump power with a linear function (black dashed line in Fig. 6.5(c)) to determine the threshold as the intercept point of the fit with the pump power axis. Fig. 6.5(d) shows the lowest lasing threshold of checkerboard lasers with δ =1, 2, 4 nm and random patch lasers with δ_{ij} <10 nm. The measured lasers have thresholds of about 20-30 % of the total laser power ($0.2 - 0.3$ μJ), which is about 2 to 3 times the threshold of a typical plasmon DFB laser such as the one shown in Fig. 5.3(d) in Chapter 5 with a threshold of about 0.1 μJ. This is actually a remarkable finding, since these thresholds are much lower than the threshold of single patches of size n. For example, we have found that an $n = 60$ single array laser (20×20 μm) has a threshold higher than 50 % of our AOM range. The reduction of the lasing threshold for closely spaced patches compared to single ones indicates that coupling between different patches occurs. Note that the slopes of the curves in Fig. 6.5(c) differ by a factor ~ 3. These do not necessarily accurately represent slope efficiency. On

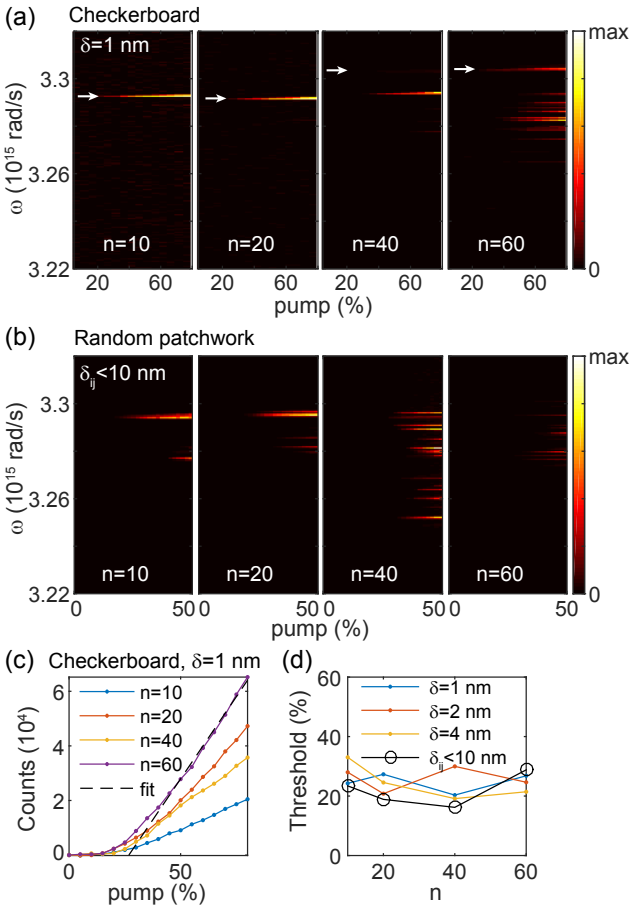

Figure 6.5: (a) Measured spectra at $k_x = 0$ of checkerboard lasers as a function of pump power. n = 10, 20, 40 and 60, δ=1 nm, (b) Measured spectra at $k_y = 0$ of random patchwork lasers as a function of pump power. n = 10, 20, 40 and 60, δ_{ij} <10 nm. (a-b) are normalized to the maxima of each image. (c) Emission intensity at $k_x = 0$ as a function of pump power of the lowest threshold lasing mode measured from checkerboard lasers with n = 10, 20, 40, 60, and δ=1 nm. (d) Lasing thresholds of the lowest threshold modes of checkerboard and random patchwork lasers, with n = 10, 20, 40, 60, δ=1, 2, 4 nm for the checkerboard lasers and δ_{ij} <10 nm for the random patchwork lasers.

the one hand, our detection scheme implies a filtering in wave vector space ($k_y = 0$), meaning that strongly different k-space output can lead to significantly different slope efficiencies. On the other hand, if multimode lasing is a desirable feature, one could also argue that the slope efficiency should be determined from the intensity in the sum of all laser lines, instead of only from the first line. However, due to the different start threshold of the different modes, summing the emission intensity of all lasing lines can result in strongly non-linear input-output behavior, making it difficult to define the

slope efficiency.

6.4.3 Lasing spectra

From Fig. 6.5(a-b) we found that both checkerboard and random patchwork lasers have multiple lasing modes at different frequencies. In this section, we compare the spectra of the lasers to the two extreme scenarios sketched in Section 6.3. First, if all the patches are independent, the checkerboard lasers would have 2 laser lines that are separated by $n_{\mathrm{wg}}\delta$, corresponding to about 1.6, 3.1 and 6.2 nm for δ = 1, 2, 4 nm. The random patchwork lasers would have $(N/n)^2$ laser lines spanning over a wavelength range of 31 nm for -10 nm $< \delta_{\mathrm{ij}} < 10$ nm near the original lasing wavelength λ_0. In the second scenario where all patches are coupled, the checkerboard lasers would have one dominate lasing mode at λ_0, while the random patchwork lasers can have multiple lines near λ_0.

Fig 6.6(a-c) show above threshold spectra from the checkerboard lasers with n = 10, 20, 40, 60, and δ=1, 2, 4 nm. The red bars on the top left indicates the expected 1.6, 3.1 and 6.2 nm lasing wavelength range, defined as the wavelength range spanned by the geometrical Bragg diffraction conditions corresponding to the pitches in the system. When n = 10, the checkerboard lasers tend to emit at one dominant wavelength. This indicates that the checkerboard lasers have a lasing mode that is coherent over the entire array instead of having two sets of patches lasing independently at two frequencies. As n and δ increases, multiple lasing modes (4 to 10 modes) with comparable intensity are obtained over a spectral range of 5 to 10 nm. This is not expected from either independent-patch or coupled-patch pictures. Furthermore, we notice that some of the lasing modes show double peak structures with small wavelength differences (~0.2 nm), as indicated by the red arrows in Fig. 6.6(b). We attribute this slight splitting to degenerate modes that split due to the symmetry breaking in x and y from fabrication defects. Finally, we note that there is a small (a few nm) red shift of the lasing spectra as δ increase from 1 nm to 4 nm. This is relevant to the fact that average particle distance increases with increasing δ in the checkerboard arrays.

The random patchworks also show lasing at multiple wavelengths (2 to 15 lines) within a similar 10 nm band as shown in Fig. 6.6(d). The number of lasing modes does not increase with the decrease of n (patch number $\propto 1/n^2$). While the laser with n = 10 only has two major modes, the laser with n = 40 has a maximum number of modes (about 15 modes). Moreover, the wavelength range is much smaller than the expected 31 nm bandwidth for uncoupled patches. This indicates that the individual patches in a random patchwork lasers likely do not act as independent lasers either, with the lasing wavelength of each patch strongly influenced by coupling between patches.

6.4.4 Angular distribution of emission

We evaluate the angular distribution of laser emission by measuring above-threshold Fourier images. Fig. 6.7(a) shows Fourier images of checkerboard lasers with δ = 1 nm

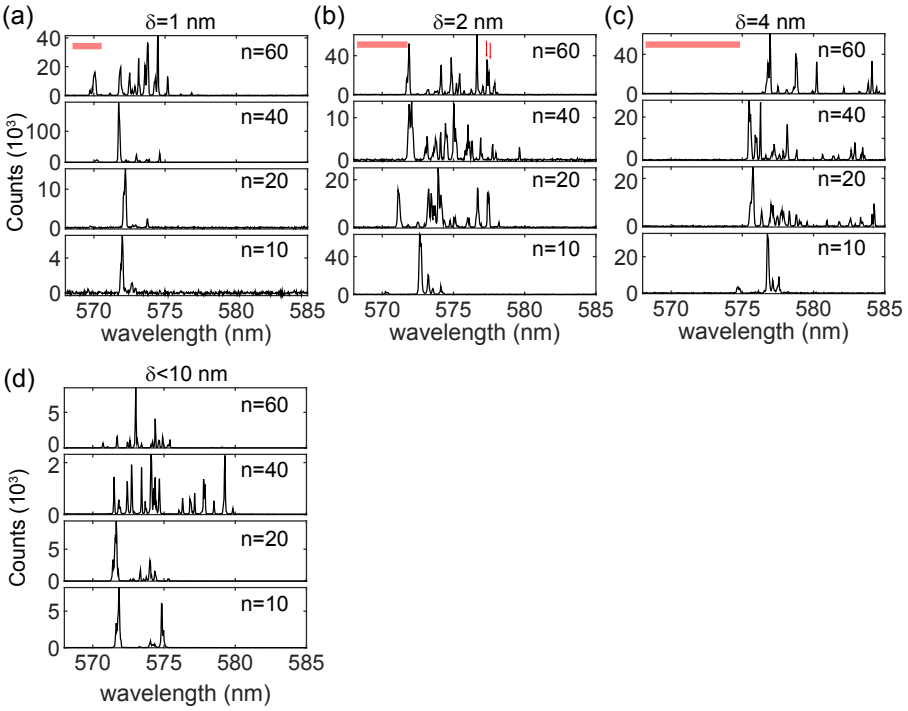

Figure 6.6: (a-c) Measured above threshold lasing spectra of checkerboard lasers at 60% pump power. n = 10, 20, 40, 60. (a) δ=1 nm, (b) δ=2 nm (c) δ=4 nm. The two red arrows in (b) indicate a pair of degenerate modes. (d) Measured above threshold lasing spectra of random patchwork lasers at 50% pump power. n = 10, 20, 40, 60, and δ_{ij} <10 nm.

and $n = 10, 20, 40, 60$ at 60 % pump power, which is well above threshold and reaches the multi-mode lasing regime for large n. For $n = 10, 20$ and 40, the Fourier images show that laser emission appears in a quadruplet of peaks arranged as the vertices of squares around $k_x = k_y = 0$, corresponding to the calculated structure factors in Fig. 6.2(b-e). The peaks shift towards $k_x = k_y = 0$ with increasing n and become indistinguishable for $n = 40$ and 60. Similar results are measured from checkerboard lasers with $\delta = 2, 4$ nm. Like the calculated Fourier transforms and band structures, the above threshold Fourier images do not show a clear dependence on δ. The fact that the Fourier images follow the structure factor of the large checkerboards directly attests to the fact that the lasing modes are coherent across the entire array. Averaging the intensity at different azimuthal angles, we obtain the per solid angle (Ω) intensity distribution as a function of the polar angle θ from the normal direction, as shown in Fig. 6.7(b). When $n = 10$, the checkerboard laser mainly emit at $\theta \approx 0.1$ rad, i.e., 6°. As n increases, the main emission angle decreases and converges to the normal direction.

Figure 6.7(c) shows the Fourier images of random patchwork lasers with $\delta_{ij} < 10$ nm and $n = 10, 20, 40, 60$ at 50 % pump power. The Fourier images also resemble the

Fourier pattern of the arrays near $(\pm 1, 0)G$ and $(0, \pm 1)G$ shown in Fig. 6.3. This is because the lasing modes are the waveguide modes with wave vector of $(\pm 1, 0)G$ and $(0, \pm 1)G$. When coupled out by the array, their resulting wave vectors are determined by the Fourier transform of the array translated by $(\pm 1, 0)G$ or $(0, \pm 1)G$. Figure 6.7(d) shows the lasing intensity distribution as a function of θ. When $n = 10$, the laser emission spans over a large angle range of $\pm 10^\circ$. The angle range decreases with increasing n. These findings are also consistent with the notion that lasing modes are extended over the entire random patchwork.

6.4.5 Coherence

From the measured lasing spectra, we have found that the investigated patchwork lasers tend to lase with inter-patch coupling, instead of having each patch lasing independently. In the meantime, the Fourier-space output supports this view, as the laser output shows diffraction features of the entire superlattice. However, it is unclear how far the inter-patch coupling extends and whether the lasers are coherent over the entire area. To answer these questions, we measure the real space distribution of the lasing spectra and study the spatial coherence with double slit experiments. Fig. 6.8(a) shows the real space spectra of checkerboard lasers with $\delta = 1$ nm, which are images taken with the spectrometer CCD camera. The entrance slit (10 μm) of the spectrometer selects a 0.4 μm wide slice from the center of the measured lasers. The position in the direction of the slit is indicated by one axis of the images. The other axis represents the spectral content of the emission dispersed by the spectrometer grating. For $n = 10$, the major lasing mode is distributed over the whole measured area. As n increases, the real space distribution become less homogeneous. While the highest frequency mode near $\omega = 3.29 \times 10^{15}$ rad/s is in general delocalized over many patches, the lower frequency mode are usually localized on single or a few neighboring patches, particularly on the edge of the array.

To study whether the delocalized modes over the entire array are spatially coherent across the array size, we conduct a double slit experiment. We refer to Chapter 5 for the details of the measurement. The double slit we use is a pair of slits with 1 mm width and 40 mm center-center distance, which selects two 2 μm wide slices near the edges of of the arrays. Fig. 6.8(b) shows the double slit interference patterns of a delocalized mode at $\omega = 3.29 \times 10^{15}$ from the checkerboard array with $n = 10$ and $\delta = 1$ nm. The interference pattern shows clear interference fringes indicating strong spatial coherence across the whole array. Note that for lasers emitting to $k_x = k_y = 0$ like the rectangular array lasers in Chapter 5, the envelope of the interference fringes follows a sinc function. However, this does not apply to the checkerboard lasers. The interference fringes here have an envelope that peaks at non-zero k_x corresponding to the lasing wave vectors. Similar results are measured from the delocalized modes of checkerboard arrays with different n and δ.

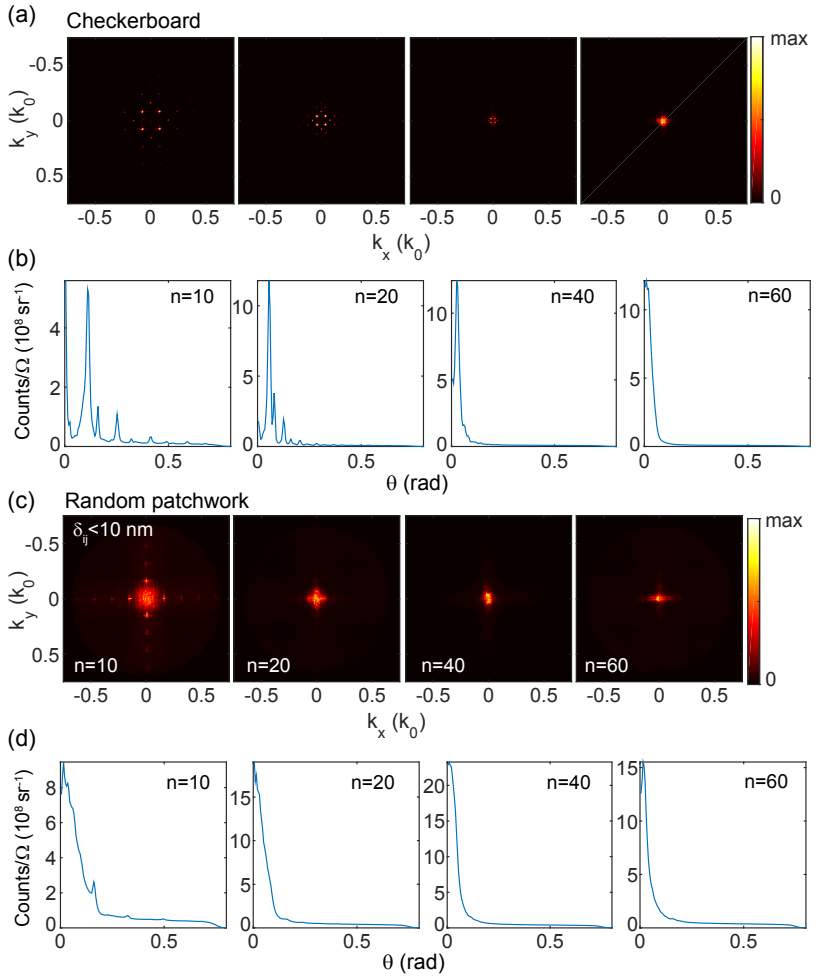

Figure 6.7: (a) Measured above-threshold Fourier images of checkerboard lasers with δ = 1 nm and $n = 10, 20, 40, 60$ at 60 % pump power after an OD 1 filter. (b) Intensity distribution as a function of polar angle θ obtained from (a) by averaging over the azimuthal angle. (c) Measured above-threshold Fourier images of random patchwork lasers with $\delta_{ij} < 10$ nm and $n = 10, 20, 40, 60$ at 50 % pump power. (d) Intensity distribution as a function of θ obtained from (c). The Fourier images are normalized to the maxima of each image.

6.5 Discussion of the physics apparent from the observations

In this section, we discuss the observations in light of the hypotheses formulated in section 6.3. The measurement results show in three aspects that both the checkerboard

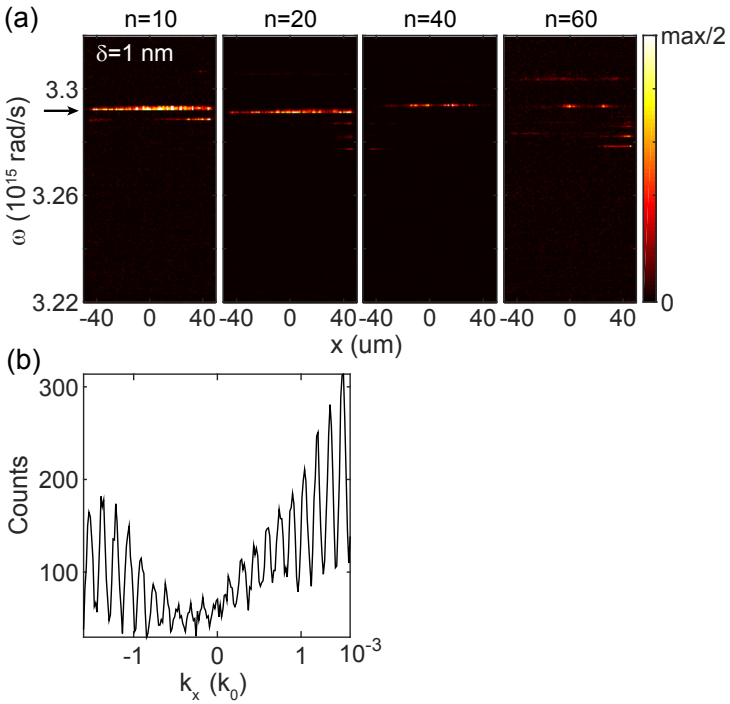

Figure 6.8: (a) Measured real space spectra images of checkerboard lasers with $\delta = 1$ nm, $n = 10$, 20, 40, 60, normalized to the half maxima of each image. (b) Measured double slit interference patterns of the delocalized modes at $\omega = 3.29 \times 10^{15}$ rad/s from checkerboard laser with $\delta = 1$ nm and $n = 10$. Pump power: 100 %.

lasers and the random patchworks support lasing modes that extend over the entire array width. First, lasing thresholds are significantly below that of the constituent single patches alone. Second, the Fourier-space output is well predicted by the array structure factors. Third, spatial imaging shows the same frequency of emission and clear fringes in double split experiments for these modes. On the other hand, the studied lasers are surprisingly multimode, especially for $n > 20$. Moreover, both checkerboards and random patchworks show many lasing frequencies outside the frequency range set by the pitches in the system, i.e., by geometric Bragg conditions. These additional modes tend to be localized on part of the array, i.e., one or a few patches. Overall, this behavior neither follows that of independent patches lasing in an uncoupled fashion, nor of simple extended superlattice modes. The behavior of a complex network of nonlinearly coupled oscillators can be notoriously rich. While working out the physics in this case is outside the scope of this work, here we look into some simpler cases to further understand how the modes emerge.

We compare the spectra of a single patch from a checkerboard, and the spectra of dimers made of just two adjoining square arrays. The lasing spectrum of a single patch

in a checkerboard is measured by only illuminating the area within one patch of pitch 370 nm at the corner of a checkerboard array with $n = 60$. The illumination area is controlled using an iris in the path of the pump laser. As shown in Fig. 6.9(a) (bottom), the single patch has exactly one lasing mode, as expected from a solitary square array laser. This indicates that the coupling phenomena that give rise to multimode output requires that more than one patch is pumped, i.e., when at least two patches feed into each other.

Further, we measure the lasing spectra of dimers of two patches. Each dimer contains two n =60 square arrays that are separated with an edge-to-edge distance of 370 nm. One square array has a period of 370 nm while the other has a period of 370 nm+δ, with δ = 1, 2, 4 nm. In addition to the original mode supported by a single patch, the dimers have more lasing modes at longer wavelength, as shown in Fig. 6.9(a). This indicates that coupling between two patches can already give rise to multi-wavelength lasing. We note that some of the lasing modes of the measured dimers appear to have an equal spacing that is independent on the pitch difference δ. This observation is corroborated by the autocorrelation of the spectra as shown in Fig. 6.9(b). The spectrum autocorrelations of all the dimers show peaks at about $\pm$0.5 nm, indicating that there is indeed a preferred nearest neighbor wavelength spacing of 0.5 nm which is independent on the pitch difference δ.

We hypothesize that the origin of this complex behavior can be found in coupled mode theory, adapted for coupled patches. According to coupled wave theory for DFB lasers, a simple square array laser can already support multiple lasing modes, at approximately equally spaced frequencies [17, 18]. This can be seen from Eq. (5.13) in Chapter 5 for 1D DFB lasers, which has a countably infinite number of solutions. Each solution corresponds to a longitudinal lasing mode with a distinct combination of frequency, threshold gain and spatial distribution. The frequency spacing between different modes from a 1D DFB laser is expected to be inversely proportional to the size of the laser array [17]. Similarly, we expect 2D DFB lasers to have multiple modes with a frequency spacing depending on the array size. We hypothesize that if coupled mode theory is extended to coupled patches, the spatial variation in local pitch will lead to an effective modulation of the coupling constants κ (which acquire an additional position dependent phase) in chapter 5, which in turn will lead to new modes with different spatial distributions, frequencies and threshold gains. A detailed numerical analysis of coupled mode theory with spatially varying coupling constants should be undertaken to ascertain if this could explain the multimode lasing behavior of the dimers and the patchwork lasers, and to see if a scheme for mode assignment is possible.

6.6 Patchwork lasers for SSL applications

In this section, we discuss whether the investigated patchwork lasers have potential advantages for SSL applications in terms of etendue and speckle reduction.

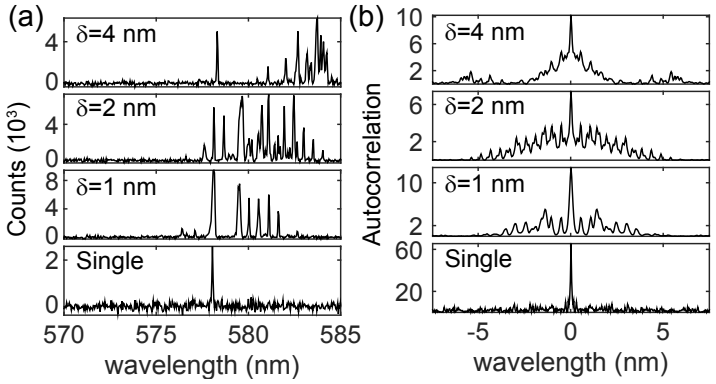

Figure 6.9: (a) Measured above threshold spectra of dimers with δ = 1, 2, 4 nm, 370 nm edge to edge distance and n =60 compared with that of a single patched from a checkerboard array with δ =4 nm and n =60. (b) Autocorrelation of the spectra from (a).

6.6.1 Etendue

From the angular distribution of emission in Fig. 6.7(b)(c), we estimate the etendue of emission. From the perspective of a source, the etendue is the product of the source area and the solid angle subtended by the entrance pupil of the detection system. The areas of the investigated patchwork lasers are $A \approx (N \cdot d)^2 \approx 7885\ \mu m^2$. To estimate the emission angle range, we consider the largest angles at which the intensity decreases to half of the maximum in Fig. 6.7(b)(c). Table 6.1 lists the half maximum angle ($\theta_{1/2}$) and the corresponding etendue calculated as

$$\text{Etendue} = A \cdot \int_{\theta<\theta_{1/2}} d\Omega = A \cdot 2\pi(1-\cos\theta_{1/2}). \tag{6.1}$$

Both checkerboard and random patchwork lasers have etendue from 30 to 400 $\mu m^2 \cdot$sr, which decreases with increasing n. These numbers are much lower than the etendue of typical projection systems using liquid-crystal display (LCD), digital light projection (DLP) and LED based luminescent concentration techniques, which are around 8 to 25 $mm^2 \cdot$sr [19, 20]. The low etendue of our lasers on the one hand benefits from the small emission angular range, and on the other hand is strongly determined by the micron size of arrays.

6.6.2 Speckle reduction

Here we discuss whether the checkerboard or random patchwork lasers carry an advantage for projection from the viewpoint of speckle reduction. When a monochromatic plane wave, or single-mode output of a laser, scatters off of a diffusely scattering screen, the diffuse reflected or transmitted light shows a typical speckle pattern due to interference. The speckle consists of a random arrangement of minima and maxima

Checkerboard, δ = 1 nm				
n	10	20	40	60
$\theta_{1/2}$ (degree)	7.2	3.7	2.0	2.3
Etendue ($\mu m^2 \cdot sr$)	389	105	30	40
Random patchwork, $\lvert\delta_{ij}\rvert < 10$ nm				
n	10	20	40	60
$\theta_{1/2}$ (degree)	4.9	3.2	2.9	2.3
Etendue ($\mu m^2 \cdot sr$)	179	75	62	40

Table 6.1: Angle at the half maximum ($\theta_{1/2}$ and Etendue of the checkerboard and random patchwork lasers estimated from the angular intensity distribution in Fig. 6.7(b)(c).

with 100 % intensity contrast (i.e., truly dark spots). The typical angular width of speckle arising from scattering off a rough surface is λ/L, with L the illuminating spot size [6]. Speckle contrast can be reduced by illuminating with a set of mutually incoherent modes that give uncorrelated speckle patterns, for instance by offering different frequencies simultaneously, or offering illumination from different spatial modes. When averaging N completely uncorrelated speckle patterns, the speckle contrast is reduced by $1/\sqrt{N}$ [6]. For our plasmon patchwork lasers, the best-case estimate for their speckle reduction qualities is obtained by assuming that each laser line gives a speckle pattern that is completely uncorrelated from that at other lines. Given that we have multimode behavior with up to 15 lines, a speckle contrast of 25 % remains. This argument is a best-case estimate, as it does not take into account that when a random medium is illuminated, speckle patterns at close frequencies are actually correlated. Indeed, frequency correlations in speckle patterns are well studied in the field of light propagation in random media [21, 22]. The bandwidth over which the plasmon patchworks lase spans up to about 15 nm, i.e., about 2.5 % relative bandwidth, corresponding to a 22 micron coherence length. Speckle patterns at different frequencies are correlated unless the scattering involves path length differences exceeding the coherence length [23]. The most common way to introduce path length differences is to use a diffusive medium in reflection (typical path length is on the order of mean free path ℓ), or transmission (typical path length is proportional to L^2/ℓ with L the thickness of the medium) [24]. For typical diffusive media such as white paint and white paper, the mean free path is between 4 µm (paint) [25] and 20 µm (paper) [26]. Therefore, the multi-wavelength emission from our lasers can indeed be useful for speckle reduction, even though a further bandwidth increase can be beneficial.

6.7 Conclusion

We have studied two types of plasmon DFB lasers (checkerboard and random patchwork) as potential multi-wavelength, low etendue, speckle free light sources for the applications of lighting and projection. To test their performance, we have conducted measurements on the lasing threshold, spectra, Fourier space intensity distribution

and spatial coherence. Both checkerboard and random patchwork lasers show multi-wavelength lasing at small angles to the normal direction, with modest thresholds which are only 2 to 3 times those of a rectangular array laser with a similar size. Real space intensity and coherence measurements show that the lasers support both local modes spanning one or a few patches and modes extended over the entire array. Measurements on dimer lasers indicate that coupling between neighboring patches can already give rise to multiple lasing modes. Further investigation on the origin of these modes requires quantitative studies on the lasing wavelengths and thresholds.

From the measurement in the Fourier space, we have found that checkerboard and random patchwork lasers with large $n = 40$ and 60 can have an etendue of 30 to 60 $\mu m^2 \cdot sr$, which is a few orders of magnitude lower than the etendue of typical state-of-the-art projection systems. Moreover, these lasers have multiple (up to 15) lasing lines over a wavelength range of about 10 to 15 nm, which can be potentially useful for speckle reduction.

Despite the possible advantages of the patchwork lasers in etendue and speckle reduction, there are a few potential issues remaining to be settled. For projection applications, a very high power output (on the level of 1000 lm) from a small emission volume is required. This requires strong material stability and efficient color conversion. The stability of our lasers under illumination of a strong pump field is unclear. Possible issue includes bleaching of the dye molecules and overheating. The efficiency of the color conversion of our lasers is limited by three factors: absorption of the pump light, Ohmic loss in the metal particles and the extraction efficiency of the emitted light. The absorption of the pump light is mainly limited by the sub-micron thick dye-doped waveguide layer. Within the investigated pump power range (below 1 μJ per pulse), a 350 nm thick layer doped with 2.5 wt% Rh6G molecules is expected to absorb about 35 % of the pump light (near normal incidence). The absorption further decreases if the pump power is increased to near saturation level at which most of the Rh6G molecules are excited within the fluorescent lifetime or in our case by one pump pulse. This gives an upper bound to the optical power conversion efficiency of 0.33 (assuming 100 % QY and extraction efficiency), which is still competitive compared with the 0.22 efficiency in Ref. [20]. The absorption in the linear regime can be further improved by engineering the illumination pattern to selectively match the optical modes supported by the structure [27, 28]. Ohmic loss in the metallic particles can strongly reduce the external QY of the lasers. Minimizing the metallic loss requires careful design of the sample structure and illumination pattern [29]. The extraction efficiency of our lasers is not ideal due to the emission to both sides of the sample plane, which result in an approximately 50 % reduction in the extraction efficiency. Unidirectional lasing can be realized, e.g., by having the plasmon particles connected with a metal film [30].

In addition, the absolute luminous flux of our lasers is also limited by the Rh6G molecule density. The molecule area density of a 350 nm SU8 layer doped with 2.5 wt% Rh6G is about 1.3×10^7 μm^{-2}. In the extreme case where all molecules are continuously pumped with sufficiently high power, each molecule would emit at a rate of about 0.1 ns^{-1} (assuming 10 ns lifetime). We can maximally obtain an areal photon emission rate of 1.3×10^{15} $\mu m^{-2} \cdot s^{-1}$, corresponding to 0.3 $lm/\mu m^2$ for a wavelength of

570 nm. To reach 1000 lm, as required for projectors, we need at least a sample area of 3300 μm^2 (assuming 100 % QY and extraction efficiency, and sufficient pump power). Note that this output would correspond to a heat dissipation area density of about 3×10^{-5} $W \cdot \mu m^{-2}$ from the Stokes shift, which cannot be sustained by the 350 nm thin film. Therefore, over-heating will be a potential issue in this case. We further consider a pulsed operation. If the lasers are excited by nanosecond pulses with a repetition rate of 1 kHz, we can have a maximum areal photon emission rate of 1.3×10^{10} $\mu m^{-2} \cdot s^{-1}$, and thus a sample area of 330 mm^2 is required for 1000 lm output.

References

[1] K. A. Denault, M. Cantore, S. Nakamura, S. P. DenBaars, and R. Seshadri, *Efficient and stable laser-driven white lighting*, AIP Adv. **3**, 072107 (2013).

[2] Y. H. Song, E. K. Ji, B. W. Jeong, M. K. Jung, E. Y. Kim, and D. H. Yoon, *High power laser-driven ceramic phosphor plate for outstanding efficient white light conversion in application of automotive lighting*, Sci. Rep. **6**, 31206 (2016).

[3] A. F. George, S. Al-waisawy, J. T. Wright, W. M. Jadwisienczak, and F. Rahman, *Laser-driven phosphor-converted white light source for solid-state illumination*, Appl. Opt. **55**, 1899 (2016).

[4] R. Knize, *Full color solid state laser projector system*, 1994, US Patent 5,317,348.

[5] B. D. Silverstein, A. F. Kurtz, J. R. Bietry, and G. E. Nothhard, *25.4: A laser-based digital cinema projector*, SID Symposium Digest of Technical Papers **42**, 326 (2011).

[6] J. W. Goodman, *Speckle phenomena in optics: theory and applications*, Roberts and Company Publishers, 2007.

[7] J. I. Trisnadi, *Speckle contrast reduction in laser projection displays*, 2002.

[8] T.-T.-K. Tran, Ø. Svensen, X. Chen, and M. N. Akram, *Speckle reduction in laser projection displays through angle and wavelength diversity*, Appl. Opt. **55**, 1267 (2016).

[9] E. Rawson, *Speckle minimization in projection displays by reducing spatial coherence of the image light*, 1977, US Patent 4,035,068.

[10] E. G. Rawson, A. B. Nafarrate, R. E. Norton, and J. W. Goodman, *Speckle-free rear-projection screen using two close screens in slow relative motion*, J. Opt. Soc. Am. **66**, 1290 (1976).

[11] L. Wang, T. Tschudi, T. Halldórsson, and P. R. Pétursson, *Speckle reduction in laser projection systems by diffractive optical elements*, Appl. Opt. **37**, 1770 (1998).

[12] S. C. Shin, S. S. Yoo, S. Y. Lee, C.-Y. Park, S.-Y. Park, J. W. Kwon, and S.-G. Lee, *Removal of hot spot speckle on laser projection screen using both the running screen and the rotating diffuser*, Displays **27**, 91 (2006).

[13] T.-K.-T. Tran, X. Chen, Ø. Svensen, and M. N. Akram, *Speckle reduction in laser projection using a dynamic deformable mirror*, Opt. Express **22**, 11152 (2014).

[14] A. H. Schokker and A. F. Koenderink, *Statistics of randomized plasmonic lattice lasers*, ACS Photonics **2**, 1289 (2015).

[15] A. H. Schokker and A. F. Koenderink, *Lasing in quasi-periodic and aperiodic plasmon lattices*, Optica **3**, 686 (2016).

[16] D. Wang, A. Yang, W. Wang, Y. Hua, R. D. Schaller, G. C. Schatz, and T. W. Odom, *Band-edge engineering for controlled multi-modal nanolasing in plasmonic superlattices*, Nat. Nanotechnol. **12**, 889 (2017).

[17] H. Kogelnik and C. V. Shank, *Coupled-wave theory of distributed feedback lasers*, J. Appl. Phys. **43**, 2327 (1972).

[18] K. Sakai, E. Miyai, and S. Noda, *Coupled-wave theory for square-lattice photonic crystal lasers with te polarization*, IEEE J. Quantum. Electron. **46**, 788 (2010).

[19] G. Derra, H. Moench, E. Fischer, H. Giese, U. Hechtfischer, G. Heusler, A. Koerber, U. Niemann, F.-C. Noertemann, P. Pekarski, J. Pollmann-Retsch, A. Ritz, and U. Weichmann, *Uhp lamp systems for projection applications*, J. Phys. D: Appl. Phys. **38**, 2995 (2005).

[20] D. K. G. de Boer, D. Bruls, and H. Jagt, *High-brightness source based on luminescent concentration*, Opt. Express **24**, A1069 (2016).

[21] C. A. Thompson, K. J. Webb, and A. M. Weiner, *Diffusive media characterization with laser speckle*, Appl. Opt. **36**, 3726 (1997).

[22] A. P. Mosk, A. Lagendijk, G. Lerosey, and M. Fink, *Controlling waves in space and time for imaging and focusing in complex media*, Nat. Photonics **6**, 283 (2012).

[23] O. L. Muskens, T. van der Beek, and A. Lagendijk, *Angle dependence of the frequency correlation in random photonic media: Diffusive regime and its breakdown near localization*, Phys. Rev. B **84**, 035106 (2011).

[24] M. B. van der Mark, M. P. van Albada, and A. Lagendijk, *Light scattering in strongly scattering media: Multiple scattering and weak localization*, Phys. Rev. B **37**, 3575 (1988).

[25] P. M. Johnson, T. van der Beek, and A. Lagendijk, *Diffuse imaging and radius dependent frequency correlations in strongly scattering media*, Opt. Express **22**, 13330 (2014).

[26] A. Badon, D. Li, G. Lerosey, A. C. Boccara, M. Fink, and A. Aubry, *Smart optical coherence tomography for ultra-deep imaging through highly scattering media*, Sci. Adv. **2**, e1600370 (2016).

[27] G. Lozano, D. J. Louwers, S. R. Rodriguez, S. Murai, O. T. Jansen, M. A. Verschuuren, and J. Gómez Rivas, *Plasmonics for solid-state lighting: enhanced excitation and directional emission of highly efficient light sources*, Light Sci. Appl. **2**, e66 (2013).

[28] G. Pirruccio, M. Ramezani, S. R.-K. Rodriguez, and J. Gómez Rivas, *Coherent control of the optical absorption in a plasmonic lattice coupled to a luminescent layer*, Phys. Rev. Lett. **116**, 103002 (2016).

[29] K. Guo, G. Lozano, M. A. Verschuuren, and J. Gómez Rivas, *Control of the external photoluminescent quantum yield of emitters coupled to nanoantenna phased arrays*, J. Appl. Phys. **118**, 073103 (2015).

[30] A. Yang, Z. Li, M. P. Knudson, A. J. Hryn, W. Wang, K. Aydin, and T. W. Odom, *Unidirectional lasing from template-stripped two-dimensional plasmonic crystals*, ACS Nano **9**, 11582 (2015).

Summary

In this thesis, we study the manipulation of light emission using plasmon nanoantennas in the context of solid state lighting (SSL) applications. The major task in SSL is to produce white light sources with very high luminous efficacy, controlled angular distribution and a sufficient color rendering index (CRI). State-of-the-art solid state lighting techniques usually use remote phosphors to convert the light from highly efficient blue LEDs or lasers to light with lower frequencies in order to generate white light. The most commonly used phosphor materials in SSL such as YAG:Ce have the advantage of a very high internal quantum yield, but typically one needs thick material to absorb sufficient blue light, and it is difficult to control etendue and emission spectrum. Main challenges are to reduce material use, and simultaneously control emission directivity and spectrum, but without penalty in external quantum yield, and ultimately also while handling very large power densities and thermal loads. Plasmon nanoantennas and arrays of plasmon nanoantennas are able to strongly modify the light emission of remote phosphors through various mechanisms including pump enhancement, emission rate enhancement and directivity control. Also, they can provide the feedback for lasing in scenarios where emitter number density and pump strength would suffice to provide net gain. In this thesis, we have conducted experimental and theoretical studies on several different optical systems with plasmon nanoantennas, and discussed their potential applications for SSL.

Chapter 2 reports LDOS enhancement measurements on periodic lattices of nanoantennas. A new method inspired by stochastic localization microscopy techniques was introduced to overcome the diffraction limit of conventional microscopy techniques. This method enables sub-wavelength resolution measurements on periodic nanostructures using a simple confocal microscope. Using this method, we have experimentally mapped the LDOS enhancement for wavelength of 605 nm from a hexagonal array of Al nano-pyramids with an in-plane resolution of about 40 nm that is well below the wavelength. The map agrees well with FDTD simulation results. Further FDTD simulation indicates that the LDOS enhancement of the investigated plasmon lattices is a result of localized surface plasmon resonances of individual antennas and nearest-neighbor coupling, while the lattice modes supported by the plasmon lattices do not introduce a significant influence on LDOS.

In Chapter 3, we introduce a new type of plasmon antennas called "dendritic optical antennas". Different from conventional optical antennas that can only be addressed optically, the dendritic antennas can in principle support both electrical connection and optical function. We have identified the optical resonances of the dendritic antennas by combining transmittance measurements and two independent theoretical methods (FEM and V-MoM). Furthermore, we have investigated the potential of using these modes to enhance the emission efficiency of emitters in a narrow gap in the center of the antennas. With FEM simulation and photoluminescence intensity and lifetime measurements, we found evidence for a 58-fold Purcell enhancement in the center of the antennas. The design of dendritic optical antennas can serve as a bridge connecting optical and electronic functionalities, and thereby point the way to the integration of optical and electronic devices.

Chapter 4 studies directivity control from a type of aperiodic arrays of plasmon antennas, i.e., Vogel's spirals. Vogel's spirals have broadband and circularly symmetric Fourier transform patterns, which is advantageous compared with periodic arrays if one desires directional enhancement of emission that is broadband in wavelength and wider in angular span. As a result, they are expected to offer broadband and isotropic emission enhancement for remote phosphors. In Chapter 4, we have measured the optical response and photoluminescence enhancement from Vogel's spirals of Au antennas using dark field microscopy, k-space microscopy and k-space polarimetry microscopy. The results indicate that the response of spirals to optical field can be modeled as arrays of uncoupled point dipoles. We further found that the spirals can out-couple the waveguide modes generated by a thin film doped with fluorescent molecules, resulting in a photoluminescence enhancement of a factor 2 in the direction normal to the surface over a broad spectral band of about 60 nm. This enhancement, in spite of the low enhancement factor, is useful for producing broadband directional enhancement to remote phosphors. Integrated over the cone of emission angles, the directional enhancement is competitive with that of narrow-angle periodic arrays.

In Chapter 5 and 6, we have looked into DFB lasers based on plasmon lattices. Compared with conventional DFB lasers using non-resonant gratings, plasmon DFB lasers have shown outstanding features such as strong Purcell enhancement and strong feedback. In Chapter 5, we have looked further into the uniqueness of plasmon DFB lasers, by comparing real space intensity and band structure measurements with coupled wave theory, i.e., a standard theory for DFB lasers. Results from experiment and theoretical calculation show that, while the coupled wave theory for dielectric DFB lasers offers a reasonable parametric fit model for the spatial intensity distribution in plasmon DFB lasers, the resulting coupling strengths that emerge as fit parameter can not be consistently interpreted in the coupled-mode framework. In particular, the coupling strengths for dielectric DFB lasers would simultaneously describe band structures and real space intensity distributions, and can be calculated from simple plane-wave analysis. Instead, for plasmonic DFB lasers, the coupling strengths that describe spatial intensities do not give consistent descriptions of stop band edges. The coupling strength and band edge shifts are strongly related to the resonant nature of the plasmon particle polarizabilities, which are very poorly captured by plane-wave based

models. This resonant characters is a main distinction from conventional DFB lasers.

In Chapter 6, we have designed two types of plasmon DFB lasers, in the forms of checkboard and random patchworks, as low-etendue, multi-wavelength, and thereby potentially speckle-free light sources for SSL applications like projection. Several performance metrics of these patchwork lasers have been measured, including the lasing threshold, spectra, etendue and spatial coherence. Both designs show multi-wavelength and low etendue lasing without significant increase in lasing threshold, which can be potentially beneficial for SSL applications.

Samenvatting

In dit proefschrift bestuderen we hoe men de emissie van licht kan optimaliseren en manipuleren met behulp van plasmonische nano-antennes, in de context van toepassingen in LED verlichting. De grootste uitdaging voor LED technologie is om witte lichtbronnen te produceren met zeer hoge efficiëntie, gecontroleerde hoekverdeling en voldoende kleurweergave-index (KWI). De nieuwste LED technieken gebruiken gewoonlijk een laag fosforen om licht van zeer efficiënte blauwe LED's of lasers om te zetten in licht met lagere energie, dat wil zeggen in groen, oranje en rood, zodat het fosfor samen met het niet geabsorbeerde blauwe licht een heldere en witte lichtbron realiseert. De meest gebruikte fosformaterialen, zoals YAG:Ce, hebben het voordeel van een zeer hoge interne kwantum efficiëntie. Helaas heeft men echter door de beperkte absorptiecoëfficiënt een dikke laag materiaal nodig om voldoende blauw licht te absorberen. Daarnaast is het moeilijk om de hoekverdeling en het emissiespectrum te manipuleren. Zo worden in LED-verlichtingstoepassingen vaak grote en verliesgevende optische componenten (zogenaamde secundaire optica) zoals reflectoren, lensen en free-form optics gebruikt om licht te bundelen. De belangrijkste uitdagingen voor nanoschaal fotonische technieken toegepast op LEDs zijn dan ook om materiaalverbruik te verminderen, en om gelijktijdig de emissiedirectiviteit en -spectrum te controleren. Deze vereisten dienen gerealiseerd te worden zonder vermindering van externe quantum efficientie en dienen uiteindelijk ook te functioneren bij zeer grote vermogensdichtheden en thermische belastingen. Plasmon nanoantennas en roosters van plasmon nanoantennas kunnen de lichtemissie van afgelegen fosforen sterk wijzigen, door middel van verschillende mechanismen inclusief nabije-veld versterking van het excitatielicht, verhoging van de emissiesnelheid en directiviteitscontrole. Ook kunnen ze de benodigde *feedback* voor lasers vormen in scenario's met hoge fluorofoordichtheid en pompsterkte. Dit proefschrift rapporteert experimentele en theoretische studies van verschillende optische systemen met plasmon nanoantennas en bespreekt hun potentiële toepassingen voor LED technologie.

Hoofdstuk 2 rapporteert metingen van een verbetering van de lokale toestandsdichtheid (LDOS) in periodieke roosters van nanoantennas. Een nieuwe methode, geïnspireerd door stochastische lokalisatiemicroscopie (zoals PALM en STORM)

wordt geïntroduceerd om de diffractielimiet van conventionele microscopie te overwinnen. Met deze methode kunnen sub-golflengte resolutie metingen op periodieke nanostructuren worden uitgevoerd met een eenvoudige confocale microscoop. Met deze methode hebben we de LDOS-versterking experimenteel in kaart gebracht bij een golflengte van circa 600 nm in een hexagonaal rooster van Al-nano-pyramiden met een resolutie in het vlak van ongeveer 40 nm, ruim kleiner dan de golflengte. Deze kaart komt goed overeen met FDTD simulatie resultaten. Verdere FDTD-simulaties geven aan dat de LDOS-versterking van de onderzochte plasmonroosters een gevolg is van gelokaliseerde oppervlakteplasmonresonanties van individuele antennes en koppeling tussen aanliggende deeltjes, terwijl de collectieve roostertoestanden die door de plasmonroosters worden ondersteund geen significante invloed op LDOS hebben.

In Hoofdstuk 3 introduceren we een nieuw type plasmon antennes genaamd "dendritische optische antennes". Anders dan conventionele optische antennes die alleen optisch kunnen worden aangeslagen, kunnen de dendritische antennes in principe zowel een elektrische verbinding als een optische functionaliteit hebben omdat ze uit een aaneengesloten vertakt netwerk bestaan van nanodraden. We hebben de optische resonanties van de dendritische antennes geïdentificeerd door transmissiemetingen en twee onafhankelijke theoretische methoden (FEM en V-MoM) te combineren. Verder hebben we de mogelijkheden onderzocht om deze resonanties te gebruiken om de emissie-efficiëntie van emitters in een smalle kloof in het midden van de antennes te verbeteren. Met FEM-simulatie en metingen van fotoluminescentie-intensiteit en levensduur vonden we bewijzen voor een 58-voudige Purcell-verbetering in het midden van de antennes. Het ontwerp van dendritische optische antennes kan een brug slaan tussen nanofotonische en nano-electronische funtionaliteit.

Hoofdstuk 4 bestudeert directiviteitscontrole in een specifiek type aperiodische roosters van plasmonantennes; de Vogel spiraal. Vogel spiralen hebben breedbandige en cirkelsymmetrische Fourier-transformatiepatronen, die voordelig zijn in vergelijking met periodieke roosters als men een directionele versterking van de emissie wenst met een breedbandig golflengtespectrum en een grote hoekverdeling. Als gevolg hiervan wordt verwacht dat ze breedbandige en isotrope emissieverbetering voor fosforen bieden. In Hoofdstuk 4 hebben we de optische respons en fotoluminescentieverbetering gemeten van Vogels spiralen van gouden antennes met behulp van donkerveldmicroscopie, Fouriermicroscopie en Fourier-opgeloste polarimetrische microscopie. De resultaten wijzen erop dat de respons van spiralen op licht kan worden gemodelleerd als dat van roosters van ontkoppelde puntdipolen. Verder vonden we dat de spiralen licht, gegenereerd door een dunne laag met fluorescerende moleculen, vanuit golfgeleidertoestanden naar het verreveld kunnen verstrooien. Dit resulteert in een fotoluminescentieverhoging van een factor 2 in de richting haaks op het oppervlak over een brede spectrale band van ongeveer 60 nm. Deze verbetering, ondanks de ogenschijnlijk lage verbeteringsfactor, is bruikbaar voor het produceren van breedband richtingsverbetering van fosforen. Geïntegreerd over de gehele kegel van emissiehoeken, is de fotoluminescentieverhoging namelijk even goed als die van periodieke roosters met een smalle hoekverdeling, die immers hele hoge verhogingen alleen bereiken voor hele kleine hoekbereiken.

In Hoofdstuk 5 en 6 hebben we gekeken naar *distributed feedback* (DFB) lasers op basis van plasmon roosters. In vergelijking met conventionele DFB lasers met niet-resonante roosters, hebben plasmon DFB lasers uitstekende eigenschappen, zoals sterke Purcell versterking en sterke feedback. In Hoofdstuk 5 hebben we de unieke eigenschappen van plasmon DFB lasers bestudeerd, door het vergelijken van metingen van intensiteitsprofielen en bandstructuur met gekoppelde-golftheorie, een standaard theorie voor DFB lasers. Resultaten van experiment en theoretische berekening tonen aan dat, hoewel de gekoppelde-golftheorie voor diëlektrische DFB-lasers een redelijk parametrisch fitmodel voor de ruimtelijke intensiteitsverdeling in plasmon DFB-lasers biedt, de resulterende koppelingssterktes die als fit-parameter verschijnen niet consistent kunnen worden geïnterpreteerd in het gekoppelde-toestandsmodel. De koppelingssterktes voor diëlektrische DFB-lasers kunnen namelijk tegelijkertijd bandstructuren en intensiteitsprofielen beschrijven, en kunnen worden berekend uit eenvoudige vlak-golfanalyse. Voor plasmonische DFB lasers daarentegen geven de koppelingssterktes die ruimtelijke intensiteiten beschrijven geen consistente beschrijvingen van de bandenstructuur, dat wil zeggen van de stopband. De koppelingssterkte en verschuivingen van de stopband houden sterk verband met de resonante aard van de polariseerbaarheid van de plasmon-deeltjes, die zeer slecht door vlakke-golf-gebaseerde modellen worden voorspeld. Dit resonante karakter vormt een belangrijk onderscheid met conventionele DFB lasers.

In Hoofdstuk 6 hebben we twee soorten plasmon DFB-lasers, in regelmatige (schaakbord) en in willekeurige lappendekenpatronen, ontworpen als lage-etendue, multi-golflengte lichtbronnen. Deze hebben hierdoor potentie als heldere lichtbronnen zonder ongewenste interferentiepatronen, zogenoemde 'spikkelpatronen', hetgeen essentieel is voor verlichtingstoepassingen als projectorbron in *beamers*. Verscheidene eigenschappen van deze patchwork lasers zijn gemeten, waaronder de laserdrempel, spectra, etendue en ruimtelijke coherentie. Beide ontwerpen werken als multi-golflengte en lage-etendue laser, zonder een significante toename van de laserdrempel. Dit maakt hen interessante kandidaten voor verlichtingstoepassingen.

List of publications

This thesis is based on the following publications:

- K. Guo, M. A. Verschuuren, and A. F. Koenderink, *Superresolution imaging of the local density of states in plasmon lattices*, Optica **3**, 289 (2016). (**Chapter 2**)
- K. Guo, A. Antoncecchi, X. Zheng, M. Sallam, E. A. Soliman, G. A. E. Vandenbosch, V. V. Moshchalkov, and A. F. Koenderink, *Dendritic optical antennas: scattering properties and fluorescence enhancement*, Sci. Rep. **7**, 6223 (2017). (**Chapter 3**)
- K. Guo, M. Du, C. I. Osorio, and A. F. Koenderink, *Broadband light scattering and photoluminescence enhancement from plasmonic vogel's golden spirals*, Laser Photonics Rev. **11**, 1600235 (2017). (**Chapter 4**)
- K. Guo and A. F. Koenderink, *Spatial intensity of plasmonic distributed feedback lasers*, In preparation. (**Chapter 5**)
- K. Guo, S. Kasture, and A. F. Koenderink, *Plasmon "patchwork" lasers: towards low etendue, speckle free light sources*, In preparation. (**Chapter 6**)

Other publications by the author:

Journal articles:

- W. C. Germs, K. Guo, R. A. J. Janssen, and M. Kemerink, *Unusual thermoelectric behavior indicating a hopping to bandlike transport transition in pentacene*, Phys. Rev. Lett. **109**, 016601 (2012).
- K. Guo, G. Lozano, M. A. Verschuuren, and J. G. Rivas, *Control of the external photoluminescent quantum yield of emitters coupled to nanoantenna phased arrays*, J. Appl. Phys. **118**, 073103 (2015).

- L. Langguth, A. H. Schokker, K. Guo, and A. F. Koenderink, *Plasmonic phase-gradient metasurface for spontaneous emission control*, Phys. Rev. B **92**, 205401 (2015).
- D. K. G. de Boer, M. A. Verschuuren, K. Guo, A. F. Koenderink, J. Gómez Rivas, and S. R.-K. Rodriguez, *Directional sideward emission from luminescent plasmonic nanostructures*, Opt. Express **24**, A388 (2016).
- S. Brittman, S. Z. Oener, K. Guo, H. Āboliņš, A. F. Koenderink, and E. C. Garnett, *Controlling crystallization to imprint nanophotonic structures into halide perovskites using soft lithography*, J. Mater. Chem. C **5**, 8301 (2017).

Patents:

- M. Verschuuren, B. Lozano, R. Gomez, and K. Guo, *Plasmonic-based illumination device*, 2015, PCT/EP2015/060719 United States Patent Application, filed May 14, 2015
- M. Verschuuren, M. Lunz, K. Guo, G. Barbero, and R. Van Brakel, *Solid state illumination device based on non-radiative energy transfer*, PCT/EP2015/060821 United States Patent Application, filed May 18, 2015

Acknowledgments

Being a PhD student in Resonant Nanophotonics group in AMOLF in the last four years has been a unique experience for me. It is meaningful not only because four years is a significant fraction of time of my life, but also because of the knowledge I have gained, the people I got to know, and the luxuriant culture of work and life I have experienced.

First of all, I would like to thank my supervisor Femius Koenderink. Your abundant knowledge in both theory and experiment, and substantial support are essential for my PhD project. As a supervisor, Femius is quite 'special' in many ways, in the large amount of time that he invests with group members, in the large varieties of help he offers from solving experiment issues to explaining textbook knowledges, and in the entertainment he brings to us as a colleague. Femius, I am grateful for the PhD position you offered, with which I have learned, grown and enjoyed. I am more grateful for the effort you have spent in helping me become a good scientist.

Next, I would like to thank my co-promoter Jaime Gómez Rivas. Thank you for your guidance during my master project, for offering me the PhD position as a co-promoter, and for the useful discussions during my PhD project.

Another name I want to mention is Marc Verschuuren, the supervisor of my master project and a collaborator of my PhD project. Marc was the person who led me into the field of solid state lighting and plasmonics, and eventually led me to my PhD project. Marc, I am grateful for your help and encouragement in the past five years. Apart from that, thank you for offering samples for my projects and being cool when I kept breaking them.

During my PhD, I have received an opportunity to supervise a master student. It was a peculiar and pleasant experience. I would like to thank Mengqi Du, for the honor of being the daily supervisor of your master project. I am grateful for your contributions to my thesis, as well as the happy moments we shared and the things we learned together.

Working in Resonant Nanophotonics group is very enjoyable thanks to the welcoming environment created by our friendly group members. A lot of thanks to all the former and current group members of the resonant nanophotonics group. Thank you for

your help in and out of working hours. And thank you for the interesting discussions at group meetings, coffee breaks and our casual group outings.

Apart from the scientific discussions with colleagues, the completion of my PhD project also largely relies on the help of the supporting staff in AMOLF, including our group technician Marko Kamp, Hinco Schoenmaker (from group of Ultrafast Spectroscopy), cleanroom staff, and other colleagues from the software, electronics, and mechanical engineering departments. I am grateful for their professional support and their patience to my questions and requests, without which none of my experiments would have worked as efficiently.

My PhD thesis contains a lot of collaboration works with colleagues from AMOLF, DIFFER, Philips and KU Leuven. I would like to thank all the collaborators. It was a pleasure to work with you and I am grateful for your contributions. Meanwhile, I also thank NWO, Philips and Lumiled for funding the projects.

AMOLF offers a very friendly and relaxed working environment which I have always enjoyed. I thank AMOLF for being a good employer that cares about the feelings of employees. I also thank all the colleagues for making the nice environment, particularly the supporting and management groups.

Finally, I would like to thank my friends and family members. Thank you for the enjoyable time we spend together and your unconditional support.